Copyright

by

Patrick Ponath

2017

The Dissertation Committee for Patrick Ponath Certifies that this is the approved version of the following dissertation:

Epitaxial Functional Oxide Integration on Germanium

Committee:

Alexander A. Demkov, Supervisor

John G. Eckerdt, Co-Supervisor

Keji Lai

Alex De Lozanne

Maxim Tsoi

Epitaxial Functional Oxide Integration on Germanium

by

Patrick Ponath

Dissertation

Presented to the Faculty of the Graduate School of

The University of Texas at Austin

in Partial Fulfillment

of the Requirements

for the Degree of

Doctor of Philosophy

The University of Texas at Austin

August 2017

Dedication

To my family and friends

Acknowledgements

There are many individuals to whom I am grateful for their guidance and support during my graduate studies. Foremost, I would like to express my sincere gratitude to my Ph.D. advisor Prof. Alexander A. Demkov for his help, support and encouragement throughout my Ph.D. I'm very thankful for the opportunity to work in his research laboratory as his first experimental student. I cannot remember a single time during my Ph.D. when he didn't have time for my questions, discussion of research results or general progress, which is exceptional. His enthusiasm for physics is encouraging and enlightening and I am glad that I could develop my research skills under his guidance. I'm also very thankful for the numerous international conferences and meetings I could attend during my Ph.D. to also experience other active research fields. It was a pleasure and honor to work with him as a supervisor.

I would also like to thank Prof. John Ekerdt, Prof. Keji Lai, Prof. Alex de Lozanne, and Prof. Maxim Tsoi for their time and valuable feedback as members of my qualifying and dissertation committee.

I am extremely grateful for our brilliant lab manager and research scientist Dr. Agham Posadas, who taught me all the necessary skills and tools in the Advanced Atomic Design Lab. He never hesitated to share his incredible knowledge and always patiently answered all of my questions in full detail. In the rare case that he didn't have

an answer, his intuition and clues were always helpful and most often correct. I'd also like to thank him for proofreading and improving my publications.

I have had the privilege of working with many wonderful graduate students within Prof. Demkov's research group. The supportive, helpful and respectful nature of each member made the time during my Ph.D. very enjoyable. Foremost, I would like to thank my former colleagues Alex Slepko, Hosung Seo, Miri Choi, Kristy Kormondy, Andrew O'Hara, Kurt Fredrickson as well as Martin McDaniel and Thong Ngo from Prof. Ekerdt's group. Kurt Fredrickson and Andrew O'Hara carried out the theoretical calculations that contributed to my publications and this dissertation. Fruitful discussions always arose from working closely with theorists in our group.

I have also had many thought provoking discussions with fellow group members Elliott Ortmann, Jaqueline Kremer, Wei Guo, Ali Hamze, Donghan Shin, Lingyuan Gao, Tobias Hadamek and our newest group member Marc Reynaud. It was a great time working with them and I wish them all the best for their research career.

There are also several members of Prof. Ekerdt's research group that I would like to acknowledge, whom I spent many hours working alongside, including Edward Lin, Bryce Edmondson, Shen Hu, and Pei-Yu Chen. It was a pleasure working with all of them.

I would also like to thank the two former post-docs Richard Hatch and Chungwei Lin who have shared their vast wealth of knowledge about ARPES and XPS with me.

Throughout the last few years, I had the opportunity to collaborate with several other research groups which have been instrumental in getting a deeper understanding of my graduate studies. These collaborations included the group of David Smith at Arizona State University with his graduate students HsinWei Wu and Sirong Lu, the group of Chadwin Young at The University of Texas at Dallas with his graduate student Jian Wang, the group of Sergei Kalinin and Rama Vasudevan at Oak Ridge National Laboratory, the group of professor Keji Lai at the University of Texas at Austin, Yujin Cho who is a graduate student at Prof. Downer's group at the University of Texas at Austin, as well as Ray Duffy and Paul Hurley at Tyndall National Institute.

I'm forever grateful for the great time I spent with my friends outside of work, in particular Abdul Zaidan, Jasim Azizi, Calina Man, Emanuel Lissek, Ahmad Hassan, my roommates Heidi Seinige and Kirsten Meemann, as well as my two best friends in Germany, Benjamin Firlus and Jan Blinne.

Finally, I'm extremely grateful for the support and love from my whole family throughout this long journey of living away from home. Although they weren't exactly excited about my plans on spending another 6 years in a foreign country to do a Ph.D., I'm very thankful to have always felt their encouragement and unconditional support.

Immense gratitude is also owed to Morgan Dhanraj for her love, patience, understanding and unconditional support throughout the whole time of my PhD, making this the best time of my life. She was always there for me and knew how to cheer me up. I couldn't have made it without her.

It was all these people who helped me accomplishing this wonderful milestone in my life.

Epitaxial Functional Oxide Integration on Germanium

Patrick Ponath, Ph.D.

The University of Texas at Austin, 2017

Supervisor: Alexander A. Demkov

Co-Supervisor: John G. Eckerdt

Germanium, with its higher hole and electron mobility is a potential candidate to replace silicon as a channel material in a field effect transistor in the future. The integration of high quality crystalline oxides on semiconductors still remains a challenge due to lattice defects, a lattice constant mismatch as well as a possible thermodynamic instability between the thin film and the substrate. In this work we report the integration of functional oxides on germanium, which exhibit a wide variety of useful physical properties such as ferromagnetism, superconductivity or ferroelectricity which are of high interest for future electronic devices as i.e. for the development of a ferroelectric field-effect transistor. The focus of this thesis lies on the study of the high-κ and ferroelectric material barium titanate, grown on germanium (001) by using an oxide molecular beam epitaxy machine. Further characterization techniques as x-ray diffraction, x-ray reflectivity, x-ray photoelectron spectroscopy, atomic force microscopy and electrical measurements are used to study the properties of the oxide films and to obtain a deeper understanding of their interface qualities with the substrate. This research contributes

significantly for the development of a ferroelectric field-effect transistor and oxide heterostructures on germanium in general.

Table of Contents

List of Tables xvi

List of Figures xvii

Chapter 1: Introduction 1

1.1 Chapter overview 8

1.2 References 10

Chapter 2. Background information 16

2.1 Ge(001) surface 16

2.2 $BaTiO_3$ 20

2.3 Ferroelectricity and Landau-Devonshire Theory 23

2.3.1 Historic background and polarization 23

2.3.2 Landau-Devonshire theory 25

2.3.3 Second order phase transition 27

2.3.4 First order phase transition 28

2.3.5 Coupling to strain 28

2.4 Ferroelectric field effect transistor 32

2.5 References 37

Chapter 3. Molecular beam epitaxy and experimental techniques 42

3.1 Molecular Beam Epitaxy 42

3.1.1 General overview 42

3.1.2 Working principle and components 43

3.1.3 Main chamber 46

3.1.4 Cryopanel 47

3.1.5 Pumps 48

3.1.6 Effusion cells 48

3.1.7 E-beam evaporator 50

3.1.8 RF plasma source 51

3.1.9 Quartz crystal microbalance 51

3.1.10 Sample stage 52
3.1.11 Kinetic theory of gases for MBE 53
3.1.12 Growth modes 55
3.2 RHEED 57
3.2.1 Working principle 57
3.2.2 Kinematic diffraction 58
3.2.3 Real RHEED patterns 60
3.3 XPS 62
3.3.1 General description 62
3.3.2 Working principle 64
3.3.3 Surface sensitivity 66
3.3.4 XPS peaks and analysis 67
3.3.5 Characteristic core level peaks 67
3.3.6 Auger peaks 69
3.3.7 Quantification 69
3.4 X-ray diffraction (XRD)/X-ray reflectivity (XRR) 71
3.4.1 Overview 71
3.4.2 2θ-θ scan 75
3.4.3 ω-scan (rocking curve) 76
3.4.5 X-ray reflectivity 77
3.4.6 Density 80
3.4.7 Thickness and surface roughness 80
3.5 AFM 82
3.5.1 Working principle 82
3.6 References 84
Chapter 4. Ge(001) surface cleaning methods for device integration 86
4.1. Cleaning conditions and metric of cleanliness 87
4.2 UV light and plasma exposure 90
4.2.1 Cleaning principle 90
4.2.2 UV light exposure 93

4.2.3 O_2 plasma treatment ... 96
4.2.4 H_2 plasma treatment and H_2 annealing ... 97
4.3 Ion sputtering and Ge regrowth ... 98
4.3.1 Sputtering process ... 99
4.3.2 Ion sputtering of the Ge surface ... 101
4.3.3 Ion sputtering and Ge regrowth ... 103
4.4 Wet-etching ... 108
4.4.1 Water rinse ... 110
4.4.2 Hydrofluoric acid (HF) ... 112
4.4.3 Ammonium hydroxide (NH_4OH) ... 120
4.4.4 Hydrochloric acid (HCl) ... 124
4.4.5 Other etchants ... 129
4.4.6 Summary of wet-etching ... 131
4.5 Conclusion ... 133
4.6 References ... 135

Chapter 5. Preparation of a clean Ge(001) surface using oxygen plasma cleaning 142
5.1 Introduction ... 142
5.2 Experimental Details ... 144
5.3 Results and Discussion ... 147
5.4 Conclusion ... 153
5.5 References ... 154

Chapter 6. Carrier density modulation in a germanium heterostructure by ferroelectric switching ... 156
6.1 Introduction ... 157
6.2 Results ... 160
6.2.1 First principal calculations ... 160
6.2.2 Sample preparation and growth ... 162
6.2.3 Lattice constant determination using XRD ... 163
6.2.4 High-Angle Annular Dark-Field Microscopy ... 164
6.2.5 Ferroelectricity confirmed by BE-PFM and BEPS ... 165

6.2.6 Field effect demonstrated by microwave impedance microscopy167
6.3 Conclusion 171
6.4 Methods..171
6.4.1 Film Deposition 171
6.4.2 Electron Microscopy 172
6.4.3 Density functional theory..173
6.4.4 Band-Excitation Piezo Force Microscopy and Spectroscopy...173
6.4.5 Microwave Impedance Microscopy...174
6.5 References..174
Chapter 7. Monolithic integration..178
7.1 Introduction..178
7.2 Experimental details...180
7.3 Materials Characterization 184
7.3.1 Reflection high-energy electron diffraction (RHEED)............184
7.3.2 X-Ray diffraction (XRD) 185
7.3.3 TEM and SEM 186
7.4 Conclusions..188
7.6 References..190
Chapter 8. Contradictory nature of Co-doping in ferroelectric $BaTiO_3$ 193
8.1 Introduction..194
8.2 Experimental Details...196
8.3 Computational details 199
8.4 Results and Discussion 200
8.4.1 RHEED 200
8.4.2 X-Ray Photoemission Spectroscopy..201
8.4.3 X-ray diffraction 203
8.4.4 Electron Microscopy 205
8.4.5 Piezo Force Microscopy measurement 208
8.4.6 Magnetic Measurements 209
8.5 Theoretical Modeling..211

8.6 Discussion 220
8.7 Conclusion 223
8.8 References 223

Chapter 9. Summary and outlook 228
9.1 Summary 228
9.2 Outlook and future work 230

Appendix 232

Bibliography 237

List of Tables

Table 4.1: Chemical bond energies of organic molecules found on the Ge surface.92

Table 4.2: Summary, results and recipes for each discussed cleaning method. Legend: ++: Excellent, +: Sufficient; -: Poorly; --: Insufficient; X: Not examined/does not apply..132

Table 5.1: Procedures for wet etching the germanium surface. Samples A1 and A2 illustrate the effect of *in situ* annealing right after wet-etching. Samples B1-B3 are used to study the effect of acid concentration on the surface roughness. All samples (except A1 and C1) are annealed at 500°C for 2.5 h and subsequently at 600°C for 0.5 h (ramping rate: 5°C/min) before the final annealing step which is shown in the Table. The mean value and the standard deviation of the surface roughness were calculated using several 5 × 5 μm^2 images of the sample's surface.147

List of Figures

Figure 2.1: Diamond crystal structure 16

Figure 2.2: Top view of the Ge(001) surface: green balls: top layer; dark green balls: lowered surface atom; purple balls: bottom layer. (a) Unreconstructed (1 × 1) surface, (b) b(2 × 1) surface reconstruction, with dimers lying parallel to the surface, (c) p(2 × 2) and (d) c(4 × 2) surface reconstruction. Side view: (e) Ge surface dimers, lying parallel to the surface. (f) For surface energy reduction the dimers buckle asymmetrically, leading to a charge transfer from the bottom to the top surface atom. 18

Figure 2.3: The cubic ABO_3 perovskite crystal structure. The B site atom (blue) is surrounded by 6 oxygen atoms (red), forming an octahedron, while the coordination number for the A atom (green) is 12. 20

Figure 2.4: Unit cell of $BaTiO_3$ (Ba: green, O: red, Ti: blue) in the (a) downward polarization and (b) upward polarization. 21

Figure 2.5: Responses of a (a) dielectric and (b) ferro-electric material to an externally applied electric field...24

Figure 2.6: Free energy as a function of the spontaneous polarization of the paraelectric phase (left) and the ferroelectric phase (right) 26

Figure 2.7: Second order phase transition: (a) Free energy as a function of temperature T, (b) spontaneous polarization vs. temperature and (c) susceptibility as a function of temperature. 27

Figure 2.8: First order phase transition: (a) free energy as a function of temperature T, (b) spontaneous polarization vs. temperature and (c) susceptibility as a function of temperature. 28

Figure 2.9: Strain vs. temperature phase diagram for BTO. Taken from [60] 30

Figure 2.10: The ferroelectric field-effect transistor is the combination of the two devices of a Fe RAM, a MOSFET and ferroelectric capacitor, by replacing the dielectric material of the transistor with a ferroelectric material. This non-volatile, low power consuming memory device would experience reduced fatigue, due to its non destructive readout and more aggressive device scaling could be achieved in comparison to Fe RAM. 32

Figure 3.1: Schematic view of an oxide molecular beam epitaxy machine. 44

Figure 3.2: The MBE is connected with the XPS and an ALD system via a transfer line to allow *in situ* sample transfer without exposing samples to the ambient..45

Figure 3.3: Left: MBE chamber in the Advanced Atomic Design Laboratory. Right: Cryopanel used to cool the inside of the chamber walls to avoid re-evaporation of adsorbed materials. 47

Figure 3.4: Low-temperature Knudsen effusion cell used in our system. Figure taken from Mantis deposition [6]. 49

Figure 3.5: 4 pocket electron beam evaporation system. Figure taken from Ajaint [7]. 50

Figure 3.6: Radio frequency plasma source. A nitrogen and oxygen plasma source are connected to the MBE. Figure taken from Scienta Omicron [8].51

Figure 3.7: A quartz crystal microbalance is used to calibrate the metal fluxes prior to deposition. Taken from [11] 52

Figure 3.8: Vapor pressure chart of selected metals as a function of temperature [12]. 54

Figure 3.9: Cross sectional view of the three different epitaxial thin film growth modes. 56

Figure 3.10: Typical RHEED geometry. Electrons are accelerated in the electron gun and impinge the sample surface under a grazing angle. The diffraction pattern can be detected by screen and CCD camera. 57

Figure 3.11: Top and side view of the reciprocal lattice rods intersecting with the Ewald sphere, producing a diffraction pattern on the phosphor screen. 59

Figure 3.12: RHEED image of (a) a cleaned single crystal Ge(001) surface. Sharp diffraction sports, arranged on a Laue ring are visible. (b) RHEED pattern of a 10 nm thick BTO film grown on Ge with monolayer roughness. (c) shows a polycrystalline RHEED pattern while (d) is an example of a 3 dimensional growth. 61

Figure 3.13: XPS system in the Advanced Material Design Lab. 62

Figure 3.14: An Al Kα X-ray beam impinges on the sample surface. Due to the photoelectric effect, electrons with a material specific kinetic energy are emitted and analyzed by the hemispherical analyzer.......................65

Figure 3.15: Survey scan of an oxygen plasma-cleaned Ge(001) surface. The core level peaks of Ge can clearly be identified. The absence of an O 1*s* and C 1*s* peak indicates an extremely clean surface..............................67

Figure 3.16: High resolution Ge 3*d* core level spectrum of a cleaned Ge(001) surface. The spin orbit split between the Ge $3d_{5/2}$ and Ge $3d_{3/2}$ peak is clearly visible. The two peaks are separated by ~0.585 eV. 68

Figure 3.17: Setup of the Rigaku Ultima IV XRD machine. The X-rays are guided through a set of optics before and after diffraction. A scintillation counter is used to detect the incoming X-ray photons. The X-ray source and detector can move independently along a circle. 71

Figure 3.18: Incoming X-rays with a wavelength λ can only diffract constructively, if Bragg's law is satisfied. 72

Figure 3.19: 2θ-θ scan of a 10 nm thick BTO film, grown on 2 nm STO on Ge(001). Each peak can be clearly identified to a crystal plane of BTO, STO or Ge, respectively. 73

Figure 3.20: High resolution BTO(002) peaks for compressively strained and unstrained BTO. Under compressive strain the peak shifts to lower 2θ values, while tensile strain shifts peaks to higher 2θ values. 76

Figure 3.21: Left: For an ω-scan the detector and X-ray source are fixed to a specific Bragg angle, while the sample slightly tilts around the Bragg angle. In the case of the Phillips XPERT and Ultima IV, the source and detector move simultaneously, while the sample stage is fixed. Right: Difference of rocking curve scans for a highly ordered crystalline and slightly more disordered thin film. 77

Figure 3.22: If the incidence X-ray beam is less than the critical angle θ_c, total external reflection occurs (red arrows). At the critical angle, the X-rays can propagate parallel to the surface (black arrow), while for incidence angles larger than the critical angle, both, reflection and refraction occurs. 78

Figure 3.23: XRR signal of a 45 nm thick BTO thin film on a STO/Si template.79

Figure 3.24: Schematics of an AFM. Taken from [29]. 83

Figure 4.1: (a) Ge surface with organic contamination (black). (b) Atomic oxygen (red) reacts with carbon on the surface and forms volatile CO, CO_2 and H_2O leaving behind a carbon-free Ge surface (c). 91

Figure 4.2: C 1*s* peak intensity as a function of UV exposure time. Reproduced from J. Vac. Sci. Technol. A **11**, 2553 (1993), with the permission of AIP Publishing. 94

Figure 4.3: O 1*s* peak intensity from a Ge wafer after undergoing process III with a 30 min UV exposure as a function of temperature. Reproduced from J. Vac. Sci. Technol. A **11**, 2553 (1993), with the permission of AIP Publishing. 95

Figure 4.4: ARPES spectrum of a Ge (001)-2 × 1 surface measured using a photon energy of 21.22 eV showing surface states. Reproduced with permission from Phys. Rev. B **89**, 115318 (2014). Copyright 2014 American Physical Society. 96

Figure 4.5: Schematics of a collision cascade. The incoming He^+ ion (ruby) can transfer a fraction of its energy and momentum to the primary atoms (green), which can in turn collide with secondary (blue), ternary (orange) and quaternary (purple) atoms. If the energy is large enough and the direction of the momentum points towards the vacuum half-space, a small number of atoms can leave the target (red arrow). 99

Figure 4.6: Top and side view of the structural model proposed by Wang [59] for the (1+2)-DV complex. Bottom: Line scan of such a defect. Reproduced with permission from Phys. Rev. B **50**, 2406 (1994). Copyright 1994 American Physical Society. 103

Figure 4.7: (a) STM image of the Ge(001) surface obtained after two ion sputtering/annealing cycles. b) STM image after enhancing the ion energy and with six cleaning cycles. Reproduced with permission from Nanotechnology **17**, 2396-2398 (2006). Copyright 2006 Institute of Physics. 104

Figure 4.8: Schematics of the H-passivation of Si. Reproduced with permission from Phys. Rev. Lett. **65**, 504-507 (1990). Copyright 1990 American Physical Society...117

Figure 4.9: GeO_2 thickness evolution during NH_4OH-based cleaning of the Ge surface. Reproduced with permission from J. Electrochem. Soc. **156** (11), 813-817 (2009). Copyright 2009 Electrochemical Society....122

Figure 4.10: Plot of the surface roughness dependency from the different wet-etching conditions using HF, HCl and H_2O_2. Reproduced with permission from Nanotechnology **22**, 145604 (2011). Copyright 2011 Institute of Physics. 126

Figure 4.11: Structural models for the Ge(001)-c(4 × 2) and Cl/Ge(001)-(2 × 1). Upon Cl chemisorptions, the asymmetric dimers become symmetric. Reproduced with permission from Phys. Rev. B. **32**, 8052-8056 (1985). Copyright 1985 American Physical Society. 128

Figure 5.1: Averaged surface roughness of samples A1-C1. Each sample corresponds to a different etching and/or annealing conditions given in Table 1.148

Figure 5.2: (a) AFM image of the germanium surface after the wet etching treatment and subsequent annealing without plasma exposure; (b) AFM image of the same sample after the oxygen plasma cleaning and subsequent annealing. The germanium surface is free of any contamination and much smoother than before the plasma cleaning. 149

Figure 5.3: RHEED image of the germanium sample along the [110] zone axis after the oxygen plasma cleaning showing intense and sharp half order spots, indicating a 2 × 1 reconstruction...150

Figure 5.4: (a) The Ge 3*d* spectrum shows the characteristic peak for pure germanium. The surface is free of any GeO_2, since no features of any possibly remaining germanium oxides, which have higher binding energies, are detectable. (b) The O 1*s* spectrum shows the non-existence of oxygen on the surface. The two broad features which can be seen are due to Ge $L_2M_{23}M_{23}$ and $L_3M_{23}M_{23}$ Auger electrons. (c) The C 1*s* spectrum shows no residue of carbon could be found on the cleaned surface, whose characteristic peak would have been at expected around 284.5 eV. 151

Figure 5.5: ARPES spectra taken at 300 K with a photon energy of $h\nu$=21.22 eV at various emission angles, θ_e, along the [010] crystallographic direction. Structures labeled with *S* are interpreted as surface-related features, and those with *A* to a direct bulk transition. The sharpness of the photoemission spectra, and the presence of the surface features are a clear indication of the surface quality. 152

Figure 6.1: Calculation supercell: The supercell used in the DFT calculations, consisting of vacuum, BTO, STO and B-doped Ge. The cell is mirrored on the other side (not shown). Note the recession of the Ti from the surface, indicating polarization away from the BTO surface, and toward the BTO/STO interface. Below we show the macroscopic average of the plane-averaged electrostatic potential for the P_1 and P_2 states. 161

Figure 6.2: Crystalline structure of BTO/STO/Ge: (a) X-ray diffraction θ-2θ scan of 16 nm $BaTiO_3$ epitaxially grown on Ge(001) substrate, with and without a 2 nm $SrTiO_3$ buffer layer. Without the buffer, the d-spacing corresponds to the *a*-axis of BTO directed out of plane. With the STO buffer, the *c*-axis of BTO is directed out of plane. (b) Reciprocal space map of the (103) Bragg reflection for BTO/STO/Ge. The centroid of the peak is consistent with a short in-plane axis and long out-of-plane axis. The inset shows a typical RHEED pattern for BTO/STO/Ge taken along the [110] azimuth showing good crystallinity and surface flatness.163

Figure 6.3: Aberration-corrected electron microscopy: (a) High-angle annular-dark-field (ADF) image of BTO/STO/Ge(001) heterostructure recorded with 200-keV probe-corrected scanning transmission electron microscope. White spots correspond to positions of metal atoms; (b) Fourier transform of ADF image confirming tetragonality of BTO layer; (c) Enlargement of ADF image showing region of BTO film; (d) Corresponding line profile from (c) showing shifts in Ti atomic-column positions. 165

Figure 6.4: PFM and voltage spectroscopy of BTO heterostructures: (a) Topography, (b) BE-PFM amplitude and (c) associated phase image after a box-in-box switching experiment on the BTO hetereostructure, showing clear ferroelectric switching (scale bar: 1 μm). A 5 × 5 μm^2 box was poled with the tip held at -6 V, and then a smaller box 2.5 × 2.5 μm^2 was subsequently scanned with the tip held at +4 V before the BE-PFM images were captured. 100 hysteresis loops were then captured on the same film using BE spectroscopy. The average response is shown in the spectrograms in (d) for amplitude (above) and phase (below), with the applied DC waveform shown in blue. Selected amplitude and phase loops are shown in (e,f), respectively with the average loop shown as a solid line in olive...167

Figure 6.5: Ferroelectric switching and electrical detection, using microwave impedance microscopy (MIM): (a) Schematic diagram illustrating the measurement setup and configuration of samples. A negative-biased conductive scanning probe makes downward to upward switching in ferroelectric polarization of BTO layer, which modulates hole density at the BTO/p-Ge interface. PFM (b), AFM (bottom right corner in b), MIM real part (c) and MIM imaginary part (bottom right corner in c) images acquired after writing a 20 × 20 μm^2 square by applying -4 V DC bias on the tip (Scale bars: 10 μm). (d) Simulated MIM-Re (blue line) and MIM-Im (red line) signals as a function of conductivity at the BTO/Ge interface. Left and right insets, respectively, show band diagrams of Ge in regions A and B in panel (c). 168

Figure 7.1: (a) Schematic of the lithographically defined polycrystalline Si overhang (white, 100 nm) and SiO_2 pattern (blue, 500 nm) on the p-type Ge wafer (brown). (b) Cross-sectional TEM image of the poly-Si/SiO_2/Ge structure. After the thin film and top gate deposition, the sacrificial SiO_2 can be lifted off by chemical etching, revealing nanoscale gate capacitor devices of 80 × 80 μm^2. 181

Figure 7.2: (a) 2 × 1 reconstructed Ge surface after oxygen plasma exposure followed by a thermal anneal at 750°C. (b) 2 nm thick STO on Ge(001) viewed along the [110] direction. (c) 16 nm of crystalline BTO grown on top of the STO/Ge viewed along the [110] direction. 183

Figure 7.3: 2θ-θ scan of a 16 nm thick BTO film grown epitaxially on 2 nm STO on Ge(001). Only peaks from Ge, STO and BTO are observed. The *c* lattice parameter of BTO is between 4.03 and 4.05 Å and is directed out of plane. The inset shows the rocking curve around the BTO (002) peak for the same film with a FWHM value of 0.5°. 186

Figure 7.4: (a) Representative XTEM image of the structure shown schematically in Figure 1. The polycrystalline-Si overhang prevents film deposition on the sacrificial SiO_2 layer, allowing its removal with BOE. (b) XTEM confirming the crystal quality of the BTO and STO layer grown on the exposed Ge areas. Both STO and BTO layers are highly crystalline with sharp interfaces between the different layers. Both oxide layers show highly uniform growth in conjunction with a very low surface roughness, (c) top-view SEM image showing the test structure after the BOE etch, revealing patterned Pt/BTO/STO/Ge capacitor devices.187

Figure 8.1: RHEED patterns of (a) 15%, (b) 25%, (c) 30%, and (d) 40% Co-substituted BTO films on STO(001) taken along the [100] direction. The BTCO thickness in all samples is 16 nm. 201

Figure 8.2: Typical x-ray diffraction 2θ-θ scan of 5% Co-substituted BTO film on STO/Ge. The film thickness is 10 nm. Only peaks from the substrate Ge as well as from STO and BTCO are observed. 205

Figure 8.3: (a) High-resolution cross-section TEM image for a 25% Co-substituted BTO film on 5 unit cells $SrTiO_3$ on Ge. High crystallinity and a sharp interface between the STO buffer and BTCO film are confirmed. (b) EDXS line profile through the BTCO layer: a homogenous distribution of the Co atoms parallel to the interface is clearly shown, excluding the formation of Co clusters. (c) and (d) EELS measurements performed at 6 different positions in the sample. Ti atoms close to the Ge interface exhibit an oxidation state of +4 as can be seen by the splitting of the Ti L- edges. The gradual disappearance of the split closer to the surface indicates the presence of some Ti atoms with an oxidation state of +3, which is attributed to a sample preparation artifact due to argon-ion milling in thinner regions. 207

Figure 8.4: (a) AFM topography, (b) vertical BE-PFM amplitude, and associated (c) vertical BE-PFM phase after a box-in-box poling experiment. A box of size 5×5 μm^2 is poled with the tip held at -5 V, and a smaller box of size 2×2 μm^2 within the larger square is poled with the tip held at +5 V. On the same sample, 100 hysteresis loops are acquired with BE spectroscopy across a 10×10 spatial grid, with the average of the 100 loops shown in (d) amplitude and (e) phase plots..........................209

Figure 8.5: (a) Magnetization vs. field measurement at 5 K for a nominally 25% Co-substituted BTCO film on an STO single crystal (001) substrate. No hysteresis curve could be obtained, confirming the absence of ferromagnetism. (b) Magnetization vs. temperature scan shows no temperature dependency for the measured film. 210

Figure 8.6: Atomistic arrangement, local site spin configuration, and projected density of states for a pair of cobalt atoms with no vacancies in a 3 × 2 × 2 supercell showing that this configuration, found to be lowest in energy, is both metallic and has a net magnetic moment. 213

Figure 8.7: Atomistic arrangement, local site spin configuration, and projected density of states for a Co^{3+} configuration consisting of two cobalt atoms and a vacancy in a 3 × 2 × 2 supercell. The lowest energy spin configuration results in two antiparallel high-spin atoms (no net moment) and an insulator..215

Figure 8.8: Atomistic arrangement, local site spin configuration, and projected density of states for a Co^{2+} configuration [two cobalt atoms and two oxygen vacancies in a 3 × 2 × 2 supercell which results in an insulating state with an antiparallel spin alignment (no net moment)]...........217

Chapter 1: Introduction

Silicon (Si) has been the workhorse of the semiconductor industry for more than 5 decades with Si-based devices, especially CMOS, memory, and optical devices, being a key component of most modern technologies. The reasons for the success of Si in the semiconductor industry are wide-ranging. On the one hand, there's an almost unlimited supply of Si, as silica and silicates are a major component of the earth's crust. Due to the high availability and demand, the acquisition costs are relatively low, and since the 1960's, single crystal silicon can be produced with such low defect density and high purity, that it was suitable for mass-produced integrated circuits. Apart from the standpoint of production, silicon also offers great advantages in terms of its electronic properties. It has a moderate bandgap of 1.12 eV [1] and a reasonably high solid solubility for dopant atoms such as As, P and B [2]. However, the most important reason for the success of Si is its superior interface quality with its native oxide SiO_2. The SiO_2/Si interface has been highly studied and an almost defect free interface can be obtained with modern growth methods leading to excellent transistor performance [3]. Due to the high bandgap of SiO_2 (~9 eV [4]) extremely low gate leakage current values can be obtained when using it as a gate dielectric, leading to the ability to move a significant amount of interface charge without using a lot of power. Furthermore, SiO_2 is an excellent blocking and passivation layer, has a rather high dielectric strength [5], possesses great thermal and mechanical stability [6], and is easy to grow.

However, with increasing chip density and decreasing transistor dimensions, the SiO_2/Si system has reached its limits. Due to CMOS scaling requirements, the SiO_2 dielectric layer is required to be only a few Å in thickness [7]. This results in high gate leakage currents (both during switching and in standby), leading to increased power consumption and device failures from power dissipation issues [7].

The replacement of SiO_2 with a high-κ material as the gate dielectric has partially solved this issue. Using a high-κ material instead of SiO_2 as the gate dielectric provides the advantage that the physical gate dielectric thickness for scaled down devices can remain relatively large, while enabling the required increase in capacitance that allows for the switchable interface charge to be maintained [8]. This is because the geometrical capacitance of a gate-oxide capacitor scales proportionally with κ and inversely with the thickness of the dielectric ($C \sim \frac{\kappa A}{d}$). In 2007, Intel Corporation announced the implementation of the high-κ material hafnium dioxide (HfO_2) as the new gate dielectric in their silicon-based devices for the 45 nm technology node [9, 10]. After initial processing and performance issues with HfO_2 on Si [11, 12], HfO_2-based silicon devices soon outperformed their SiO_2 based counterparts [9, 13-15]. However, with the incorporation of high-κ materials instead of SiO_2 as the gate dielectric, the key performance advantage of Si is lost and the use of Si as the channel material may eventually become obsolete, making other semiconductors with higher electron and hole mobilities than Si more attractive [8].

A well-studied alternative to Si is GaAs which has a slightly larger bandgap (1.42 eV [1]) than Si and much higher intrinsic electron mobility (μ_e: 8500 $\frac{cm^2}{Vs}$ vs μ_e: 1500 $\frac{cm^2}{Vs}$ for Si at room temperature) [16]. The disadvantages of GaAs, however, are the lack of a good native oxide [17], higher production cost [18], processing limitations and lower hole mobility than Si (μ_h: 400 $\frac{cm^2}{Vs}$ vs μ_h: 450 $\frac{cm^2}{Vs}$ for Si [19] at room temperature), which have so far hindered the extensive industrial use of GaAs for logic and memory applications.

Germanium (Ge), another alternative to Si, possesses a 4 times higher intrinsic hole mobility (μ_h = 1900 $\frac{cm^2}{Vs}$ vs. μ_h: 450 $\frac{cm^2}{Vs}$ for Si) and 2.5 times higher electron mobility than silicon (μ_e: 3900 $\frac{cm^2}{Vs}$ vs. μ_e: 1500 $\frac{cm^2}{Vs}$ for Si) at room temperature [16, 20, 21], with a smaller band gap of only 0.67 eV [1]. The simultaneously higher electron and hole mobility of Ge can potentially lead to lower power consumption [16], making it a promising replacement for silicon-based p-type MOSFETs (pMOS) in particular [22-24].

Currently, Ge is mainly used as a dopant in fiber optics [25, 26], as the absorbing material in IR detectors [27] and infrared night vision systems [28], and as an integration platform for III-V semiconductors [29]. Interest in studying Ge was revived after successfully alloying Ge with Si to form strained $Si_{1-x}Ge_x$, leading to improvements in the electron and hole mobility of Si-based devices [30], with applications in high performance devices [31], emitters [32], RF [33] and microwave devices [33, 34], modulators [35, 36], and photodetectors [37]. Although Ge was used in the early years of transistor research [38], it was quickly replaced by Si in the 1960s [39].

One of the major drawbacks for Ge transistors at that time was that Ge transistors weren't reliable and GeO_2 is thermally unstable, since it evaporates at temperatures as low as 390°C [40]. These properties of GeO_2 make it impractical as a gate dielectric material for MOSFETs [41]. However, the advent of using high-κ and alternative oxides as gate dielectric materials provides a suitable alternative to the use of GeO_2 on Ge, making Ge a serious candidate to replace Si in the future. The main thrust is on the possibility of making non-silicon CMOS structures based on high mobility and low power III-V nMOS and Ge pMOS channels [42, 43]. In 2002 Chui *et al.* integrated 20-30 Å ZrO_2 on Ge and demonstrated roughly 2-fold enhancement of the effective hole mobility compared to the universal mobility model for Si MOSFETs with SiO_2 [44]. In the same year, Shang *et al.* reported a Ge pMOSFET using a 6-nm-thick germanium oxynitride (GeO_xN_y) and 3 nm low temperature oxide (LTO), and reported a 40% hole mobility enhancement over Si with an equivalent oxide thickness (EOT) of 80 Å [45]. The use of GeO_xN_y as an interfacial layer has been especially important for achieving improved scaling and C-V characteristics of germanium-based devices [45-50]. A stable GeO_xN_y layer prevents the excessive growth of a low-κ interfacial layer on Ge during dielectric deposition, allowing high-performance Ge MOSFETs with enhanced mobility over Si MOSFETs with SiO_2 [51-53]. Chui *et al.* showed that using GeO_xN_y as an interlayer between Ge and a high-κ dielectric leads to an improved EOT with a leakage current reduction of roughly 4-5 orders of magnitude [47] in comparison to using only a high-κ dielectric on Ge directly. In 2014, Wu *et al.* were the first to demonstrate a completely Ge-based CMOS device [54].

In 1998, McKee *et al.* published a pioneering paper, where he demonstrated the epitaxial integration of $SrTiO_3$ on Si(001) without forming an interfacial SiO_2 layer [55]. This was the first time that an oxide material was epitaxially grown directly on Si in a crystalline fashion. This demonstration was a big breakthrough because crystalline oxide materials can possess a variety of useful properties, such as ferroelectricity [56, 57], ferromagnetism [58], superconductivity [59, 60], multiferroicity [61-64] or very high dielectric-constant [65-70] and are therefore of great research interest especially if they can be integrated with Si or other conventional semiconductors. However, in the case of epitaxial integration, new challenges arise, such as lattice matching between the substrate and thin film, avoidance of an amorphous interfacial layer, or atomic intermixing at interfaces.

An interesting material property which has already been utilized for some device applications is ferroelectricity. Applications of ferroelectric materials can be found in transducers [71], sensor applications [72] or in ferroelectric random-access memory (FeRAM) [73]. So far, FeRAM has a rather small market share and is a rather niche product. Its advantages in comparison to other memory devices are its non-volatility, lower power consumption, fast writing speed and long data retention times [74]. However, the main disadvantages of FeRAM are the high production cost, low storage density and a destructive readout. Especially the latter property of FeRAM requires a larger number of polarization reversals in the ferroelectric material, promoting faster fatigue of the material. Its nearest competitor on the memory market is Flash, which also

offers non-volatility, but possesses a non-destructive readout. Additionally, Flash drives are conveniently portable and quite robust with respect to durability and temperature. However, write operation speed is rather low and endurance is greatly decreased in comparison to other memory devices [75, 76]. A promising alternative to Flash is magnetoresistive random-access memory (MRAM), which offers the same advantages as Flash, such as non-volatility and non-destructive readout, but its writing speed is much faster and endurance is nearly infinite [77]. However, operating voltages can be high which leads to increased power consumption and scalability can be an issue due to overlapping magnetic fields into adjacent cells, resulting in a false write operation.

An alternative future memory device could be the ferroelectric field-effect transistor (FeFET), whose working principle is described in more detail in chapter 2.4. It combines the advantageous properties of non-volatility of FeRAM with the non-destructive read out of Flash and would therefore require even less power than FeRAM. Additionally, it possesses fast write/erase and read-access speeds. Scalability could also be improved in comparison to FeRAM, due to the reduction to only 1 instead of 2 devices (transistor and capacitor) per bit. For these reasons, there's a strong interest in creating such a device. However, its production still remains elusive, mainly because of integration and operation issues. A variety of FeFETs have been reported in literature so far, some Si-based while others used other materials, often oxides, as a substrate material. In the case of Si-based devices, their main drawbacks are often their high operating voltages (above 20 V), which is due to the formation of an interfacial low-κ SiO_2 layer in between the

ferroelectric material and the Si channel [78-82]. Such high operating voltages are unacceptable for a competitive memory device in comparison to other technologies. In 2004, Aizawa *et al.* demonstrated a Pt/$SrBi_2Ta_2O_9$(SBT)/HfO_2/Si and Pt/$(Bi,La)_4Ti_3O_{12}$(BLT)/HfO_2/Si FeFET structure with a on/off drain current ratio of approximately 10^5 even after 15.9 days. However, a voltage of ± 10 V was needed to flip the polarization state of the devices [81]. Basit *et al.* reported a FeFET based on $Pb(Zr,Ti)O_3$ grown on MgO buffered oxidized silicon [82]. While they experimented with rather thick buffer layers of MgO lying between 7-100 nm, a write pulse of 15 V was needed to change the state of the transistor, which is too high to be commercially competitive. On the other hand, FeFETs demonstrated on non-Si substrates, mostly oxide channel materials, offer the advantage that they generally show a much lower write operating voltage, due to the lack of the low-κ interfacial layer. However, in their cases they often either suffer from an extremely low charge carrier mobility, low resistance change upon switching [83], or the substrate materials cannot easily be integrated with Si [56, 84-87]. In 1995, Watanabe demonstrated an all-perovskite FeFET, based on $(Pb,La)(Zr,Ti)O_3$ as the ferroelectric material and $La_{1.99}Sr_{0.01}CuO_4$ as a channel material with a write and erase operating voltage of 7 V and a memory retention time of 10 days [87]. Prins *et al.* demonstrated a Sb:SnO_2-based FeFET with $PbZr_{0.2}Ti_{0.8}O_3$ as the ferroelectric material, however, with a measured charge carrier mobility of only 5 $cm^2V^{-1}s^{-1}$ [84].

A goal of this thesis is the development of a germanium-based ferroelectric field-effect transistor using $BaTiO_3$ as the ferroelectric material. While the complete device hasn't been demonstrated yet, several key milestones are reported which will facilitate its development in the future. First of all, the development of a reliable Ge(001) surface cleaning method is reported, which produces atomically flat and contamination-free Ge surfaces, which is necessary for the epitaxial integration of the ferroelectric material $BaTiO_3$ on Ge. One key requirement for a working ferroelectric FET is that the direction of the ferroelectric polarization is normal to the semiconductor surface. In our case this is achieved by an ultrathin buffer layer of $SrTiO_3$ in between BTO and Ge, which exerts compressive strain on BTO, leading to a polarization perpendicular to the Ge surface. Additionally, the ferroelectric field-effect in the germanium substrate is demonstrated using microwave impedance microscopy, showing that charge can be modulated in the Ge channel material upon switching of the ferroelectric polarization. Lastly, a method to pattern thin films of $BaTiO_3$ on Ge is demonstrated, allowing the fabrication of electrically isolated gate stacks.

1.1 CHAPTER OVERVIEW

This dissertation not only provides a detailed and step by step approach describing our efforts in creating a ferroelectric FET using $BaTiO_3$ on Ge(001), but also shows the attempt of creating multiferroic $BaTiO_3$ by incorporation of Co atoms.

Chapter 2 provides some background information about the semiconductor Ge and the ferroelectric material $BaTiO_3$. Additionally, details about ferroelectricity as well as the

working principles and the challenges involved in the development of a ferroelectric FET are presented. Chapter 3 provides an overview of the laboratory equipment in the Material Physics Lab at the University of Texas at Austin and the main characterization tools which are used in this thesis to study thin films. Chapter 4 reviews the existing Ge(001) surface cleaning methods, such as UV light, O_2 plasma and H_2 plasma exposure, ion sputtering and Ge regrowth, as well as wet-etching of the Ge surface. The mechanism of each cleaning method is described in detail and its effect on the carbon and oxygen removal as well as the surface roughness is reported. Chapter 5 discusses the surface cleaning recipe which was developed to obtain an atomically flat and perfectly clean Ge(001) surface. A surface free of oxides, metals and organic contamination is of utmost importance as any kind of surface contamination can affect the transistor performance negatively. This cleaning method provides the foundation for every subsequent epitaxial thin film growth on Ge. Chapter 6 discusses the integration of $BaTiO_3$ on a $SrTiO_3$/Ge template which leads to an out-of-plane polarization of $BaTiO_3$. Furthermore the ferroelectric field-effect on Ge is demonstrated for the first time which is an important step towards the development of a working ferroelectric field effect transistor. Chapter 7 focuses on a method to pattern titanate materials by lifting off a sacrificial SiO_2 layer which reveals nanoscale MOSCAPs. This method can be used to create the gate structure for a ferroelectric field-effect transistor, but can also be applied to any kind of titanate material. In chapter 8, the nature of Co-doped $BaTiO_3$ (BTCO) is discussed with the motivation to create a new multiferroic material, which could find applications in memory devices. While the BTCO films are still ferroelectric, no ferromagnetism is

observed and an explanation on why that is the case is provided. Finally, chapter 9 concludes the dissertation and provides an outlook for future work.

1.2 References

[1] B. G. Streetman, S. Banerjee, *Solid State electronic Devices,* p 524 (Hall, New Jersey, 2000).

[2] J. D. Plummer, M. D. Deal, P. B. Griffin, *Silicon VLSI Technology*, (Prentice Hall, Upper Saddle River, 2013).

[3] T. Hattori, Crit. Rev. Solid State **20**, 339-382 (1995).

[4] E. Vella, F. Messina, M. Cannas, R. Boscaino, Phys. Rev. B **83**, 174201 (2011).

[5] E. Harari, J. Appl. Phys. **49**, 2478-2489 (1978).

[6] B. El-Kareh, *Fundamentals of Semiconductor Processing Technologies, (*Springer US, New York, 1995).

[7] H. Iwai, Microelectron. Eng. **86**, 1520-1528 (2009).

[8] J. Robertson, R. M. Wallace, Mater. Sci. Eng. R. **88**, 1-41 (2015).

[9] K. Mistry, C. Allen, C. Auth, B. Beattie, D. Bergstrom, M. Bost, M. Brazier, M. Buehler, A. Cappellani, R. Chau, C.-H. Choi, G. Ding, K. Fischer, T. Ghani, R. Grover, W. Han, D. Hanken, M. Hattendorf, J. He, J. Hicks, R. Heussner, D. Ingerly, P. Jain, R. James, L. Jong, S. Joshi, C. Kenyon, K. Kuhn, K. Lee, H. Liu, J. Maiz, B. McIntyre, P. Moon, J. Neirynck, S. Pae, C. Parker, D. Parsons, C. Prasad, L. Pipes, M. Prince, P. Ranade, T. Reynolds, J. Sandford, L. Shifren, J. Sebastian, J. Seiple, D. Simon, S. Sivakumar, P. Smith, C. Thomas, T. Troeger, P. Vandervoorn, S. Williams, K. Zawadzki, 2007 Int. El. Devices Meet. 247-250 (2007).

[10] M. T. Bohr, R. S. Chau, T. Ghani, K. Mistry, IEEE Spectrum **44** (29), (2007).

[11] R. Chau, S. Datta, M. Doczy, B. Doyle, J. Kavalieros, M. Metz, IEEE Electr. Device L. **25**(6), 408-410 (2004).

[12] J. H. Choi, Y. Mao, J. P. Chang, Mater. Sci. Eng. R. **72**(6), 97-136 (2011).

[13] M. Gutowski, J. E. Jaffe, Mater. Res. Soc. Symp. Proc. 716, B 3.2.1 - B 3.2.5 (2002).

[14] E. P. Gusev, C. Cabral Jr., M. Copel, C. D'Emic, M. Gribelyuk, Microelectron. Eng. **69**, 145–151 (2003).

[15] Y.-S. Lin, R. Puthenkovilakam, and J. P. Chang, Appl. Phys. Lett. **81**(11), 2041-2043 (2002).

[16] Y. Kamata, Mater Today **11**, 30-38 (2008).

[17] P. D. Ye, G. D. Wilk, J. Kwo, B. Yang, H.-J. L. Gossmann, M. Frei, S. N. G. Chu, J. P. Mannaerts, M. Sergent, M. Hong, K. K. Ng, J. Bude, IEEE Electron. Device Letters **24**, 209-211 (2003).

[18] D. Poelman, P. Clauws, B. Depuydt, Solar Energy Materials and Solar Cells 76, 167-173 (2003).

[19] M. Levinshtein, S. Rumyantsev, M. Shur, *Handbook series on Semiconductor parameters*, (World scientific, Singapore, 2000).

[20] J. A. Kubby, J. J. Boland, Surf. Sci. Rep. **26**, 61-204 (1996).

[21] M. Bosi, G. Attolini, Prog. Cryst. Growth Ch. **56**, 146-174 (2010).

[22] R. Pillarisettty, Nature **479**, 324-328 (2011).

[23] K. Saraswat, C. O. Chui, T. Krishnamohan, D. Kim, A. Nayfeh, A. Pethe, Mater. Sci. Eng. B **135,** 242-249 (2006).

[24] P. Ponath, K. Fredrickson, A. B. Posadas, Y. Ren, X. Wu, R. K. Vasudevan, M. Baris Okatan, S. Jesse, T. Aoki, M. R. McCartney, D. J. Smith, S. V. Kalinin, K. Lai, A. A. Demkov, Nat. Commun. **6**, 6067 (2015).

[25] J. Stone, J. Appl. Phys. **62**, 4371 (1987).

[26] K. O. Hill, B. Malo, F. Bilodaeu, D. C. Johnson, J. Albert, Appl. Phys. Lett. **62**, 1035 (1993).

[27] A. Rogalski, *Infrared detectors* (CRC Press, Boca Raton, 2011).

[28] X. H. Zhang, Y. Guimond, Y. Bellec, J. Non-Cryst. Solids **326**, 519–523 (2003).

[29] E. P. A. M. Bakkers, J. A. van Dam, S. De Franceschi, L. P. Kouwenhoven, M. Kaiser, M. Verheijen, H.Wondergem, P. van der Sluis, Nat. Mater. 3, 769-773 (2004).

[30] K. Ismail, J. O. Chu, B. S. Meyerson, Appl. Phys. Lett. **64**, 3124-3126 (1994)

[31] K. Oda, E. Ohue, M. Tanabe, H. Shimamoto, K. Washio, Thin Solid Films **369**, 358-361 (2000).

[32] J. H. Comfort, G. L. Patton, J. D. Cressler, W. Lee, E. F. Crabbe, B. S.Meyerson, J. Y.-C. Sun, J. M. C. Stork, P.-F. Lu, J. N. Burghartz, J. Warnock, K. Kenkins, K.-Y. Toh, M. D'Agostino, G. Scilla, Tech. Dig. Int. Electron. Device Meeting, 21–24 (1990).

[33] J. D. Cressler, IEEE T. Microw. Theory **46**, 572-589 (1998).

[34] K. Washio, E. Ohue, H. Shimamoto, K. Oda, R. Hayami, Y. Kiyota, M. Tanabe, M. Kondo, T. Hashimoto, T. Harada, IEEE T. Electron. Dev. **49**, 271- 278 (2002).

[35] Y.-H. Kuo, Y. K. Lee, Y. Ge, S. Ren, J. E. Roth, T. I. Kamins, D. A. B. Miller, J. S. Harris, Nature **437**, 1334-1336 (2005).

[36] Y. Rong, Y. Ge, Y. Huo, M. Fiorentino, M. R. T. Tan, T. I. Kamins, T. J. Ochalski, G. Huyet, J. S. Harris Jr., IEEE J. Sel. Top. Quant. **16**, 85-92 (2010).

[37] J. Oh, J. C. Campbell, S. G. Thomas, S. Bharatan, R. Thoma, C. Jasper, R. E. Jones, T. E. Zirkle, IEEE J. Quantum Elect. **38**, 1238-1241 (2002).

[38] J. Bardeen, W. H. Brattain, Phys. Rev. **74**, 230-231 (1948).

[39] C. Claeys, E. Simoen, *Germanium-based technology* (Elsevier, Oxford, 2007).

[40] X. J. Zhang, G. Xue, A. Agarwal, R. Tsu, M. A. Hasan, J. E. Greene, A. Rockett, J. Vac. Sci. Technol. A **11**, 2553 (1993).

[41] K. Kita, Appl. Phys. Lett. **254**, 6100-6105 (2008).

[42] C. H. Huang, M. Y. Yang, Albert Chin, W. J. Chen, C. X. Zhu, B. J. Cho, M.-E Li, and D. L. Kwon, 2003 VLSI Tech. Dig. 119-120 (2003).

[43] E. Simoen, J. Mitard, G. Hellings, G. Eneman, B. De Jaeger, L. Witters, B. Vincent, R. Loo, A. Delabie, S. Sioncke, M. Caymax, C. Claeys, Materials Science in Semiconductors Processing **15**, 588-600 (2012).

[44] C. O. Chui, H. Kim, D. Chi, B. B. Triplett, P. C. McIntyre, and K. C. Saraswat, Int. El. Devices Meet. 437-440 (2002).

[45] H. Shang, H. Okom-Schmidt, K. K. Chan, M. Copel, J. A. Ott, P. M. Kozlowski, S. E. Steen, S. A. Cordes, H.-S. P. Wong, E. C. Jones, W. E. Haensch, Int. El. Devices Meet. 441-444 (2002).

[46] W. P. Bai, N. Lu, J. Liu, A. Ramirez, D. L. Kwong, D. Wristers, A. Ritenour, L. Lee, D. Antoniadis, 2003 VLSI Tech. Dig. 121-122 (2003).

[47] C. O. Chui, F. Ito, K. C. Saraswat, IEEE Electr. Device L. **25** (9), (2004).

[48] E. P. Gusev, H. Shang, M. Copel, M. Gribelyuk, C. D'Emic, P. Kozlowski, and T. Zabel, Appl. Phys. Lett. **85**, 2334 (2004).

[49] S. Van Elshocht, B. Brijs, M. Caymax, T. Conard, T. Chiarella, S. De Gendt, B. De Jaeger, S. Kubicek, M. Meuris, B. Onsia, O. Richard, I. Teerlinck, J. Van Steenbergen, C. Zhao, and M. Heyns, Appl. Phys. Lett. **85**, 3824 (2004).

[50] N. Lu, W. Bai, A. Ramirez, C. Mouli, A. Ritenour, M. L. Lee, and D. Antoniadis, D. L. Kwong, Appl. Phys. Lett. **87** (5), 1922 (2005).

[51] H. Shang, H. Okorn-Schimdt, J. Ott, P. Kozlowski, S. Steen, E. C. Jones, H.-S. P.Wong, and W. Hanesch, IEEE Electr. Device L. **24** (4), (2003).

[52] D. S. Yu, C. H. Huang, A. Chin, C. Zhu, M. F. Li, B. J. Cho, and D.-L. Kwong, IEEE Electr. Device L. **25** (3), (2004).

[53] A. Dimoulas, E. Gusev, P. C. McIntyre, M. Heyns, *Advanced Gate Stacks for High-Mobility Semiconductors* (Springer, New York 2007).

[54] H. Wu, N. Conrad, W. Luo, and P. D. Ye, 2014 Int. El. Devices. Meet. 227-230 (2014).

[55] R. A. McKee, F. J. Walker, M. F. Chisholm, Phys. Rev. Lett. **81,** 3014-3017 (1998).

[56] S. Mathews, R. Ramesh, T. Venkatesan, J. Benedetto, Science **276**, 238-240 (1997).

[57] A. von Hippel, Rev. Mod. Phys. **22**, 221 (1950).

[58] R. M. Cornell, U. Schwertmann, *The iron oxides: structure, properties, reactions, occurrences and uses* (Wiley-VCH, Weinheim, 2003).

[59] Z.-A. Ren, G.-C. Che, X.-L. Dong, J. Yang, W. Lu, W. Yi, X.-L. Shen, Z.-C. Li, L.-L. Sun, F. Zhou, Europhys. Lett. **83**, 17002 (2008).

[60] R. J. Cava, J. Am. Ceram. Soc. **83**, 5-28 (2000).

[61] T. Kimura, S. Kawamoto, I. Yamada, M. Azuma, M. Takano, Y. Tokura, Phys. Rev. B **67**, 180401 (2003).

[62] J. Wang, J. B. Neaton, H. Zheng, V. Nagarajan, S. B. Ogale, B. Liu, D. Viehland, V. Vaithyanathan, D. G. Schlom, U. V. Waghmare, N. A. Spaldin, K. M. Rabe, M. Wuttig, R. Ramesh, Science **299**, 1719-1722 (2003).

[63] A. Moreira dos Santos, S. Parashar, A. R. Raju, Y. S. Zhao, A. K. Cheetham, C. N. R. Rao, Solid State Commun. **122**, 49-52 (2002).

[64] X. H. Zhu, H. Béa, M. Bibes, S. Fusil, K. Bouzehouane, E. Jacquet, A. Barthélémy, D. Lebeugle, M. Viret, D. Colson, Appl. Phys. Lett. **93**, 082902 (2008).

[65] D. Fuchs, C. W. Schneider, R. Schneider, H. Rietschel, J. Appl. Phys. **85**, 7362 (1999).

[66] H. Tabata, H. Tanaka, T. Kawai, J. Appl. Phys. **65**, 1970 (1994).

[67] B. H. Hoerman, G. M. Ford, L. D. Kaufmann, B. W. Wessels, Appl. Phys. Lett. **73**, 2248 (1998).

[68] A. Kersch, D. Fischer, J. Appl. Phys. **106**, 014105 (2009).

[69] A. Linz, Jr., K. Herrington, Crystal, J. Chem. Phys. **28**, 824, (1958).

[70] A. Outzourhit, J. U. Trefny, T. Kito, B. Yarar, A. Naziripour, A. M. Hermann, Thin Solid Films, **259** , 218 (1995).

[71] L. E. Cross, Mater. Chem. Phys. **43**, 108-115 (1996).

[72] D. Damjanovic, P. Muralt, N. Setter, IEEE Sens. J. **1**, 191-206 (2001).

[73] H. Takasu, J. Electroceram. **4:2/3**, 327 (2000).

[74] T. Endoh, H. Koike, S. Ikeda, T. Hanyu, H. Ohno, IEEE J. Em. Sel.Top. C. **6**, 109-119 (2016).

[75] P. Pavan, R. Bez, P. Olivo, E. Zanoni, P. IEEE **85**, 1248-1271 (1997).

[76] J. S. Meena, S. M. Sze, U. Chand, T.-Y. Tseng, Nanoscale Res. Lett. **9**, 526 (2014).

[77] D. Apalkov, B. Dieny, P. IEEE **104**, 1796-1830 (2016).

[78] T. A. Rost, H. Lin, T. A. Rabson, Appl. Phys. Lett. **59**, 3654 (1991).

[79] T. S. Böscke, J. Müller, D. Bräuhaus, U. Schröder, U. Böttger, Appl. Phys. Lett. **99**, 102903 (2011).

[80] K. Sugibuchi, Y. Kurogi, N. Endo, J. Appl. Phys. **46**, 2877 (1975).

[81] K. Aizawa, B.-E. Park, Y. Kawashima, K. Takahashi, H. Ishiwara, Appl. Phys. Lett. **85**, 3199-3201 (2004).

[82] N. A. Basit, H. K. Kim, J. Blachere, Appl. Phys. Lett. **73**, 3941-3943 (1998).

[83] C. H. Ahn, R. H. Hammond, T. H. Geballe, M. R. Beasley, J. M. Triscone, M. Decroux, O. Fisher, A. Antognazza, K. Char, Appl. Phys. Lett. **70**, 206 (1997).

[84] M. W. J. Prins, K.-O. Grosse-Holz, G. Müller, J. F. M. Cillessen, J. B. Giesbers, R. P. Weening, R. M. Wolf, Appl. Phys. Lett. **68**, 3650-3652 (1996).

[85] A. G. Schrott, J. A. Misewich, V. Nagarajan, R. Ramesh, Appl. Phys. Lett. **82**, 4770 (2003).

[86] T. Zhao, S. B. Ogale, S. R. Shinde, R. Ramesh, R. Droopad, J. Yu, K. Eisenbeiser, J. Misewich, Appl. Phys. Lett. 84, 750-752 (2004).

[87] Y. Watanabe, Appl. Phys. Lett. **66**, 1770 (1995).

Chapter 2. Background information

This chapter is dedicated to give some background information about the Ge(001) surface and $BaTiO_3$ as well as about the theoretical background of ferroelectricity and the ferroelectric FET.

2.1 Ge(001) surface

*This chapter is taken from P. Ponath, A. B. Posadas and A. A. Demkov, Appl. Phys. Rev. **4**, 021308 (2017).*

Similar to Si, Ge crystallizes in the diamond crystal structure, which can be described as two interpenetrating face-centered cubic Bravais lattices with their origins at **0** and $\frac{a_0}{4}$ (**x** + **y** + **z**) (see Fig. 2.1) [1]. Ge has the electronic configuration of [Ar]$4s^2 4p^2$, but in bulk,

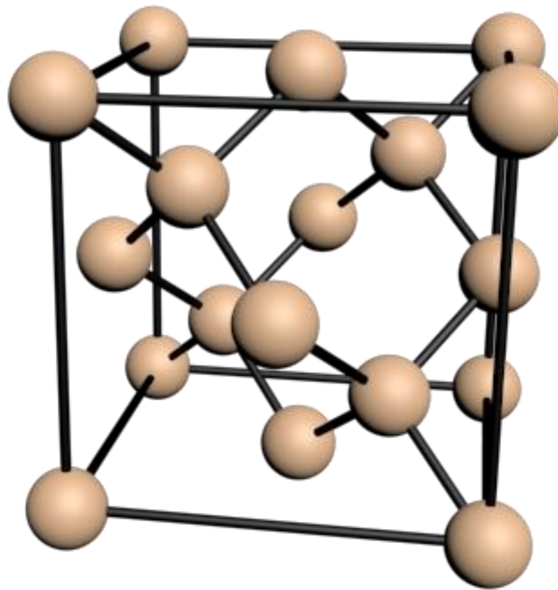

Figure 2.1: Diamond crystal structure

Ge atoms hybridize and form sp^3 orbitals, which lowers the total energy of a given Ge atom by bonding covalently to four adjacent Ge atoms. If a Ge crystal is truncated along the (001) plane, the three-dimensional periodicity of the crystal no longer exists and the surface atoms can only bond to two neighboring Ge atoms below [2]. This leaves each surface atom in an excited state with two unpaired dangling bonds. As a result of this high energy state, the surface atoms undergo a surface reconstruction along the [110] direction. Nearest neighbor surface atoms dimerize to reduce the number of dangling bonds and to lower their total energy, leaving the surface atoms with only one dangling bond each, which can lead to several surface reconstructions for clean Ge surfaces. For completeness, the unreconstructed 1 × 1 case is considered first, where the surface Ge atoms possess two dangling bonds each with a surface unit cell size of $\frac{a_0}{\sqrt{2}} \times \frac{a_0}{\sqrt{2}}$ (see Fig. 2.2 (a)), with a_0 as the bulk Ge conventional lattice constant of 5.65 Å.

The unreconstructed case is usually found for as-received (native oxide covered) or H-terminated germanium wafers. For a clean surface, a 2 × 1 surface reconstruction is commonly observed at room temperature (see Fig. 2.2 (b)). However, the formed dimers are not parallel to the surface plane, and instead they buckle asymmetrically by moving one surface atom up from its initial position, while the other atom is slightly lowered (see Fig. 2.2 (e), (f)) [3]. In the case of the Si(001) surface, theoretical calculations show that the buckling reduces the energy by 0.46 eV/dimer with a charge transfer of 0.36 electrons from the down to the up-shifted atom, while a gap between filled and empty states opens up [4, 5]. This buckling of surface atoms allows not only a 2 × 1 symmetry (see Fig. 2.2 (b)) but also other types of surface reconstruction, i.e. the p(2 × 2) (p: primitive) and the

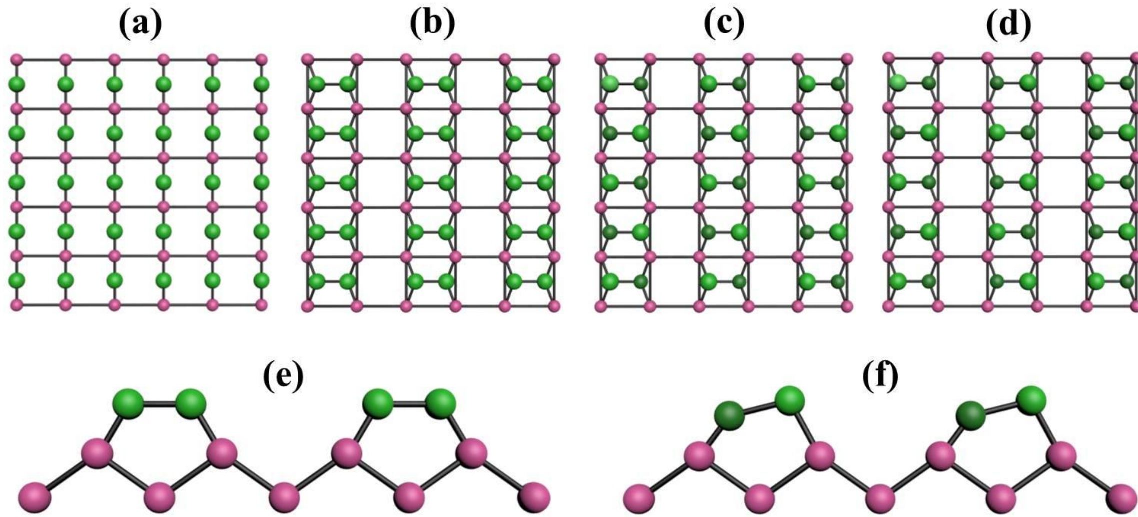

Figure 2.2: Top view of the Ge(001) surface: green balls: top layer; dark green balls: lowered surface atom; purple balls: bottom layer. (a) Unreconstructed (1 × 1) surface, (b) b(2 × 1) surface reconstruction, with dimers lying parallel to the surface, (c) p(2 × 2) and (d) c(4 × 2) surface reconstruction. Side view: (e) Ge surface dimers, lying parallel to the surface. (f) For surface energy reduction the dimers buckle asymmetrically, leading to a charge transfer from the bottom to the top surface atom.

c(4 × 2) (c: centered) surface reconstruction, which are due to in-phase and out of-phase buckling of adjacent dimer rows (see Figure 2.2 (c), (d)). Both these higher order surface reconstructions can be readily observed at low temperatures [6, 7] but can also appear at room temperature in combination with the 2 × 1 surface reconstruction [8-11].

To better understand the different surface reconstructions, one has to look at the formation energies of the different configurations. The main 2 × 1 surface reconstruction due to dimerization is driven by short-range interaction with energies lying at around >1 eV [6], while an energetically weaker long-range order of less than 100 meV [6] is responsible for the higher order reconstruction, due to the interaction between the dimers.

This dimer interaction energy is on the order of room temperature ($k_B T \approx 26$ meV), which explains why the higher order reconstructions are more easily seen at low temperatures. Using *ab initio* calculations, it could theoretically be shown that the higher order p(2×2) and c(4×2) reconstructions are almost degenerate in energy for the Ge(001) surface and possess the lowest total energy out of all surface reconstructions considered [2, 12-14] (b(2×1): 0.000 eV/dimer; p(4×1): +0.035 eV/dimer; c(4×2): -0.066 eV/dimer; c(2×2): -0.069 eV/dimer) [2].

Similar to Si, which is highly reactive with oxygen in air, forming its thermodynamically stable native oxide SiO_2, Ge also forms an oxide layer in air, consisting mainly of GeO_2 plus a variety of suboxides (GeO_x with $x < 2$). Germanium dioxide is found to be the most prominent oxide [15] on the Ge surface and can be found in three different structures: a water-insoluble rutile phase [15, 16], a hexagonal phase [17, 18], and an amorphous phase, with the latter two being soluble in water [19-21]. GeO on the other hand is not water soluble [20] and was found to be thermally more stable than GeO_2 [22]. All Ge oxides can be thermally desorbed by heating the Ge surface in vacuum to temperatures between 390 - 600°C [19, 23, 24, 25, 26], where GeO_2 and Ge react to form volatile GeO ($GeO_2 + Ge \Rightarrow 2\ GeO$) [21].

2.2 BaTiO$_3$

One of the most studied materials in this thesis is the complex oxide barium titanate ($BaTiO_3$, BTO), which belongs to the family of titanate materials and crystallizes in the perovskite crystal structure with the chemical formula ABO_3 (see Fig. 2.3), which includes other well-known materials such as $CaTiO_3$, $SrTiO_3$ or $PbTiO_3$. The perovskite

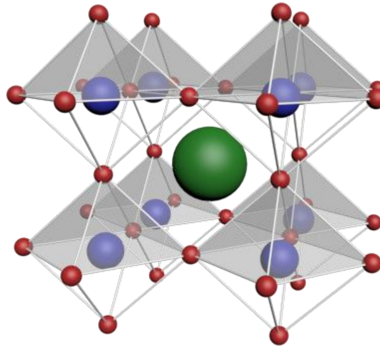

Figure 2.3: The cubic ABO_3 perovskite crystal structure. The B site atom (blue) is surrounded by 6 oxygen atoms (red), forming an octahedron, while the coordination number for the A atom (green) is 12.

crystal structure can be visualized as a cubic crystal with the A^{2+} cation occupying the corners, the B^{4+} cation the center and the O^{2-} ions the face center positions of the crystal.

A broad range of interesting material properties can be found in perovskite materials [27-31], such as ferromagnetism [32], ferroelectricity [33, 34], superconductivity [35], multiferroicity [36], high-κ dielectric constant [37], metal-insulator transitions [38] or colossal magnetoresistance [39] due to the partially filled or unfilled *d* or *f* orbitals of the B-atom which is often a transition metal.

BTO was intensively studied for the first time during World War II, due to its high dielectric constant of several thousand, with the intention of making high dielectric constant capacitors [40-42]. Since then, researchers have continued studying BTO extensively, because it exhibits a variety of other interesting properties such as piezoelectricity [42, 43], large electro-optical coefficient [44, 45] and ferroelectricity [33]. It is mechanically and chemically stable upon substitution with other atoms such as Sr ($Ba_{1-x}Sr_xTiO_3$), which can be used to tailor the Curie temperature or dielectric constant [46]. Due to these unique properties, BTO finds application in high-dielectric constant capacitors, piezoelectric transducers, and actuators. Characteristically for titanate materials, the melting temperature of BTO is rather high and is found to be around

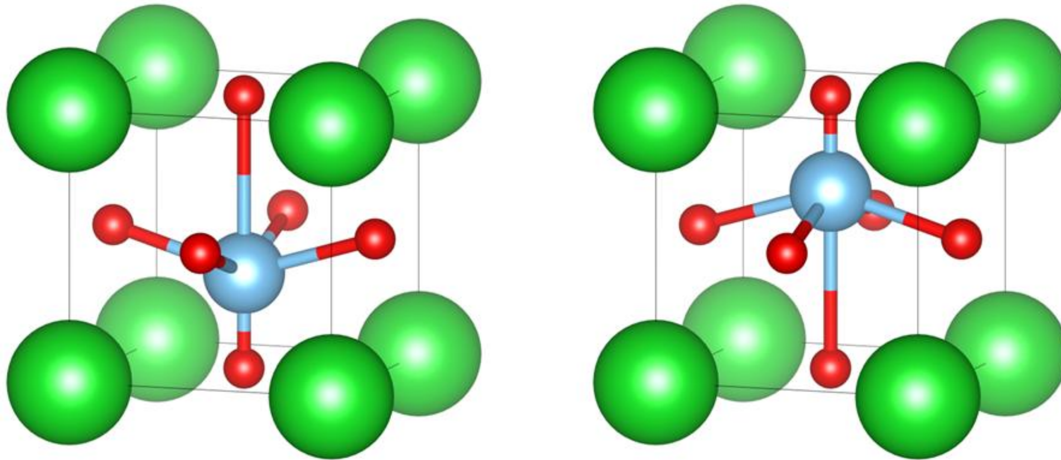

Figure 2.4: Unit cell of $BaTiO_3$ (Ba: green, O: red, Ti: blue) in the (a) downward polarization and (b) upward polarization.

1620°C [42]. Its energy band structure near the band edges is determined by the Ti 3*d* and O 2*p* levels giving rise to a band gap of about 3.2 eV [42, 47].

Bulk $BaTiO_3$ undergoes several structural phase transitions. Above 1460°C, bulk BTO is hexagonal and becomes cubic between 1460°C and 130°C [48]. Below 130°C to 9°C, BTO is found in a tetragonal phase and becomes orthorhombic [42, 49] between 9°C and -90°C [42]. Finally, below -90°C it transitions into a rhombohedral phase [42]. Above the Curie temperature (T_C) of 130°C, BTO is paraelectric, while it becomes ferroelectric in every phase below T_C. As will be shown in the next chapter, compressive and tensile strain can dramatically shift the transition temperature of oxide ferroelectrics up to a few hundred degrees, demonstrating the importance of strain on thin films.

Figure 2.4 shows the non-centrosymmetric tetragonal phase of $BaTiO_3$ at room temperature (space group *P*4*mm*) with one axis larger than the other two (c > a). In the tetragonal phase, the central Ti^{4+} atom is slightly off center, while the oxygen atoms in the TiO_2 plane shift towards the opposite direction leading to a spontaneous total polarization of P = 26 μC/cm^2 for bulk BTO [50]. In all known ferroelectric crystals, the spontaneous polarization is caused by the atomic arrangement of ions in the crystal structure [51]. The details and the origin of ferroelectricity in $BaTiO_3$ are explained in more detail in the following section.

2.3 FERROELECTRICITY AND LANDAU-DEVONSHIRE THEORY

2.3.1 Historic background and polarization

By definition, a ferroelectric is an insulating material which possesses two or more discrete stable or metastable states of different nonzero electric polarization in zero applied electric field, referred to as “spontaneous” polarization. For a system to be considered ferroelectric, it must be possible to switch between these states with an applied external electric field [51]. Ferroelectricity is the electric analog to ferromagnetism and was first discovered in Rochelle salt ($NaKC_4H_4O_6{\bullet}4H_2O$) in 1921 by Valasek [52] after Debye postulated the existence of permanent electric dipoles in 1912 [53]. Ferroelectricity in $BaTiO_3$ was discovered in the 1940’s while searching for high-dielectric-constant capacitors during World War II [40]. Since then other new ferroelectrics have been discovered and intensively studied such as $PbTiO_3$, $Pb(Zr, Ti)O_3$, $LiNbO_3$ or $KNbO_3$. With the advent of thin film technology, there was renewed interest in ferroelectric materials, due to new possible applications such as the use of ferroelectrics to lower the 60 mV/dec limit of the subthreshold swing (SS) in silicon metal-oxide-semiconductor field-effect transistors (MOSFET) [54], in FeRAM devices or as the dielectric in a FeFET. In general, there are 3 different responses of a material’s spontaneous polarization P to an externally applied electric field E. For most materials a linear response of their polarization with the application of an external electric field can be observed, which is called dielectric polarization (see Fig. 2.5 (a)). However, once the external electric field is switched off, the polarization vanishes. In comparison, some materials show a non-linear response to an applied electric field, and the electric

permittivity depends on the field, but similar to a linear dielectric polarization, the polarization also vanishes with the removal of the external electric field. On the other hand, ferroelectric materials also respond non-linearly to an external electric field (see Fig. 2.5 (b)), but the key difference to normal dielectric materials is their ability to keep a non-vanishing polarization even when the external electric field is zero. This non-vanishing polarization is called a remnant polarization P_r, while the spontaneous polarization is extrapolated from the saturation limit. Similar to ferromagnetic materials, a hysteresis behavior can be observed for ferroelectrics, which means that the exact value and sign of polarization depends on the "history" of the material. Only if an opposite external electric field E larger than the coercive field (E_C) of the material is applied can the polarization of the ferroelectric be reversed.

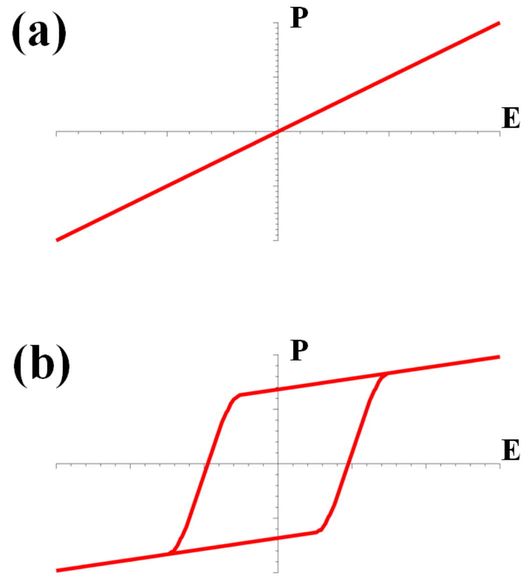

Figure 2.5: Responses of a (a) dielectric and (b) ferro-electric material to an externally applied electric field.

As mentioned in section 2.2, ferroelectricity in bulk $BaTiO_3$ is observed in the tetragonal phase below the Curie temperature of T_C = 130°C. For temperatures above the Curie temperature ($T > T_C$), ferroelectricity in $BaTiO_3$ is completely lost and it becomes paraelectric.

2.3.2 Landau-Devonshire theory

The theoretical background for describing a continuous phase transition between two phases of different symmetries was first developed by Lev Landau in 1937 [55]. Landau theory (LT) provides a reliable description of a system's equilibrium behavior near a phase transition and serves as a conceptual bridge between microscopic models and observed macroscopic phenomena. Landau introduced an order parameter, a physical entity that is zero in the high-symmetry phase that changes continuously to a finite value once the symmetry is lowered. In the case of a ferroelectric-paraelectric phase transition, this order parameter is the polarization P. Because LT assumes spatial averaging of all local fluctuations, it is particularly well-suited to systems with long-range interactions such as superconductors and ferroelectrics [56]. The main concept of the LT is based on expressing the free energy F as a series expansion of the order parameter around the phase transition where only symmetry compatible terms are kept. Devonshire was the first to apply LT to paraelectric-ferroelectric phase transitions [57].

In the Landau-Devonshire theory, the thermodynamic state of any system in equilibrium can be completely specified by the values of specific variables; for bulk ferroelectrics these include temperature (T), polarization (P), electric field (E), strain (η), and stress (σ). When expanding the free energy for a ferroelectric in the vicinity of a phase transition and truncating it at the sixth term, we obtain [58]:

$$F_P = \frac{1}{2}aP^2 + \frac{1}{4}bP^4 + \frac{1}{6}cP^6 - EP \qquad (2.1)$$

with F_P being the free energy, a, b and c are coefficients that have yet to be determined, P is the order parameter (the polarization), and E is the externally applied electric field.

By finding the minimum of the free energy, the equilibrium conditions can be found:

$$\frac{\partial F_P}{\partial P} = 0 = aP + bP^3 + cP^5 - E \tag{2.2}$$

$$E = aP + bP^3 + cP^5 \tag{2.3}$$

The reciprocal of the electric susceptibility χ is defined as:

$$\frac{1}{\chi} = \frac{dE}{dP}/_{P=0} = a \tag{2.4}$$

Around the Curie point, a is considered to be of the form $a = a_0(T\text{-}T_0)$, where a_0 is a positive constant, T is the temperature and T_0 the Curie point, leading to:

$$\chi = \frac{1}{a_0(T - T_0)} \tag{2.5}$$

a is the only coefficient which depends on temperature and captures the Curie behavior near the phase transition of a diverging χ for ferroelectrics very well.

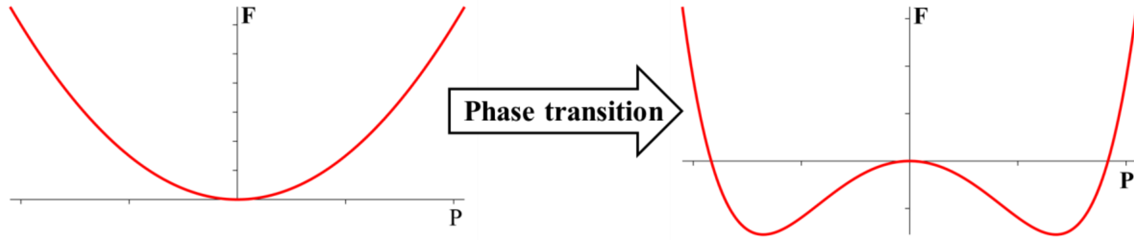

Figure 2.6: Free energy as a function of the spontaneous polarization of the paraelectric phase (left) and the ferroelectric phase (right)

a_0 must be experimentally determined for each material and is always a positive number as well as the coefficient c. In Figure 2.6 the free energy is shown for the paraelectric case where $T >> T_0$ and after a phase transition for the ferroelectric case with $T << T_0$. Whether the phase transition between both configurations is either continuous or discontinuous is mainly determined by the sign of the coefficient b. If $b < 0$, the system

undergoes a discontinuous phase transition (first order), while for b > 0, a continuous phase transition (second order) occurs.

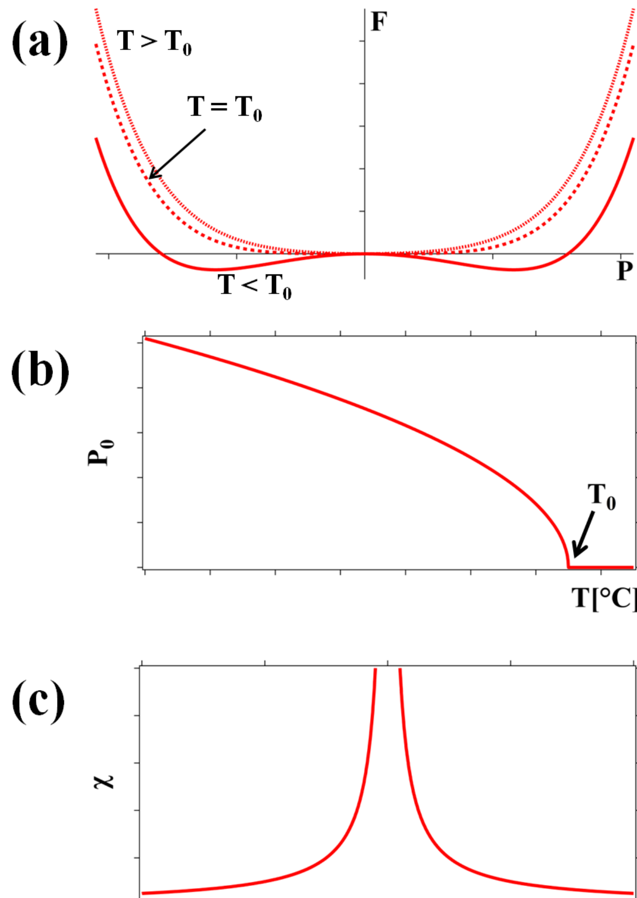

Figure 2.7: Second order phase transition: (a) Free energy as a function of temperature T, (b) spontaneous polarization vs. temperature and (c) susceptibility as a function of temperature.

2.3.3 Second order phase transition

If b > 0, a second order transition takes place at T = T_0 and the free energy can evolve continuously as a function of decreasing temperature with minima at P = $\pm P_0$ [59]. The spontaneous polarization can be determined by using equation 2.3 with E = 0. Keeping only the lowest two orders leads to:

$$P_0 = \sqrt{\frac{a_0}{b}(T_0 - T)} \tag{2.6}$$

From this equation it is obvious that the spontaneous polarization increases with decreasing temperature. The evolution of the free energy, polarization and dielectric susceptibility for a second order phase transition is schematically drawn in Figure 2.7.

2.3.4 First order phase transition

For the case where b < 0, it is possible that the free energy may have other minima at non-zero P despite $T > T_0$. Depending on the value of *a*, the total energy minimum can drop below the unpolarized state (P = 0), being the thermodynamically favored configuration [56]. In this case, the Curie temperature T_C can exceed T_0 and the order parameter jumps discontinuously to zero at T_C (see Fig. 2.8), which is called a first order phase transition.

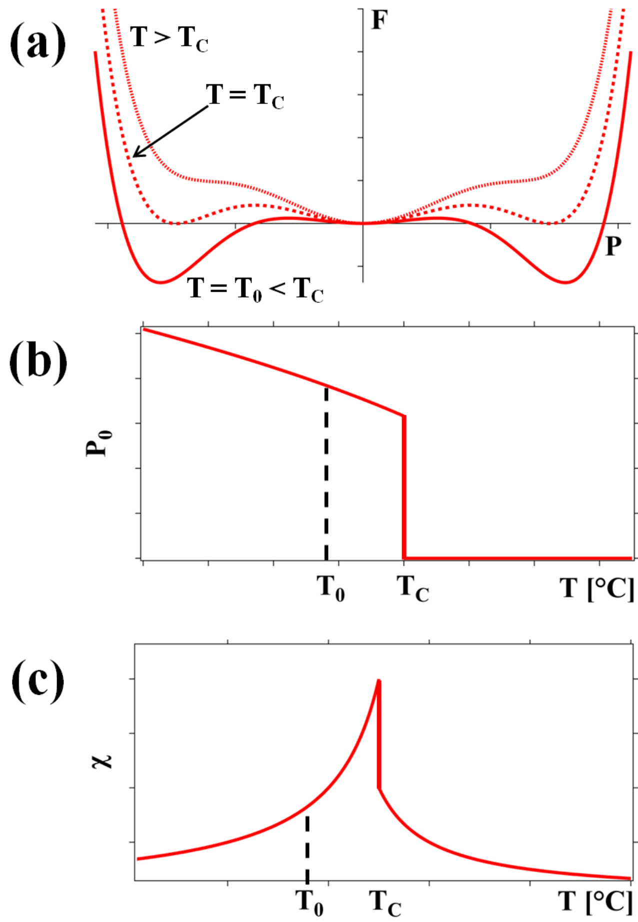

Figure 2.8: First order phase transition: (a) free energy as a function of temperature T, (b) spontaneous polarization vs. temperature and (c) susceptibility as a function of temperature.

2.3.5 Coupling to strain

Strain plays an important role for ferroelectrics, as it affects the Curie temperature T_C and the remnant polarization. Strain is generally measured by how the displacement **u** of a point in a solid varies with position **r**. The strain tensor is given by:

$$\eta_{ij} = \frac{1}{2}\left(\frac{\partial u_i}{\partial r_j} + \frac{\partial u_j}{\partial r_i}\right) \tag{2.7}$$

with i and j representing the x, y and z components. For a uniaxial ferroelectric such as BTO, the leading order terms of the strain including the free energy component F_η are given by [56]:

$$F_\eta = \frac{1}{2}K\eta^2 + Q\eta P^2 + \ldots - \eta\sigma \tag{2.8}$$

Here η is a component of the strain field, K is an elastic constant, Q a coupling constant between elastic strain and the polarization and σ is externally applied stress. The new free energy, taking strain into account, is the summation of F_P and F_η:

$$F = F_P + F_\eta \tag{2.9}$$

The parameters of F can now be determined in a similar fashion as in equation 2.2 [56]:

$$\frac{\partial F(P,\eta)}{\partial P} = \frac{\partial F(P,\eta)}{\partial \eta} = 0 \tag{2.10}$$

For the second case where

$$\frac{\partial F(P,\eta)}{\partial \eta} = K\eta + QP^2 - \sigma = 0 \tag{2.11}$$

there are three cases to consider: First, if the polarization P is zero, then Hooke's law with $\eta = \frac{\sigma}{K}$ is obtained. Second, if stress is applied forcing the strain to be exactly zero at all times, this is the case in a thin epitaxial film, where the thin film's in-plane lattice constants match the crystal spacing of the substrate and can only relax in the out-of plane direction. Third, if no external stress is applied, we obtain:

$$\eta = -\frac{QP^2}{K} \tag{2.12}$$

demonstrating that strain is proportional to the polarization. In 2004, Choi *et al.* experimentally showed that strain highly influences the remnant polarization of BTO

[58]. They reported a remnant polarization of ~50 μC/cm^2 for BTO/$GdScO_3$ (-1.0% strain) and ~50 μC/cm^2 for BTO/$DyScO_3$ (-1.7% strain). In comparison, bulk BTO only possesses a remnant polarization of ~26 μC/cm^2. To investigate the influence of strain on the Curie temperature, Li *et al.* theoretically calculated the different phases of BTO as a function of temperature and applied strain (see Fig. 2.9) [59]. Huge shifts from the bulk BTO Curie temperature of ~130°C are expected with increased compressive or tensile strain. However, the Curie temperature of BTO can also be lowered by partially substituting Ba with Sr atoms, making BTO a very interesting material to study [46].

Up until the late 1990s, it was widely accepted that ferroelectricity in perovskite oxides would disappear below a critical size of about 10 nm. This suppression is an extrinsic effect, produced by electrical and mechanical boundary conditions rather than by intrinsic size effects related to the collective nature of the ferroelectric instability A key result in initiating this change of view was the experimental finding that PZT films can maintain switchable polarization normal to the film down to thicknesses of only a few nm [51, 60]. Establishing ferroelectricity in ultra thin films opens up new

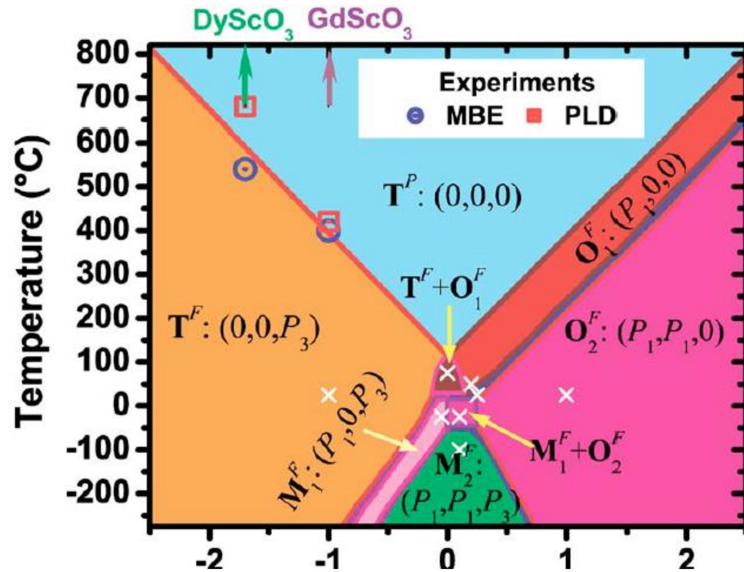

Figure 2.9: Strain vs. temperature phase diagram for BTO. Taken from [60]

possibilities for electronic applications such as the creation of a ferroelectric field effect transistor which is explained in the next chapter.

2.4 FERROELECTRIC FIELD EFFECT TRANSISTOR

A large part of this thesis focuses on the development of a ferroelectric FET. This chapter is dedicated to explaining its working principle and the challenges encountered during its development.

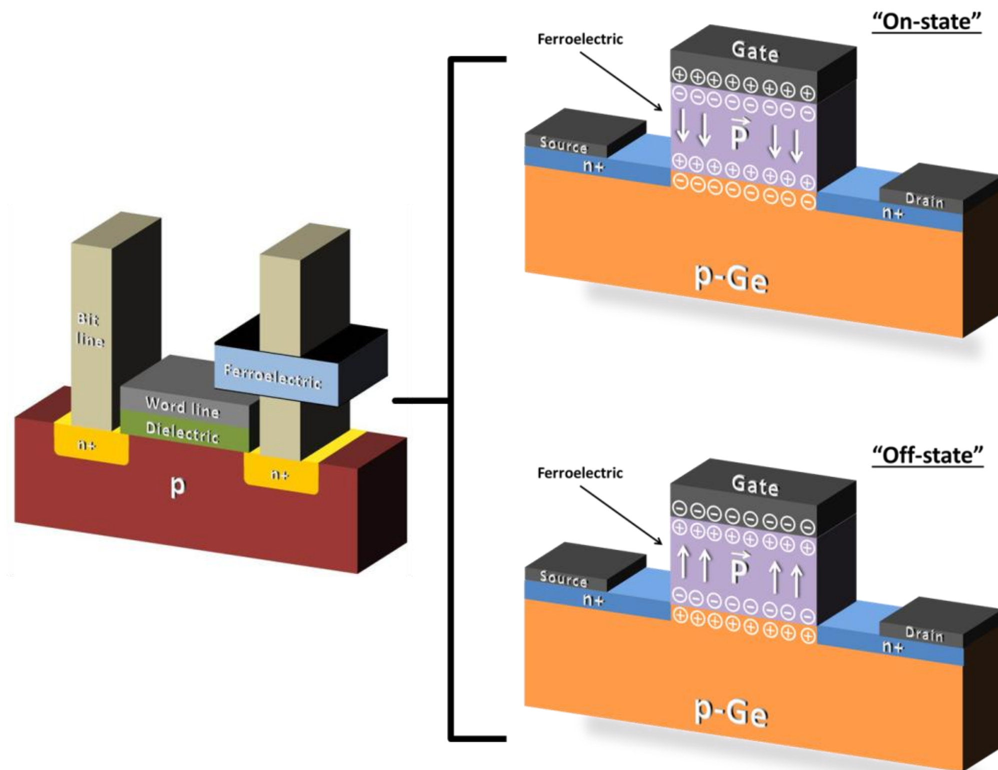

Figure 2.10: The ferroelectric field-effect transistor is the combination of the two devices of a Fe RAM, a MOSFET and ferroelectric capacitor, by replacing the dielectric material of the transistor with a ferroelectric material. This non-volatile, low power consuming memory device would experience reduced fatigue, due to its non destructive readout and more aggressive device scaling could be achieved in comparison to Fe RAM.

The idea of a ferroelectric FET is to combine both devices of a FeRAM cell, the transistor and ferroelectric capacitor, into one device (see Figure 2.10), that is the gate dielectric material of the transistor is replaced with a ferroelectric material. Similar to FeRAM, the hysteretic behavior of the ferroelectric material acts as the basis for the memory function of the ferroelectric FET. The computational "0" and "1" states can be represented by the two stable polarization states –P and +P of the ferroelectric material, which are stable even in the absence of an externally applied electric field [61]. If the polarization of the ferroelectric material is directed perpendicular to the semiconductor surface, it induces electric charges in the semiconductor channel region. However, if an electric field is applied across the ferroelectric layer exceeding the coercive field of the ferroelectric material, the direction of its electric polarization can be switched, inducing electric charges of the opposite sign in the channel region. The state of the device can then be read in a non-destructive fashion by measuring the resistance between source and drain. Depending on the sign of the induced charge carriers in the channel region, either a low or high resistance is measured, representing a logical "0" or "1", respectively.

The ferroelectric FET offers a variety of advantages over already existing memory devices. Apart from being non-volatile, it offers a non-destructive readout which gives it an advantage over FeRAM, where the state has to be rewritten after it is read. The non-destructive readout has another major advantage, since it decreases the number of polarization switches for the read and write cycle. Large numbers of polarization switching in ferroelectric materials generally lead to fatigue of the material, which can be minimized with the ferroelectric FET structure. Additionally, the operating voltage of a

FeFET is low, erase and programming speed is fast, and scaling is enhanced, which lowers cost per device in comparison to FeRAM devices, since the number of devices per bit is reduced by half [61, 62].

However, the reasons why the ferroelectric FET is still elusive in production are manifold since its development isn't straight forward. A couple of reports demonstrate a ferroelectric FET with an oxide substrate as the channel material [63-67]. This offers the advantage that a substrate with the same crystal structure as the ferroelectric material can be chosen, allowing easier epitaxial integration and preventing interfacial oxide layers. However, oxide channel materials usually suffer from their low charge carrier mobility. On the other hand, Si-based ferroelectric FETs provide a much higher charge carrier mobility. However, in most cases a thin interfacial layer of SiO_2 forms in between the ferroelectric material and the Si substrate, leading to unacceptably high (20-30 V) operating voltages necessary to flip the electric polarization of the ferroelectric [68-70]. Both cases of low charge carrier mobility and high operating voltage are unacceptable in terms of competitiveness in comparison with other non-volatile memory devices.

Another key requirement for a ferroelectric FET is the close proximity of the ferroelectric material with the channel material, so that the polarization can actually modulate charge carriers in the channel region. Some reports show the integration of BTO on Si with a thick interfacial layer such as TiN, $SrTiO_3$, $MgAl_2O_4$ or BaO [71-74]. In this case, the ferroelectric is not only spatially too far away from the channel region, but the thick interfacial layer also increases the operating voltage. Apart from the spatial distance between the ferroelectric material and the semiconductor channel, a thick interfacial layer

also enhances the depolarizing field E_{dp} which is intrinsic to a ferroelectric FET structure on a semiconductor and opposes the remnant polarization [75]:

$$\boldsymbol{E}_{dp} = \frac{-\boldsymbol{P}C_F}{\varepsilon(C_{IS} + C_F)} \tag{2.13}$$

Here $\boldsymbol{P}$ is the polarization vector, C_F the capacitance and ε the permittivity of the ferroelectric film while C_{IS} is the effective capacitance of the semiconductor in series with a non-ferroelectric buffer layer [62] As long as C_{IS} is not infinity (unlike a metal-ferroelectric-metal structure), there will always be a non-zero depolarizing field which will affect the retention time of the device. On the other hand, an interfacial layer can also improve the device characteristics. An appropriate interfacial layer can improve the interface properties between the semiconductor and ferroelectric material. Large amounts of interfacial charges can be observed at the ferroelectric-semiconductor interface, which screen the polarization of the ferroelectric, leading to retention loss [61]. Additionally, interfacial layers can reduce the leakage current during device operation, which is another major problem when dealing with retention loss. An estimate of the retention time t was given by Ma *et al.* [62]:

$$t = \frac{P_r}{I\alpha} \tag{2.14}$$

with P_r being the remnant polarization, I the leakage current in A/cm^2 and α being the trapping probability. This formula clearly demonstrates the importance of a low leakage current in combination with a low interfacial trap density as both can drastically reduce the retention time of the device.

In this thesis, Ge is chosen as the channel material because it offers a variety of advantages over other semiconductor and oxide substrate materials. Ge possesses a 4× higher hole mobility and 2.5× higher electron mobility than Si and is almost perfectly lattice matched with $BaTiO_3$ (4.00 Å in plane lattice constant), which reduces strain and facilitates the integration. Additionally, Ge has a reduced tendency to form an interfacial amorphous GeO_x layer with epitaxially grown oxide materials. As can be seen in chapter 6, no interfacial GeO_x layer is formed between the Ge substrate and the $SrTiO_3$ buffer layer. The high operating voltage of Si based ferroelectric FET devices is generally attributed to a thin low-κ SiO_2 interfacial layer between the ferroelectric and Si which can be prevented with Ge-based devices [68-70, 76-79]. These reasons make Ge the ideal channel material for the creation of a ferroelectric FET.

While most reported FeFET devices used PZT as their ferroelectric material [63-67], $BaTiO_3$ has the advantage that it is lead free [80], which avoids any environmental contamination issues. Furthermore, BTO's bulk electric polarization of 26 $\mu C/cm^2$ is large enough to induce a large amount of electric charges in the semiconductor channel (which will be shown in chapter 6) and its lattice constant is very well matched with Ge, facilitating epitaxial integration.

2.5 REFERENCES

[1] N. W. Ashcroft, N. D. Mermin, *Solid State physics* (Harcourt, Orlando, 1976) p.76.

[2] M. Needels, M. C. Payne, J. D. Joannopoulos, Phys. Rev. B **38**, 5543-5546 (1988).

[3] J. C. Fernandez, W. S. Yang, H. D. Shih, F. Jona, D. W. Jepsen, P. M. Marcus, J. Phys. C. Solid State Phys. **14**, L55-60 (1981).

[4] H. J. W. Zandvliet, Phys. Rep. **388**, 1-40 (2003).

[5] D. J. Chadi, Phys. Rev. Lett. **43**, 43 (1979).

[6] S. D. Kevan, Phys. Rev. B **32**, 2344 (1985).

[7] S. D. Kevan, N. G. Stoffel, Phys. Rev. Lett. **53**, 702-705 (1984).

[8] J. A. Kubby, J. E. Griffith, R. S. Becker, J. S. Vickers, Phys. Rev. B **36**, 6079 (1987).

[9] H. J. W. Zandvliet, B. S. Swartzentruber, W. Wulfhekel, B. J. Hattink, B. Poelsema, Phys. Rev. B **57**, R6803-R6806 (1998).

[10] A. Molle, M. N. K. Bhuiyan, G. Tallarida, M. Fanciulli, Mat. Sci. Semicon. Proc. **9**, 673–678 (2006).

[11] O. Gurlu, H. J. W. Zandvliet, B. Poelsema, Phys. Rev. Lett. **93**, 066101 (2004).

[12] M. Needels, M. C. Payne, J. D. Joannopoulos, Phys. Rev. B. **58**, 1765-1768 (1987).

[13] Y. Yoshimoto, Y. Nakamura, H. Kawai, M. Tsukada, M. Nakayama, Phys. Rev. B **61**, 1965-1970 (2000).

[14] M. C. Payne, N. Roberts, R. J. Needs, M. Needels, J. D. Joannopoulos, Surf. Sci. **211/212**, 1-20 (1989).

[15] A. W. Laubengayer, D. S. Morton, J. Am. Chem. Soc. **54**, 2303-2320 (1932).

[16] M. Micoulaut, L. Cormier, G. S. Henderson, J. Phys.: Condens. Matter **18**, R753 (2006).

[17] V. M. Goldschmidt, Naturwissenschaften **14**, 295-297 (1926).

[18] W. Zachariasen, Z. Kristallogr. **67**, 226 (1928).

[19] K. Prabhakaran, T. Ogino, Surf. Sci. **325,** 263-271 (1995).

[20] S. R. Amy, Y. J Chabal, F. Amy, A. Kah, C. Krugg, P. Kirsch, Mater. Res. Soc. Symp. Proc. **917**, (2006).

[21] V. I. Davydov, *Germanium* (Gordon and Breach, New York, 1966) p.150 & p.160.

[22] H. J. Kuhr, W. Ranke, Surf. Sci. **201**, 408-418 (1988).

[23] X. J. Zhang, G. Xue, A. Agarwal, R. Tsu, M. A. Hasan, J. E. Greene, A. Rockett, J. Vac. Sci. Technol. A **11**, 2553 (1993).

[24] K. Kita, Appl. Phys. Lett. **254**, 6100-6105 (2008).

[25] A. Toriumi, T. Tabata, C. H. Lee, T. Nishimura, K. Kita, K. Nagashio, Microelectron. Eng. **86**, 1571-1576 (2009).

[26] K. Prabhakaran, F. Maeda, Y. Watanabe, T. Ogino, Appl. Phys. Let. **76**, 2244 (2000).

[27] A. S. Bhalla, R. Guo, R. Roy, Mat. Res. Innovat. **4**, 3-26 (2000).

[28] B. R. Sutherland, E. H. Sargent, Nat. Photon. **10**, 295-302 (2016).

[29] M. Johnsson, P. Lemmens, *Handbook of magnetism and advanced magnetic materials*, (John Wiley & Sons, Hoboken NJ, 2005).

[30] H. D. Megaw, Proc. Phys. Soc. **58**, 133 (1946).

[31] M. A. Peña, J. L. G. Fierro, Chem. Rev. **101**, 1981-2007 (2001).

[32] A. B. Posadas, C. Mitra, C. Lin, A. Dhamdhere, D. J. Smith, M. Tsoi, A. A. Demkov, Phys. Rev. B **87**(14), 144422 (2013).

[33] P. Ponath, K. Fredrickson, A. B. Posadas, Y. Ren, X. Wu, R. K. Vasudevan, M. B. Okatan, S. Jesse, T. Aoki, M. R. McCartney, D. J. Smith, S. V. Kalinin, K. Lai, A. A. Demkov, Nat. Commun. **6**, 6067 (2015)

[34] L. Mazet, S. M. Yang, S. V. Kalinin, S. Schamm-Chardon, C. Dubourdieu, Sci. Technol. Adv. Mater. **16**, 036005 (2015).

[35] Y. Maeno, H. Hashimoto, K. Yoshida, S. Nishizaki, Nature **372**, 532 (1994).

[36] W. Eerenstein, N. D. Mathur, J. F. Scott, Nature **442**, 759-765 (2006)

[37] J. A. Kittl, K. Opsomer, M. Popovici, N. Menou, B. Kaczer, X. P. Wang, C. Adelmann, M. A. Pawlak, K. Tomida, A. Rothschild, B. Govoreanu, R. Degraeve, M. Schaekers, M. Zahid, A. Delabie, J. Meersschaut, W. Polspoel, S. Clima, G. Pourtois, W. Knaepen, C. Detavernier, V. V. Afanas'ev, T. Blomberg, D. Pierreux, J. Swerts, P. Fischer, J. W. Maes, D. Manger, W. Vandervorst, T. Conard, A.

Franquet, P. Favia, H. Bender, B. Brijs, S. Van Elshocht, M. Jurczak, J. Van Houdt, D. J. Wouters, Microelectron. Engin. **86**, 1789-1795 (2009).

[38] M. Imada, A. Fujimori, Y. Tokura, Rev. Mod. Phys. **70**, 1039 (1998).

[39] A. J. Millis, Boris I. Shraiman, R. Mueller, Phys. Rev. Lett. **77**, 175 (1996).

[40] Gene H. Haertling, J. Am. Ceram. Soc. **82** (4), 797–818 (1999)

[41] C. J. Johnson, Appl. Phys. Lett. **7**, 221 (1965).

[42] M. B. Klein, in *Photorefractive materials and their applications I*, 195-236 (2005) (Springer, Berlin Heidelberg).

[43] S. Roberts, Phys. Rev. **71**, 890 (1947).

[44] S. Abel, T. Stoferle, C. Marchiori, C. Rossel, M. D. Rossell, R. Erni, D. Caim, M. Sousa, A. Chelnokov, B. J. Offrein, J. Fompeyrine, Nat. Commun. **4**, 1671 (2013).

[45] B. W. Wessels, Annu. Rev. Mater. Res. **37**, 659-679 (2007).

[46] C. Ménoret, J. M .Kiat, B. Dkhil, M. Dunlop, H. Dammak, O. Hernandez, Phys. Rev. B **65**, 224104 (2002).

[47] K Suzuki, K. Kijima, Jpn. J. Appl. Phys. **44**, 2081-2082 (2005).

[48] D. E. Rase, R. Roy, J. Am. Ceram. Soc. **38**, 102 (1955).

[49] K. I. Sakayori, Y. Matsui, H. Abe, E. Nakamura, M. Kenmoku, T. Hara, D. Ishikawa, A. Kokubu, K.-I. Hirota, T. Ikeda, Jpn. J. Appl. Phys. **34**(9S), 5443 (1995).

[50] C. Ederer, N. A. Spaldin, Phys. Rev. Lett. **95**, 257601 (2005).

[51] K. M. Rabe, M. Dawber, C. Lichtensteiger, C. H. Ahn, J.-M. Triscone, (Springer, Berlin, Heidelberg, 2007).

[52] J. Valasek, Phys. Rev. **17**, 475–81 (1921).

[53] P. Debye, Phisik. Zeits. **13**, 97-100 (1912).

[54] S. Salahuddin, S. Datta, Nano Lett. **8**, 405-410 (2008).

[55] L. Landau, Zh. Eksp. Teor. Fiz. **7**, 19-32 (1937).

[56] P. Chandra, P. B. Littlewood, "A Landau primer for ferroelectrics. In *Physics of ferroelectrics,"* (pp. 69-116) (Springer, Berlin Heidelberg, 2007).

[57] A. F. Devonshire, Philos. Mag. **40**(309), 1040-1063 (1949).

[58] K. J. Choi, M. Biegalski, Y. L. Li, A. Sharan, J. Schubert, R. Uecker, P. Reiche, Y. B. Chen, X. Q. Pan, V. Gopalan, L.-Q. Chen, D. G. Schlom, C. B. Eom, Science **306**, 1005 (2004).

[59] Y. L. Li, L. Q. Chen, Appl. Phys. Lett. **88**, 072905 (2006).

[60] T. Tybell, C. H. Ahn, J.-M. Triscone, Appl. Phys. Lett. **75**, 856-858 (1999).

[61] J. Hoffman, X. Pan, J. W. Reiner, F. J. Walker, J. P. Han, C. H. Ahn, T. P. Ma, Adv. Mater **22**, 2957-2961 (2010).

[62] T. P. Ma, J.-P. Han, IEEE Electron Device Lett. **23**, 386 (2002).

[63] M. W. J. Prins, K.-O. Grosse-Holz, G. Müller, J. F. M. Cillessen, J. B. Giesbers, R. P. Weening, R. M. Wolf, Appl. Phys. Lett. **68**, 3650-3652 (1996).

[64] A. G. Schrott, J. A. Misewich, V. Nagarajan, R. Ramesh, Appl. Phys. Lett. **82**, 4770 (2003).

[65] T. Zhao, S. B. Ogale, S. R. Shinde, R. Ramesh, R. Droopad, J. Yu, K. Eisenbeiser, J. Misewich, Appl. Phys. Lett. 84, 750-752 (2004).

[66] S. Mathews, R. Ramesh, T. Venkatesan, J. Benedetto, Science **276**, 238-240 (1997).

[67] Y. Watanabe, Appl. Phys. Lett. **66**, 1770 (1995).

[68] T. A. Rost, H. Lin, T. A. Rabson, Appl. Phys. Lett. **59**, 3654 (1991).

[69] T. S. Böscke, J. Müller, D. Bräuhaus, U. Schröder, U. Böttger, Appl. Phys. Lett. **99**, 102903 (2011).

[70] K. Sugibuchi, Y. Kurogi, N. Endo, J. Appl. Phys. **46**, 2877 (1975).

[71] M.-B. Lee, M. Kawasaki, M. Yoshimoto, H. Koinuma, Appl. Phys. Let. **66**, 1331 (1995).

[72] C. Dubourdieu, J. Bruley, T. M. Arruda, A. Posadas, J. Jordan-Sweet, M. M. Frank, E. Cartier, D. J. Frank, S. V. Kalinin, A. A. Demkov, V. Narayanan, Nat. Nanotech. **8**, 748-754 (2013).

[73] S. Matsubara, S. Miura, Y. Miyasaka, N. Shohata, J. Appl. Phys. **66**, 5826 (1989).

[74] R. A. McKee, F. J. Walker, J. FL Conner, E. D. Specht, D. E. Zelmon, Appl. Phys. Lett. **59**, 782 (1991).

[75] P. Wurfel, I. P. Batra, Phys. Rev. B **8**, 5126 (1973).

[76] K. Aizawa, B.-E. Park, Y. Kawashima, K. Takahashi, H. Ishiwara, Appl. Phys. Lett. **85**, 3199-3201 (2004).

[77] N. A. Basit, H. K. Kim, J. Blachere, Appl. Phys. Lett. **73**, 3941-3943 (1998).

[78] J. Senzaki, K. Kurihara, N. Nomura, O. Mitsunaga, Y. Iwasaki, T. Ueno, Jpn. J. Appl. Phys. 37, 5150-5153 (1997).

[79] J. Yu, Z. Hong, W. Zhou, G. Cao, J. Xie, X. Li, S. Li, Z. Li, Appl. Phys. Lett. **70**, 490 (1996)

[80] E. Cross, Nature **432**, 24-25 (2004).

Chapter 3. Molecular beam epitaxy and experimental techniques

Chapter 3 of this thesis is dedicated to shine some light on the experimental tools which I used. I will start with explaining molecular beam epitaxy, which is the main thin film deposition tool used for this thesis and continue with RHEED, XPS, XRD and AFM.

3.1 MOLECULAR BEAM EPITAXY

3.1.1 General overview

Molecular beam epitaxy (MBE) is an epitaxial growth technique involving the reaction of one or more thermal beams of atoms or molecules with a crystalline surface under ultra high vacuum (UHV) conditions [1].

The foundation for the invention of MBE was laid in 1958 by Günther *et al.*, who proposed a "three-temperature" technique for the growth of III-V compounds [2]. A few years later, in the late 1960s, MBE was developed under the leadership of A. Y. Cho and J. R. Arthur at Bell Laboratories [3]. The incentive for its development can be attributed to the need for high quality III-V semiconductor components for high-speed and optical devices [4]. The main advantage of MBE in comparison to other deposition techniques lies in the high degree of control of atomic fluxes allowing even the deposition of fractional monolayers. Due to this precise control of atomic fluxes, controlled alloying of GaAs became possible, which allowed one to tune the bandgap, lattice constant and refractive index of the material. While initially the main purpose was to grow GaAs and

$Al_xGa_{1-x}As$ compounds, MBE is nowadays used to grow elemental semiconductors, insulating materials, single-crystal metal films, superconductors or thin oxide films [5].

3.1.2 Working principle and components

In molecular beam epitaxy, solid phase elemental sources (in our lab: Ba, Sr, Eu, Al, Ti, La) are placed inside Knudsen effusion cells and heated up to a material-specific temperature until evaporation at a desired rate occurs. Once the vapor phase is in equilibrium, a constant beam of atoms/molecules is focused onto the heated sample stage and combines with other atoms/molecules to form an epitaxial film on the substrate (see Fig. 3.1). The term "beam" is used because under UHV conditions the mean free path of the evaporating species is much larger than the distance between source and sample and the evaporated atoms can reach the substrate surface without colliding with any other molecules in the growth chamber. The term epitaxy can be best described as the growth of a crystalline overlayer following the crystallographic orientation of the single-crystal substrate which acts as a seed layer.

Shutters, which are placed in front of the orifice of the effusion cells, are used to physically block the molecular beam. Opening a shutter exposes the substrate to a beam of atoms thus high precision of shutter control is of fundamental importance. For the MBE deposition system used in this thesis, the shutters can be controlled to 0.1 s precision, allowing submonolayer deposition and layer by layer growth. In MBE a thin

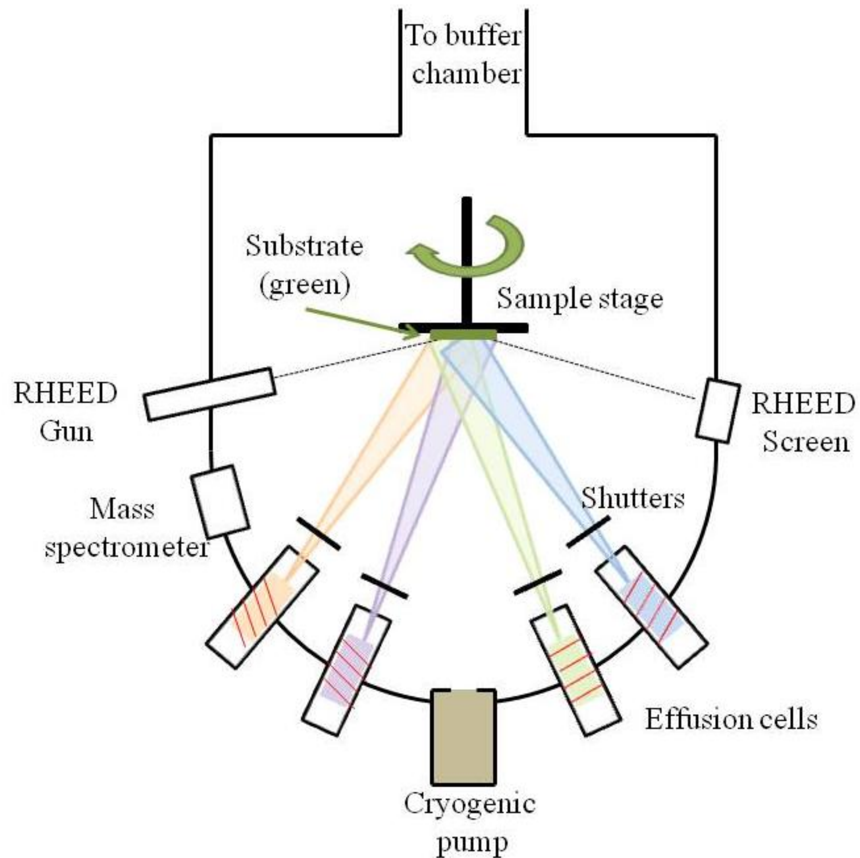

Figure 3.1: Schematic view of an oxide molecular beam epitaxy machine.

film can be deposited either in an amorphous (disordered), polycrystalline (random crystalline domains) or single crystalline (fully ordered) fashion. In which phase a thin film crystallizes depends on film stoichiometry, substrate temperature, surface potentials and lattice mismatch with the substrate. To induce crystallization, the sample stage can be heated to provide the energy needed for the atoms to rearrange from an amorphous to a crystalline structure. If the film grows epitaxially on the substrate, three different growth modes can be described: Volmer-Weber (island growth), Frank-van der Merwe (2d

growth) and Stranski-Krastanov (2d + island growth). The three different growth modes are discussed in more detail in section 3.1.12.

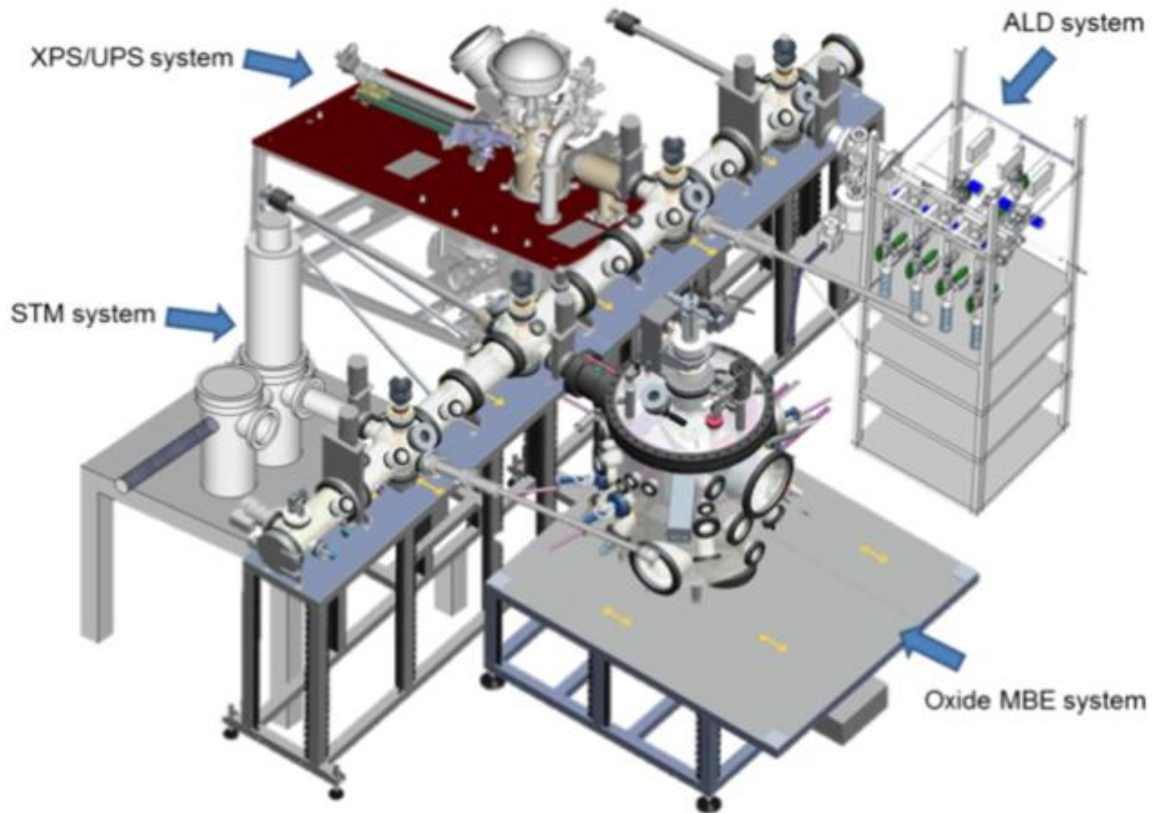

Figure 3.2: The MBE is connected with the XPS and an ALD system via a transfer line to allow *in situ* sample transfer without exposing samples to the ambient.

The MBE in the Advanced Atomic Design Laboratory is a DCA 600 oxide MBE deposition system with a base pressure of ~3×10^{-10} torr. The MBE is connected to an X-ray photoelectron spectroscopy (XPS) system and an atomic layer deposition (ALD) system via a UHV transfer line, allowing sample transfer without breaking the vacuum. The base pressure of the transfer line is ~6×10^{-10} torr. The schematics of the laboratory setup can be seen in Fig 3.2. From an engineering point of view, the system design of an MBE is

quite challenging. In modern MBE systems, the purity level of compound semiconductors must be better than ten parts per billion, with device quality minority and majority carrier characteristics and with excellent uniformity and reproducibility. Growth rates should be in the few microns per hour with thickness control of tenths of a monolayer [5]. In order to achieve such performance under UHV conditions, the individual components of the MBE must conform to the highest quality standards and are described in the following sections.

3.1.3 Main chamber

The stainless steel MBE chamber is custom made by DCA in Finland (see Fig. 3.3) and was designed to withstand a bake out temperature of ~200°C. It has a diameter of about 70 cm, and is equipped with ports for the effusion cells, e-beam evaporator, RHEED, quartz crystal microbalance, plasma sources residual gas analyzer (RGA), cryopump and sample stage. After occasional venting of the chamber for maintenance, air streams into the chamber leading to adsorption of gas and water molecules on the inside of the chamber walls. To facilitate their removal in order to reach UHV conditions again, the chamber is baked out at ~180°C for a few days.

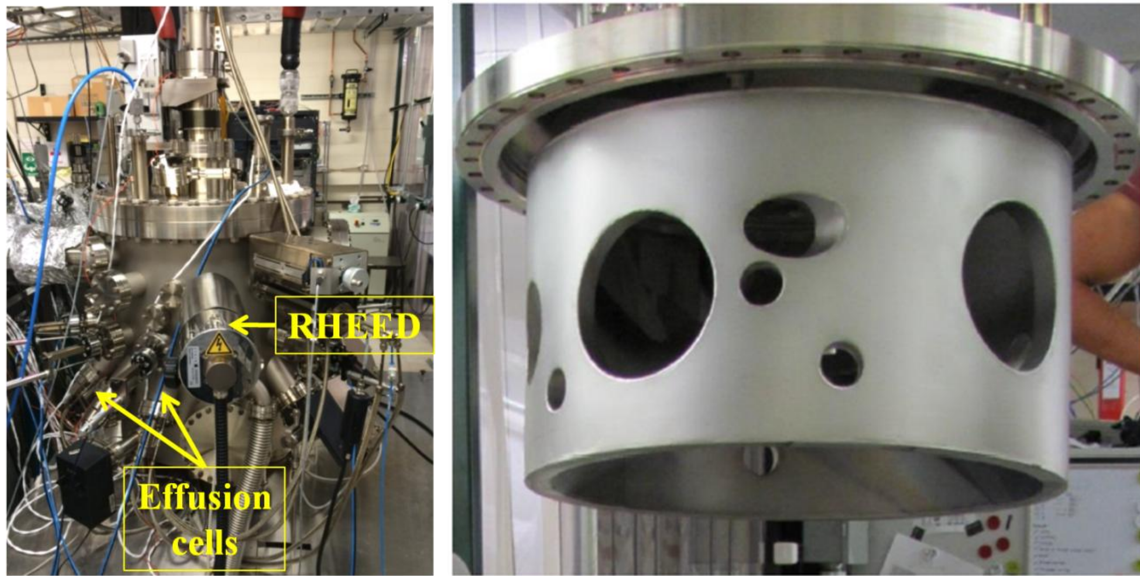

Figure 3.3: Left: MBE chamber in the Advanced Atomic Design Laboratory. Right: Cryopanel used to cool the inside of the chamber walls to avoid re-evaporation of adsorbed materials.

3.1.4 Cryopanel

During longer operation of the effusion cells, the temperature of the chamber wall can increase significantly. To avoid a re-evaporation of material which is adsorbed at the wall, an alcohol- and water-cooled cryopanel are used for the upper and lower part of the chamber, respectively (see Fig. 3.3). To maintain cooled sidewalls of the reactor, the alcohol is constantly flowing and cooled in a closed cycle refrigerator.

3.1.5 Pumps

Vacuum pumps have to constantly operate to maintain UHV conditions in the system. Our facility is equipped with three different kinds of pumps. After a complete vent, a scroll pump is used to reach at least ~10^{-3} torr. Once the pressure in the chamber is low enough, pumping is switched over to a Brooks On-Board cryogenic pump to reach UHV conditions in the MBE chamber. A cryogenic pump is oil free and traps gases by condensing them on a cold surface. Over time this surface saturates with molecules and the pump has to be regenerated to stay fully operational. To maintain UHV conditions in the transfer line, it is equipped with 3 Gamma Vacuum TiTan ion pumps, which are equally spaced out over the whole length of the transfer line. The TiTan ion pumps also operate without oil and ionize atoms or molecules in anode tubes. The ions are then accelerated towards a Ti covered cathode where they react with Ti by forming a stable bond.

3.1.6 Effusion cells

The effusion cells are one of the most delicate and crucial components of the MBE, since their design heavily influences the atomic flux stability. As can be seen in Figure 3.4, the solid source material is placed inside an inert crucible (pyrolytic boron nitride (PBN) for low-temperature cells) which is heated up using a filament surrounding the crucible. For ideal effusion cells, the beam flux can be accurately calculated if the condensed phase and vapor are in equilibrium (see chapter 3.1.11) [5]. To avoid heat propagation from the

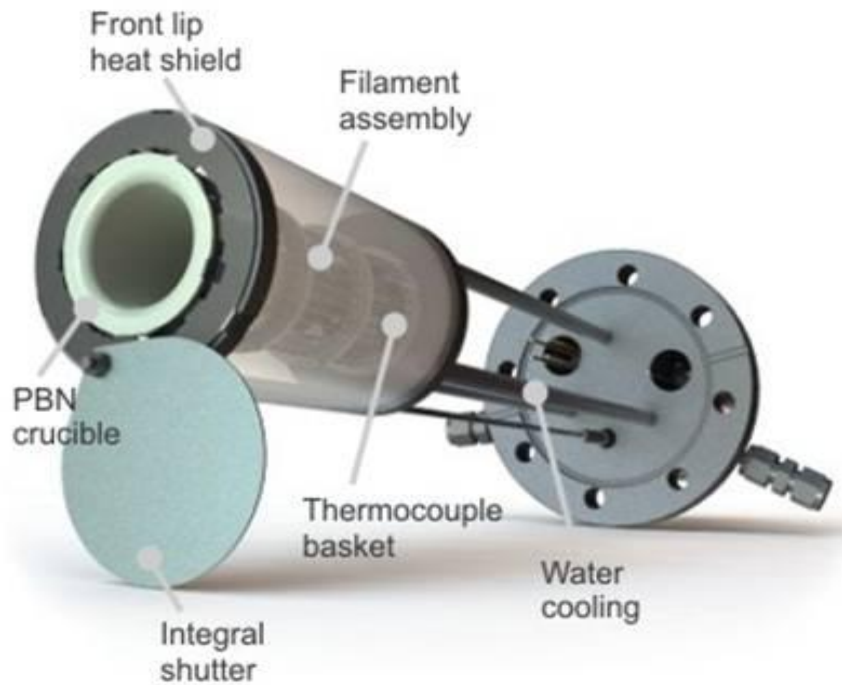

Figure 3.4: Low-temperature Knudsen effusion cell used in our system. Figure taken from Mantis deposition [6].

effusion cell to the rest of the MBE machine, the cell is water cooled and a radiation shield surrounds the filament and crucible. This design provides a temperature control of 0.1°C even for the high temperature cells, allowing a high degree of flux stability. The temperature is monitored through a thermocouple attached to the bottom of the crucible mount and is controlled using a Eurotherm interfaced to the computer. In our laboratory, three types of effusion cells are in use: For titanium and lanthanum, high-temperature effusion cells are needed, while low-temperature cells are used for barium, strontium and europium. For aluminum a cold-lip cell must be used. The effusion cells are placed in such a way that they are all directed towards the centered sample stage, as can be seen in

Figure 3.1. A shutter is placed in front of the orifice of each of the effusion cells to have the capability to physically block the evaporated atoms from reaching the substrate.

3.1.7 E-beam evaporator

Some materials possess a very high melting point, which even exceed the temperatures reached in high-temperature effusion cells. For such materials, electron beam evaporation is used.

Figure 3.5: 4 pocket electron beam evaporation system. Figure taken from Ajaint [7].

Ejected electrons from a tungsten filament are focused and accelerated (~7.75 kV) towards the target material (anode) through magnetic and electrostatic fields. As a consequence, the anode material is heated up locally to very high temperatures and evaporation of the target material occurs. The DCA 600 MBE system is equipped with a 4 pocket e-beam evaporator (see Figure 3.5). Each pocket can hold a crucible and a target material for evaporation. For the growth of Co-doped $BaTiO_3$ samples, Co was evaporated through e-beam evaporation, which is discussed in detail in chapter 8.

3.1.8 RF plasma source

The growth of some compound materials requires dissociated monatomic gas species, since molecular gases are much less reactive. For example, atomic nitrogen is required for the growth of stoichiometric TiN and a nitrogen radio frequency (RF) plasma source must be used (see Fig. 3.6). The MBE is equipped with two RF plasma sources that are each connected to either an oxygen or nitrogen gas supply. The RF plasma source is operated at 13.56 MHz to generate highly reactive atomic and excited molecular oxygen/nitrogen. In chapter 5, I will describe how oxygen plasma can be used as a cleaning mechanism for the Ge(001) surface.

Figure 3.6: Radio frequency plasma source. A nitrogen and oxygen plasma source are connected to the MBE. Figure taken from Scienta Omicron [8].

3.1.9 Quartz crystal microbalance

One of the most important parameters for growing highly stoichiometric thin films is the individual metal fluxes. For their calibration, a quartz crystal microbalance (QCM) is used. The principle of operation is that any change in mass which corresponds to a certain deposition rate would induce a frequency shift in the characteristic frequency of an

oscillator [9]. The measuring technique was first proposed by Sauerbrey in 1959 [10] and follows the formula:

$$\Delta m = -C\Delta f \quad (3.1)$$

Where Δm is the change in mass, C being a constant which depends on the thickness of the quartz slab and on intrinsic properties of quartz, and Δf is the change in frequency. As can be seen in Figure 3.7, the QCM is made out of a thin and round piezoelectric quartz crystal which has gold electrodes on both sides. When an AC electric field is applied to the quartz crystal, it oscillates at its resonance frequency, which changes with the adsorption of atoms on the surface. For flux calibrations, several measurements are carried out and averaged to compensate for small flux variations.

Figure 3.7: A quartz crystal microbalance is used to calibrate the metal fluxes prior to deposition. Taken from [11]

3.1.10 Sample stage

For an oxide MBE, direct heating (resistive heating) of the sample stage is not practical, as the connecting wires to the sample would quickly burn, due to oxygen gas being streamed into the chamber. Instead a silicon carbide block is used which is located right above the sample stage, heating the samples indirectly though heat radiation. The

maximum temperature which can be reached is 1000°C at a maximum oxygen pressure of 10^{-4} torr. To ensure uniformity during sample growth, the sample stage can be rotated. A disadvantage of this indirect heating method is that the temperature reading can become slightly inaccurate for elevated temperatures.

3.1.11 Kinetic theory of gases for MBE

To describe the conditions of the atoms/molecules that are leaving the Knudsen cell, the kinetic theory of gases must be considered. In this case, no interaction between the gas molecules and only elastic scattering between the molecules is assumed.

If we assume a box with an opening of area *A*, then the flux *F* of particles (number of particles per unit area and unit time) leaving the opening is defined as:

$$F = \frac{\#\, molecules}{dA\, dt} = \rho v cos\theta \tag{3.2}$$

Where ρ is the density of the gas and $vcos\theta$ is the velocity of molecules leaving the opening with an angle θ. If we further assume that the velocities of the molecules follow a Maxwell-Boltzmann distribution, the average flux *J* is given by:

$$J = \rho \left(\frac{m}{2\pi kT}\right)^{3/2} \int_0^{\infty} e^{\frac{-mv^2}{kT}} v^3 dv \int_0^{\frac{\pi}{2}} cos\,(\theta) sin\,(\theta) d\theta \int_0^{2\pi} d\varphi \tag{3.3}$$

With *m* being the mass of the molecule, *T* being the temperature and *k* being the Boltzman constant. This result can be further reduced to:

$$J = \frac{\rho}{4}\sqrt{\frac{8kT}{\pi m}} = \frac{\rho \bar{v}}{4} \tag{3.4}$$

As shown in equation 3.4, the total flux of molecules leaving the Knudsen cell is related to the vapor pressure of a material at a certain temperature. In order to find the vapor pressure for a metal, vapor pressure charts can be used. Figure 3.8 shows the vapor pressure vs. temperature of various metals. From the vapor pressure chart one can estimate a rough starting temperature for each metal evaporated from effusion cells.

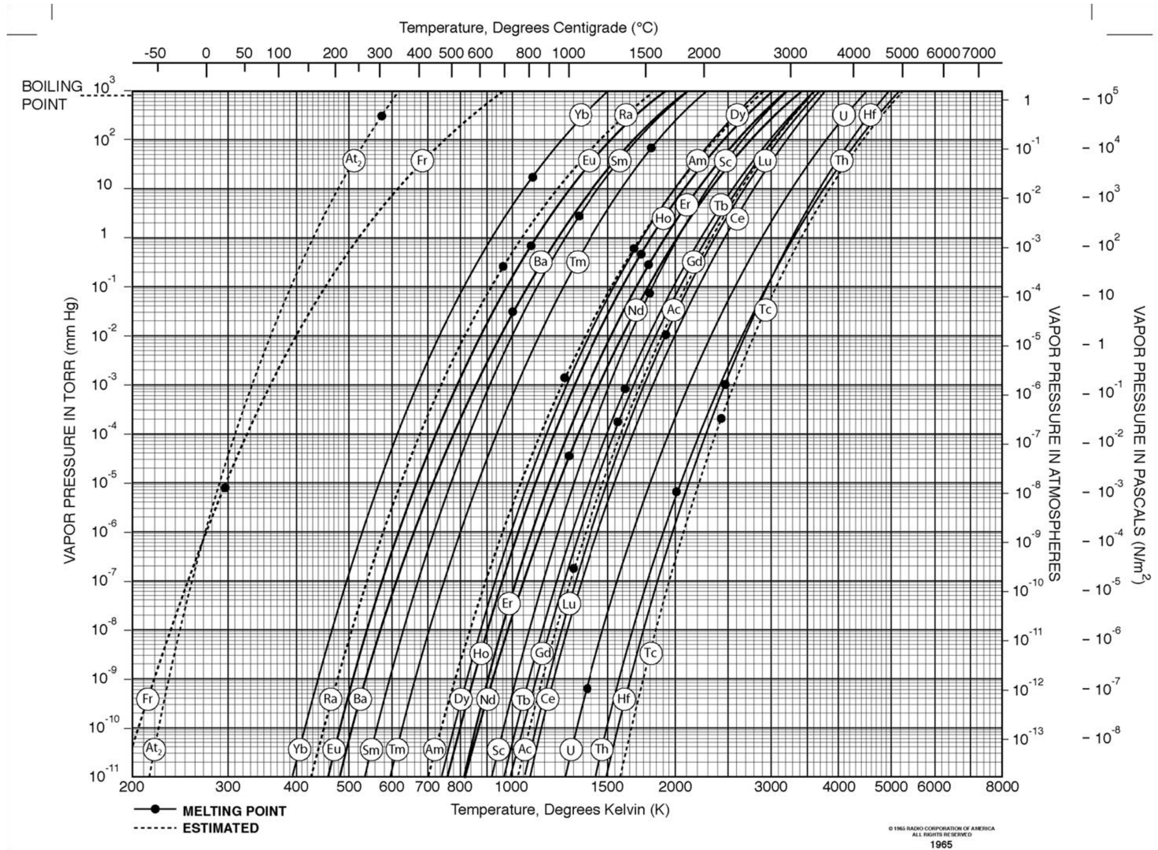

Figure 3.8: Vapor pressure chart of selected metals as a function of temperature [12].

3.1.12 Growth modes

Generally, three different growth modes are observed when growing epitaxial thin films (see Fig. 3.9):

1) Volmer-Weber: In this case, the deposited atoms couple more strongly with each other than with the surface atoms of the substrate. This leads to 3-dimensional clusters or islands which can be observed in RHEED as seen in Figure 3.12 (d).

2) Frank-van der Merwe: This growth mode depicts the opposite of the Volmer-Weber growth mode, since the adatoms nucleate in a layer by layer fashion and attach to surface sites, resulting in a 2-dimensional growth. Additional layers are only formed after layer completion.

3) Stranksi-Krastanov: This growth mode constitutes a mix between the 2D and 3D growth modes. Initially, the thin film grows 2-dimensional until a critical thickness is reached which is highly dependent on surface energies. Beyond this critical point, 3-dimensional growth occurs.

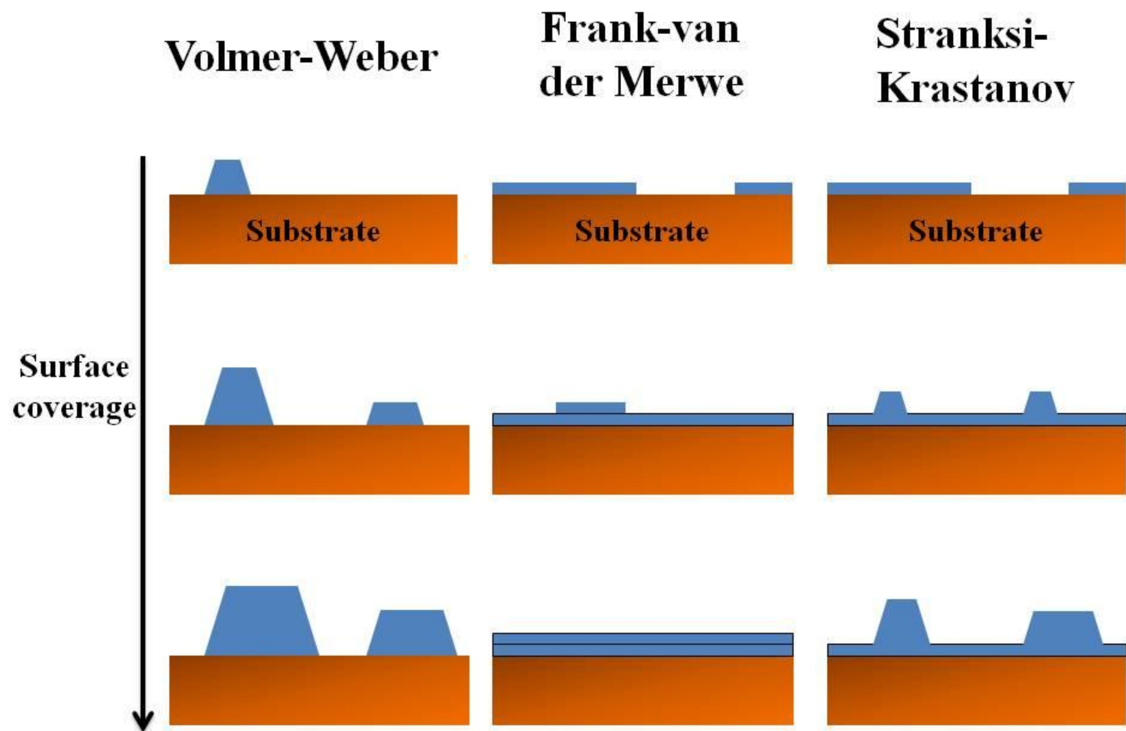

Figure 3.9: Cross sectional view of the three different epitaxial thin film growth modes.

3.2 RHEED

3.2.1 Working principle

RHEED is a very common method for surface structural analysis in combination with an MBE as it visualizes the reciprocal lattice of a surface layer [13]. The advantage of a RHEED setup in comparison to other diffraction methods, i.e. Low Energy Electron Diffraction (LEED), lies in its high surface sensitivity and *in situ* compatibility with MBE growth [14]. Generally, a RHEED setup consists of 3 parts: An electron gun, a rotating sample stage and a phosphor screen (see Fig 3.10).

The electron gun accelerates a well-collimated electron beam to energies between 10-30

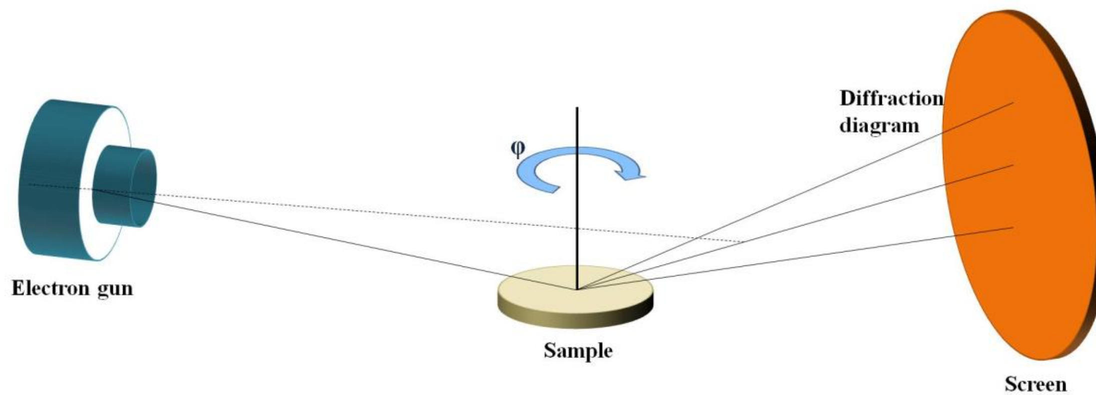

Figure 3.10: Typical RHEED geometry. Electrons are accelerated in the electron gun and impinge the sample surface under a grazing angle. The diffraction pattern can be detected by screen and CCD camera.

keV, which strikes the sample surface typically at an angle of less than 5°. This combination of grazing incidence angle and high electron energy leads to an electron penetration depth of only a few atomic layers into the sample surface making RHEED a

highly surface sensitive technique [13]. The electron beam then diffracts from the sample surface resulting in a diffraction pattern which depends on various parameters, such as atomic spacing, crystal structure, and wavelength of the incoming electrons. The diffracted electron beam impinges on a phosphor-coated screen which illuminates the point of impact due to fluorescence. A charge-coupled device (CCD) camera then captures the image on the screen and the diffraction pattern can be monitored with the kSA software. Only a small fraction of the incident electron beam diffracts constructively which, depending on the surface morphology, creates unique patterns on the screen. Since the sample can be rotated by an azimuthal angle φ, the diffraction pattern of different surface orientations can be observed.

3.2.2 Kinematic diffraction

There are two types of diffraction processes happening on the sample surface which can be distinguished. On the one hand, the incident electrons can scatter kinematically at the sample surface if they undergo a single scattering event without losing energy (elastic scattering). Kinematically scattered electrons produce the high intensity RHEED spots which are visible on the screen. On the other hand, if the incident electrons scatter multiple times, they lose some of their energy. This process is called dynamical scattering. These inelastically scattered electrons add to the background RHEED pattern which can disturb the diffraction features [15].

In kinematical theory, the total electron momentum and energy are conserved, leading to the condition that $|\mathbf{k_0}| = |\mathbf{k'}|$, where $\mathbf{k_0}$ and $\mathbf{k'}$ are the incident and scattered wavevectors,

respectively. To understand under which conditions diffraction occurs, the Ewald sphere can be used for visualization, as diffraction can only occur if the incident and diffracted beams differ by a reciprocal-lattice vector **G** in reciprocal space:

$$\boldsymbol{k'}\text{-}\boldsymbol{k}_0 = \boldsymbol{G} \tag{3.5}$$

$\mathbf{k_0}$, the incident wavevector, determines the radius of the Ewald sphere (see Fig. 3.11) which is defined in the non-relativistic case as:

$$|\boldsymbol{k_o}| = \frac{2\pi}{h}\sqrt{2m_0E} \tag{3.6}$$

For electrons with an energy of 21 keV (the electron energy used in our lab), the radius of

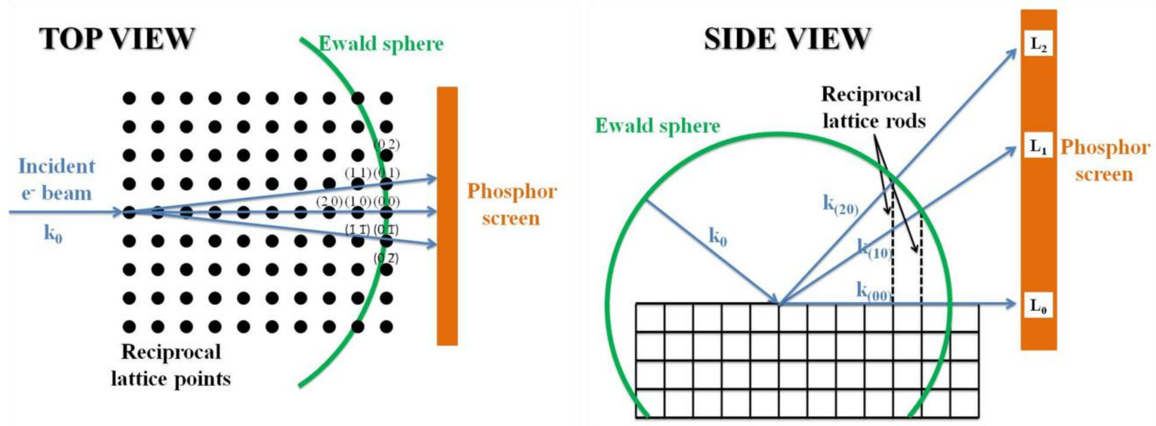

Figure 3.11: Top and side view of the reciprocal lattice rods intersecting with the Ewald sphere, producing a diffraction pattern on the phosphor screen.

the Ewald sphere is about 70 Å^{-1} which is many times larger than the reciprocal lattice constants of Ge (1.57 Å^{-1}), $SrTiO_3$ (1.61 Å^{-1}) or $BaTiO_3$ (1.57 Å^{-1}).

Due to the grazing angle of impinging electrons, the surface normal component $\mathbf{k_{0z}}$ usually has a magnitude below 1000 eV which results in a very small sampling depth. This justifies the approximation of assuming a 2-dimensional layer instead of a 3-

dimensional volume. In this case, the reciprocal lattice becomes a set of one dimensional reciprocal lattice rods, perpendicular to the surface normal [14]. Due to this approximation, only two Miller indices (hk) are needed to describe the surface reflections completely as is shown in Figure 3.11.

The intersections of these lattice rods with the Ewald sphere then give rise to diffraction spots which project on the screen as semi-circles called Laue rings. These rings are labeled with 0th, 1st 2nd... order, however, in practice only the very lowest orders are visible.

3.2.3 Real RHEED patterns

Real RHEED patterns can deviate drastically from the one predicted by kinematic theory. An illustration of the variety of RHEED images possible is shown in Figure 3.12. Figure 3.12 (a) shows the RHEED pattern of an almost perfectly ordered single crystal Ge(001) surface. The diffraction reflections appear as small dots, arranged on the 1st Laue ring. The growth of a thin film on such a substrate usually results in more “streaky” or elongated spots, which can be seen in Fig. 3.12 (b) and can be explained by two reasons. First, the crystal lattice of the grown film is more defective, leading to a broadening of the reciprocal lattice rods of the film. Second, in reality the Ewald sphere has a thickness

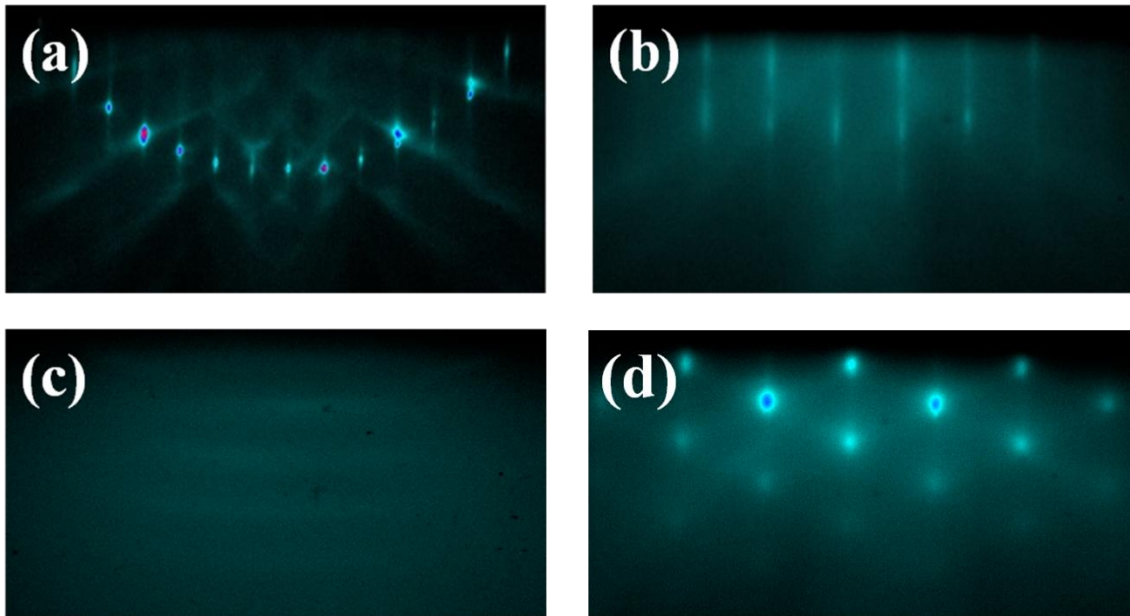

Figure 3.12: RHEED image of (a) a cleaned single crystal Ge(001) surface. Sharp diffraction sports, arranged on a Laue ring are visible. (b) RHEED pattern of a 10 nm thick BTO film grown on Ge with monolayer roughness. (c) shows a polycrystalline RHEED pattern while (d) is an example of a 3 dimensional growth.

due to electron divergence and slight variations in the electron energy which is directly related to the radius of the Ewald sphere. As a result, the Ewald sphere cuts through broadened reciprocal lattice rods, leading to streaks instead of spots. In Figure 3.12 (c) polycrystalline rings are visible, indicative of a polycrystalline surface. If a thin film grows in a 3-dimensional mode (Volmer-Weber type), a RHEED pattern similar to Figure 3.12 (d) can be observed where the broad diffraction spots don't lie on Laue rings anymore and appear as a transmission diffraction pattern.

3.3 XPS

3.3.1 General description

X-ray photoelectron spectroscopy (XPS) is a highly surface sensitive and widely used analytical tool to determine film stoichiometry, the chemical state of elements, valence band spectra and even the spatial distribution of materials [16]. The method is based on the photoelectric effect for which Einstein received the Nobel Prize in 1921 [17].

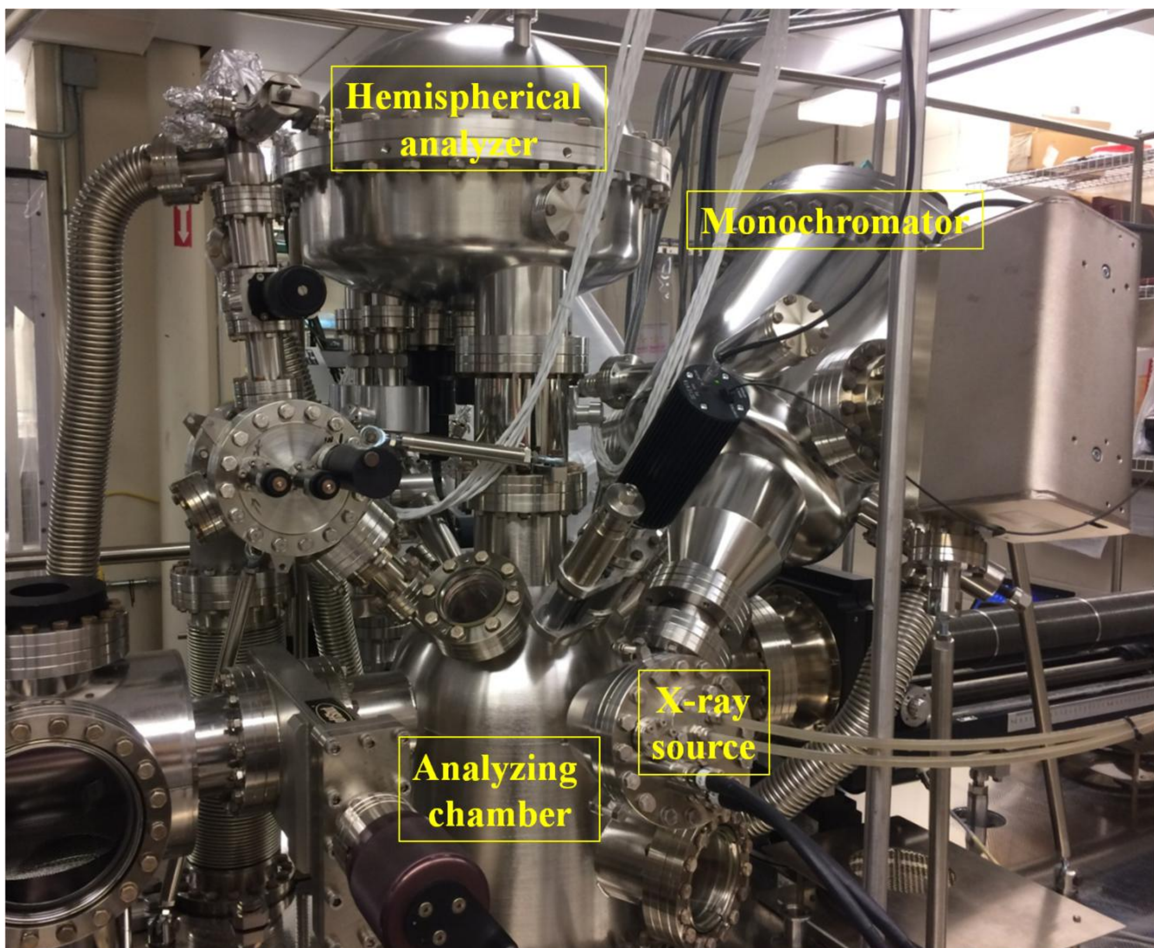

Figure 3.13: XPS system in the Advanced Material Design Lab.

The XPS analysis chamber used for this thesis was designed by VG Scienta and is made out of stainless steel (see Fig. 3.13). It is connected to the MBE via a transfer line, allowing *in situ* sample transfer without breaking the vacuum (see Figure 3.2).

The analyzer chamber's base pressure is ~3×10^{-10} torr and equipped with an Al Kα X-ray source. Highly energetic electrons, ejected from a tungsten filament, are focused on an aluminum target, resulting in material specific characteristic Kα and Kβ radiation from interatomic Al energy transitions and continuous X-ray spectrum caused by Bremsstrahlung. The X-rays are then guided to a quartz crystal monochromator which is kept at 55°C to have a lattice spacing that allows only the Kα X-rays to satisfy Bragg's law (Al Kα: 1486.6 eV) and oriented in such a way that only the monochromatic X-rays impinge on the sample surface, illuminating a sample area of ~1×3 mm^2. Additionally, the monochromator also improves the peak resolution by reducing the X-ray line-width down to ~ 0.25 eV. The 5-axis manipulator holding the sample allows angle-resolved X-ray spectroscopy and can be cooled down to about 150K. A series of electrostatic lenses placed before the hemispherical analyzer are used to maximize the collection angle and to accelerate or retard the energy of the photoelectrons to a user-defined pass energy which allows high resolution core level scans [16]. The photoelectrons then pass through a hemispherical R3000 energy analyzer and are detected using a microchannel plate detector. A schematic of the XPS setup is shown in Figure 3.14.

3.3.2 Working principle

The focused beam of monochromatic X-rays hits the sample and excites not only bound valence electrons but also core electrons which are emitted from the surface. Since energy must be conserved, the kinetic energy E_{kin} of the emitted electrons is given by:

$$E_{kin} = h\nu - E_B - \varphi \tag{3.7}$$

where $h\nu$ is the energy of the X-ray photon (1486.6 eV), E_B is the binding energy of the electron and φ is the work function of the spectrometer. Electrons from deeper regions are more likely to scatter inelastically, and most of them only contribute to the background signal if they are able to leave the sample surface at all. However, electrons from the near surface region can leave the surface without inelastic scattering, resulting in element-specific characteristic peaks, making XPS a highly surface sensitive technique. Electrons emitted from the material through this process are called photoelectrons.

Due to the ultra high vacuum condition inside the analyzer chamber, the mean free path of the ejected photoelectrons is much larger than the distance between the sample and the detector, allowing the electrons to reach the detector without additional scattering with molecules inside the chamber. The kinetic energy of the emitted photoelectrons is then analyzed by the hemispherical analyzer. Electrostatic lenses before the analyzer retard the kinetic energy of the incoming electrons to a pre-defined pass energy allowing only photoelectrons to reach the detector if their kinetic energy is exactly [16]:

$$E = e\Delta V\left(\frac{R_1 R_2}{R_2^2 - R_1^2}\right) \tag{3.8}$$

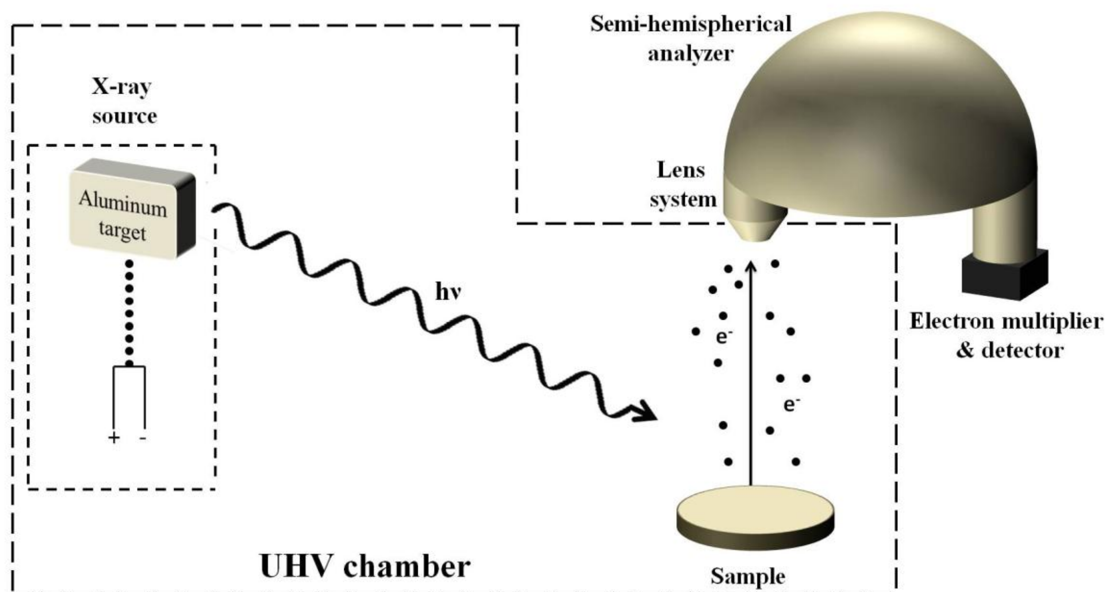

Figure 3.14: An Al Kα X-ray beam impinges on the sample surface. Due to the photoelectric effect, electrons with a material specific kinetic energy are emitted and analyzed by the hemispherical analyzer.

With *E* being the kinetic energy of incoming electrons (pass energy), *e* being the elementary charge, and ΔV being the potential difference between the inner and outer hemispheres with radii R_1 and R_2.

Generally, the peak resolution can be enhanced by choosing a smaller pass energy at the expense of the intensity. For most core levels reported in this thesis, a pass energy of 100 eV was chosen, resulting in high count rate and decent peak resolution. The slit size is also a determining factor for peak resolution, since the theoretical energy resolution ΔE is approximated by:

$$\Delta E = s\,\frac{E_P}{2R} \tag{3.9}$$

With s being the slit width, E_P being the pass energy and $R = \frac{R_1 + R_2}{2}$ being the analyzer radius.

3.3.3 Surface sensitivity

Despite the X-rays penetrating several micrometers into the material, only electrons from the top surface layers (~ < 10 nm) are able to escape the material due to electron-electron and electron-phonon scattering. The surface sensitivity of XPS and analysis depth varies with the kinetic energy of the emitted electrons and is described by a quantity called the attenuation length "λ", a distance for which the probability that the electrons are not absorbed by the material has reduced by a factor of e. While there are several reports discussing the calculation of the attenuation length λ [18-20], a generally accepted description was published by Seah and Dench [21]:

$$\lambda = \frac{538a_A}{E_A^2} + 0.41a_A(a_A E_A)^{0.5} \quad (3.10)$$

where E_A is the energy of the electron in eV and a_A^3 is the volume of the atom in nm^3. The intensity I of electrons from a depth d is described by the modified Beer-Lambert equation:

$$I = I_o exp(- \frac{d}{\lambda cos\theta}) \quad (3.11)$$

where I_o is the intensity from an infinitely thick, uniform substrate and θ is the emission angle with respect to the surface normal. For normal emission with an angle of $\theta = 0°$, 95% of the detected electrons originate from a depth $d < 3\lambda$ which is called the sampling depth.

3.3.4 XPS peaks and analysis

When scanning over the whole kinetic energy range (0 - 1486.6 eV) of photoelectrons emitted by a sample, several different types of peaks can be observed in the recorded spectrum. An example of such a survey scan can be seen in Figure 3.15. In the following I will explain the two most common peaks observable in an XPS scan, namely the element-specific characteristic core levels and Auger peaks.

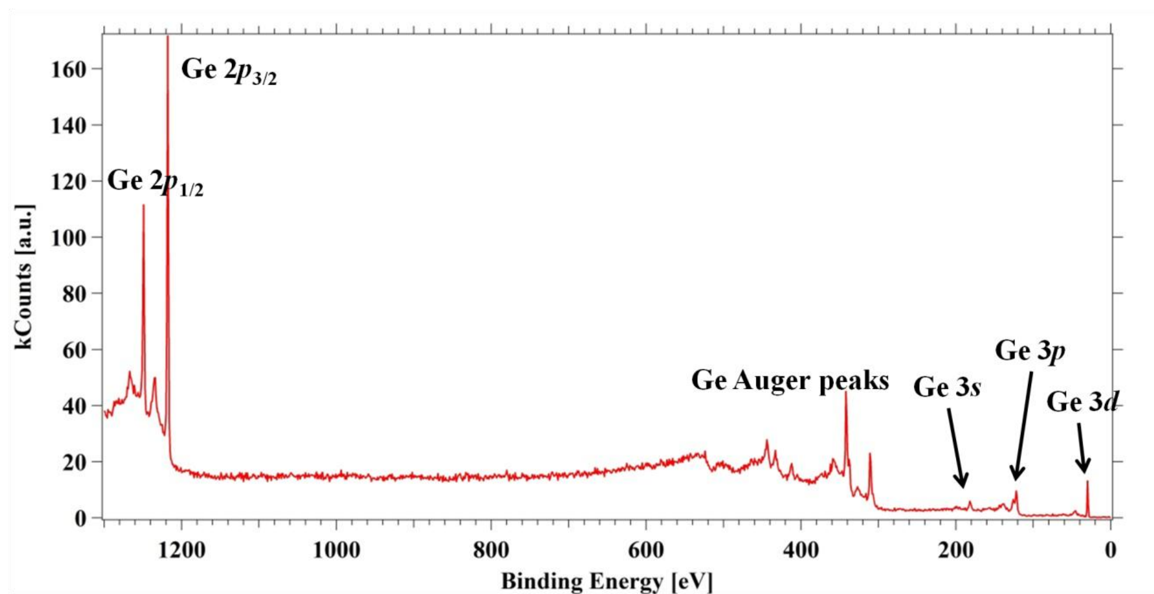

Figure 3.15: Survey scan of an oxygen plasma-cleaned Ge(001) surface. The core level peaks of Ge can clearly be identified. The absence of an O 1*s* and C 1*s* peak indicates an extremely clean surface.

3.3.5 Characteristic core level peaks

By far the strongest and most pronounced peaks are the characteristic core level peaks. It is noteworthy that core levels originating from orbitals with an angular momentum

greater than 0 yield two peaks (doublet) with different binding energies. An example of such a doublet can be seen for the Ge 3*d* core level (see Fig. 3.16). This split is called spin-orbit splitting or spin-orbit coupling and can be explained by a shift of atomic energy levels which is a result from the interaction between the electron spin angular momentum of the ejected photoelectron and the orbital angular momentum. For a 3*d* core level the quantum numbers are n = 3, L = 2 and S = ½ and the total angular momentum J = L ± S can be calculated to be 3/2 and 5/2. The relative peak intensity of the two peaks depend on the relative population of the atomic energy levels which is given by the expression 2J + 1 [16]. Thus for the $d_{5/2}$ and $d_{3/2}$ orbital the relative peak intensity is 3:2.

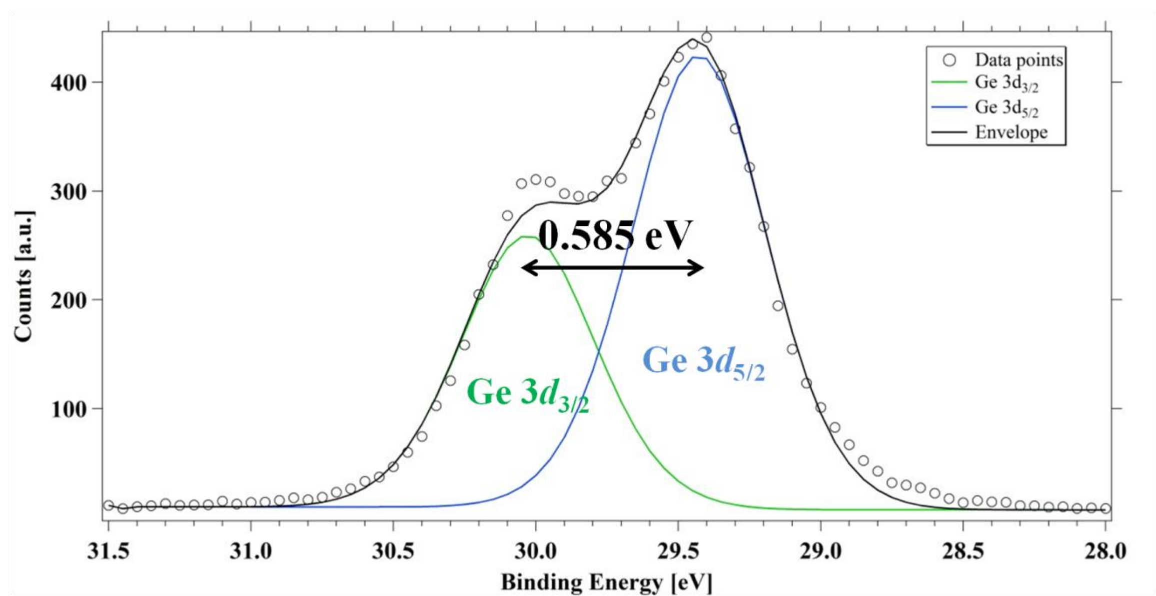

Figure 3.16: High resolution Ge 3*d* core level spectrum of a cleaned Ge(001) surface. The spin orbit split between the Ge $3d_{5/2}$ and Ge $3d_{3/2}$ peak is clearly visible. The two peaks are separated by ~0.585 eV.

3.3.6 Auger peaks

The other type of peaks commonly observed in a survey spectrum are Auger peaks. If the X-ray photon ejects an electron from an inner shell, thus creating a photoelectron, a vacancy is left behind. Electrons from higher energy levels can fill the vacancy which releases energy that can lead to the ejection of an additional electron called an Auger electron. Generally, Auger peaks can also be used for sample analysis, but the much stronger core level peaks are usually preferred.

3.3.7 Quantification

To quantify spectra from XPS, the obtained peaks have to be converted into atomic concentrations [16]. Several sample and detector related factors have to be considered when analyzing the integrated area of a peak. In a simplified version, one can write the intensity I as:

$$I = nf\sigma D\lambda \tag{3.12}$$

with n being the concentration of the atom or ion in the solid, f being the X-ray photon flux, σ being the orbital cross section (the main component responsible for different peak sizes), D being the instrumental factors (spectrometer transmission function, detector efficiency, influence of stray magnetic fields) and λ being the attenuation length. The integrated area can then be calculated by subtracting a background function (i.e. Linear, Shirley, Tougaard) from the intensity. The division of the integrated area with a relative sensitivity factor (RSF) is needed to normalize the obtained intensity with respect to other core levels. The RSF highly depends on the specific element and core level and even

weakly depends on the actual spectrometer and thus must be empirically determined for each element and XPS machine separately. When the RSF is known, the relative atomic concentration can be calculated using:

$$A_i\,[atomic]\,\% = \frac{\frac{I_i}{RSF_i}}{\sum \frac{I_j}{RSF_j}} \times 100\% \qquad (3.13)$$

With A_i being the relative atomic concentration of atom i, I_i and RSF_i being the integrated area and relative sensitivity factor of element i, respectively, and $\Sigma I_j/RSF_j$ being the summation of all normalized intensities. The complete evaluation of the obtained XPS spectra was performed using the analysis tools of the CasaXPS software [22].

3.4 X-RAY DIFFRACTION (XRD)/X-RAY REFLECTIVITY (XRR)

3.4.1 Overview

X-ray diffraction (XRD) and X-ray reflectivity (XRR) are powerful non-destructive analyzing techniques to extract important properties from thin films, such as the in- and out-of plane lattice constants, crystal quality, crystal orientation, film thickness and surface roughness. The two commercial XRD machines used in this thesis are the Philips X'Pert Theta-Theta and Rigaku Ultima IV Diffractometer. Both of them are equipped with a copper X-ray source, producing Cu Kα_1 X-rays with a wavelength of 1.5406 Å. All measurements were performed *ex situ*. The general setup of the XRD system can be seen in Figure 3.17.

After creating X-rays in the X-ray

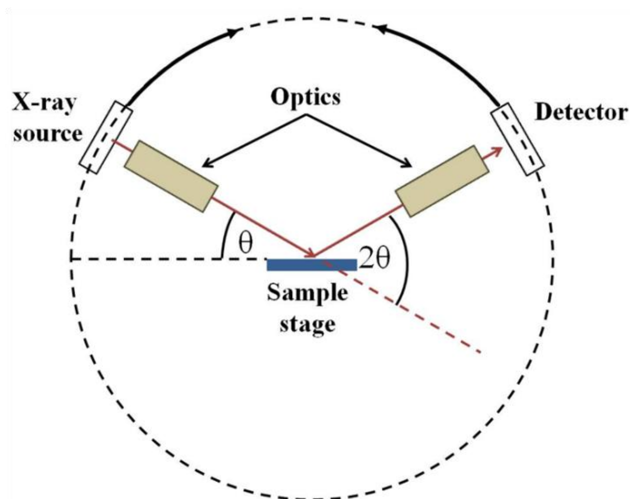

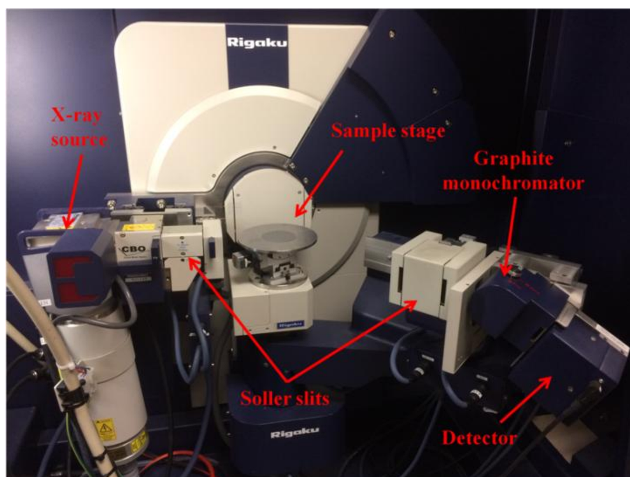

Figure 3.17: Setup of the Rigaku Ultima IV XRD machine. The X-rays are guided through a set of optics before and after diffraction. A scintillation counter is used to detect the incoming X-ray photons. The X-ray source and detector can move independently along a circle.

source, the X-ray beam is guided either through a 2-bounce Ge monochromator or a Soller slit (0.5°, 2.5° or 5.0°) which collimates the beam prior to reaching the sample. The X-rays are then elastically scattered by the electrons of the periodically arranged atoms in the crystal lattice. For constructive interference to occur, the difference in path length of X-ray photons diffracted from different crystal planes must be an integer multiple of the wavelength which is described by Bragg's law (see Fig. 3.18) [23]:

$$n \times \lambda = 2d_{hkl}sin(\theta) \tag{3.14}$$

with n being an integer, λ being the wavelength, d_{hkl} being the lattice spacing of the crystal planes with index hkl and θ being the incidence angle. To increase resolution, the

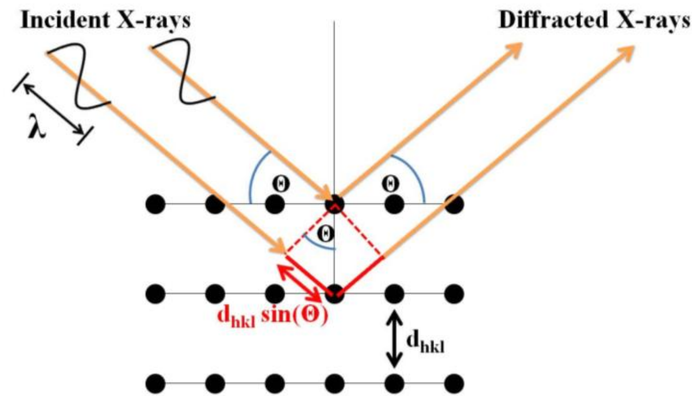

Figure 3.18: Incoming X-rays with a wavelength λ can only diffract constructively, if Bragg's law is satisfied.

diffracted beam is then guided through another set of optics, including a scattering slit, cutting off other parasitic scattered (non-diffracted) X-rays from entering the receiving slit, which defines the width of the beam admitted to the detector. Optionally, a graphite

monochromator can be mounted right before the detector, to filter out peaks originating from the Kβ radiation.

As can be seen from Bragg's law, constructive interference can occur only at specific angles, which results in strong peaks in the obtained spectrum. These peaks can be assigned to specific crystal planes, which are defined by three integers *h*, *k* and *l* (Miller indices) (see Figure 3.19).

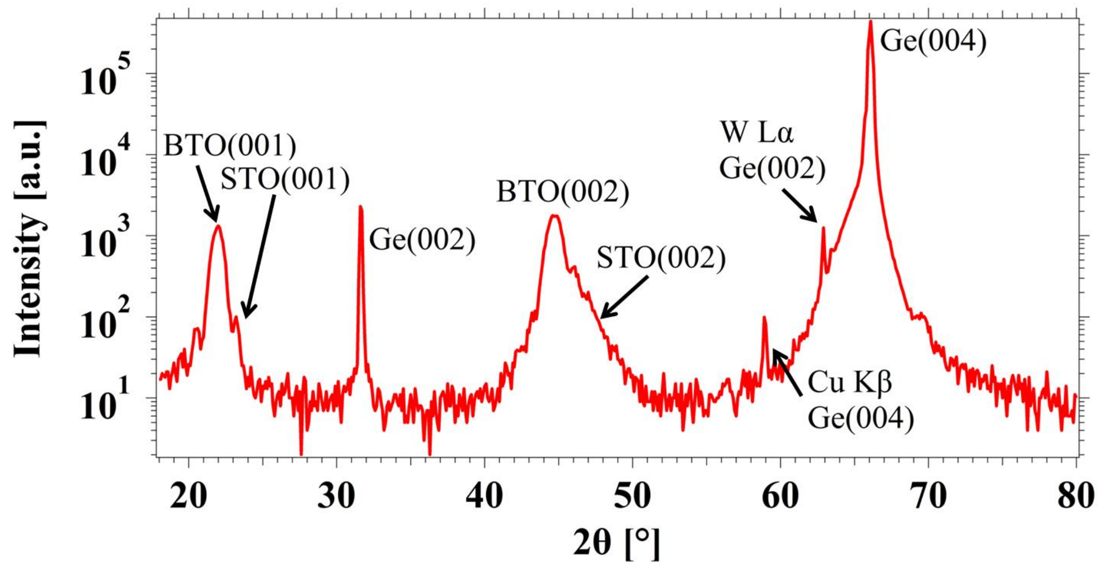

Figure 3.19: 2θ-θ scan of a 10 nm thick BTO film, grown on 2 nm STO on Ge(001). Each peak can be clearly identified to a crystal plane of BTO, STO or Ge, respectively.

In the case of unstrained STO which crystallizes in the simple cubic perovskite crystal structure, the in- and out-of plane lattice constants are equal and the lattice spacing d_{hkl} is defined as:

$$d_{hkl} = \frac{a}{\sqrt{h^2 + k^2 + l^2}} \tag{3.15}$$

with a being the cubic lattice constant and h, k, l being the Miller indices. Plugging equation (3.15) into Bragg's law yields:

$$\sin^2(\theta) = \frac{\lambda^2}{4a^2}(h^2 + k^2 + l^2) \tag{3.16}$$

which can be used to assign the obtained peaks of a spectrum to the associated lattice planes.

An equivalent description of X-ray diffraction was given by von Laue, who assumed diffraction from each lattice site, which leads to the following condition of constructive interference:

$$\boldsymbol{d}(\boldsymbol{k} - \boldsymbol{k'}) = 2\pi m \tag{3.17}$$

with $\boldsymbol{d}$ being a Bravais lattice vector, $\boldsymbol{k}$ and $\boldsymbol{k'}$ the incoming and outgoing wavevector, respectively, and m being an integer. Rewriting equation 3.17 leads to:

$$e^{i\boldsymbol{R}(\boldsymbol{k'} - \boldsymbol{k})} = 1 \tag{3.18}$$

Which states that constructive interference can only occur if the change in wave vector $\mathbf{k'} - \mathbf{k}$ is a reciprocal lattice vector $\mathbf{G}$, which is defined as $\mathbf{G} = m_1\mathbf{b_1} + m_2\mathbf{b_2} + m_3\mathbf{b_3}$, with m_i being integers and $\boldsymbol{b_i}$ being the reciprocal primitive lattice vectors. It can be easily shown that the von Laue equations are equivalent to Bragg's law.

3.4.2 2θ-θ scan

A 2θ-θ scan is often used to perform a survey scan to detect possible secondary phases in the crystal structure and to determine out-of plane lattice constants of the examined crystals. θ is the angle of incidence with respect to the lattice planes, while 2θ is the angle between the incident and diffracted beams (see Figure 3.18). In a 2θ-θ scan, the X-ray source moves by an angle θ, while the detector moves by 2θ, thus the diffraction spectrum can be captured over a wide angular range. Once the diffraction pattern is obtained, the out-of plane lattice constants can be calculated using equation 3.14. The 2θ-θ scan can also be used to determine strain. Depending on whether the thin film is under compressive or tensile strain, the peak position of the (*00l*) plane either shifts to lower or higher 2θ values, respectively, in accordance with the material's Poisson ratio. In Figure 3.20, two BTO(002) peaks are shown. One peak corresponds to unstrained bulk BTO while the other peak is obtained from a compressively strained BTO thin film. The (002) peak position of the unstrained BTO film lies at 44.921°, while the 2θ value for strained BTO can be determined to be 44.739°, corresponding to out-of plane lattice constants of 4.03 Å and 4.05 Å, respectively. As shown in Figure 3.20, two peaks can be observed for the single crystal BTO, which correspond to the long axis being either normal or parallel to the surface. The second domain where the long axis is parallel to the surface is at a 2θ value of ~ 45.46°.

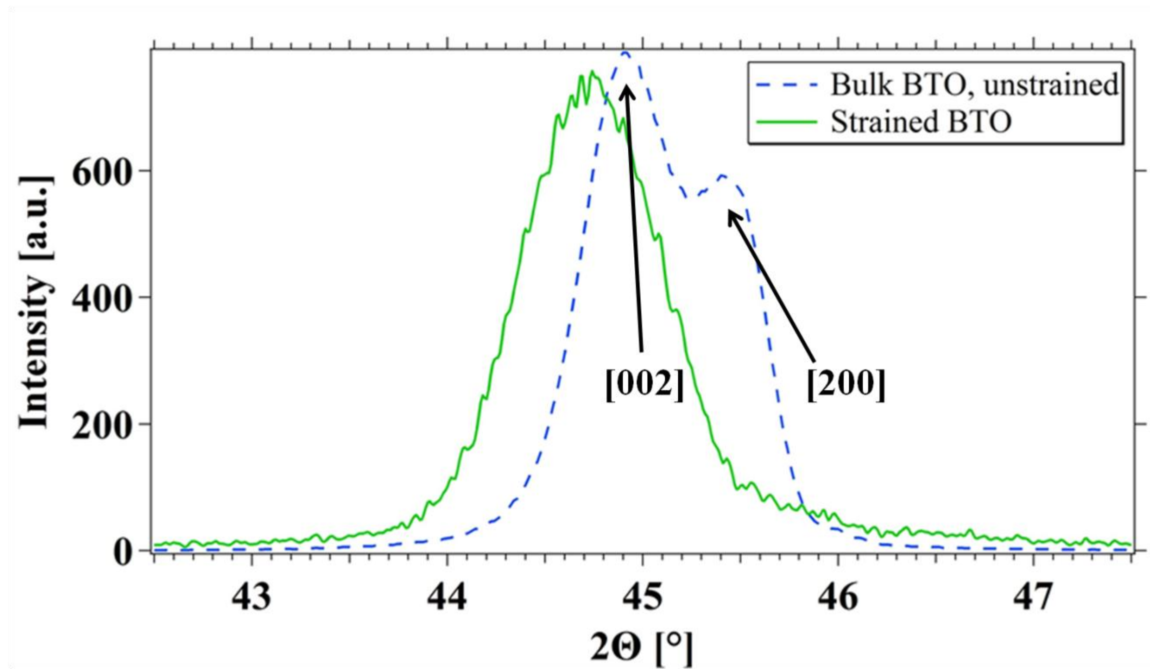

Figure 3.20: High resolution BTO(002) peaks for compressively strained and unstrained BTO. Under compressive strain the peak shifts to lower 2θ values, while tensile strain shifts peaks to higher 2θ values.

3.4.3 ω-scan (rocking curve)

Another useful method to determine the crystal quality of a thin film is the ω-scan, or rocking curve scan. It provides information about the crystalline disorder for a particular orientation in epitaxial thin films. Typically, for an ω-scan the X-ray source and detector are fixed at a specific Bragg peak, while the sample rocks slightly around the angle of its maximum peak intensity. However, the sample stages of the Phillips XPERT and Ultima IV X-ray machines are fixed. In this case, the ω-scan can be achieved by rocking the X-ray source and detector by the same angle simultaneously around a specific Bragg peak,

while the sample stage is kept at a fixed position. The full width at half maximum (FWHM) of the obtained peak contains information about the crystalline disorder. Generally, the narrower the rocking curve and smaller the FWHM value of the peak, the more crystal planes are well aligned fulfilling the Bragg condition at the Bragg angle, while a wider FWHM represents more crystalline disorder, since the Bragg condition is also fulfilled at different ω positions (see Fig. 3.21). The difference in Bragg condition is only fulfilled at one θ value, resulting in a very sharp peak. Typical FWHM values for an

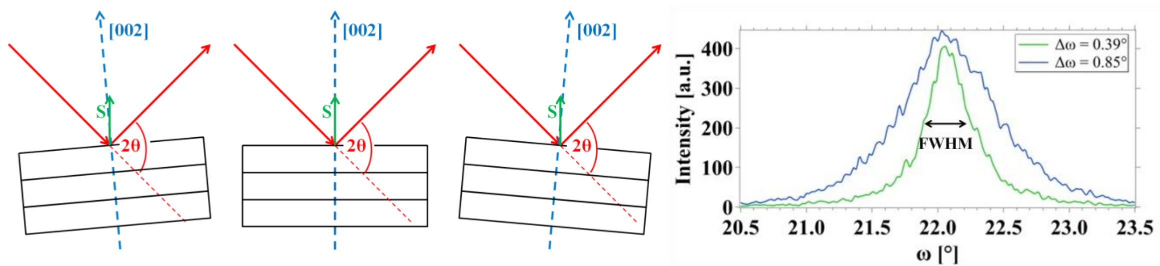

Figure 3.21: Left: For an ω-scan the detector and X-ray source are fixed to a specific Bragg angle, while the sample slightly tilts around the Bragg angle. In the case of the Phillips XPERT and Ultima IV, the source and detector move simultaneously, while the sample stage is fixed. Right: Difference of rocking curve scans for a highly ordered crystalline and slightly more disordered thin film.

epitaxially grown BTO/STO/Ge heterostructure are between 0.3 - 0.8°. Samples which exhibit a higher FWHM value were discarded.

3.4.5 X-ray reflectivity

X-ray reflectivity measurements are ideal to determine thin film parameters such as film thickness, film density and film roughness in a non-destructive fashion. The measurement is done in the 2θ-θ mode where a beam of monochromated X-rays is guided to the sample

under a grazing angle $\omega = \frac{2\theta}{2}$ and the reflected intensity is monitored by the detector. Typically an XRR scan is done between a 2θ angle of 0-6°. For X-rays, the refractive index n of a material is always slightly less than 1:

$$n = 1 - \delta - i\beta \quad (3.19)$$

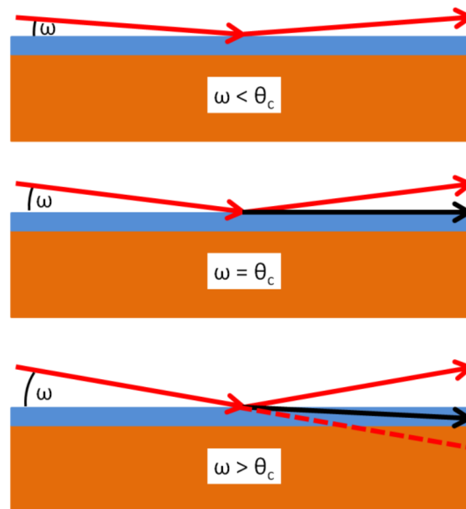

Figure 3.22: If the incidence X-ray beam is less than the critical angle θ_c, total external reflection occurs (red arrows). At the critical angle, the X-rays can propagate parallel to the surface (black arrow), while for incidence angles larger than the critical angle, both, reflection and refraction occurs.

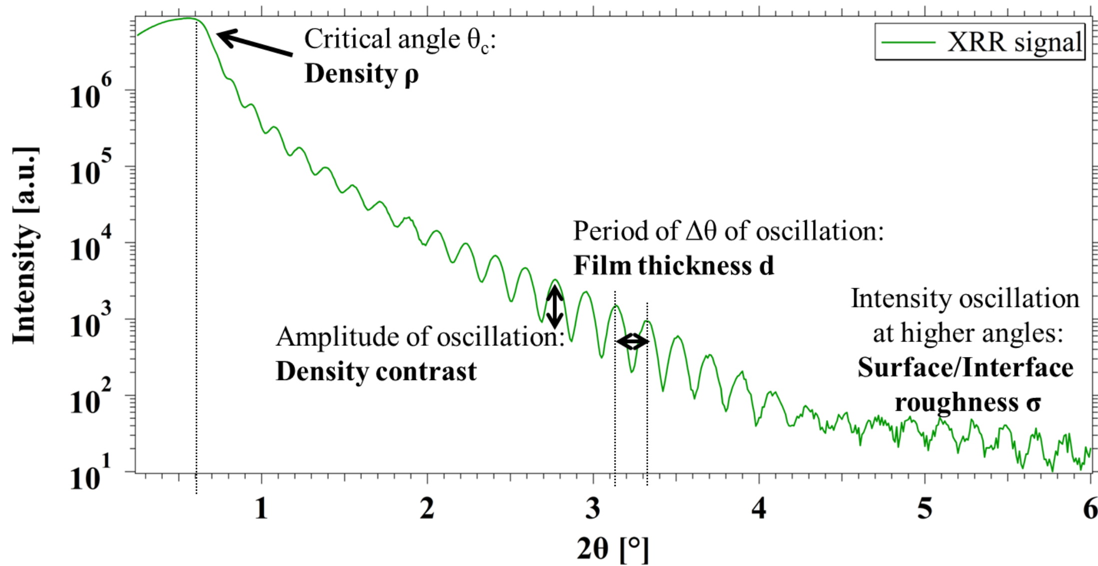

Figure 3.23: XRR signal of a 45 nm thick BTO thin film on a STO/Si template.

with δ and β representing dispersion and absorption which means that if the incident angle ω is less than the critical angle θ_c, total external reflection occurs [24] (see Figure 3.22) since XRR measurements are carried out in air. If ω is increased to a value > θ_c X-rays can enter the medium and refraction from the film/substrate interface occurs in conjunction with reflection from the film surface. This can be explained by the different scattering behavior of different electron densities in different layers of the film which corresponds to different refractive indices. Constructive interference can occur between the reflected beam from the surface and the refracted beam from the film/substrate interface. This interference can be seen as oscillations and are called Kiessig fringes [25]. A typical XRR profile of a BTO/STO/Si heterostructure showing the critical angle and Kiessig fringes can be seen in Figure 3.23.

3.4.6 Density

The density of an unknown material can be calculated by determining the critical angle while the density difference between thin film and substrate is represented in the amplitude of the Kiessig fringes [24]. Using Snell's law for the critical angle:

$$n_1 cos(\theta_1) = n_2 cos(\theta_2) \tag{3.20}$$

$$\Rightarrow \quad cos(\theta_c) = n_{medium}\, cos(\theta_2) \tag{3.21}$$

For small angles, Snell's law can be approximated to

$$cos(\theta_c) \approx 1 - \frac{\theta_c^2}{2} = 1 - \delta \tag{3.22}$$

if absorption is ignored ($\beta = 0$), this leads to:

$$\theta_c = \sqrt{2\delta} \tag{3.23}$$

δ is defined as:

$$\delta = K \times \rho \tag{3.24}$$

where K is a constant and ρ is the density of the film which leads to

$$\theta_c \sim \sqrt{\rho} \tag{3.25}$$

[26].

3.4.7 Thickness and surface roughness

To determine the thickness, we also need to consider the influence of different indices of refraction for the thin film and air. This leads to a modified Bragg's law, due to the incorporation of Snell's law:

$$m\lambda = 2t\sqrt{\theta_m^2 - 2\delta_c} \tag{3.26}$$

with m being an integer or the diffraction order, t the thickness of the film and θ_m the mth angular position of the Bragg reflection. The surface roughness of the film can then be determined by fitting the intensity decay at higher angles.

3.5 AFM

Invented in 1986, atomic force microscopy (AFM) is another useful non-destructive surface analysis technique to extract the surface topography and roughness from grown samples [27]. In comparison to a scanning tunneling microscope (STM), AFM has the advantage that it can also measure non-conducting surfaces. The AFM and MFM images shown in Chapter 5 and 8 were obtained using a Veeco Multi-mode V commercial AFM. All measurements were done *ex situ* under ambient conditions. The used gold coated tips had a resonant frequency of 325 kHz with a spring constant of k = 40 $\frac{N}{m}$ and were bought from MikroMasch

3.5.1 Working principle

The main idea of an AFM is that a cantilever with a sharp tip at its front is oscillating at its resonance frequency in close proximity to a sample surface. The repulsive or attractive force between the tip and the sample affects the cantilever's deflection according to Hooke's law, thus also its oscillation frequency. This change in frequency is detected and can be directly related to the topography of the surface.

The approach of the cantilever to the sample surface is often achieved through a combination of a mechanical coarse manual approach and a piezoelectric element for the fine approach, when the tip has almost reached the surface. When scanning a surface, the deflection of the cantilever is measured by a laser which is reflected from the backside of the cantilever to a photodiode detector [28] (see Fig. 3.24). The photodiode is divided

into four quadrants A, B, C, D which produce an electric signal when hit by the laser beam. The difference of the electric signal between the top two (A+B) and bottom two

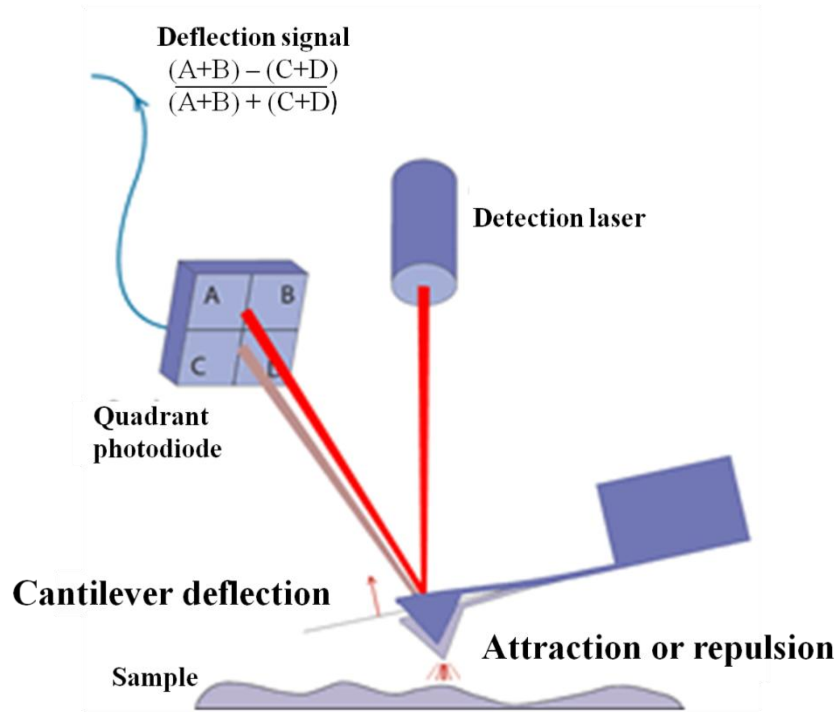

Figure 3.24: Schematics of an AFM. Taken from [29].

quadrants (C+D) are used to extract the surface height, while the difference between the left (A+C) and right quadrants (B+D) are used for detecting a lateral motion of the tip. The signals received from the detector are then used to create a 3d topographical image.

In general, there are 3 common modes that are used to scan the surface: contact, non-contact and tapping mode. In contact mode, the tip is dragged across the sample's surface and the deflection of the cantilever is used to directly image the topography. In non-contact mode, the tip oscillates at its resonance frequency without ever being in direct

contact with the sample. The deflection of the cantilever due to the acting forces is used for imaging the surface. However, most AFM images for this thesis were obtained using tapping mode. A problem with contact mode is the large lateral forces acting on the tip which can lead to tip degradation. Tapping mode circumvents this issue. The cantilever oscillates at its resonant frequency and a fixed amplitude and touches the surface only for a short time hence it "taps" the surface. Variations of the surface height cause a change in amplitude which is used to extract the topography and surface roughness.

A common parameter for characterizing the roughness of a surface is the root mean square (RMS) which is the average of the height difference of the mean image plane.

3.6 REFERENCES

[1] A. Y. Cho, J. R. Arthur, Prog. Solid State Chem. **10**, 157-191 (1975).

[2] K. G. Günther, Z. Naturforschg. A. **13** (12), 1081-1089 (1958).

[3] J. R. Arthur Jr., J. Appl. Phys. **39** (8), 4032-4034 (1968).

[4] A. Y. Cho, F. K. Reinhart, Appl. Phys. Lett. **21** (8), 355-356 (1972).

[5] E. H. C. Parker, "*The Technology and Physics of Molecular Beam Epitaxy,"* (Plenum Press, New York and London, 1985).

[6] www.mantisdeposition.com

[7] www.ajaint.com

[8] www.scientaomicron.com

[9] M. Rodahl, F. Höök, A. Krozer, P. Brzezinski, B. Kasemo, Rev. Sci. Instrum. **66** (7), 3924-3930 (1995).

[10] G. Sauerbrey, Z. Phys. **155** (6)**,** 206-222 (1959).

[11] www.piezo-parts.co.jp

[12] International Union for Vacuum Science Technique and Application http://iuvsta.org/iuvsta2/index.php?id=643

[13] A. Ichimiya, P. I. Cohen, *Reflection High Energy Electron Diffraction* (Cambridge University Press 2004).

[14] Braun W, *Applied RHEED: Reflection High-Energy Electron Diffraction During Crystal Growth* (Springer-Verlag, Berlin, 1999).

[15] Y. Horio, Y. Hashimoto, A. Ichimiya, Appl. Surf. Sci. **100/101**, 292-296 (1996).

[16] John F. Watts, John Wolstenholme, *An Introduction to Surface Analysis by XPS and AES* (John Wiley & Sonst Ltd, West Sussex, England, 2003).

[17] A. Einstein, Ann. Phys. **322** (6), 132-148 (1905).

[18] A. Jablonski, Surf. Interface Anal. **20**, 317 (1993).

[19] S. Tanuma, C. J. Powell, D. R. Penn, Surf. Interface Anal. **21**, 165 (1994).

[20] W. H. Gries, Surf. Interface Anal. **24**, 38 (1996).

[21] M. P. Seah, W. A. Dench, Surf. Interface Anal. **1**, 2-11 (1979).

[22] http://www.casaxps.com/

[23] C. Suryanarayana, M. Grant Norton, *X-Ray diffraction - A practical approach*, (Springer US, New York, 1998).

[24] M. Yasaka, X-ray thin-film measurement techniques, The Rigaku Journal **26**(2), (2010).

[25] H. Kiessig, Ann. Phys. **402** (6), 715-769 (1931).

[26] J. Als-Nielsen, D. McMorrow, *Elements of Modern X-ray Physics* (John Wiley & Sons, Ltd, West Sussex, England, 2001).

[27] G. Binnig, C. F. Quate, C. Gerber, Phys. Rev. Lett. **56**, 930-934 (1986).

[28] G. Meyer, N. M. Amer, Appl. Phys. Lett. **53**, 1045 (1988).

[29] http://usa.jpk.com/index.2.us.html

Chapter 4. Ge(001) surface cleaning methods for device integration

In recent years, research on Ge nanodevices has experienced a renaissance, as Ge is being considered a possible high mobility channel material replacement for Si MOSFET devices. However, for reliable high performance devices, an atomically flat and perfectly clean Ge surface is of utmost importance. In this review, the existing methods for cleaning the Ge(001) surface are reviewed and compared for the first time. The review discusses three broad categories of cleaning techniques that have been successfully demonstrated to obtain a clean Ge surface. First, the use of ultraviolet light and/or oxygen plasma is discussed. Both techniques remove carbon contamination from the Ge surface and simultaneously form an oxide passivation layer. Second, *in situ* ion sputtering in combination with germanium regrowth, which can lead to extremely clean and well-ordered Ge surfaces, is discussed. Lastly, various wet-etching recipes are summarized, with focus on HF, NH_4OH and HCl. Despite the success of HF for Si surface preparation, it is demonstrated that in the case of Ge, HF is outperformed by other chemicals with respect to surface roughness, carbon and oxide removal efficiency. It is shown that several cleaning methods can lead to a perfectly clean Ge surface, but only a few methods can be considered for actual device integration due to their effectiveness, simplicity and scaling ability.

This work was published in: Patrick Ponath, Agham B. Posadas, and Alex A. Demkov, Appl. Phys. Rev. ***4****, 021308 (2017).* In this chapter of the dissertation, I will only focus on the results of the different investigated cleaning methods.

4.1. CLEANING CONDITIONS AND METRIC OF CLEANLINESS

One of the most crucial steps prior to high-κ dielectric integration on Ge is the surface cleaning procedure. From a device fabrication point of view, understanding the Ge surface chemistry is critical, as only extremely clean Ge surfaces can be used for successful high-κ integration to fabricate reliable high-performance devices with low interface-trap density [1, 2]. To obtain an atomically flat, contamination- and oxide-free Ge surface, several essential requirements are imposed on the cleaning process:

I) An effective surface cleaning process must remove all organic contaminants from the Ge surface. On Si it is known that carbides have a deleterious effect on device performance [3] and can introduce microvoids in the oxide [4], which are believed to have a similar effect on Ge. While Si has the ability to incorporate excess C into its crystal structure [5], Ge is much less tolerant. Even under high temperature or pressure, Ge incorporates C only in minuscule amounts into its crystal structure [6-9]. Instead, residual C atoms prefer to precipitate on the Ge surface, forming C clusters [9]. Carbon must therefore be completely removed from the semiconductor surface to achieve optimal device characteristics. Additionally, carbon also hinders the formation of higher Ge surface reconstructions, making layer-by-layer epitaxial growth impossible.

II) All metals, particulates and adsorbed molecules must be stripped off the surface. Although the effect of trace metals on device performance has not been studied in detail for Ge-based transistors, it is well-known for Si that any metal contamination can lead to severe degradation of the transport characteristics [10, 11], increased junction leakage,

and a reduction of minority carrier lifetime [11, 12]. Furthermore, metals are found to enhance the growth of voids and the decomposition of SiO_2 [13], leading to a reduced oxide quality.

III) The cleaning process must also ensure the complete removal of the native oxides to remove impurities that are trapped inside the oxide. At the same time, minimal substrate consumption with little or no increase in surface roughness is desirable. Zhang *et al.* [14] showed that as little as 1 Å of GeO_x is sufficient to prevent the formation of a 2×1 or higher order Ge surface reconstruction.

IV) The formation of a stable passivation layer under ambient conditions in the final cleaning step is crucial, i.e. a chemically grown clean germanium oxide, if the primary surface cleaning is carried out *ex situ*. This passivation layer prevents carbon, metals and other contamination from re-adsorbing to the Ge surface after cleaning while transferring into the ultra-high vacuum (UHV) system.

In this review, we define an atomically smooth and contamination-free Ge surface the following way: The surface contamination of organic residues, germanium oxides and metals must be below the detection limit of X-ray photoelectron spectroscopy (XPS)/Auger electron spectroscopy (AES), which generally lies between 0.1-1 at.% depending on the element [15, 16]. Additionally, the cleaning method must result in a 2×1 or higher order surface reconstruction. To guarantee a 2-dimensional uniform growth of the dielectric material, an atomically smooth surface is essential. Here, we consider

surfaces atomically smooth if their root mean square (rms) surface roughness is below 3 Å, which has been the standard for Si surfaces [17]. Using the root mean square has the advantage that it accounts for defects and protrusions on the Ge surface which contribute to surface roughness, but weren't specifically studied by most groups in detail.

For the existing cleaning processes, a distinction between *in situ* and *ex situ* cleaning methods can be made. The utilized *in situ* cleaning methods include thermal desorption, oxygen plasma cleaning, and ion sputtering of the Ge surface, which is often combined with a thermal anneal and/or Ge regrowth. Although a simple thermal desorption can remove the GeO_2 layer completely, it is rather ineffective in removing other kinds of residues from the surface. Oxygen plasma is able to completely decompose and volatilize organic compounds, effectively removing them from the Ge surface. Sputtering in combination with Ge regrowth will be shown to be a very effective way of cleaning the Ge surface. However, with the additional regrowth step that is required to heal the sputtering damage, the preparation time for this method can be quite long. The *ex situ* cleaning methods consist of ultraviolet (UV) light oxidation and wet-etching, which are promising methods for successfully removing organic contamination while, at the same time, the formation of a newly-grown oxide passivation layer successfully protects the Ge surface. Nevertheless, the reliable preparation of large scale, contamination- and defect-free Ge(001) surfaces is still challenging.

4.2 UV LIGHT AND PLASMA EXPOSURE

Relatively little information has been published on the impact of ultraviolet (UV) light and oxygen plasma exposure on the Ge(001) surface, despite their success in removing carbon from the Ge surface [14, 18-22].

4.2.1 Cleaning principle

Both cleaning methods rely on the same chemical principle and are based on two reactions happening simultaneously. First, UV light radiation breaks down most of the chemical bonds (C-H, C-C) from organic contamination on the Ge surface [23], leaving organic free radicals and excited molecules on the surface. In the case of oxygen plasma, the UV light is created through a continuous recombination process of all oxygen species involved. Second, highly reactive oxygen species, which are either formed in the oxygen plasma or through photolysis of oxygen molecules due to UV light, bond with the remaining carbon and other organic radicals on the Ge surface, forming volatile CO, CO_2 and H_2O [24], resulting in a practically carbon-free surface (see Figure 4.1). At the same time a thin protective layer of germanium oxide of up to 70 Å [18] forms as a result of the oxidation of surface Ge. The newly oxidized layer also consumes contaminants that have segregated to the near surface region of Ge. This thin oxide layer is advantageous when using a UV light source *ex situ* as it acts as a passivation layer, preventing carbon from re-depositing on the Ge surface during the loading process into the vacuum system. As a final step, the passivating germanium oxide needs to be removed through an annealing step, which is usually done *in situ*.

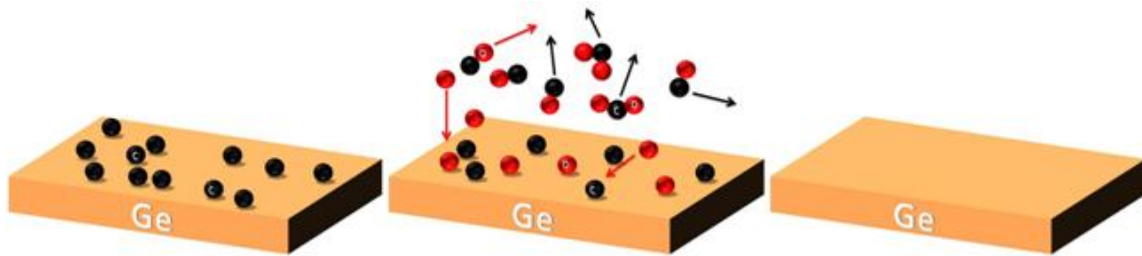

Figure 4.1: (a) Ge surface with organic contamination (black). (b) Atomic oxygen (red) reacts with carbon on the surface and forms volatile CO, CO_2 and H_2O leaving behind a carbon-free Ge surface (c).

Both cleaning methods rely on the same cleaning principle, however, the creation process of the UV light radiation, which breaks down the organic bonds, and the formation of the highly reactive oxygen species differs. Oxygen plasma is created by using a radio frequency electrical excitation of a cavity containing molecular oxygen gas at some pressure in order to ionize the gas to form the plasma. Usually, an oxygen plasma consists of a variety of highly excited atomic, molecular, ionic and radical species (O, O^+, O^-, O_2^+, O_2^-, O_3), as well as free electrons and metastable molecules [24]. Although other gases such as He, N_2, NH_3, N_2O, CO_2, CF_4 or Ar could be used for plasma cleaning as well [24], molecular O_2 is usually the preferred gas to remove organic residues from wafer surfaces, due to the formation of several highly reactive oxygen species, some of which are shown below:

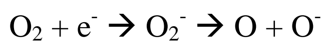

$O_2 + e^- \rightarrow O_2^- \rightarrow O + O^-$

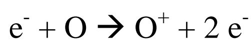

$e^- + O \rightarrow O^+ + 2\ e^-$

$e^- + O_2 \rightarrow O_2^+ + 2\ e^-$

$$e^- + 2O_2 \rightarrow O_2^- + O_2$$

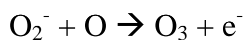

$$O_2^- + O \rightarrow O_3 + e^-$$

For cleaning Ge wafers with an *ex situ* UV light source, generally a low pressure Hg discharge lamp is used, due to Hg having two major emission lines at wavelengths λ_1 = 253.7 nm and λ_2 = 184.9 nm. These photons have energies of E_1 = 472 kJ/mol and E_1 = 647 kJ/mol, respectively, and can dissociate most organic compounds (see Table 4.1). Furthermore the 184.8 nm wavelength is important as it is capable of dissociating O_2, leading to the formation of highly reactive ozone gas [14, 25, 26].

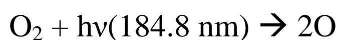

$$O_2 + h\nu(184.8\ nm) \rightarrow 2O$$

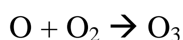

$$O + O_2 \rightarrow O_3$$

$$O_3 + h\nu(254\ nm) \rightarrow O_2 + O$$

When both wavelengths are present, highly reactive ozone is continuously formed and decomposed which results in the formation of atomic oxygen - a strong oxidizing agent.

Bond	Bond energy (kJ/mol)	Bond	Bond energy (kJ/mol)
C-C	347.7	C=C	607
C-H	413.4	C-O	724
C-N	291.6	C-Cl	328.4
C=N	791	C-F	441
C-O	351.5		

Table 4.1: Chemical bond energies of organic molecules found on the Ge surface.

The major advantage of using UV light or oxygen plasma, apart from its effectiveness in completely removing any organic contamination from the Ge surface, is the economical and environmental aspects. The use of hazardous and toxic acids can be circumvented and, unlike wet-etching methods that produce a high volume of liquid hazardous waste resulting in expensive chemical disposal, excess oxygen, CO_2 and H_2O can be released directly into atmosphere [27]. This cleaning method also provides the advantage that no time consuming Ge regrowth is needed to obtain a highly ordered and atomically clean Ge surface, which is often needed after ion sputtering (see chapter 4.3).

4.2.2 UV light exposure

Three different surface preparation methods were reported in a pioneering paper by Zhang *et al.* [14]. They used a combination of XPS, AES and reflection high-energy electron diffraction (RHEED) to compare the surface quality of I) degreased only, II) degreased and water-rinsed, and III) degreased, water-rinsed and UV light-exposed Ge surfaces with and without an *in situ* thermal anneal. For samples that underwent only a degreasing step (treatment I) a high amount of carbon and oxygen could be detected on the Ge surface. The residual oxygen and carbon amount could be reduced by a factor of 5 (for oxygen) and 2 (for carbon) when a DI water rinse was performed right after degreasing (treatment II). Similar to the results of Chui *et al.* [28], this is explained by the water solubility of GeO_2, leaving an oxide layer of only 0.1 - 0.2 nm thickness on the surface. For both sample treatments I) and II), a thermal anneal after the surface cleaning lowered the carbon and oxygen concentration significantly. However, best results were

obtained when the Ge surface was degreased, water-rinsed and then exposed to UV light followed by a thermal anneal above 390°C for 30 min *in situ* (treatment III). XPS measurements confirmed the absence of any germanium oxides and carbon on the surface and a clean 2 × 1 reconstructed surface could be observed by RHEED.

The authors also carried out a study of the optimal UV light exposure time and found that the amount of carbon left on the surface can be drastically reduced if the exposure time is increased from 10 to 30 min. Longer UV exposure times did not result in any significant further decrease of the carbon concentration at the surface (see Figure 4.2). A subsequent final thermal anneal removes the newly formed GeO_2 layer at a temperature of 350°C, with complete oxide layer removal at a temperature of 390°C (see Figure 4.3).

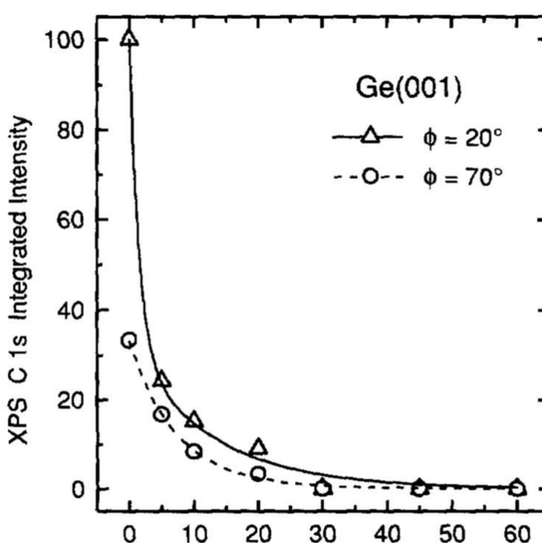

Figure 4.2: C 1*s* peak intensity as a function of UV exposure time. Reproduced from J. Vac. Sci. Technol. A **11**, 2553 (1993), with the permission of AIP Publishing.

Studies of UV light exposure on the Ge(001) surface were also carried out by three other groups [19-21] with slightly different results from Zhang *et al.* Hovis *et al.* [19] performed a pre-cleaning step by dipping the sample into HCl(36%)/H_2O (1:4) and H_2O_2(30%)/H_2O (1:10) prior to the UV light exposure. Gan *et al.* [20] performed only a

degreasing step, while Chan *et al.* [21] did not perform any surface treatment prior to UV light exposure at all.

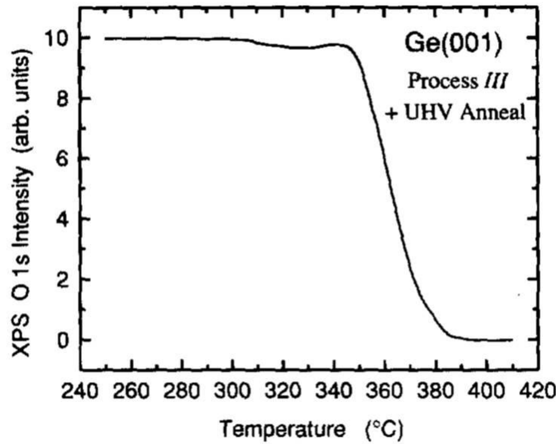

Figure 4.3: O 1*s* peak intensity from a Ge wafer after undergoing process III with a 30 min UV exposure as a function of temperature. Reproduced from J. Vac. Sci. Technol. A **11**, 2553 (1993), with the permission of AIP Publishing.

All three groups reported the presence of residual carbon on the surface even after a thermal anneal *in situ*. In the cases of Gan *et al.* and Chan *et al.* who also carried out STM studies of the Ge surface, small protrusions (0.2 - 1.0 nm) were found on the surface, whose origin was not definitively identified. These protrusions are suspected to be either carbon clusters [20, 21, 29, 30], dopant residues of highly doped Ge wafers [31, 32], or Ge “flakes” [33] that redeposited near the defects. Since the protrusions were also seen on undoped Ge samples by Chan *et al.*, dopant segregation can be ruled out. Nevertheless, the removal of these protrusions is a crucial step in the surface preparation, as they may act as nucleation sites [31].

4.2.3 O_2 plasma treatment

Chan *et al.* performed an oxygen plasma cleaning of their Ge substrates and confirmed the reduction of carbon and oxygen on the surface. But they only obtained a faint 2 × 1 LEED pattern in combination with a rough Ge surface, which may be related to the absence of an *ex situ* surface pre-cleaning or degreasing step prior to oxygen plasma exposure.

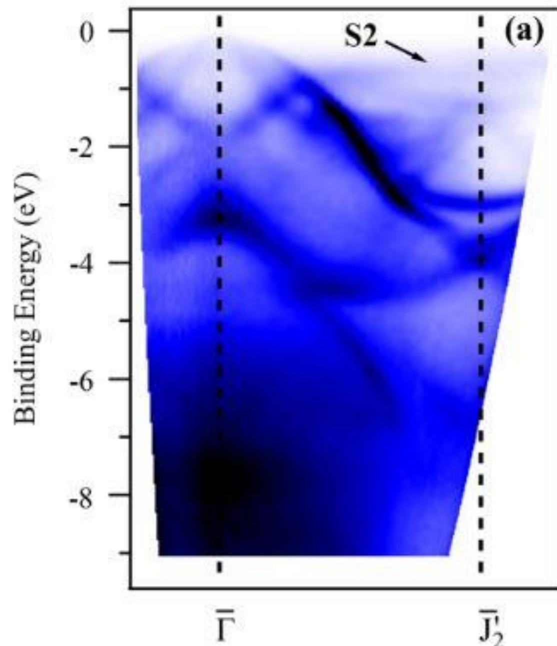

Figure 4.4: ARPES spectrum of a Ge (001)-2 × 1 surface measured using a photon energy of 21.22 eV showing surface states. Reproduced with permission from Phys. Rev. B **89**, 115318 (2014). Copyright 2014 American Physical Society.

In 2013, Ponath *et al.* could demonstrate that oxygen plasma can be successfully used as a cleaning method leading to an atomically smooth and contamination-free 2 × 1 reconstructed surface [18] when an *ex situ* pre-cleaning step is performed. Prior to loading their samples into the vacuum system, a combination of degreasing and wet-etching the Ge surface with HCl (15%) and H_2O_2 (7%) was performed (see wet-etching details in section VI D.). The samples were then exposed to oxygen plasma *in situ* using an rf power of 300 W at an oxygen pressure of 1.0×10^{-5} torr for 30 min at 100°C,

followed by a thermal anneal at 700°C for 1 h. This resulted in an atomically smooth, 2 × 1 reconstructed and contamination-free Ge surface. No signs of carbon, metals or oxygen could be detected by XPS. AFM measurements confirmed a very low mean surface roughness of only ~3 Å. Furthermore, bands, due to Ge surface states, could be detected with angle-resolved photoemission spectroscopy (ARPES), indicative of an extremely clean Ge surface (see Figure 4.4) [34].

4.2.4 H_2 plasma treatment and H_2 annealing

A few studies also discuss H_2 plasma cleaning of the Ge(001) surface [35-38], which relies on a similar cleaning principle as oxygen plasma. The main advantage of using H_2 plasma cleaning is the fact that H_2 plasma reacts with carbon and volatilizes germanium oxides at the same time. As a consequence the cleaning process can take place at temperatures as low as 230°C [36] because the final annealing step to volatilize the formed germanium oxide at higher temperatures can be skipped. While a 2 × 1 reconstructed Ge surface can be obtained after an H_2 plasma exposure, most studies report that H_2 plasma cannot remove germanium oxides and carbon contamination completely, making it not ideal as a cleaning technique.

The effect of a H_2 anneal on the Ge(001) surface has also been studied. It could be shown that an anneal under a hydrogen environment can further decrease the surface roughness of epitaxially grown Ge on Si [39-44]. Saraswat *et al.* reported that a hydrogen anneal of epitaxially grown Ge layers on Si with a subsequent annealing step reduces the Ge surface roughness by 90% [39, 43]. Similar results were reported by Yu *et al.*, where a

multistep lateral overgrowth with hydrogen annealing (MLHA) reduced the mean roughness of epitaxially grown Ge on Si from 3.5 nm for untreated samples down to 0.7 nm for hydrogen-annealed surfaces [42]. For bulk Ge(001) wafers, Nishimura *et al.* showed that atomically smooth terraces can be achieved when the Ge wafer is annealed for 15 min at temperatures higher than 700°C under a hydrogen environment *ex situ* [40].

Despite partly contradictory results from different groups, the use of UV light and oxygen plasma is shown to be very effective in removing carbon completely from the Ge surface. In combination with a thermal anneal *in situ*, an oxide-free, atomically clean and smooth 2×1 reconstructed surface can be obtained. An exposure to H_2 plasma, however, leaves small amounts of carbon and germanium oxides on the surface, making this method not ideal for surface cleaning. While most groups haven't studied the surface roughness after UV and oxygen plasma exposure in detail, a surface roughness of ~3 Å was reported for oxygen plasma-treated Ge surfaces [18].

4.3 Ion sputtering and Ge regrowth

Ion sputtering was discovered more than 150 years ago [45] and is an indispensable tool for surface cleaning, high quality thin film deposition, as well as surface- and microanalysis of solids [46] and is one of the most common cleaning methods, especially for STM studies. A significant amount of literature discusses the use of sputtering as a cleaning method for the Ge(001) surface, which can lead to a very clean and almost defect- and contamination-free surface. [21, 31, 32, 47, 48, 49-55]. However, most of

these studies do not report their final surface roughness, which makes this cleaning process difficult to compare.

4.3.1 Sputtering process

Physical sputtering is the removal of surface and near-surface material through the impact of highly energetic ions (mostly Ar^+ or Ne^+ with kinetic energies of a few keV) and must be performed in vacuum [46]. These highly energetic ions can be supplied by a variety of techniques, e.g. by a plasma- or ion source or a particle accelerator and are focused on the sample target. For sputter cleaning, ions are commonly generated using electron impact ionization of an inert gas in an apparatus commonly known as an ion gun. Only a small fraction of the incident ions impinging on a surface is backscattered [56]; the majority of the incoming ions transfer some or all of their energy and momentum to the surface

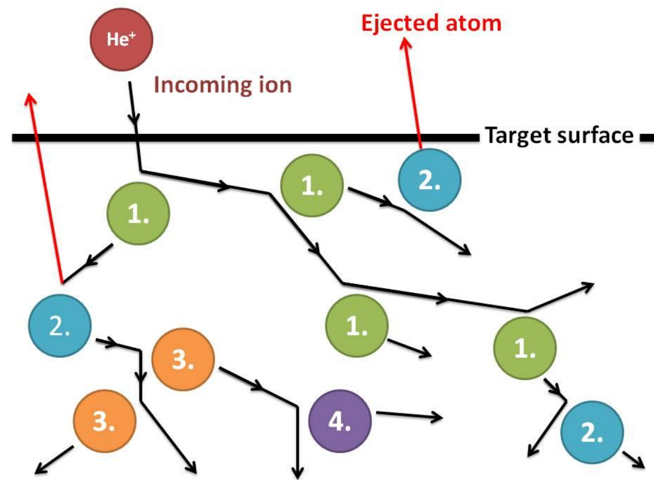

Figure 4.5: Schematics of a collision cascade. The incoming He^+ ion (ruby) can transfer a fraction of its energy and momentum to the primary atoms (green), which can in turn collide with secondary (blue), ternary (orange) and quaternary (purple) atoms. If the energy is large enough and the direction of the momentum points towards the vacuum half-space, a small number of atoms can leave the target (red arrow).

atoms of the target. A cascade of collisions can be triggered in the target surface and subsurface if the energy and momentum transfer to the surface atoms is high enough to overcome the surface binding energy, usually resulting in the ejection of secondary and tertiary atoms from the target [46, 56] (see Figure 4.5). However, the effectiveness of ejecting atoms from a surface not only depends on the energy and angle of the incident ions, but also on the target mass and crystal orientation with respect to the incoming beam. Only about 60% of the ejected atoms are primary atoms, while 40% stem from secondary, tertiary or quaternary recoils [46]. Sputtering a wafer for several minutes eventually strips off contamination from the target surface. However, the sputtering process on a Ge surface also ejects Ge atoms and leaves an amorphized and extremely rough surface with new contamination originating from the incident ions. For this reason, a thermal anneal usually follows the sputtering process in order to recrystallize the Ge surface layer and to heal the large troughs that were created through the ion bombardment. To further improve the surface quality, Ge homoepitaxy is often performed on top of the healed surface, to ensure a highly crystalline and contamination-free Ge surface [21, 33, 54, 55, 57].

The major advantage of this cleaning technique is the successful removal of most contamination from the top surface layer due to their physical ablation, leading to an ultra-clean Ge surface. In conjunction with a thermal anneal, ion sputtering is often chosen as the primary surface cleaning method for STM studies. On the other hand, the main disadvantage of ion sputtering is the surface degradation and a long processing

time. Multiple sputtering and annealing cycles of the Ge surface in combination with Ge homoepitaxy can take many hours and might therefore not be practical for industrial purposes.

4.3.2 Ion sputtering of the Ge surface

One of the first groups to use ion sputtering on Ge(001) was Farnsworth *et al.* [49] in 1958 who also proposed the 2×1 surface reconstruction. In their work, they first cleaned the Ge wafers with a CP4 etch (HF:Nitric:Acetic) and rinsed it in doubly-distilled water, prior to outgassing the Ge wafer between 50 - 100 h at 700 - 800°C *in situ*. A thermal anneal slightly below the melting temperature of Ge of 938°C [58] did not show a satisfactory diffraction pattern and an ion bombardment between 0.5 - 1 h in conjunction with a thermal anneal was used. For samples that were sputtered without the initial outgassing, a clean Ge surface was never obtained. Once the samples were sputtered and annealed no deterioration in the diffraction pattern was found between 1 day and 1 month. Furthermore, it was found that no oxides form on the surface of the Ge wafer after the ion bombardment and annealing, while an upper limit for carbon contamination was determined to be 0.2 monolayer.

Another surface study was carried out by Kevan *et al.* [47], who used Ne^+ ions to sputter their Ge(001) samples for 10 min followed by a thermal anneal at 800 K for 5 min, which resulted in a well-ordered 2×1 surface at room temperature, confirmed by LEED and AES. However, they found two types of residual surface contamination leading to a degradation of surface quality. First, they found that a complete removal of all carbon

contamination was not achieved. Even after a couple of sputtering and annealing cycles, small amounts of carbon contamination could still be detected on the surface. Second, the authors found that their sample surface quality deteriorated with time. Hydrogen and water were suspected to be the origin of this contamination. A gentle flashing to 400°C was found to remove this type of contamination, resulting in reproducible and clean surfaces when flashing every 15 min.

Kubby *et al.* [48] performed Ar^+ and Ne^+ sputtering on a Ge surface, followed by a thermal anneal to 800 - 850°C between 1 to 20 minutes with a cool down rate of 1°C/s. LEED patterns indicated a clean and sharp 2 × 1 reconstructed surface, while STM scans also revealed local domains of p(2 × 2) and c(4 × 2). Lucas *et al.* [52] carried out *in situ* x-ray diffraction and scattering measurements of the c(4 × 2) => (2 × 1) temperature dependent phase transition on the Ge(001) surface. The authors found that at least 8 cycles of sputtering with Ar^+ ions followed by a thermal anneal at 700°C for 5 min with a cool down rate of 0.5°C/s is needed to observe no further reduction of the (2 × 1) Bragg reflection widths, indicative of a clean Ge surface. Slower cooling rates were found to have no effect on the 2 × 1 domain size or the intensities of the superlattice reflections. Yang *et al.* [53] cleaned their surface by Ar^+ sputtering followed by a thermal anneal at 820°C for 10 min which resulted in a clean and mostly 2 × 1 reconstructed surface, confirmed by LEED, but STM scans also revealed long and thin domains of c(4 × 2) and p(2 × 2) surface reconstructions and many dimer vacancy (DV) defects.

The majority of the observed defects are of the (1+2) DV complex type, where an intact dimer lies between a single and a twin missing dimer. The line scans of their Ge surface supports a theoretical defect model for the (1+2) DV defect structure for the Si(001) surface proposed by Wang *et al*. [59], where a broken bond is assumed only at the top surface layer (see Figure 4.6). While the (1+2) DV defect only contributes to 37% of the total defect density on a Si(001) surface [59], it represents the majority of the defects found on the Ge(001) surface. Since the (1+2) DV defect possesses the lowest formation energy out of all defects on the Si(001) surface [59], the authors deduce that it is very likely that it also applies to the Ge(001) surface explaining the high concentration of this type of defect.

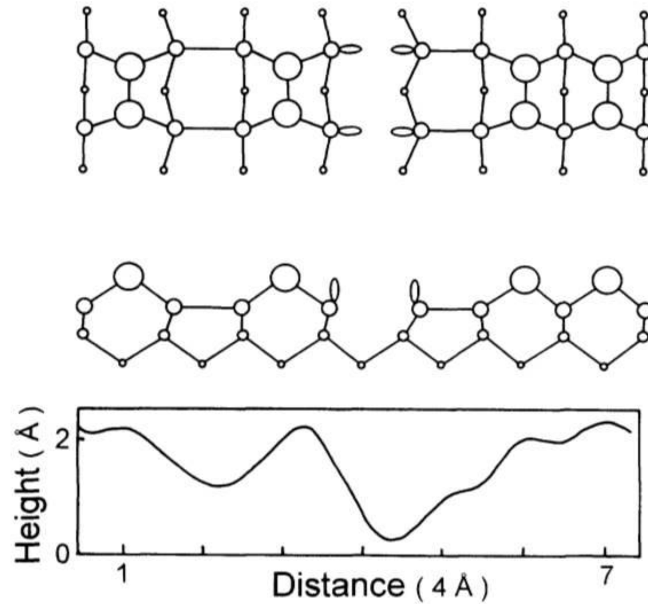

Figure 4.6: Top and side view of the structural model proposed by Wang [59] for the (1+2)-DV complex. Bottom: Line scan of such a defect. Reproduced with permission from Phys. Rev. B **50**, 2406 (1994). Copyright 1994 American Physical Society.

4.3.3 Ion sputtering and Ge regrowth

As shown by Kevan *et al.,* sputtering, in conjunction with a thermal anneal, doesn't always result in a total removal of all organic contamination from the surface, and defects

can also remain as was also shown by Yang *et al.* [53]. One way to deal with the problem of contamination and defective Ge surfaces is to perform germanium homoepitaxy on the sputtered and annealed Ge samples, which buries the defects under a newly grown defect- and contamination-free Ge surface.

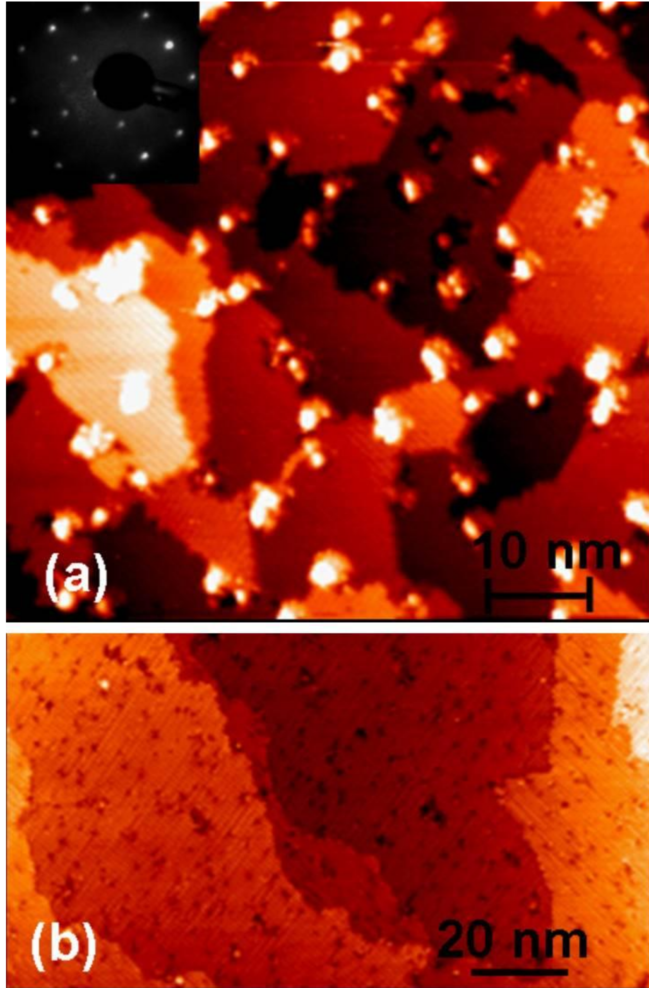

Figure 4.7: (a) STM image of the Ge(001) surface obtained after two ion sputtering/annealing cycles. b) STM image after enhancing the ion energy and with six cleaning cycles. Reproduced with permission from Nanotechnology **17**, 2396-2398 (2006). Copyright 2006 Institute of Physics.

To study the influence of a Ge regrowth, Qin *et al.* performed two cycles of Ar^+ sputtering at room temperature for 10 min in combination with a thermal anneal at 800°C, which lead to randomly distributed dimer defects and protrusions on the Ge surface (see Fig. 4.7(a)) [31]. They found, that the protrusions could be removed by increasing the ion flux from 4.6 $\mu A/cm^2$ to 5.7 $\mu A/cm^2$ in conjunction with performing several cycles of sputtering/annealing, which lead to a mixture of 2×1 and

$c(4 \times 2)$ reconstructed domains on the surface with a total defect density of 12%. However, the authors pointed out that it is possible that some of the missing dimer defects could be caused by the STM tip, as was shown in other STM studies [60]. After increasing the tunneling current from 0.24 nA to 0.34 nA and scanning the same area twice, new defects appeared, which is explained by the enhanced tip-sample interaction. An evaluation of the dimer defects on the surface revealed a depth of 1.3 ± 0.1 Å, which corresponds to a monoatomic layer of Ge, indicative that these defects are only present on the top layer of the Ge surface, which was also seen by Yang *et al*. and Wang *et al.* [53, 59]. A thin layer of 0.1 monolayer of Ge was then deposited at 300°C on top of the sputtered and annealed surface to repair the damaged surface. Due to the mobility of the additional deposited Ge atoms at 300°C, defects, created through the sputtering process, could be healed. Using this method, large scale and atomically smooth Ge(001) surfaces could be obtained repeatedly.

In most cases, however, a thicker Ge layer is homoepitaxially deposited, to ensure complete coverage of all protrusions and defects which were formed during the sputtering/annealing cycles. Both Fukuda *et al.* [55] and Chan *et al.* [21] carried out STM studies of sputtered/annealed Ge surfaces with a subsequent Ge regrowth of 6-30 nm thickness and found that an almost defect-free surface [55], with the formation of long, highly ordered step terraces after a final anneal at 920 K [21], could be observed.

Klesse *et al.* carried out a more comprehensive cleaning study of the Ge(001) surface, including wet-etching, thermal annealing and Ge homoepitaxy [33]. A summary of their

results related to Ge regrowth will be presented here and their wet-etching results will be discussed in the next section. After wet-etching the Ge surface with HCl and H_2O_2, the surface morphology was characterized using STM where bright protrusions with a typical area of 3×3 nm^2 and a height of up to 5 Å were observed, which coincides with the results of other groups [20, 21, 31, 32]. However, the authors attribute the protrusions to Ge "flakes", formed during the *in situ* high-temperature flash anneal, performed right after the wet-etching. They argue that due to thermal desorption of GeO_x, small amounts of Ge are removed from the surface that redeposit nearby as Ge clusters.

Apart from the protrusions, monatomic terraces and irregularly oriented step-edges were found on the surface with a defect density of only 2% and an overall rms roughness of only 1.1 Å, showing higher order of p(2×2) and c(4×2) rows. To further improve the surface quality, a 25 nm thick Ge buffer layer was deposited homoepitaxially at three different substrate temperatures: T_{sample} = 450°C, T_{sample} = 500°C and T_{sample} = 600°C. The authors find that an increase in substrate temperature decreases the surface roughness from ~3.8 Å to ~1.8 Å, but only the Ge layer grown at 600°C substrate temperature showed a lower surface roughness (0.8 Å) than the initial value of 1.1 Å. This result is attributed to an island-like growth of homoepitaxially deposited germanium at lower temperatures which transitions gradually into a step-flow growth at 500°C to 600°C. It is worth noting that none of the samples with a Ge buffer layer showed indications of protrusions, regardless of the substrate temperature. To study the influence of a final thermal anneal, all Ge buffered samples were heated up to 760°C for 10 s leading to an

extremely clean, protrusion-free surface, with single step terrace widths between 80 - 100 nm for the Ge layers grown at a substrate temperature of 500°C and 600°C. The surface roughness for all three buffered and annealed samples was found to be below the initial value of 1.1 Å with the lowest surface roughness of ~0.63 Å for the layers deposited at 500°C and 600°C. However, an investigation of the defect density revealed that an extremely low value of only 0.2 % was found for Ge grown at 500°C, while a much higher value was reported for the samples grown at 450°C and 600°C, making Ge homoepitaxy at 500°C in conjunction with a final anneal at 760°C for 10 s the best sample preparation process for an atomically flat, nearly defect- and protrusion-free surface.

To summarize, using sputtering as the only cleaning tool, some contamination can remain on the Ge surface. However, an increase in the number of sputtering/annealing cycles can reduce the amount of organic contamination from the surface. Since the sputtered Ge surfaces are generally very rough and amorphized, a thermal anneal is needed to heal the surface, which reduces the surface roughness significantly, resulting in a well-ordered 2×1 reconstructed surface that can exhibit domains of $p(2 \times 2)$ and $c(4 \times 2)$ reconstructions. STM studies have shown that surfaces which were prepared only by sputtering and annealing revealed protrusions and a significant amount of defects on the surface. The best results are obtained when Ge homoepitaxy is performed on the sputtered and annealed Ge surface at 500°C in conjunction with a final thermal anneal at 760°C for 10 s, leading to a 2×1 reconstructed Ge surface with a roughness of about 0.6 Å, which

fulfills every requirement of a contamination-free and atomically smooth Ge surface. However, the extremely long processing times make ion sputtering in combination with a Ge regrowth not practical for industrial purposes.

4.4 WET-ETCHING

Section 5.4 of this review is dedicated to wet-etching, which is one of the most established cleaning methods for the Ge(001) surface. As a matter of fact, the majority of the published cleaning methods include at least one wet-etching step. Despite the enormous amount of literature and knowledge about etching the Si(001) surface [61-63], comparatively little is known about the influence of wet-chemicals on the Ge(100) surface, which is primarily due to the historic technological interest in Si. Nowadays, the use of buffered HF in conjunction with the RCA cleaning process has become a standard in Si device manufacturing to clean the Si surface and etch SiO_2.

By definition, wet-etching is the removal of material (particulates, organic contamination, oxide, metals etc.) from a wafer surface by using liquid chemicals or etchants and can be divided into three steps: (1) Diffusion of the etchant to the Ge surface, (2) the reaction between the etchant and Ge and (3) the diffusion of byproducts from the Ge surface [64]. Instead of looking at the detailed mechanisms of etching, the focus of this review is on the total cleaning efficiency of the various etchants. To clean a semiconductor surface, it is common to perform several cycles of etching which often contain some kind of oxidizing agent, i.e. H_2O_2, to form a chemical oxide as a passivation layer. To ensure clean and atomically flat Ge surfaces, the selection of the appropriate wet-chemistry is

crucial and must meet several criteria: 1) The etchant must remove all germanium oxides from the surface while avoiding strong consumption of the Ge surface in order to prevent surface roughening [22, 65]; 2) It must efficiently remove organic and metal contamination from the surface; 3) The etchant should not exhibit a high anisotropy, as this could lead to an undesired etching behavior. Often, liquid etchants tend to be highly anisotropic, resulting in a strong dependency between the etch rate and the crystal plane which the etchant is facing [66]. Furthermore, one needs to consider the formation of a surface passivation layer at the end of the etching cycles to avoid further metal and organic contamination. This passivation layer must be stable in air to prevent the diffusion of contaminants to the Ge surface. However, at the same time, it should be easily removable *in situ*, which is often done through a thermal anneal. Germanium oxide is generally the preferred passivation layer, as it is easily formed and can be easily removed through a thermal anneal *in situ*. However, due to the water solubility of GeO_2, the stability of the oxide passivation layer is not clear. Okumura *et al.* [67] reported problems forming an oxide passivation layer when dipping a cleaned Ge wafer into a H_2O_2/H_2O (1:10) solution, as the oxide removal rate of H_2O was suspected to be higher than the oxide formation rate through H_2O_2. Due to the high Ge etch rate using pure H_2O_2 (30 wt%), H_2O_2 is often diluted with H_2O to reduce the etch rate and consumption of the Ge wafer. For a volume ratio of H_2O_2/H_2O (1:10) Brunco *et al.* and Sioncke *et al.* reported a Ge etch rate for n-type and p-type Ge between 20.8 - 22 nm/s and 12.5 - 17 nm/s, respectively [68, 69]. Further dilution of H_2O_2 down to H_2O_2/H_2O (3:5000) leads to an even lower Ge etch rate of only 4.4 nm/s, which allows a much better control over the

Ge consumption [69]. Other passivation mechanisms such as S-bridge bonds [70], and H- or Cl-terminated Ge(001) are also possible and have also been reported in the literature [1, 22, 65, 71-73].

The main advantage of using wet-chemicals is the already existing industrial infrastructure for wet-etching due to Si device manufacturing. Depending on the concentration of the etchant and etching time, a total removal of oxygen and carbon can be obtained, leading to an atomically flat and contamination-free Ge surface. The disadvantage of using wet-etching is that the use of hazardous chemicals requires special attention for their disposal.

This review focuses on three different chemicals which are most studied and utilized: HF, NH_4OH, and HCl. Each of these chemical's oxide- and contamination removal efficiency is discussed in detail. Ge wet etch rates for a variety of other wet chemistries were published by Brunco *et al.* [68], Ehman *et al.* [74] and Kagawa *et al.* [75]. The section ends with a short summary of two other halide acids: HBr and HI, which have also been used to etch the Ge surface. However, at first, the effect of a simple water rinse is discussed since it is often part of a wet-etching process.

4.4.1 Water rinse

Only a few groups have studied the effect of de-ionized (DI) water rinsing as the only cleaning method for the Ge(001) surface, [28, 71, 76, 77]. The cleaning method makes

use of the water solubility of GeO_2, as the rinsing water will slowly remove the native oxide from the Ge surface which is always present on air exposed Ge surfaces.

Although rinsing Ge in water is a quick way to remove GeO_2 from the sample surface, it has many drawbacks. Water neither removes metals, organic contamination or germanium suboxides from the Ge surface nor does it promote the formation of a clean passivation layer, protecting the oxide-free surface. This lack of passivation ultimately leads to an oxide regrowth during the sample loading process and leaves the surface unprotected from organic deposition.

In 2004, Chui *et al.* [28] carried out a study of DI water-rinsed Ge wafers using AFM. The authors find that the surface roughness of the Ge substrate increased from initially ~2.5 Å to ~3.5 Å within the first 5 seconds of the water rinse, due to the incomplete removal of the native oxide leading to a rougher Ge surface. After rinsing the Ge substrate for 60 s in water, a minimum surface roughness of only ~1.25 Å was obtained which is attributed to a full removal of germanium oxides from the Ge substrate. However, the exposure to water for more than 60 s resulted in a further increase of the surface roughness. This increase is explained by the authors as resulting from the adsorption of H_2O on the surface, forming germanium hydroxides and ultimately leading to an increase of the surface roughness for longer rinsing times. However, surface characterization to support their assumptions was not carried out.

Somewhat different results were obtained by Kim *et al.* [76], who rinsed as-received Ge(001) wafers in ozonated DI water (DI-O_3). The authors found that with rinsing times up to 300 s, the surface roughness continuously decreased down to 1.25 Å. *In situ* XPS measurements indicated a total removal of GeO_2, while a small amount of suboxides was still present on the surface. Two other studies by Amy *et al.* [71] and Onsia *et al.* [77] could confirm the non-removal of GeO_x ($x<2$) after a DI water rinse. XPS measurements indicated that a DI water rinse alone leaves about 10% of the initial oxygen and carbon contamination on the surface.

In conclusion, a DI-water rinse can effectively remove GeO_2 from the Ge surface and produce a smooth Ge surface with an rms of ~1.25 Å which is considered atomically smooth. However, it was shown that this cleaning method is ineffective in removing suboxides from the surface. Additionally, DI-water cannot remove organic contamination from the Ge surface, making a purely water rinsed Ge surface unsuitable for further device integration.

4.4.2 Hydrofluoric acid (HF)

HF is a weak acid (pK_a = 3.15 [78]) and is industrially used to clean Si due to its superior properties in etching the native oxide SiO_2. Because of the wide use of HF in the semiconductor industry, investigating its effects on the Ge surface seems natural [1, 2, 22, 63, 65, 66, 71, 72, 74, 76, 77, 79-83].

One of the first groups to etch Ge surfaces with HF was Prabhakaran *et al.* [2]. In their study, Ge wafers were etched with several cycles of HF:H_2O (9:1) and H_2O_2/H_2O (9:1). A DI water rinse was performed in between each etching step. As the final cleaning step, a thin passivation layer of germanium oxide was formed by dipping the etched Ge wafers into an H_2O_2 bath. The sample was immediately loaded into the UHV system and thermally annealed for 15 min at 500°C to remove the germanium oxide passivation layer. UPS measurements were carried out before and after the thermal anneal, which reveal the presence of surface states of the oxide-free layer, indicative of an extremely clean sample. Using LEED, the authors report a 2 × 1 reconstructed surface which could be confirmed by STM scans that also revealed clear dimer rows. However, there was no mention of a possible carbon contamination, which is often observed after an HF etch by other groups.

In the study of Sun *et al.* [1], the influence of the HF concentration on the etching behavior of the Ge surface was investigated. First, DI water was used to remove the oxide of the as-received Ge wafers, before they were exposed to H_2O_2 for 30 s to grow a clean chemical oxide. Finally, three different HF:H_2O (1:3, 1:5, 1:25) concentrations were used to etch the wafers. XPS measurements of the O 1*s* peak revealed that oxygen residues can be found for all three HF concentrations. A scan of the Ge 3*d* peak revealed a small peak chemically shifted by 1.1 eV to higher binding energies relative to the Ge $3d_{5/2}$ peak. The authors presume the formation of OH^- groups on the wafer surface, since an oxide involving Ge^{+1} would be expected to have a smaller chemical shift of only ~0.85 eV

instead [84]. HF was also found to be ineffective in removing C completely from the etched surface. A thermal anneal for 30 min at 400°C in ultrahigh vacuum could remove the hydroxide groups, but traces of oxygen and carbon were still present on the surface after the anneal. All HF treated surfaces showed a relatively rough surface of ~6 Å.

Many other groups have investigated the performance of HF on the Ge(001) surface [22, 63, 65, 66, 67, 71- 73, 76, 77, 79, 80, 84], often in combination with other etchants or cleaning methods, and come to results that contradict those by Prabhakaran *et al.* [2]. While some groups report a complete oxygen removal from the Ge surface [71, 72, 79], others report the existence of Ge suboxides, especially if low HF concentrations are used [22, 76, 77, 80, 83]. Seo *et al.* [22] observed that a final HF etch can even trigger a quicker oxidation of the Ge surface, which can lead to a thicker oxide layer than was found initially on the as-received wafers. All groups investigating the C removal efficiency of HF found that HF can reduce the C concentration in comparison to as-received wafers, but at least small traces of C would always remain on the Ge surface after etching [22, 71, 82]. Furthermore, it was shown that an HF etch creates rather rough surfaces, with rms values ranging between 6 Å and 100 Å [22, 33, 65, 67, 71].

A possible explanation for the different HF etching results was given by Seo *et al.* [22]. They argue that H_2O, which is used to dilute HF solutions, could significantly enhance the removal of GeO_2 from the Ge surface, which makes the determination of the actual etching rate of HF solutions difficult.

A study of the metal recovery rate, which is defined as the percentage of metal contaminants recovered from an intentionally contaminated Ge surface, after HF etching was performed by Kim *et al.* [80] by intentionally contaminating two Ge wafers with Ca, Cr, Co, Cu, Fe, Mn, Ni, K, Na and Ti. The contaminated surfaces were then etched by little droplets of HF, which were scanned by inductively coupled plasma mass spectrometry (ICP-MS) for their metal concentrations. All metals showed a recovery rate of more than 80% except for Cu whose rate was at about 35% for both wafers, meaning that at least several cycles of HF etching are needed to remove Cu from the Ge surface.

It is well-known that an HF etch of a Si wafer not only removes SiO_2, but has the additional effect of forming an air stable hydrogen terminated Si surface which was crucial for the advances of Si device manufacturing. Inspired by the ability of creating a stable H-passivation layer on Si, the air stability of hydrogen terminated Ge surfaces was also investigated [22, 65, 71, 72]. From a thermodynamical point of view, one would assume that the Ge surface atoms favor the bond with F rather than with H, due to the higher bond energy of Ge-F (485 kJ/mol) [65] than Ge-H (322 kJ/mol) [65, 85]. However, identical to the Si surface, H-termination of Ge can be observed after an HF etch. Due to the lack of published work studying the mechanism of this phenomenon on Ge, the H-termination of Si is considered since the Si surface chemistry is much better understood and the mechanism is believed to be very similar for Ge. Analogue to Ge, the Si-F bond energy is much higher (553 KJ/mol) [1] than for Si-H (272 kJ/mol) [86], and yet, H-termination of Si is observed. In 1984, Ubara *et al.* [87] correctly proposed the

mechanism which leads to the H-termination of Si. In 1990, Trucks *et al.* performed *ab initio* quantum-chemical calculations of Ubara's results and showed that the H-termination is a consequence of kinetics rather than thermodynamics [88]. In Figure 4.8, the initial Si surface with F-termination is shown. Due to the high electronegativity of F (4.0) [1] and the strongly ionic nature of the Si-F bond, the Si back bond (second-layer Si) is negatively polarized and is prone to further H attack. The much smaller difference in electronegativity between Si and H (Si-H: 0.2) leads to a stable H-terminated surface, due to the lack of polarizing adjacent Si-Si bonds, which makes a continuous etching of this surface energetically unfavorable. Ultimately, this leads to the removal of the surface Si atoms, which form SiF_4 and is found in HF solutions after etching [87], while the second-layer Si is fully H-terminated. For the mechanism leading to a H-terminated surface, the authors calculated an activation barrier of 1.0 eV while an energy barrier of 1.4 eV is found for forming a F-terminated surface. This difference in activation energy ensures that F-termination is much less likely to form than a H-terminated surface. Since the electronegativity for both, Si (1.90) and Ge (2.01), only differ by 0.11 [1], a similar hydrophobic H-termination mechanism is presumed for Ge.

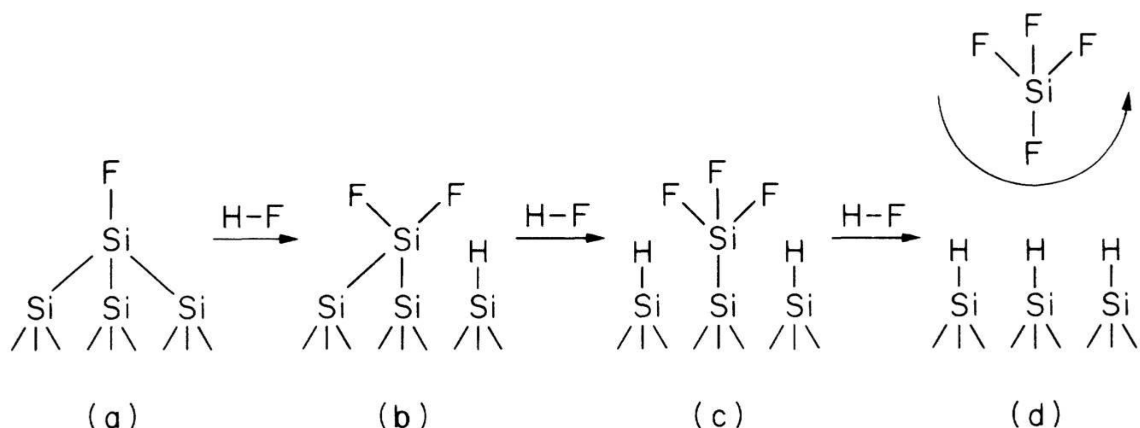

Figure 4.8: Schematics of the H-passivation of Si. Reproduced with permission from Phys. Rev. Lett. **65**, 504-507 (1990). Copyright 1990 American Physical Society.

Pioneering work on studying the stability of H-terminated Ge surfaces was done by Choi *et al.* [65], who carried out infrared spectroscopy of HF-etched Ge wafers. They found that the H-termination highly depends on the etching time and HF concentration [1, 65], with GeH_x not being kinetically stable since a decrease of the H-coverage with etching times longer than 10 min was observed. They further report that the Ge hydride termination was found to be stable up to 1 h in air.

A more thorough study of the hydrogen termination and stability of HF-etched Ge wafers was carried out by Rivillon *et al.* [72]. In their study, the Ge wafers were sequentially dipped into DI water, H_2O_2 (30%) and HF (10%) to obtain full H-termination of the Ge surface. Infrared absorption spectroscopy (IRAS) measurements indicated the formation of germanium mono- and dihydride species on the surface with a weak signal of 10% trihydride. Such a non-uniform H-termination is also reported by other groups and is typical for an atomically rough Ge-H surface [65, 89]. However, the total H-coverage

was found to be only 80% of a monolayer, indicative of the lower stability of the Ge-H bond than Si-H. The incomplete surface hydrogenation has also been attributed to carbon, which is insoluble in Ge and hence forms clusters, or germanium suboxides on the surface that could not be completely removed by the HF etch. As a matter of fact, the carbon level of the HF-etched surface was found to be even higher than on as-received wafers, which is in accordance with results from other groups [71] who reported a rapid growth of CH_x after etching the Ge surface with HF, indicating that hydrocarbons are prone to react with H on the Ge surface. Both groups report a higher amount of carbon on their HF-treated surface in comparison to as-received wafers. An XPS analysis of the Ge 3*d* core level revealed a small peak shifted by +1.6 eV from the Ge 3*d* core level which was associated to germanium carbide by Maruyama *et al.* [90]. The authors attribute the higher carbon concentration to a tendency of hydrophobic H-terminated surfaces to attract more hydrocarbons than hydrophilic oxides that are found on the Si surface [3]. While the H-termination was found to be stable over a few hours in an N_2 environment [71] with no detectable loss of H, the H-coverage decreased quickly upon air exposure [71, 72, 83] or under ultrahigh vacuum conditions [91]. A 20% loss of hydrogen from the Ge surface was reported by Amy *et al.* [71] after an air exposure of only 1 min, with a linear decrease of H for the first 5 min of air exposure. This shows that the H-terminated Ge surface is not stable in air since the majority of H is removed within a few minutes. However, even after exposing a H-terminated surface to air for 1 h, no sign of additional oxide growth could be detected, indicative of carbon efficiently passivating the surface.

An important value characterizing the electronic properties and performance of a MOS device is the interface trap density (D_{it}), which is highly dependent on the interface quality between the dielectric and channel material and therefore on the initial semiconductor surface cleanliness. Due to the long tradition with HF etching of the Si surface for transistor devices, most reported D_{it} values for Ge MOS devices were obtained using an HF pre-cleaning step. To our knowledge, no D_{it} values are reported for Ge transistor devices with a UV/O_2 plasma-exposed or ion sputtered Ge surface prior to further device processing, which is why a comparison of the D_{it} values between the different cleaning methods isn't possible. However, a wide range of D_{it} values between 8×10^{10} cm^{-2} eV^{-1} and $\sim 10^{12}$ cm^{-2} eV^{-1} for HF and diluted HF-treated Ge surfaces are reported [39, 92-95], demonstrating that D_{it} is not only a function of the surface preparation but is also heavily influenced by the interface quality between the high-κ material and Ge surface.

To summarize the effect of HF etching, most groups report that etching the Ge surface with HF leaves residual germanium oxides or suboxides on the surface. All groups that investigated the C-removal efficiency find that small amounts of C are always found on the surface after etching. Furthermore, HF produces very rough surfaces of up to 10 nm roughness and is not very effective in removing Cu from the Ge surface. Studies investigating the H-passivation of Ge come to the conclusion that the H-terminated surface is not stable in air, making HF etched and passivated Ge surface not suitable for

device integration. It will be shown that NH_4OH and HCl produce much cleaner and smoother surfaces than HF.

4.4.3 Ammonium hydroxide (NH_4OH)

The second chemical to be discussed is NH_4OH. In comparison to HF, which is a weak acid, NH_4OH is a very strong base (pH: 11.63) [22] (pk_B: 4.75 [96]) that can effectively etch germanium oxides from the Ge surface. Unlike HF and HCl that form H- and Cl-terminated Ge surfaces, NH_4OH does not naturally form a passivation layer. For that reason, a different chemical must be used in the last etching step to form a passivation layer.

One of the first groups to investigate NH_4OH as an etchant for the Ge surface was Anderson *et al.* [70], who carried out wet-etching experiments using aqueous ammonium sulfide ($(NH_4)_2S$). Previous experiments had shown that other semiconductors i.e. GaAs and InP could be successfully etched and passivated with $(NH_4)_2S$ [97-100]. In Anderson's study, the Ge wafers were first dipped into HF (1%) for 1 min and then etched in $(NH_4)_2S$ for 20 min at 340 K and either water or methanol rinsed prior to loading into a vacuum system. XPS and AES measurements performed directly after loading confirmed that only a small amount of oxygen and carbon were left on the surface. A higher resolution scan around the Ge 3*d* peak revealed a small peak at higher binding energies (+0.67 eV) that was attributed to the formation of surface Ge-S bridge bonds, since the scan of the S 2*p* peak could be fit as a single doublet, indicative of only one S species present on the surface. LEED was then used to monitor the crystal quality

upon annealing. S begins to break its bond with Ge between 460 - 515 K, leading to a S-free Ge surface at 775 K. However, instead of the expected 2×1 reconstructed surface, a 1×1 reconstruction was observed. This could be caused by the presence of a small amount of carbon, which the authors report on the Ge surface after wet-etching. AFM scans which were taken of annealed and non-annealed surfaces showed that the surface roughness for both cases was between 3 - 12 Å.

Two other groups, Akane *et al.* [101] and Okumura *et al.* [67], have carried out wet-etching experiments using a solution of NH_4OH/H_2O (1:4). Akane *et al.* rinsed the wafers in DI water after etching the surface for 30 - 300 s and found that a 30 s etch only leads to the removal of GeO_2 while an etching time of 120 s was needed to completely remove the Ge suboxides from the surface. In their study, nothing was stated about the carbon removal efficiency of their etching method. Slightly different results were found by Okumura *et al.* who showed that GeO_2 was still present after etching the surface for 120 s and that an etching time of 300 s is needed for full oxide removal. AES measurements confirmed the complete removal of all organic contamination from the surface. Both groups confirmed a low surface roughness after etching the Ge surface for 300 s, with values of 3.3 Å and 7 Å, respectively. While Akane *et al.* formed a chemical oxide passivation layer by dipping Ge into H_2O_2 (35%), Okumura *et al.* found that a chemical Ge oxide could only be formed when a $NH_4OH/H_2O_2/H_2O$ (0.5/1/10) solution was used right after etching. With a solution of H_2O_2/H_2O (1:10), the authors found that the water oxide removal rate is higher than the oxide formation rate of H_2O_2, resulting in an

unprotected surface. When adding NH_4OH to the H_2O_2/H_2O solution, this effect was not observed and a protective Ge oxide could be formed. A final thermal anneal *in situ* at 400°C for 30 min of the passivated surfaces then led to a 2 × 1 reconstructed surface for both groups.

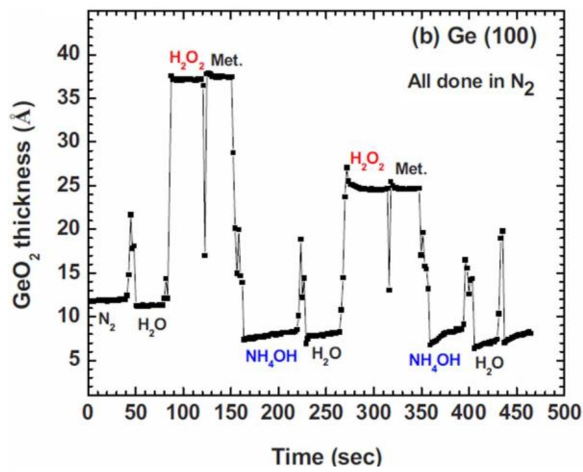

Figure 4.9: GeO_2 thickness evolution during NH_4OH-based cleaning of the Ge surface. Reproduced with permission from J. Electrochem. Soc. **156** (11), 813-817 (2009). Copyright 2009 Electrochemical Society.

Seo *et al.* investigated the Ge oxide removal efficiency and growth rate of NH_4OH-treated Ge wafers with real-time visible-UV spectroscopic ellipsometry (SE) measurements [22]. The Ge surfaces were cleaned by cycles of sequential etching in DI water, H_2O_2 (6%), and methanol (for carbon removal), followed by an NH_4OH (10%) and DI water rinse. In between each chemical etching step, the surface was N_2 purged to remove all chemicals from the Ge surface and to prevent further oxide formation. As can be seen in Figure 4.9, the initial GeO_2 thickness was 1.2 nm after the DI water rinse, due to the water solubility of GeO_2.

As expected, 5 s after rinsing the sample with H_2O_2, the Ge surface formed a thick oxide layer of 3.8 nm. A subsequent dip into NH_4OH etches most of the formed Ge oxide to a

thickness of only 0.7 nm. Due to the lack of NH_4OH to form a passivation layer, the Ge surface can quickly re-oxidize when exposed to H_2O_2.

After etching, the Ge oxide regrowth rate was examined by performing real-time visible-UV SE. The initial GeO_2 thickness was 0.8 nm right after the last NH_4OH etch and after 1 min, a thickness of 1.4 nm was reached. After an air exposure time of almost 7 min, the thickness saturated at 1.7 nm. However, the authors point out that if the water vapor on the surface is incorporated, the real GeO_2 thickness after 1 min might be slightly less than 1.4 nm. *In situ* AES measurements which were performed after etching indicated that C was not completely removed from the Ge surface but significantly reduced by the NH_4OH cleaning. A final exposure to O_2 plasma for 15 s then led to a C-free surface.

In conclusion, NH_4OH can completely remove GeO_2 and germanium suboxides, when etching times are increased up to 5 min. NH_4OH is also effective in reducing organic contamination significantly, but an additional cleaning step, e.g. O_2 plasma, might be needed for complete carbon removal from the Ge surface. Since NH_4OH does not naturally form a passivation layer, a chemical oxide can be formed by dipping the wafer into a $NH_4OH/H_2O_2/H_2O$ (0.5/1/10) or a pure H_2O_2 solution. A thermal anneal *in situ* can remove the oxide passivation layer, revealing a 2×1 reconstructed surface. The lowest reported surface roughness for NH_4OH treated surface was 3.3 Å, being slightly rougher than our definition for atomically smooth. Experiments with sulfur passivating the Ge surface on the other hand resulted in a 1×1 surface reconstruction with small traces of carbon left on the surface.

4.4.4 Hydrochloric acid (HCl)

The group of Okumura *et al.* [67] etched Ge wafers with HCl as part of a study comparing the effects of HF, HCl and NH_4OH. HCl is a highly corrosive and strong acid (pK_a = -6.3 [78]) and is commonly used for industrial purposes. In their study, the wafers were first etched in HF (2.5%) for several minutes, followed by an H_2O_2 dip for 30 s to form an oxide layer of 19 Å thickness. Next, they exposed their sample to HCl (36%)/H_2O (1/4) and found that an etching time of 30 s in conjunction with an *in situ* anneal at 400°C for 30 min is sufficient to completely remove C and germanium oxides from the surface, which is a much faster etching rate than was found for NH_4OH (up to 300 s for the same result). Furthermore, a comparison between HF (47%), HF (2.5%), NH_4OH (27%)/H_2O (1/4) and HCl (36%)/H_2O (1/4) reveals that HCl-etched Ge surfaces show the lowest surface roughness of only ~7 Å after 1 cleaning cycle. After 3 cycles of etching in HCl (36%)/H_2O (1/4), the surface roughness could be even lowered to ~1.3 Å.

Chen *et al.* [102] followed the cleaning procedure presented by Okumura *et al.*, but added a thermal anneal for 30 min at 650°C in UHV at the end of the *ex situ* wet-etching process. The authors then used XPS to confirm that all oxides and C could be successfully removed from the Ge surface.

More recent studies, investigating the differences between HF and HCl, were carried out by Kim *et al.* [83] and Sun *et al.* [1]. Kim *et al.* dipped Ge(001) wafers for 2 min into 2%, 10% and 20% concentrated HF and HCl. In accordance with the results of other groups, the authors confirmed that all HF solutions, independent of their concentration, leave

oxygen on the surface. Wafers that were etched in a solution of HCl with concentrations of 2% and 10% showed small amounts of oxygen on the surface, while etching with HCl (20%) resulted in the total removal of all oxides on the surface.

They also investigated the metal recovery rate for HCl droplets using ICP-MS, similar to the study described for HF [80]. In the case of HCl, the recovery rates for all metals, including Cu, were above 80%, showing that HCl is more effective in removing metals than HF. Nevertheless, the authors point out that several cycles of etching with HCl are needed to obtain a metal-free surface.

In addition to studying the effect of different HF concentrations on the Ge surface, Sun *et al.* [1] also studied the etching behavior of a HCl (10%) solution on Ge. The surfaces were prepared by a DI water rinse, H_2O_2 dip and an etch in HCl, which resulted in a detectable amount of oxygen and carbon on the surface. However, a thermal anneal for 30 min at 480°C *in situ* resulted in the complete removal of oxygen but a trace amount of C was still present on the surface. AFM scans of the etched surfaces revealed that the HCl-treated wafers exhibit a surface roughness of ~2.9 Å which is close to the 2.3 Å value for the as-received wafers, implying that the original morphology is preserved.

In the study of Klesse *et al.* [33], the ideal H_2O_2 concentration for forming an oxide layer after an HCl etch was investigated (see Figure 4.10). The wafers were first degreased and then dipped into either an HF (10%) or HCl (36%) solution for 60 s. A chemical oxide was then grown by dipping the etched wafers for 30 s into an H_2O_2/H_2O bath of 30%,

10% and 7% concentration. A total of 4 etching cycles were performed to clean the wafer surface. A thermal anneal for 1 h at 250°C followed by a flash anneal at 760°C for 60 s removed the GeO_x passivation layer. While the surface roughness for HF-etched wafers was determined to be ~10 Å, the roughness could be reduced by a factor of 5 using HCl. With a decrease in the H_2O_2 concentration to 7%, the surface roughness could even be lowered to 1.1 Å. For wafers that were wet-etched with HCl (36%) and H_2O_2/H_2O (7%), a 2 × 1 surface reconstruction as well as domains of c(4 × 2) and p(2 × 2) could be observed. Using STM, the defect density of this sample was found to be 2%.

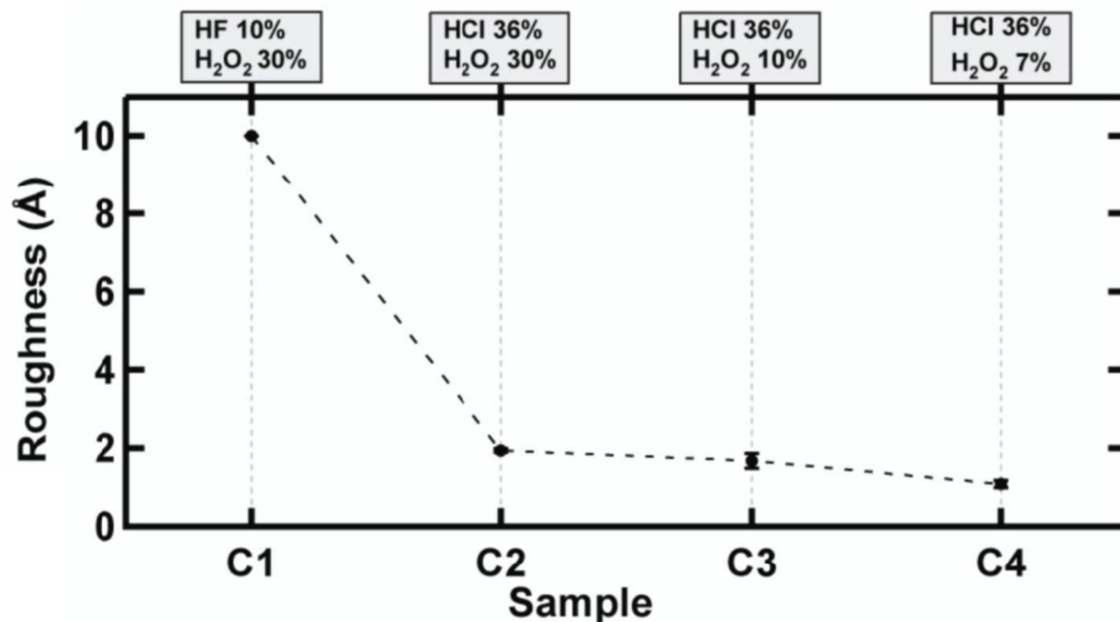

Figure 4.10: Plot of the surface roughness dependency from the different wet-etching conditions using HF, HCl and H_2O_2. Reproduced with permission from Nanotechnology **22**, 145604 (2011). Copyright 2011 Institute of Physics.

The dependence of the Ge surface roughness on a thermal anneal and HCl concentration and etching time was carried out by Ponath *et al.* [18]. In their study, Ge wafers were cleaned by sequential etching in HCl and H_2O_2/H_2O (7%). Following the result of Klesse *et al.* [33] for obtaining a minimum surface roughness, the H_2O_2 concentration was kept at 7% throughout their study. The etched samples were then loaded into a UHV system for a final thermal anneal at temperature between 650 - 750°C. It was found that a thermal anneal *in situ* of a Ge wafer that was etched in a HCl (36%) solution could reduce the surface roughness by more than 50% from 113 Å to 50 Å. A reduction of the etching time from 60 s to 20 s per etching cycle led to a further reduction of the surface roughness to 26 Å. As a final step, the HCl concentration was lowered to 15% which was found to give the best results in combination with an *in situ* thermal anneal and oxygen plasma exposure, leading to a very low surface roughness of only 3 Å.

Interestingly, etching Ge in a HCl solution results in a Cl-terminated surface. Sun *et al.* [1] explained this behavior through the smaller electronegativity of Cl (3.16) compared to F (3.98) [103]. For both acids, HCl and HF, the top surface atoms either bond to F or Cl. While F strongly polarizes the Ge back bonds, making it prone to further attack by HF, the polarization effects from Cl are weaker due to the smaller electronegativity of Cl vs. F. Furthermore, Ge-Cl has a weaker binding energy (349 kJ/mol) [104] and longer bond length (2.16 Å) [105] than Ge-F (485 kJ/mol) [65] (bond length: 1.75 Å [105]). Taking all these factors into account, the Ge back bonds are less susceptible for further HCl attack, leading to a stable hydrophilic Cl-termination.

Sun *et al.* [1] also studied the Cl-termination of Ge. The Cl-terminated surfaces were prepared by sequentially dipping the Ge wafers into DI water and H_2O_2 for 30 s each, followed by an HCl (10%) etch for 10 min. XPS scans of the Ge 3*d* core level show two peaks with a chemical shift of 0.6 eV and 1.15 eV towards higher binding energies, which were attributed to Ge mono- and dichlorides, respectively [73]. The authors determined the monochloride coverage to be 0.29 ± 0.06 ML and the dichloride coverage to be 0.5 ± 0.1 ML. However, a thermal anneal in vacuum at 400°C for 30 min was sufficient to completely remove Cl from the Ge surface.

In 1985, Schnell *et al.* [73] performed a study of the surface core level shifts for Cl-covered Ge. The Ge surface was prepared by repeated cycles of mild Ar^+ sputtering (600 - 800 eV) with a subsequent thermal anneal at 600°C, resulting in a c(4 × 2) reconstructed surface. Cl-termination was achieved by dissociation of AgCl in a solid-state electrochemical cell. For a fully chlorinated surface, they

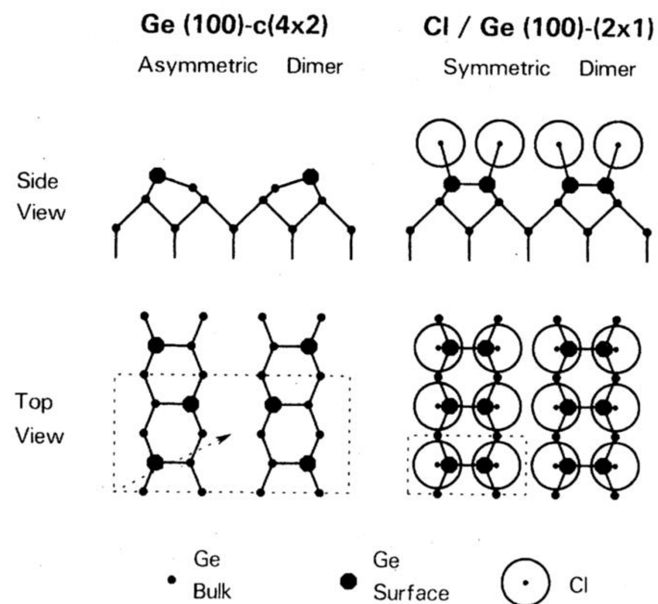

Figure 4.11: Structural models for the Ge(001)-c(4 × 2) and Cl/Ge(001)-(2 × 1). Upon Cl chemisorptions, the asymmetric dimers become symmetric. Reproduced with permission from Phys. Rev. B. **32**, 8052-8056 (1985). Copyright 1985 American Physical Society.

observe a 2×1 reconstructed surface, with monochloride as the only species present on the Ge surface. The transition from a $c(4 \times 2) \Rightarrow 2 \times 1$ reconstruction is explained by the adhesion of Cl to the remaining dangling bonds of the surface dimers, leading to a symmetric dimer model as can be seen in Figure 4.11. With Cl saturating the dangling bonds, the response of dimers on a cleaned Ge surface to buckle asymmetrically is hindered. A similar effect is seen on Si(001), where Sr deposition leads to a charge transfer from the metal to the Si substrate resulting in the disappearance of the asymmetry of Si dimers [106].

In summary, it was shown that HCl as the main etchant can lead to a completely oxide and carbon-free Ge surface. The metal recovery rate of HCl for many metals is greater than 80%, with several cycles necessary for total metal removal. Using HCl in combination with H_2O_2 (7%) was shown to result in higher order surface reconstructions with a surface roughness as low as 1.1 Å. HCl prepared Ge surface can therefore be considered atomically smooth and contamination-free, being suitable for high-κ device integration. Cl-termination of the Ge surface was shown to be possible but the air stability of such a surface still remains to be investigated.

4.4.5 Other etchants

Onsia *et al.* [77] did a comparison study between several etchants (H_2O_2, HF, HCl, HBr, HI) and found that a 5 min etch in HBr (pK_a = -8.7 [78]) removes all oxides from the Ge surface, including the suboxides. The authors suspect that the soft base character of Br^- and the soft acid character of Ge favors the reaction. Interestingly, an oxide regrowth was

discovered when the sample was rinsed in water prior to loading. Similar results were obtained for an HI etch (pK_a = -9.3 [78]), which could remove GeO_2 and suboxides from the wafer surface. However, no oxide formation was detected after a water rinse and the surface roughness was not reported.

Slightly deviating results were reported by Kim *et al.* [83]. They studied the native oxide removal efficiency for the Ge surface using 2%, 10% and 20% concentrated HBr. They find that even for a 20% HBr concentration, small amounts of suboxides are still present on the Ge surface. Additionally, they tested the stability of Br- and I-passivated Ge surface after etching wafers in 20% HBr and HI for 2 min each. The Br-passivated Ge surface was stable for up to 12 h in air without re-oxidizing. HI etched surfaces showed an even better passivation behavior – no re-oxidation of the Ge surface was observed for more than 12 h. The Br-passivation layer could then be completely removed by rinsing the Br-passivated surface in de-ionized water for 120 s or by annealing the surface at 300°C for 3.5 h *in situ*.

A variant of the Piranha etch (H_2SO_4, H_2O_2, H_2O) was used to etch the Ge surface by Blumenstein *et al.*, followed by a rapid dry oxidation *ex situ* [30]. The Ge wafers were then annealed for 250°C for several hours, followed by a quick anneal at 600°C to remove all oxides from the Ge surface, resulting in a mixed 2 × 1 and 4 × 2 reconstructed surface. However, a drawback of this etchant is the non-removal of all carbon contamination on the Ge surface.

In conclusion, the reports whether HBr can remove germanium oxides aren't conclusive, while an excellent oxide removal behavior was found for HI etched surfaces. For both acids the carbon removal efficiency hasn't been studied yet and further studies need to be carried out also to investigate the resulting surface reconstruction and roughness. Additionally, HI etched Ge surfaces show excellent passivation behavior, making HI a promising candidate for further wet-etching experiments.

4.4.6 Summary of wet-etching

Studies have clearly shown that the use of HF is rather disadvantageous in comparison to other chemicals. Not only is HF mostly ineffective in removing O, C and Cu, it also produces a rough Ge surface, making it unsuitable as an etchant. A simple DI water rinse was also shown to be ineffective in removing anything other than GeO_2. HBr and HI are promising etchants due to their excellent passivation behavior of the Ge surface. Additionally, HI effectively removes germanium oxides. However, it isn't clear whether both acids can remove organic contamination or produce an atomically smooth and 2×1 reconstructed Ge surface.

By far the most promising candidates for a chemical cleaning of the Ge surface are NH_4OH and HCl. While NH_4OH-etched surfaces lead to a slightly rougher surface than HCl, both chemicals are able to remove germanium oxides and C from the surface completely. Furthermore, the etch rate of HCl was found to be higher than that of NH_4OH. Unlike NH_4OH, which does not form a passivation layer naturally, HCl can form a Cl-terminated Ge surface. However, the stability of such a passivation layer still

needs to be studied. HCl also effectively removes selected metals from the Ge surface, making HCl, in combination with the formation of a germanium oxide passivation layer using H_2O_2, the preferred chemical to obtain an atomically flat, contamination- and oxide-free Ge surface (see Table 4.2).

	Organic residues	Native oxide	Surface roughness	Advantages	Disadvantages
UV/Ozone	30 min (++) (complete removal) [14]	X	X	• Environmental friendly • No Ge regrowth needed	• X
O_2 plasma	30 min (++) (complete removal) [18]	X	3 Å (+) [18]	• Environmental friendly • No Ge regrowth needed	• X
Ion sputtering	10 min (-) (traces of C left) [47]	X	X	• Well established	• Possible Ar residues • Traces of C can be left
Ion Sputtering and Ge regrowth	0.1 ML - 30 nm (++) [21, 31, 55]	X	0.6 Å (++) (Ge regrowth at 500°C => flash anneal to 760°C for 10s) [33]	• Extremely clean and smooth surfaces	• Long processing time
H_2O	30 s (--) (High C amount left) [71]	GeO_2: 300 s (++) (complete removal) GeO_x ($x<2$): 300 s (--) (non-removal) [71, 77]	1.25 Å (++) (60 s water rinse) [28]	• Very quick	• Doesn't remove organic contamination or suboxides • No passivation layer
HF	10 min (-) (traces can be left) [1]	10 min (-) (suboxides can be left) [1]	6 Å (-) (10 min; HF(49%)/H2O (1/3)) [1]	• Well established/infrastructure from wet-etching Si	• Traces of C and suboxides possible
NH_4OH	5 min (++) (complete removal) [67]	120 - 300 s (++) (complete removal) [67, 101]	3.3 Å (+) (300 s; NH4OH(28%)/H2O (1/4)) [101]	• X	• Longer etching times necessary for carbon and oxide removal
HCl	30 s (++) (complete removal) [67, 102]	(++) (complete removal) c(HCl) > 20% (-) (traces of suboxides left) c(HCl) < 20% [1, 83]	1.3 Å (++) (30 s; HCl(36%)/H2O (1/4)) [67]	• Fastest wet-etching cleaning method	• High HCl concentrations are needed to remove C and oxides completely

Table 4.2: Summary, results and recipes for each discussed cleaning method. Legend: ++: Excellent, +: Sufficient; -: Poorly; --: Insufficient; X: Not examined/does not apply.

4.5 CONCLUSION

We reviewed three broad categories of *in situ* and *ex situ* cleaning methods for the Ge(001) surface. All of them lead to an atomically smooth and contamination-free Ge(001) surface, but only a few are practical for device processing. In Table 4.2 we give a summary of all the reviewed cleaning methods, their effectiveness and suggested cleaning recipes.

UV light and/or O_2 plasma exposure are very promising cleaning methods for device processing. Both show excellent carbon removal efficiency. In the case of an *ex situ* UV light prepared surface, a thin GeO_x layer naturally forms which acts as a passivation layer. A thermal *in situ* anneal is then required to remove the oxidized Ge surfaces, revealing extremely smooth (~3 Å), 2 × 1 reconstructed, carbon- and oxygen-free Ge surfaces.

On the other hand, ion sputtering generally produces rough and amorphized Ge surfaces. To obtain a clean and 2 × 1 reconstructed surface, several time-consuming sputtering and annealing cycles are needed to heal the damaged surface. However, even after several cleaning cycles, carbon and ion (Ar^+, Ne^+) residues can still remain on the surface. Ion sputtering in combination with a Ge regrowth results in extremely clean and highly ordered surfaces. Surfaces prepared this way fulfill every requirement for an atomically smooth and contamination-free surface and could in principle be used for device processing. However, the biggest drawback of this cleaning method is its extremely long

processing time, which makes this surface cleaning method more useful for scientific studies of the Ge surface rather than for device processing.

Most of the published reports to date on Ge surface cleaning are studies of the effect of wet-etching the Ge surface. While HF is commonly used for preparing Si surfaces, it turns out that it is rather disadvantageous for cleaning the Ge(001) surface, since HF-treated surfaces are rather rough (>6 Å) and in most cases, germanium suboxides and carbon remain on the surface. Additionally, the Ge-H bond is unstable in air and does not provide an effective passivation layer as it does for the Si surface, making HF-etched surfaces not ideal for further device processing. On the other hand, NH_4OH can completely remove oxygen and organic contamination from the Ge surface leading to a 2×1 reconstructed surface. However, NH_4OH does not form a natural passivation layer with Ge, requiring additional etching steps with other chemicals. Additionally, NH_4OH-prepared surfaces typically result in a higher surface roughness than HCl-treated surfaces with etching times almost six times longer than for HCl, making NH_4OH also not ideal for etching the Ge surface.

HCl in relatively high concentrations (>15%) turns out to be the most effective acid to clean the Ge(001) surface. It removes germanium oxides and organic contamination completely in a few seconds and produces atomically smooth surfaces (~1.3 Å). Furthermore, HCl-treated surfaces show higher order surface reconstructions after an *in situ* anneal, making this acid the ideal wet-etching cleaning method for Ge surface.

It turns out that especially HCl etching and UV/O_2 cleaning provide the quickest and most reliable way to obtain atomically smooth and completely carbon- and oxygen-free Ge surfaces making these cleaning methods preferred for device processing. They also circumvent the need to perform a time-consuming Ge regrowth which is often performed after ion sputtering. While wet-etching generally produces large amounts of toxic waste, excess oxygen, CO_2 and H_2O can be released directly into the atmosphere when using UV light or O_2 plasma. Additionally, UV light and O_2 plasma are easier and safer to use, while caution has to be taken when etching Ge surfaces with concentrated HCl. On the other hand, due to the extensive use of HF for etching Si, the infrastructure for wet-etching on a larger scale is already established, possibly making the integration of HCl etching into the cleaning process easier.

ACKNOWLEDGMENTS

We thank Andrew Kummel for stimulating and insightful discussions. The work is supported by the Air Force Office of Scientific Research under grants FA9550-12-10494 and FA9550-14-0090.

4.6 References

[1] S. Sun, Y. Sun, Z. Liu, D.-I. Lee, S. Peterson, P. Pianetta, Appl. Phys. Lett. **88**, 021903 (2006).

[2] K. Prabhakarana, T. Ogino, R. Hull, J. C. Bean, L. J. Peticolas, Surf. Sci. **316**, 1031-1033 (1994).

[3] K. A. Reinhardt, W. Kern, *Handbook of Silicon Wafer Cleaning Technology* (William Andrew, Norwich, 1993) Chapter 9.

[4] M. Liehr, J. E. Lewis, G. W. Rubloff, J. Vac. Sci. Technol. A **5**, 1559 (1987).

[5] P. A. Stolk, D. J. Eaglesham, H.-J. Gossmann, J. M. Poate, Appl. Phys. Lett. **66**, 1370 (1994).

[6] R. I. Scace, G. A. Slack, J. Chem. Phys. **30**, 1551 (1959).

[7] A. Taylor, N. J. Doyle, Scr. Metal. **1**, 161-162 (1967).

[8] R. W. Olesinski, G. J. Abbaschian, J. Phase Equilib. **5**, 484-486 (1984).

[9] E. E. Haller, W. L. Hansen, P. Luke, R. McMurray, B. Jarrett, IEEE T. Nucl. Sci. **29**, 745-750 (1982).

[10] S. Verhaverbeke, M. Meuris, P. W. Mertens, M. M. Heyns, A. Philipossian, D. Graf, A. Schnegg, 1991 Int. El. Devices. Meet. 71-74 (1991).

[11] T. Hattori, *Ultraclean Surface Processing of Silicon Wafers* (Springer, Berlin, 1998).

[12] A. L. P. Rotondaro, T. Q. Hurd, A. Kaniava, J. Vanhellemont, E. Simoen, M. M. Heyns, C. Claeys, G. Brown, J. Electrochem. Soc. **143**, 3014-3019 (1996).

[13] H. Dallaporta, M. Liehr, J. E. Lewis, Phys. Rev. B. **41**, 5075 (1990).

[14] X. J. Zhang, G. Xue, A. Agarwal, R. Tsu, M. A. Hasan, J. E. Greene, A. Rockett, J. Vac. Sci. Technol. A **11**, 2553 (1993).

[15] A. G. Shard, Surf. Interface Anal. **46**, 175-185 (2014).

[16] J. C. Riviere, Contemp. Phys. **14**, 513-539 (1973).

[17] Y. Coffinier, G. Piret, M. R. Das, R. Boukherroub, C. R. Chim. **16**, 65–72 (2013).

[18] P. Ponath, A. B. Posadas, R. C. Hatch, A. A. Demkov, J. Vac. Sci. Technol. B **31**, 031201 (2013).

[19] J. S. Hovis, R. J. Hamers, C. M. Greenlief, Surf. Sci. **440**, 815-819 (1999).

[20] S. Gan, L. Li, T. Nguyen, H. Qi, R. F. Hicks, M. Yang, Surf. Sci. **395**, 69-74 (1998).

[21] L. H. Chan, E. I. Altman, Y. Liang, J. Vac. Sci. Technol. A **19**, 976 (2001).

[22] H. Seo, K. B. Chung, J. P. Long, G. Lucovsky, J. Electrochem. Soc. **156** (11), 813-817 (2009).

[23] D. A. Bolon, C. O. Kunz, Polym. Eng. Sci. **12**, 109-111 (1972).

[24] A. Pizzi, K. L. Mittal, *Handbook of Adhesive Technology* (Marcel Dekker Inc., New York, 2003).

[25] J. R. Vig, J. Vac. Sci. Technol. A **3**, 1027 (1985).

[26] W. Kern, *Handbook of semiconductor wafer cleaning technology* (Noyes Publications, Park Ridge, 1993) Chapter 6.

[27] A. Belkind, S. Gershman, *Vacuum Coating and Technology November* 2008, 46-57.

[28] C. O. Chui, H. Kim, P. C. McIntyre, K. C. Saraswat, IEEE Electr. Device L. **25**, 5, (2004).

[29] K. Kiantaj, T. Kaufman-Osborn, A. C. Kummel, Silicon-Germanium Technology and Device Meeting (ISTDM), 2012 International, 1-2 (2012).

[30] C. Blumenstein, S. Meyer, A. Ruff, B. Schmid, J. Schäfer, R. Claessen, J. Chem. Phys. **135**, 064201 (2011).

[31] Z. Qin, D. Shi, W. Ji, S. Pan, H.-J. Gao, Nanotechnology **17**, 2396-2398 (2006)

[32] D. J. Bottomley, M. Iwami, Y. Uehara, S. Ushioda, J. Vac. Sci. Technol. A **17**, 698 (1999).

[33] W. M. Klesse, G. Scappucci, G. Capellini, M. Y. Simmons, Nanotechnology **22**, 145604 (2011).

[34] H. Seo, R. C. Hatch, P. Ponath, M. Choi, A. B. Posadas, A. A. Demkov, Phys. Rev. B **89**, 115318 (2014).

[35] M. Walker, M. S. Tedder, J. D. Palmer, J. J. Mudd, C. F. McConville, Appl. Surf. Sci. **379**, 1-7 (2016).

[36] J. Cho, R. J. Nemanich, Phys. Rev. B **46**, 12421-12426 (1992).

[37] T. Kaufman-Osborn, K. Kiantaj, C.-P. Chang, A. C. Kummel, Surf. Sci. **630**, 254-259 (2014).

[38] T. P. Schneider, D. A. Aldrich, J. Cho, R. J. Nemanich, Mat. Res. Soc. Symp. Proc. **220**, 21 (1991).

[39] C. O. Chui, H. Kim, D. Chi, P. C. McIntyre, K. C. Saraswat, IEEE T. Electron. Dev. **53**(7), 1509-1516 (2006).

[40] T. Nishimura, S. Kabuyanagi, W. Zhang, C. H. Lee, T. Yajima, K. Nagashio, A. Toriumi, Appl. Phys. Express **7**, 051301 (2014).

[41] Y. Moriyama, N. Hirashita, K. Usuda, S. Nakaharai, N. Sugiyama, E. Toyoda, S.-I. Takagi, Appl. Surf. Sci. **256**, 823–829 (2009).

[42] H.-Y. Yu, S.-l. Cheng, J.-H. Park, A. K. Okyay, M. C. Onba, B. Ercan, Y. Nishi, K. C. Saraswat, Appl. Phys. Lett. **97**, 063503 (2010).

[43] A. Nayfeh, C. O. Chui, K. C. Saraswat, T. Yonehara, Appl. Phys Lett. **85**, 2815 (2004).

[44] J. M. Hartmann, A. Abbadie, J. P. Barnes, J. M. Fédéli, T. Billon, L. Vivien, J. Cryst. Growth **312**, 532–541 (2010).

[45] W. R. Grove, Philos. Mag **5**, 203 (1853).

[46] R. Behrisch, K Wittmaack, *Sputtering by Particle Bombardment III* (Springer Verlag, Berlin 1991).

[47] S. D. Kevan, Phys. Rev. B **32**, 2344 (1985).

[48] J. A. Kubby, J. E. Griffith, R. S. Becker, J. S. Vickers, Phys. Rev. B **36**, 6079 (1987).

[49] H. E. Farnsworth, R. E. Schlier, T. H. George, R. M. Burger, J. Appl. Phys. **29**, 1150 (1958).

[50] G. Schulze, M. Henzler, Surf. Sci. **73**, 553-559 (1978).

[51] H. J. W. Zandvliet, A. van Silfhout, M. J. Sparnaay, Phys. Rev. B **39**, R5576 (1989).

[52] C. A. Lucas, C. S. Dower, D. F. McMorrow, G. C. L. Wong, F. J. Lamelas, P. H. Fuoss, Phys. Rev. B **47**, 10375 (1993).

[53] W. S. Yang, X. D. Wang, K. Cho, J. Kishimoto, S. Fukatsu, T. Hashizume, T. Sakurai, Phys. Rev. B **50**, 2406 (1994).

[54] J. E. Van Nostrand, S. J. Chey, M.-A. Hasan, D. G. Cahill, J. E. Greene, Phys. Rev. Lett. **74**, 1127 (1995).

[55] T. Fukuda, T. Ogino, Phys. Rev. B **56**, 13190 (1997).

[56] R. V. Stuart, *Vacuum technology, thin films, and sputtering: an introduction* (Academic Press, New York, 1983).

[57] K. M. Horn, E. Chason, J. Y. Tsao, J. A. Floro, S. T. Picraux, Surf. Sci. **320**, 174-184 (1994).

[58] H. T. Hall, J. Phys. Chem. **59**, 1144-1146 (1955).

[59] J. Wang, T. A. Arias, J. D. Joannopoulos, Phys. Rev. B **47**, 10497-10508 (1993).

[60] H. J. W. Zandvliet, W. Wulfhekel, B. L. M. Hendriksen, B. J. Hattink, B. Poelsema, Phys. Rev. B **57**, 1356 (1998).

[61] A. Ishizaka, Y. Shiraki, J. Electrochem. Soc.**133**, 666-671 (1986).

[62] W. Kern, D. A. Puotinen, RCA Rev. **31**, 187-206 (1970).

[63] W. Kern, J. Electrochem. Soc. **137**, 1887-1892 (1990).

[64] M. Ombaba, S. B. Inayat, M. S. Islam, *Encyclopedia of Nanotechnology* (Springer, Netherlands, 2016).

[65] K. Choi, J. M. Buriak, Langmuir **16**, 7737-7741 (2000).

[66] P. R. Camp, J. Electrochem. Soc. **102**, 586-593 (1955).

[67] H. Okumura, T. Akane, S. Matsumoto, Appl. Surf. Sci. **125**, 125-128 (1998).

[68] D. P. Brunco, B. De Jaeger, G. Eneman, J. Mitard, G. Hellings, A. Satta, V. Terzieva, L. Souriau, F. E. Leys, G. Pourtois, M. Houssa, G. Winderickx, E. Vrancken, S. Sioncke, K. Opsomer, G. Nicholas, M. Caymax, A. Stesmans, J. Van Steenbergen, P. W. Mertens, M. Meuris, M. M. Heynsa, J. Electrochem. Soc. **155** (7), H552-H561 (2008).

[69] S. Sioncke, D. P. Brunco, M. Meuris, O. Uwamahoro, J. Van Steenbergen, E. Vrancken, M. M. Heyns, ECS Trans. **16** (10), 451-460 (2008).

[70] G. W. Anderson, M. C. Hanf, P. R. Norton, Z. H. Lu, M. J. Graham, Appl. Phys. Lett. **66**, 1123 (1995).

[71] S. R. Amy, Y. J Chabal, F. Amy, A. Kah, C. Krugg, P. Kirsch, Mater. Res. Soc. Symp. Proc. **917**, 0917 E01 (2006).

[72] S. Rivillon, Y. J. Chabal, F. Amy, A. Kahn, Appl. Phys. Lett. **87**, 253101 (2005).

[73] R. D. Schnell, F. J. Himpsel, A. Bogen, D. Rieger, W. Steinmann, Phys. Rev. B. **32**, 8052-8056 (1985).

[74] M. F. Ehman, J. W. Faust Jr., W. B. White, J. Electrochem. Soc. **118** (9) 1443-1447 (1971).

[75] S. Kagawa, T. Mikawa, T. Kaneda, Jpn. J. Appl. Phys. **21** (11), 1616-1618 (1982).

[76] J. Kim, K. Saraswat, Y. Nishi, 2005 ECS Meeting, Abstract #779 (2005).

[77] B. Onsia, T. Conard, S. De Gendt, M. Heyns, I. Hoflijk, P. Mertens, M. Meuris, G. Raskin, S. Sioncke, I. Teerlinck, A. Theuwis, J. Van Steenbergen, C. Vinckier, Solid State Phenom. **103-104**, 19-22 (2005).

[78] W. L. Jolly, *Modern Inorganic Chemistry* (McGraw-Hill Inc., New York, 1984), p.207.

[79] T. Deegan, G. Hughes, Appl. Surf. Sci. **123/124**, 66-70 (1998).

[80] J. Kim, S. Liu, S. Tan, J. McVittie, K. Saraswat, Y. Nishi, ECS Trans. **3**, 1191-1196 (2006).

[81] N. Tabet, M. Faiz, N. M. Hamdan, Z. Hussain, Surf. Sci. **523**, 68–72 (2003).

[82] L. Y. L. Shen, Surf. Sci. **47**, 685-691 (1975).

[83] J. Kim, J. McVittie, K. Saraswat, Y. Nishi, Solid State Phenom. **134**, 33-36 (2008).

[84] D. Schmeisser, R. D. Schnell, A. Bogen, F. J. Himpsel, D. Rieger, G. Landgren, J. F. Morar, Surf. Sci. **172**, 455-465 (1986).

[85] A. V. Hamza, G. D. Kubiak, R. H. Stulen, Surf. Sci. **237**, 35-52 (1990).

[86] P. Gupta, V. L. Colvin, S. M. George, Phys. Rev. B **37**, 8234-8243 (1988).

[87] H. Ubara, T. Imura, A. Hiraki, Solid State Commun. 50, 673-675 (1984).

[88] G. W. Trucks, K. Raghavachari, G. S. Higashi, Y. J. Chabal, Phys. Rev. Lett. **65**, 504-507 (1990).

[89] F. Maroun, F. Ozanam, J.-N. Chazalviel, J. Phys. Chem. B **103**, 5280-5288 (1999).

[90] T. Maruyama, H. Akagi, J. Electrochem. Soc. **143**, 4087-4089 (1996).

[91] J. Y. Maeng, J. Y. Lee, Y. E. Cho, S. Kima, S. K. Jo, Appl. Phys. Lett. **81**, 3555-3557 (2002).

[92] W. P. Bai, N. Lu, J. Liu, A. Ramirez, D. L. Kwong, D. Wristers, A. Ritenour, L. Lee, D. Antoniadis, Proc. Symp. VLSI Technol. 121-122 (2003).

[93] R. Xie, M. Yu, M. Y. Lai, L. Chan, C. Zhu, Appl. Phys. Lett. **92**, 163505 (2008).

[94] G. Mavrou, P. Tsipas, A. Sotiropoulos, S. Galata, Y. Panayiotatos, A. Dimoulas, C. Marchiori, J. Fompeyrine, Appl. Phys. Lett. **93**, 212904 (2008).

[95] R. Zhang, P. C. Huang, N. Taoka, M. Takenaka, S. Takagi, IEEE VLSI symp. 161-162 (2012).

[96] D. R. Lide, *Handbook of Chemistry and Physics* (CRC Press, Boca Raton, 1994), p. 8/45.

[97] C. J. Sandroff, R. N. Nottenburg. J.-C. Bischoff, R. Bhat, Appl. Phys. Lett. **51**, 33 (1987).

[98] Y. Tao, A. Yelon, E. Sacher, Z. H. Lu, M. J. Graham, Appl. Phys. Lett. **60**, 2669 (1992).

[99] O. Takahisa, Surf. Sci. 255, 229-236 (1991).

[100] Z. H. Lu, M. J. Graham, X. H. Feng, B. X. Yang, Appl. Phys. Let. **60**, 2773 (1992)

[101] T. Akane, J. Tanaka, H. Okumura. S. Matsumoto, Appl. Surf. Sci. **108**, 303-305 (1997).

[102] J. J.-H. Chen, N. A. Bojarczuk, Jr., H. Shang, M. Copel, J. B. Hannon, J. Karasinski, E. Preisler, S. K. Banerjee, IEEE T. Electron. Dev. **51**, 1441-1447, (2004).

[103] K. D. Sen, C. K. Jørgensen, *Electronegativity* (Springer, Berlin, 1987) p.9.

[104]http://www.wiredchemist.com/chemistry/data/bond_energies_lengths.html for the bond energy of Ge-Cl.

[105] http://cccbdb.nist.gov/bondlengthmodel2.asp?method=12&basis=5 for the bond length of Ge-Cl and Ge-F.

[106] M. Choi, A. B. Posadas, H. Seo, R. C. Hatch, A. A. Demkov, Appl. Phys. Lett. **102**, 031604 (2013).

Chapter 5. Preparation of a clean Ge(001) surface using oxygen plasma cleaning

We demonstrate a method to obtain a clean and smooth Ge (001) surface using oxygen plasma cleaning without sputtering or Ge regrowth. The preparation of the germanium surface consists of four cycles of *ex situ* wet etching using HCl as the etchant and H_2O_2 as the oxidant. Subsequently the sample is outgassed and exposed to an oxygen plasma for 30 min followed by thermal desorption of the newly formed oxide layer. Reflection high-energy electron diffraction shows a clear 2 × 1 reconstruction of the germanium surface. *In situ* x-ray photoelectron spectroscopy measurements confirm that the cleaned surface is free of carbon contamination and that no GeO_2 remains. Angle-resolved photoemission spectra of the cleaned Ge show the peak associated with the Ge surface state indicating a very clean surface. Atomic force microscope images further indicate a smooth germanium surface with a mean surface roughness of approximately 3 Å after plasma cleaning.

This work was published in: P. Ponath, Agham B. Posadas, R. C. Hatch and Alexander A. Demkov, J. Vac. Sci. Technol. B ***31****, 031201 (2013).*

5.1 Introduction

Germanium with its higher hole and electron mobility than silicon is a potential candidate to replace silicon in complementary metal-oxide-semiconductor (CMOS) [1]. However, the main drawback of germanium in comparison to silicon is that its native oxide, GeO_2, is water soluble [2] and is, therefore, unsuitable for creating a stable dielectric oxide layer

on the germanium surface. Recent studies have shown that other materials with a high dielectric constant (so called high-κ materials) such as $BaTiO_3$, ZrO_2, HfO_2, or La_2O_3 could be successfully grown on germanium and thus substitute for GeO_2 as a gate dielectric [3-6]. For optimal growth with minimal interface defects, the surface preparation of germanium is a critical step. Several ways of cleaning the surface have been previously investigated such as ion sputtering or wet etching processes [7-10]. In order to achieve a smooth and clean Ge surface, the wet etching process appears to be a more promising method since ion sputtering has been shown to lead to a degradation of the surface smoothness [8]. However, the specific etchants and their concentration are a crucial point [10]. Early attempts revealed that the Ishizaka-Shiraki method [11], which uses hydrofluoric acid (HF) as the etchant, did not show satisfactory results for germanium because it lead to a high surface roughness and, more importantly, HF does not completely remove germanium sub-oxides GeO_x from the surface [12-14]. Instead, it has been shown that using hydrochloric acid (HCl) as the etchant in conjunction with hydrogen peroxide (H_2O_2) as the oxidant reduces the surface roughness dramatically [10]. A further *in situ* treatment to remove the germanium sub-oxides and carbon contamination is also necessary. A study by Jones *et al.* [15] showed that using H_2SO_4 for wet-etching SiGe with subsequent flash annealing leads to particulates on the surface with a typical height of 5 nm. However, they showed that exposing SiGe to UV-ozone results in a significant decrease in the number of particulates on the surface.

In this study, we propose an alternative method to obtain a contamination-free, smooth Ge(001) surface suitable for surface science studies without the use of sputtering or Ge

regrowth. The surface preparation procedure consists of a wet etching process using HCl as the etchant and H_2O_2 as an oxidant, in combination with oxygen plasma cleaning to volatilize any carbon contamination and to oxidize the topmost layers of germanium. The method of using oxygen plasma cleaning has been investigated previously by Chan *et al.* [16], however, they could not achieve a sharp 2×1 reconstruction pattern in electron diffraction. A subsequent annealing in vacuum removes the newly created oxide layer resulting in a smooth, contamination-free Ge(001) surface suitable for epitaxial growth and surface analysis.

5.2 Experimental Details

The samples used in this study are Sb-doped n-type Ge(001) wafers (0.029-0.054 Ω-cm) that are diced into 16×16 mm^2 squares. The samples are first degreased in acetone, deionized water (18.2 MΩ-cm) and isopropyl alcohol before undergoing etching. For the *ex situ* wet etching study, HCl and H_2O_2 are chosen since these have previously been shown to yield good results [10]. The oxygen plasma cleaning and annealing steps and the *in situ* surface analysis are carried out in a combined molecular beam epitaxy (MBE)/photoelectron spectroscopy system with a base pressure of 2×10^{-10} Torr for the MBE chamber and 5×10^{-10} Torr for the photoemission chamber. The MBE system is a DCA Instruments M600 model and the photoemission system is a VG Scienta custom-built unit with monochromated Al Kα and He plasma sources and an R3000 analyzer. The total energy resolution is ~300 meV and <30 meV for x-ray photoelectron spectroscopy (XPS) and angle-resolved photoemission spectroscopy (ARPES). For

angle-resolved measurements, the angular resolution was ~0.3°. The two systems are coupled through a common vacuum transfer line, and the sample holders are compatible allowing for in-vacuum transfer between the two chambers. Reflection high-energy electron diffraction (RHEED) (Staib Instruments) using 18 keV electrons at a grazing angle of 3° is used to observe the 2 × 1 reconstruction of the germanium surface. *Ex situ* AFM measurements (Veeco DI Multi Mode V) using contact mode is carried out to measure the surface roughness immediately after being unloaded from the MBE/XPS system.

All samples are degreased in an ultrasonic cleaner for 5 min each in acetone, deionized water and isopropyl alcohol prior to the wet etching process. Experiments on two sample series, A and B, are carried out without using oxygen plasma, to determine the effect of subsequent annealing (A1, A2), etching time (A2, B1), and acid concentration (B1-B3) on the surface roughness of Ge. The results of this study are summarized in Table 5.1. Using the conditions yielding the smoothest surface from the etching study, a third sample series is prepared to study the effect of oxygen plasma (C1).

The wet etching process consists of four repeated cycles of dipping the sample alternately into hydrochloric acid and hydrogen peroxide. Throughout the series of tests, the dipping time in the acid is reduced to 20 s for all four cycles. The dipping time in H_2O_2, however, is kept constant at 30 s for the first three cycles and increased to 60 s in the fourth cycle. Based on the previous results of Klesse [10], the concentration of the hydrogen peroxide for the wet etching process is kept constant at 7% throughout the whole series of tests. The acid removes the native oxide and most of the contamination on the surface, while

the H_2O_2-bath creates a new and clean passivation layer after the etching. Before the sample is transferred into the MBE-chamber for the pre-annealing or the plasma cleaning, it is dipped for 60 s into deionized water, dried using nitrogen gas and outgassed in the load lock chamber for 30 min at approximately 130°C.

After wet-etching, samples from the series A1-B2 were thermally annealed at 550°C (ramp rate: 20°C/min) for 2.5 h and at 650°C (ramp rate: 5°C/min) followed by a final annealing step shown in Table 5.1. We also found that a pre-annealing prior to the plasma cleaning has no effect on the surface roughness, so samples undergoing oxygen plasma treatment subsequent to the etching study (C1) were no longer pre-annealed. The oxygen plasma treatment consists of exposure for 30 min to a radio-frequency (RF) plasma source operated at a background oxygen pressure of 1×10^{-5} torr and a forward power of 300 W. Extrapolating manufacturer's data for the atomic oxygen flux given the power, oxygen pressure and source to substrate distance, we estimate the atomic oxygen flux to be ~ 5×10^{13} ($cm^{-2}s^{-1}$). Throughout the plasma cleaning, the temperature of the sample is kept at 100°C. After plasma treatment, a post-annealing at 550°C (ramp rate: 20°C/min) and 650°C (5°C/min) for 4 h each, and additional 30 min at 700°C (5°C/min) is performed to remove the newly grown oxide layer on the surface. After the post-annealing, the sample is cooled down to room temperature with a cooling rate of 20°C/min. RHEED images of the germanium surface are taken to confirm the presence of a sharp 2×1 reconstruction pattern indicative of a flat, oxide-free surface. The sample is transferred to the XPS chamber without breaking the vacuum. High resolution XPS spectra of the Ge 3*d*, Ge 2*p*, O 1*s* and C 1*s* core levels are measured to check for oxygen

and carbon contamination on the surface of the germanium sample. *Ex situ* AFM measurements of the samples are carried out under ambient conditions to determine the mean surface roughness immediately after unloading from the vacuum system.

5.3 Results and Discussion

A comparison between sample A1 and A2, which have experienced identical etching conditions, reveals that a subsequent annealing after etching significantly reduces the surface roughness of the sample. Sample A2, which is annealed, has a surface roughness of 4.5 nm compared to sample A1, which is not annealed and has a surface roughness of 11.6 nm.

Sample	HCl (%)	H_2O_2 (%)	Etching/oxidation times per cycle (s)	Final annealing step (°C)	Oxygen plasma treatment (100 °C)	Surface roughness (nm)
A1	36	7	60/30, 45/30, 45/30, 45/60	—	—	11.3 ± 0.7
A2	36	7	60/30, 45/30, 45/30, 45/60	$750 \Rightarrow 0$ h	—	5.0 ± 0.6
B1	36	7	20/30, 20/30, 20/30, 20/60	$700 \Rightarrow 0.5$ h	—	2.6 ± 0.2
B2	20	7	20/30, 20/30, 20/30, 20/60	$750 \Rightarrow 10$ min	—	1.0 ± 0.2
B3	15	7	20/30, 20/30, 20/30, 20/60	$650 \Rightarrow 0.5$ h	—	0.9 ± 0.2
C1	15	7	20/30, 20/30, 20/30, 20/60	—	Yes	0.3 ± 0.1

Table 5.1: Procedures for wet etching the germanium surface. Samples A1 and A2 illustrate the effect of *in situ* annealing right after wet-etching. Samples B1-B3 are used to study the effect of acid concentration on the surface roughness. All samples (except A1 and C1) are annealed at 500°C for 2.5 h and subsequently at 600°C for 0.5 h (ramping rate: 5°C/min) before the final annealing step which is shown in the Table. The mean value and the standard deviation of the surface roughness were calculated using several 5 × 5 μm^2 images of the sample's surface.

Another factor that is found to greatly influence the surface roughness is the etching time. It turns out that shorter etching times lead to a lower surface roughness. For example, a

comparison of the surface roughness of sample A2 and B1 shows a reduction from 4.5 to 2.4 nm, when the etching time is reduced from 45-60 s to 20 s in each of the four etching cycles. The HCl concentration is also found to influence the surface roughness. A comparison between samples B1-B3 clearly shows that a reduction of the concentration leads to a lower surface roughness (see Table 5.1). The sample wet-etched at the HCl concentration of 36% shows a surface roughness that is about three times greater than that of the sample etched with the HCl concentration of 15%. As shown in Table 5.1, best results are achieved when using the HCl concentration of 15% with a reduced etching time of 20 s, which results in a surface roughness of only 0.9 nm. The root mean square (RMS) roughness of all six samples (A1-C1), averaged over several 5 × 5 μm AFM images from different locations in the sample, are summarized in Table 5.1 and plotted in Figure 5.1.

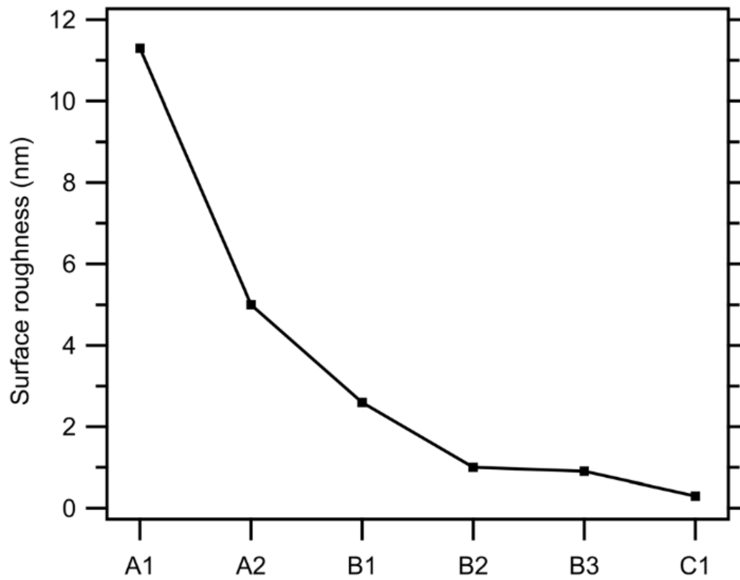

Figure 5.1: Averaged surface roughness of samples A1-C1. Each sample corresponds to a different etching and/or annealing conditions given in Table 1.

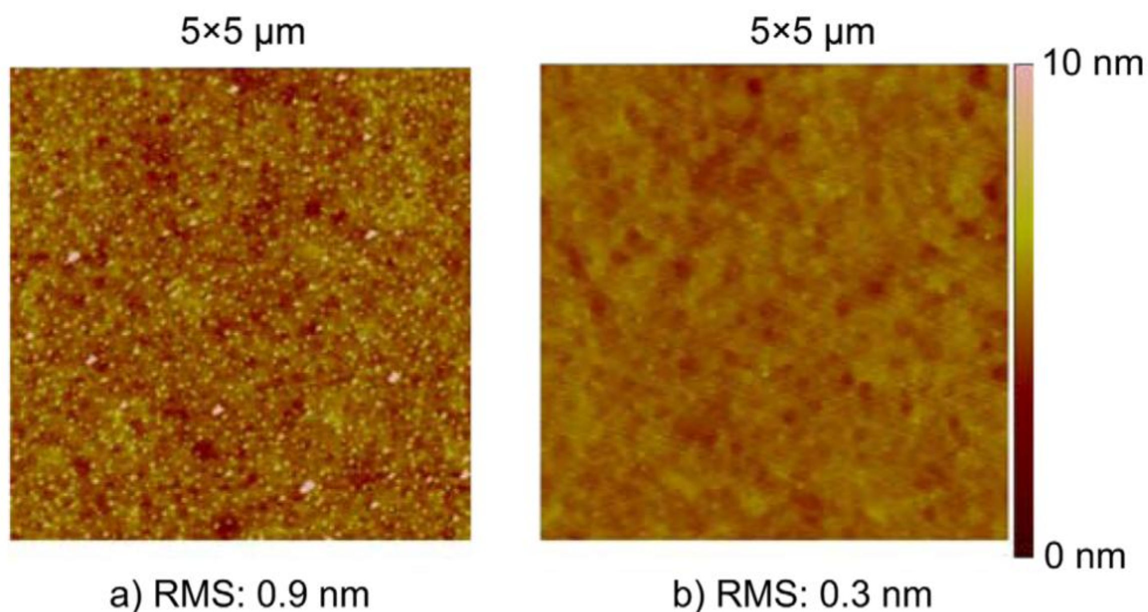

Figure 5.2: (a) AFM image of the germanium surface after the wet etching treatment and subsequent annealing without plasma exposure; (b) AFM image of the same sample after the oxygen plasma cleaning and subsequent annealing. The germanium surface is free of any contamination and much smoother than before the plasma cleaning.

In Figure 5.2, we show an AFM image of sample B3 after the wet etching process and a subsequent annealing, both before and after the plasma cleaning. Clearly, the oxygen plasma causes a reduction of the surface roughness of the sample from 0.9 nm to 0.3 nm which is less than the surface roughness of 0.4 nm of the untreated but degreased germanium sample. In addition to making the surface smoother, the oxygen plasma is also very effective in removing any carbon contamination. XPS measurements show slight carbon residue on the untreated surface, whereas the plasma cleaned surface shows no detectable carbon signal, as will be discussed later. Small particles distributed over the whole surface that are visible in the sample before plasma cleaning are removed after exposure to oxygen plasma.

We also confirm that annealing after wet etching but before plasma cleaning is not necessary, since no significant differences in surface roughness or morphology are observed.

As a result of the exposure to the oxygen plasma, a relatively thick (70 Å) oxide layer forms on the germanium surface. A subsequent heat treatment is necessary to remove this newly formed oxide. In order to prevent carbon contamination during annealing which might evaporate from the heater material, a low ramping rate of 5°C/min is used when the sample temperature is above 500°C. A final annealing step at 650°C or higher for 30 min turns out to be crucial for obtaining a sharp and intense 2 × 1 surface reconstruction in RHEED. The long annealing times, which need to be optimized if to be used for commercial processes, in conjunction with the plasma cleaning at 100°C is believed to be the reason for the smoothness of the surface and the sharp 2 × 1 reconstruction, which could not be achieved by L. H. Chan *et al.* [16]. We believe that the atomic oxygen volatilizes any remaining contamination and oxidizes

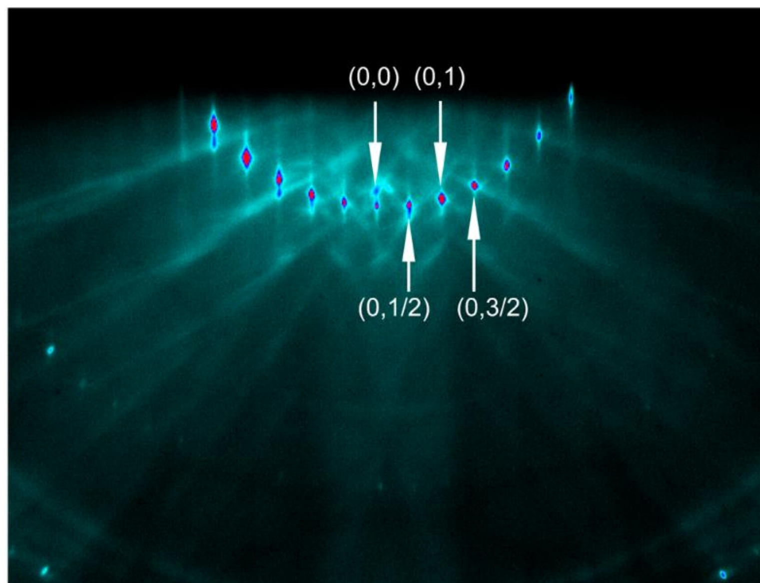

Figure 5.3: RHEED image of the germanium sample along the [110] zone axis after the oxygen plasma cleaning showing intense and sharp half order spots, indicating a 2 × 1 reconstruction.

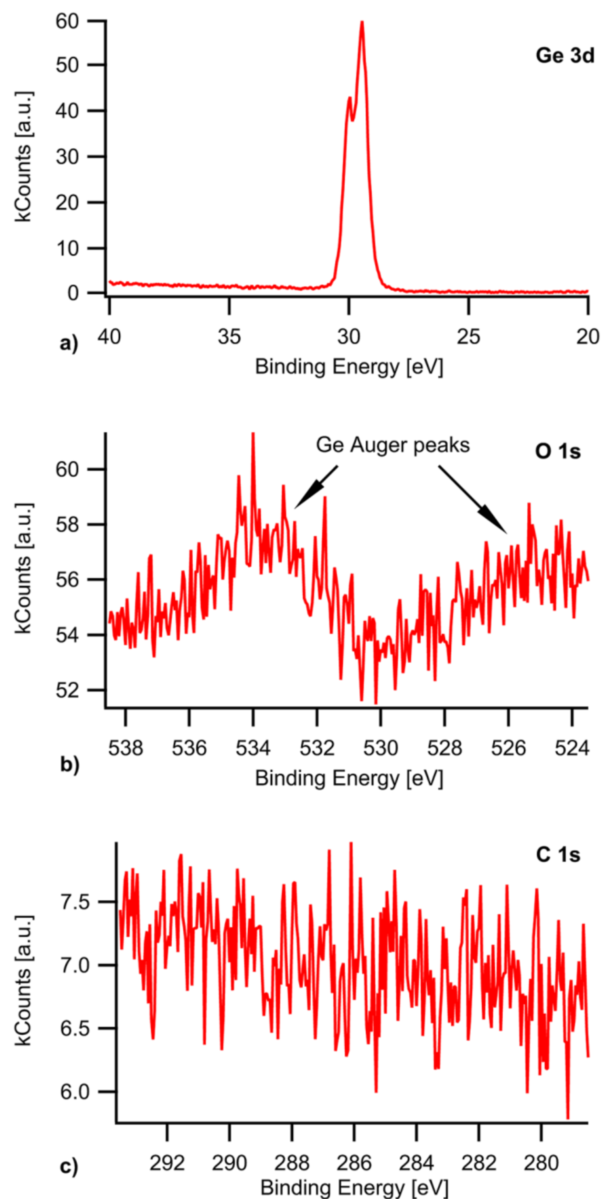

Figure 5.4: (a) The Ge 3*d* spectrum shows the characteristic peak for pure germanium. The surface is free of any GeO_2, since no features of any possibly remaining germanium oxides, which have higher binding energies, are detectable. (b) The O 1*s* spectrum shows the non-existence of oxygen on the surface. The two broad features which can be seen are due to Ge $L_2M_{23}M_{23}$ and $L_3M_{23}M_{23}$ Auger electrons. (c) The C 1*s* spectrum shows no residue of carbon could be found on the cleaned surface, whose characteristic peak would have been at expected around 284.5 eV.

the topmost layers of Ge, creating a smooth surface. Slight traces of carbon were detected if a higher final annealing temperature was chosen or the annealing time was extended.

In Figure 5.3, we show a typical RHEED image obtained after the plasma cleaned sample was annealed. The very sharp and intense spots along a circular arc indicate an atomically flat surface. The 2 × 1 reconstruction spots are also clearly visible and distinct with intensities similar to the main diffraction spots, indicating a clean, oxide-free Ge surface.

XPS measurements of the Ge 3*d* (Figure 5.4(a) and Ge 2*p* (not shown) spectra both indicate that no GeO_x remains on the surface, which would show a feature on the higher binding energy side of the main Ge peak, indicating that the subsequent annealing completely removes the GeO_2

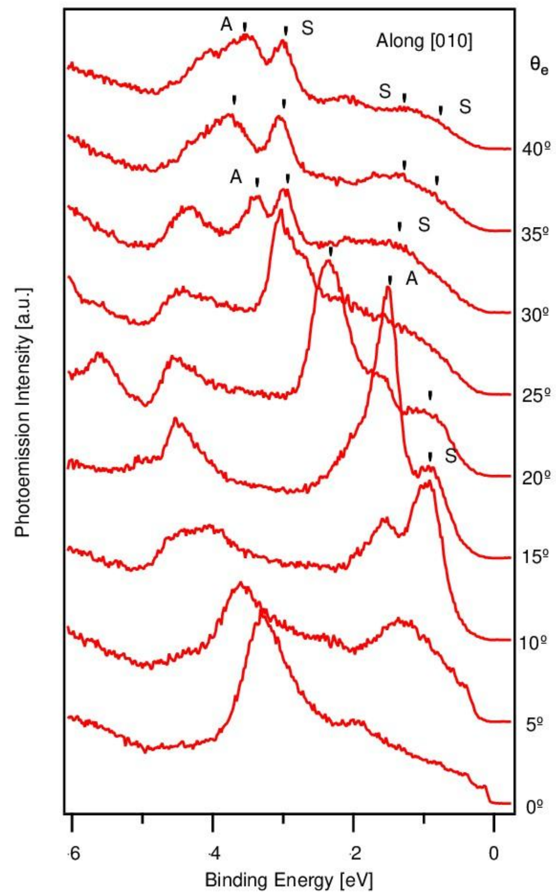

Figure 5.5: ARPES spectra taken at 300 K with a photon energy of *hv*=21.22 eV at various emission angles, θ_e, along the [010] crystallographic direction. Structures labeled with *S* are interpreted as surface-related features, and those with *A* to a direct bulk transition. The sharpness of the photoemission spectra, and the presence of the surface features are a clear indication of the surface quality.

layer formed during oxygen plasma exposure. O 1*s* spectra (Figure 5.4(b)) also show that there is no detectable oxygen on the surface. The broad features centered at 525 and 534 eV are due to Ge $L_2M_{23}M_{23}$ and $L_3M_{23}M_{23}$ Auger electrons [17]. C 1*s* spectra show no indication of residual carbon on the surface after the plasma cleaning (Figure 5.4(c)). XPS survey scans also show that no signals other than those due to pure germanium could be detected from the sample. The detection limit for oxygen and carbon for XPS is typically quoted to be in the range of 0.1-1 atomic % [18]. A further demonstration of the surface quality obtained by the cleaning procedure are the ARPES measurements shown in Figure 5.5 using He I radiation ($h\nu$ = 21.22 eV). Because of the small escape-depth of photoelectrons excited by He I radiation, ARPES is a highly surface-sensitive technique. The sensitivity of ARPES to surface quality has long been established, and even a small adatom-coverage of 0.02 monolayers can noticeably perturb surface states [19]. In Figure 5.5, states shown by E. Landemark *et al*. [20] to be related to the surface are marked with an *S* and a state shown to be related to a direct bulk transition is labeled with an *A*. Because the surface-related states are highly sensitive to surface contamination and disorder, their presence in the ARPES spectra yet again confirms the effectiveness of our surface processing.

5.4 CONCLUSION

In conclusion, we have developed a process to obtain a smooth and contamination-free Ge(001) surface for subsequent epitaxial growth or surface analysis without sputtering or Ge regrowth. This process involves an *ex situ* wet etch using HCl (15%) and H_2O_2 (7%),

followed by *in situ* oxygen plasma cleaning for 30 min which removes all the contamination and smoothens the sample surface. A subsequent final heat treatment removes the newly formed oxide layer, and a clear 2×1 surface reconstruction of germanium is visible in RHEED. XPS and ARPES measurements confirm that the surface is carbon- and oxide-free.

5.5 References

[1] T. Krishnamohan, Z. Krivokapic, K. Uchida, Y. Nishi, K. C. Saraswat, IEEE Trans. Elect. Dev. **53**, 990-999 (2006).

[2] H. Shang, M. M. Frank, E. P. Gusev, J. O. Chu, S. W. Bedell, K. W. Guarini, M. Ieong, IBM J. Res. & Dev. **50**, 377-386 (2006).

[3] N. Wu, Q. Zhang, C. Zhu, IEEE Elect. Dev. Letters, **25**, 631-633 (2004)

[4] C. O. Chui, S. Ramanathan, B. B. Triplett, P. C. McIntyre, K. C. Saraswat, IEEE Elect. Dev. Letters, **23**, 473-475 (2002).

[5] R. A. McKee, F. J. Walker, M. F. Chisholm, Science **293**, 468-471 (2001).

[6] G. Mavrou, S. F. Galata, A. Sotiropoulos, P. Tsipas, Y. Panayiotatos, A. Dimoulas, E. K. Evangelou, J. W. Seo, C. Dieker, Microelectron. Eng. **84**, 2324-2327 (2007).

[7] H. Okumura, T. Akane, S. Matsumoto, Appl. Surf. Sci. **125**, 125-128 (1998).

[8] X.-J. Zhang, G. Xue, A. Agarwal, R. Tsu, M.-A. Hasan, J. E. Greene, A. Rockett, J. Vac. Sci. Technol. A **11**, 2553-2561 (1993).

[9] J. S. Hovis, R. J. Hamers, C. M. Greenlief, Surf. Sci. **440**, 815-819 (1999).

[10] W. M. Klesse, G. Scappucci, G. Capellini, M. Y. Simmons, Nanotechnology **22**, 145604 (2011).

[11] A. Ishizaka, Y. Shiraki, J. Electrochem. Soc. **133**, 666-671 (1986).

[12] D. Bodlaki, H. Yamamoto, D. H. Waldeck, E. Borguet, Surf. Sci. **543**, 63-74 (2003).

[13] J. Kim, S. Liu, S. Tan, J. McVittie, K. Saraswat, Y. Nishi, ECS Trans. **3**, 1191-1196 (2006).

[14] C. O. Chui, H. Kim, P. C. McIntyre, K. C. Saraswat, IEEE Elect. Dev. Letters, **25**, 274-276 (2004).

[15] D. E. Jones, J. P. Pelz, Y. H. Xie, P. J. Silverman, E. A. Fitzgerald, Surf. Sci. Lett. **341**, 1005-1010 (1995).

[16] L. H. Chan, E. I. Altman, Y. Liang, J. Vac. Sci. Technol. **19**, 976-981 (2001).

[17] J. F. Moulder, W. F. Stickle, P. E. Sobol, K. D. Bomben, *Handbook of x-ray photoelectron spectroscopy* (Physical electronics Inc., Eden Prairie, 1995).

[18] M. H. Engelhard, *Handbook of Deposition Technologies for Films and Coatings* (Elsevier, Boston, 2010).

[19] S. D. Kevan, R. H. Gaylord, Phys. Rev. B **33**, 5809-5818 (1986).

[20] E. Landemark, C. J. Karlsson, L. S. O. Johansson, R. I. G. Uhrberg, Phys. Rev. B **49**, 16523-16533 (1994).

Chapter 6. Carrier density modulation in a germanium heterostructure by ferroelectric switching

The development of nonvolatile logic through direct coupling of spontaneous ferroelectric polarization with semiconductor charge carriers is nontrivial, with many issues, including epitaxial ferroelectric growth, demonstration of ferroelectric switching, and measurable semiconductor modulation. Here, we report a true ferroelectric field effect – carrier density modulation in an underlying Ge(001) substrate by switching of the ferroelectric polarization in epitaxial *c*-axis-oriented $BaTiO_3$ grown by molecular beam epitaxy. Here, using density functional theory, we demonstrate that switching of $BaTiO_3$ polarization results in a large electric potential change in Ge. Aberration-corrected electron microscopy confirms $BaTiO_3$ tetragonality and the absence of any low permittivity interlayer at the interface with Ge. The non-volatile, switchable nature of the single domain out-of-plane ferroelectric polarization of $BaTiO_3$ is confirmed using piezoelectric force microscopy. The effect of the polarization switching on the conductivity of the underlying Ge is measured using microwave impedance microscopy, clearly demonstrating a ferroelectric field effect.

This work was published in Patrick Ponath, Kurt Fredrickson, Agham B. Posadas, Yuan Ren, Xiaoyu Wu, Rama K. Vasudevan, M. Baris Okatan, S. Jesse, Toshihiro Aoki, Martha R. McCartney, David J. Smith, Sergei V. Kalinin, Keji Lai and Alex A. Demkov, Nature Commun. ***6****, 6067 (2015).*

6.1 Introduction

Direct deposition of a ferroelectric oxide on a semiconductor typically results in chemical reaction at the boundary between the two materials, yielding a thick amorphous interfacial layer and a polycrystalline ferroelectric film. The interfacial layer prevents the ferroelectric oxide from contacting the semiconductor in an atomically intimate manner and from having a measurable effect on the underlying semiconductor. Thus, the ferroelectric field-effect transistor (FeFET) has so far eluded development [1]. The conceptual simplicity of the FeFET architecture, combined with the large surface polarization charge density of a typical ferroelectric (~20 μCcm^{-2}), an order of magnitude larger than what dielectrics can typically sustain, contribute to the obvious attraction of having a ferroelectric gate in a field-effect transistor. This seemingly straightforward approach has not yet worked because of the fundamental challenge of combining a ferroelectric oxide directly with a semiconductor without any interfacial reaction. In order to have a substantial effect on the semiconductor charge carrier density, the ferroelectric polarization charge must be as close to the transistor channel as possible. To achieve this proximity, one must ensure the highest quality ferroelectric oxide/semiconductor interface, which requires heterogeneous epitaxy between the covalently bonded semiconductor and the ionically bonded oxide. In pioneering work, McKee *et al.* were able to interface strontium titanate (STO) epitaxially with Si [2], thus opening up a path to integrate ferroelectric oxides such as lead zirconium titanate (PZT) and $BaTiO_3$ (BTO) with Si, using STO buffer layers [3-7]. However, it is nearly impossible to prevent formation of a low permittivity SiO_2 layer at the STO-Si interface during subsequent

deposition of the ferroelectric oxide due to the very high reactivity of Si with oxygen. This intermediate layer prevents the ferroelectric polarization field from having any influence on the semiconductor, and also results in a depolarizing field that eventually kills the ferroelectric polarization [8-9].

An additional challenge for achieving functioning ferroelectric devices is that in order to modulate the semiconductor charge density by switching the polarization field, the latter must be aligned normal to the oxide/semiconductor interface. However, due to thermal expansion mismatch, for example between BTO and Si, a residual in-plane tensile stress is present when the materials are cooled down after ferroelectric deposition. Hence, BTO tends to grow with its long tetragonal axis (*c*-axis), which is the direction of ferroelectric polarization, in the film plane. BTO has been epitaxially grown on Si using a variety of buffer layers but ferroelectric measurements show in-plane polarization [10-12]. Despite these difficulties, several groups have reported BTO grown on Si using various buffer layers, with *c*-axis normal to the interface [4-7]. Vaithnayathan *et al*. [5] demonstrated *c*-axis-oriented BTO growth on Si but only after using a thick (30 nm), fully-relaxed $Ba_{1-x}Sr_xO_3$ (BST) layer to counteract the in-plane tensile stress due to the thermal expansion mismatch between BTO and Si. Niu *et al.* [6] reported *c*-axis-oriented BTO grown on Si using a 5-nm-thick STO buffer layer and showed a 0.75 V memory window in C-V measurements for 90-nm-thick film grown by PLD. Most recently, ferroelectric switching of perpendicular polarization without a bottom electrode has been demonstrated in epitaxial BTO films grown on STO-buffered Si for film thicknesses ranging from 8-40 nm with a smaller buffer thickness of 6 nm [7]. However, the presence of a low-

permittivity 2-nm-thick interfacial SiO_2 layer required relatively high voltages to achieve switching. More importantly, the modulation of charge density in the semiconductor, in other words the ferroelectric field effect, was not demonstrated. Hence, one is faced with a dual challenge when trying to realize a FeFET on Si. On the one hand, most of the electric field is dropped across the low permittivity SiO_2 layer, making it difficult to switch the ferroelectric. Conversely, even if switched, the polarization charge is removed from the channel because of the same SiO_2 layer. An alternative approach to integrating a ferroelectric directly on Si was proposed by Warusawithana *et al.* [13], who grew ultrathin (<4 nm) strained STO directly on Si and showed using piezoelectric force microscopy (PFM) that the compressively strained STO film was ferroelectric. However, no measurements of the properties of Si were made, possibly due to the difficulty in dealing with device fabrication using such ultrathin films.

There has recently been renewed interest in using Ge as a channel material [14-17]. As germanium is not as readily oxidized as silicon, one stands a much better chance of growing a ferroelectric oxide on Ge without any interface layer. Using Zintl templates several groups have made significant progress in interfacing BTO with Ge [18-21]. Merckling *et al*. reported epitaxial BTO on thick Ge films grown on Si substrates [19]: a ½-monolayer Ba template layer was used in analogy to the ½-monolayer Sr on Si used for STO on Si heteroepitaxy. Mixed *c*-axis-oriented and cubic phase growth was reported, and no measurements of the ferroelectricity or analysis of the interface structure were made. Because the BTO was grown using atomic oxygen, the interface was possibly oxidized with a buried GeO_2 layer that would be detrimental to direct coupling of the

BTO polarization to Ge. We have recently demonstrated the fabrication of clean interfaces between Ge and BTO grown by molecular beam epitaxy (MBE), and between Ge and STO grown by atomic layer deposition (ALD) [21, 22]. We were able to infer the atomic structure of the BTO/Ge interface, but out-of plane polarization was not demonstrated, due to thermal expansion mismatch. By inserting an ultrathin STO layer between BTO and Ge, one can impose compressive in-plane strain on BTO that can overcome tensile stress caused by the thermal expansion mismatch and thereby achieve BTO on Ge with out-of-plane polarization [5]; a similar approach was recently used to grow BTO on GaAs. Ferroelectric switching of *c*-axis-oriented BTO on STO-buffered GaAs was demonstrated by Huang *et al*. [23] using preferentially oriented films with columnar crystallites, and by Contreras-Guerrero *et al*. [24] using flat epitaxial films.

6.2 RESULTS

6.2.1 First principal calculations

To establish the feasibility of achieving the field effect in the presence of the STO layer, we performed first-principles calculations of the BTO/STO/Ge stack. Previous density functional theory (DFT) calculations have shown that BTO strained to STO remains ferroelectric even with only 1 unit cell of BTO present [25], but the effect of polarization on the potential in the semiconductor layers beneath has not yet been considered. In simulations, we use (001)-oriented eight-layer-thick p-type-doped Ge slab capped with three unit cells of STO on either side (for the STO-Ge interface we use the 2×1 model described in [21]). These are followed by seven-and-a-half unit cells of BTO with TiO_2-

terminated surface facing vacuum. To satisfy the periodic boundary conditions, we use a large cell with mirror symmetry (see Supplementary methods for details). The simulation cell and the macroscopic average of the electrostatic potential across it are shown in Figure 6.1. We find that there are two stable states of polarization. One, which we call P_1, is essentially un-polarized and another, which we call P_2, is polarized "down" with Ti shifted away from the vacuum. In state P_1 the few near-surface planes of BTO are polarized "down" with the remainder of the layers being essentially flat. This is an

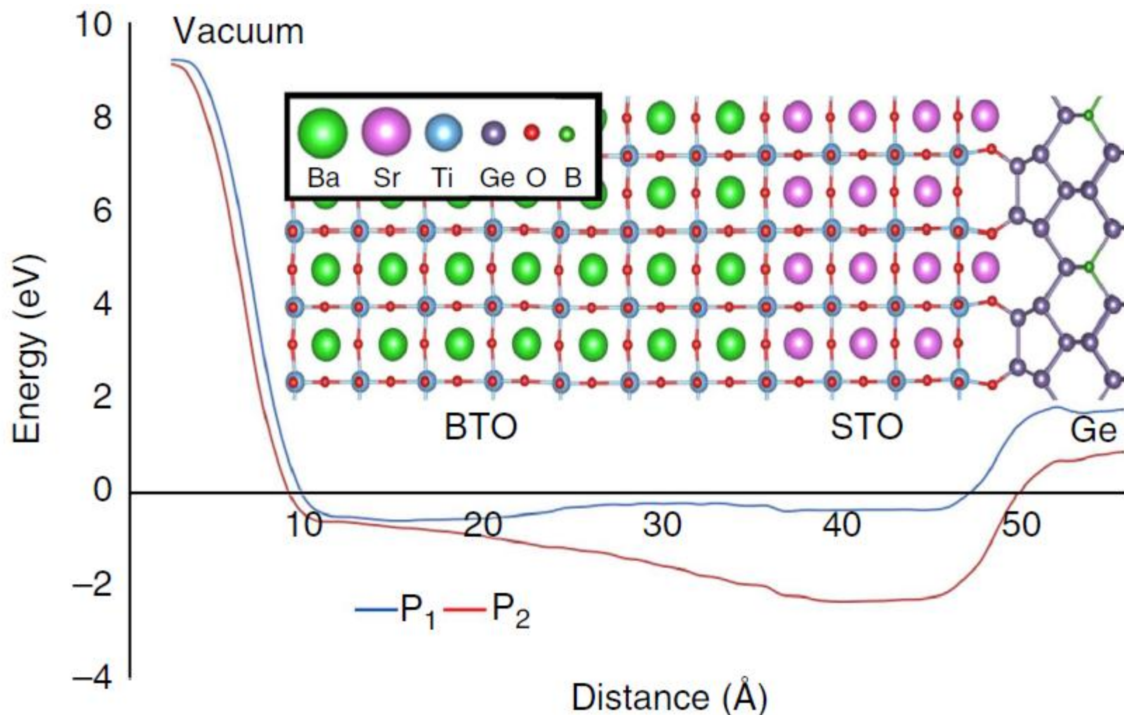

Figure 6.1: Calculation supercell: The supercell used in the DFT calculations, consisting of vacuum, BTO, STO and B-doped Ge. The cell is mirrored on the other side (not shown). Note the recession of the Ti from the surface, indicating polarization away from the BTO surface, and toward the BTO/STO interface. Below we show the macroscopic average of the plane-averaged electrostatic potential for the P_1 and P_2 states.

artifact of the 2.8 nm thickness of BTO used in the calculation. The initial inward ("down") relaxation of Ti is induced by the surface and is well documented in TiO_2 [26]. Of course, the local potential in the BTO bulk is totally symmetric. Therefore, polarization could be "up" or "down", but the "up" polarization requires a head-to-head domain wall as one approaches the film surface. As the energy of such a wall, 0.11 J m^{-2} [27], is too high it is suppressed in ultra-thin films. We will revisit this issue when discussing the electron microscopy results. We then examine the electrostatic potential for both polarization states. When comparing the difference in potential of the polarized and unpolarized heterostructures, we find a clear difference in electrostatic potential in the Ge layer as a result of switching between the two stable states of BTO polarization. This indicates that the presence of high-permittivity STO layer does not interfere with a robust field effect.

6.2.2 Sample preparation and growth

The Ge surface is prepared using a combination of wet-etching, oxygen plasma cleaning and annealing, resulting in a (2 × 1) reconstruction, low surface roughness, and clear surface signal in the angle resolved photoemission spectrum [28]. Prior to BTO growth, ½ monolayer of strontium is deposited to prevent germanium from oxidizing during the initial growth of the first 5 unit cells of STO at 200°C. After increasing the temperature to 600°C to crystallize the STO, BTO is co-deposited on the STO/Ge template at a temperature of 650°C. A reflection-high-energy electron diffraction (RHEED) pattern of a 15-nm-thick film of BTO is shown in the inset of Figure 6.2(a). *In situ* X-ray

photoelectron spectroscopy (XPS) measurements are carried out, to determine the stoichiometry of the grown film (Supplementary Fig. 1).

6.2.3 Lattice constant determination using XRD

Films were characterized by X-ray diffraction (XRD) performed on the BTO/Ge samples using a Philips X'Pert double-crystal diffractometer. Figure 6.2(a) shows symmetric θ-2θ scans of a 160-Å-thick BTO film grown on Ge, both with and without a 20-Å-thick STO buffer layer. The BTO peaks correspond to a single orientation with an out-of-plane

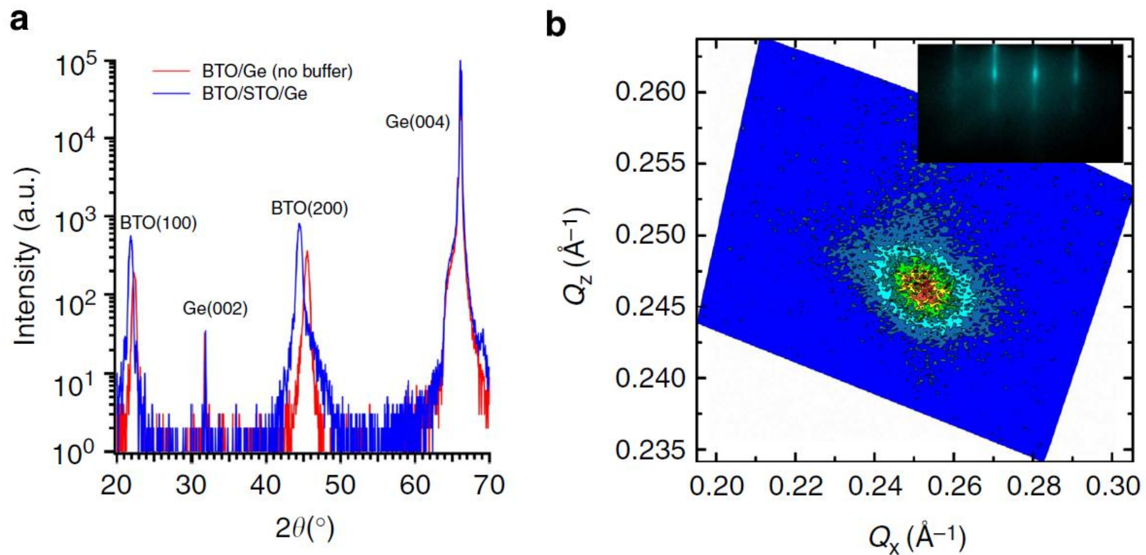

Figure 6.2: Crystalline structure of BTO/STO/Ge: (a) X-ray diffraction θ-2θ scan of 16 nm $BaTiO_3$ epitaxially grown on Ge(001) substrate, with and without a 2 nm $SrTiO_3$ buffer layer. Without the buffer, the d-spacing corresponds to the *a*-axis of BTO directed out of plane. With the STO buffer, the *c*-axis of BTO is directed out of plane. (b) Reciprocal space map of the (103) Bragg reflection for BTO/STO/Ge. The centroid of the peak is consistent with a short in-plane axis and long out-of-plane axis. The inset shows a typical RHEED pattern for BTO/STO/Ge taken along the [110] azimuth showing good crystallinity and surface flatness.

spacing of 4.06 Å for the film with the STO buffer, and 3.98 Å for the film without the buffer. This result clearly demonstrates the *c*-axis orientation for the STO-buffered sample compared with the *a*-axis orientation for the BTO layer grown directly on Ge. Figure 6.2(b) shows a reciprocal space map around the (103) Bragg reflection for the *c*-axis oriented sample. The measured lattice constants after fitting with a 2D Gaussian are a = 3.96 Å and c = 4.06 Å. Rocking curve scans around the BTO 002 Bragg peak typically show a full-width at half-maximum of 0.5-0.8°.

6.2.4 High-Angle Annular Dark-Field Microscopy

The crystalline quality of the BTO layer and the GeO_2-free Ge surface are confirmed using cross-section aberration-corrected electron microscopy. Electron micrographs clearly reveal that the BTO layer is coherently strained to the partly relaxed STO buffer, with no dislocations visible along considerable lengths of the BTO/STO interface. Aberration-corrected images were recorded using a probe-corrected JEOL-ARM200F, as shown in Figure 6.3(a). Individual Ti, Ge, Sr and Ba atomic column locations can be identified in both bright-field and high-angle annular-dark-field images, while Fourier transforms (diffractograms) of these images also confirm the tetragonality of the BTO with the longer *c*-axis pointing out of the plane (Figure 6.3(b)). Closer examination at higher magnification reveals that the Ti atomic columns close to the top of the BTO film are shifted downwards from the cell center whereas in regions close to the STO film they are displaced slightly upwards (Figures 6.3c, d). The “down” polarization near the surface is in agreement with the theoretical prediction.

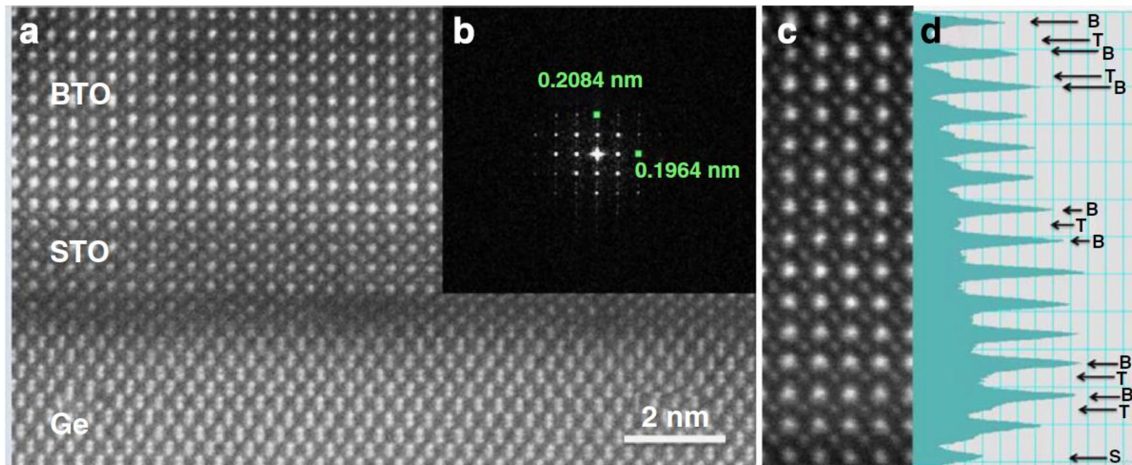

Figure 6.3: Aberration-corrected electron microscopy: (a) High-angle annular-dark-field (ADF) image of BTO/STO/Ge(001) heterostructure recorded with 200-keV probe-corrected scanning transmission electron microscope. White spots correspond to positions of metal atoms; (b) Fourier transform of ADF image confirming tetragonality of BTO layer; (c) Enlargement of ADF image showing region of BTO film; (d) Corresponding line profile from (c) showing shifts in Ti atomic-column positions.

6.2.5 Ferroelectricity confirmed by BE-PFM and BEPS

The ferroelectric properties of the BTO layer were then tested using Band-Excitation Piezoresponse Force Microscopy (BE-PFM) [29-30]. Results from a typical BE-PFM switching experiment are shown in Figures 6.4(a-c), where a 5×5 μm^2 square was initially poled with the tip held at -6 V, and a smaller 2.5×2.5 μm^2 square within the original square was then poled with the tip held at +4 V. The topography in Figure 6.4(a) shows no change in the poled areas, suggesting no irreversible electrochemical reactions at the surface. At the same time, the vertical BE-PFM amplitude and phase images in

(b,c) indicate clear and sharp boundaries, which are signatures of written ferroelectric domains, and largely obviate tip-injected surface charge effects dominating the contrast. This experiment also confirms that the BTO film outside the poled regions is monodomain, with polarization oriented towards the STO/Ge substrate in agreement with the theoretical predictions.

In order to further characterize the ferroelectric properties of the BTO film, we carried out BE- Piezoresponse Spectroscopy measurements (BEPS [31]), where the tip is placed at a particular position, a DC waveform is applied to the tip and simultaneously the BE-response is captured to yield the system's response. We performed a BEPS measurement on the BTO film across a 10×10 grid to yield a dataset of 100 measurements in total; the average spectrogram of the response (amplitude and phase) is shown in Figure 6.4(d), with the DC waveform shown inset. Three selected responses at individual points from the 100 measurements, after fitting to a simple harmonic oscillator (SHO) model are shown in Figures 6.4(e,f). The average of 100 measurements is shown as a solid olive line. The amplitude curves clearly follow the expected butterfly-like hysteresis typical of ferroelectrics, while the phase loop appears to show a change somewhat less than 180°. The latter effect is probably due to a slight electrostatic contribution to the signal, which cannot be ruled out due to the lack of a bottom electrode in this sample. We also note that the coercive voltage appears largely symmetric with only a small offset, with values around ~ +4 V and ~ -5 V.

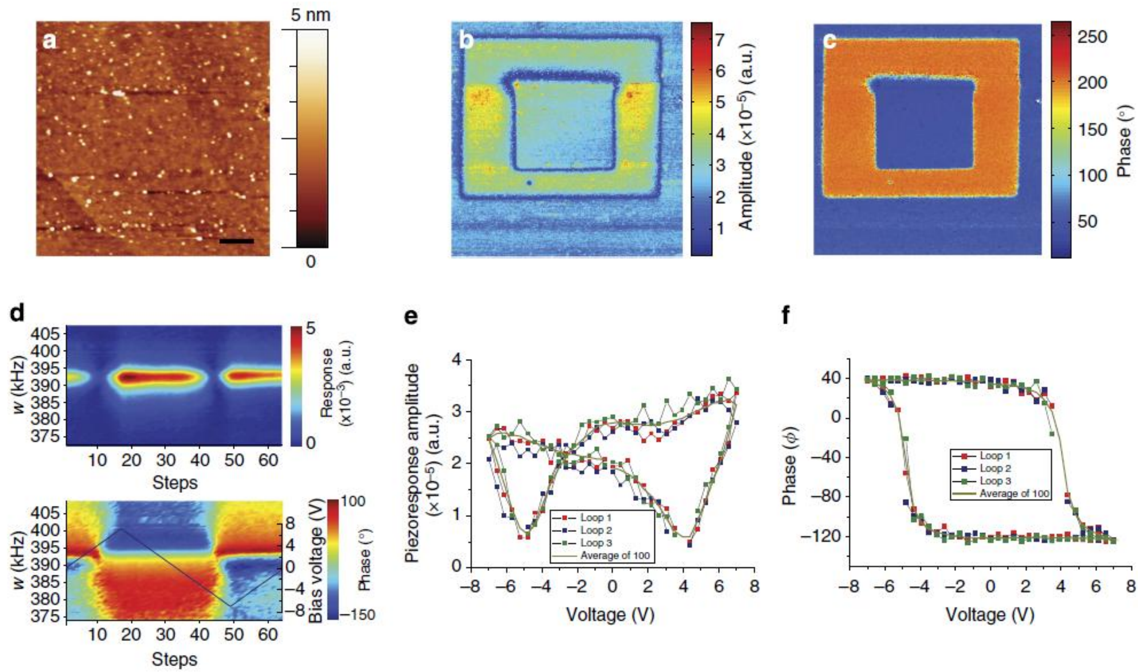

Figure 6.4: PFM and voltage spectroscopy of BTO heterostructures: (a) Topography, (b) BE-PFM amplitude and (c) associated phase image after a box-in-box switching experiment on the BTO hetereostructure, showing clear ferroelectric switching (scale bar: 1 μm). A 5 × 5 μm^2 box was poled with the tip held at -6 V, and then a smaller box 2.5 × 2.5 μm^2 was subsequently scanned with the tip held at +4 V before the BE-PFM images were captured. 100 hysteresis loops were then captured on the same film using BE spectroscopy. The average response is shown in the spectrograms in (d) for amplitude (above) and phase (below), with the applied DC waveform shown in blue. Selected amplitude and phase loops are shown in (e,f), respectively with the average loop shown as a solid line in olive.

6.2.6 Field effect demonstrated by microwave impedance microscopy

Having demonstrated that the BTO layer is both polar and ferroelectric, we next turn to addressing the field effect. Due to the difficulty in fabricating BTO/Ge transistors, we

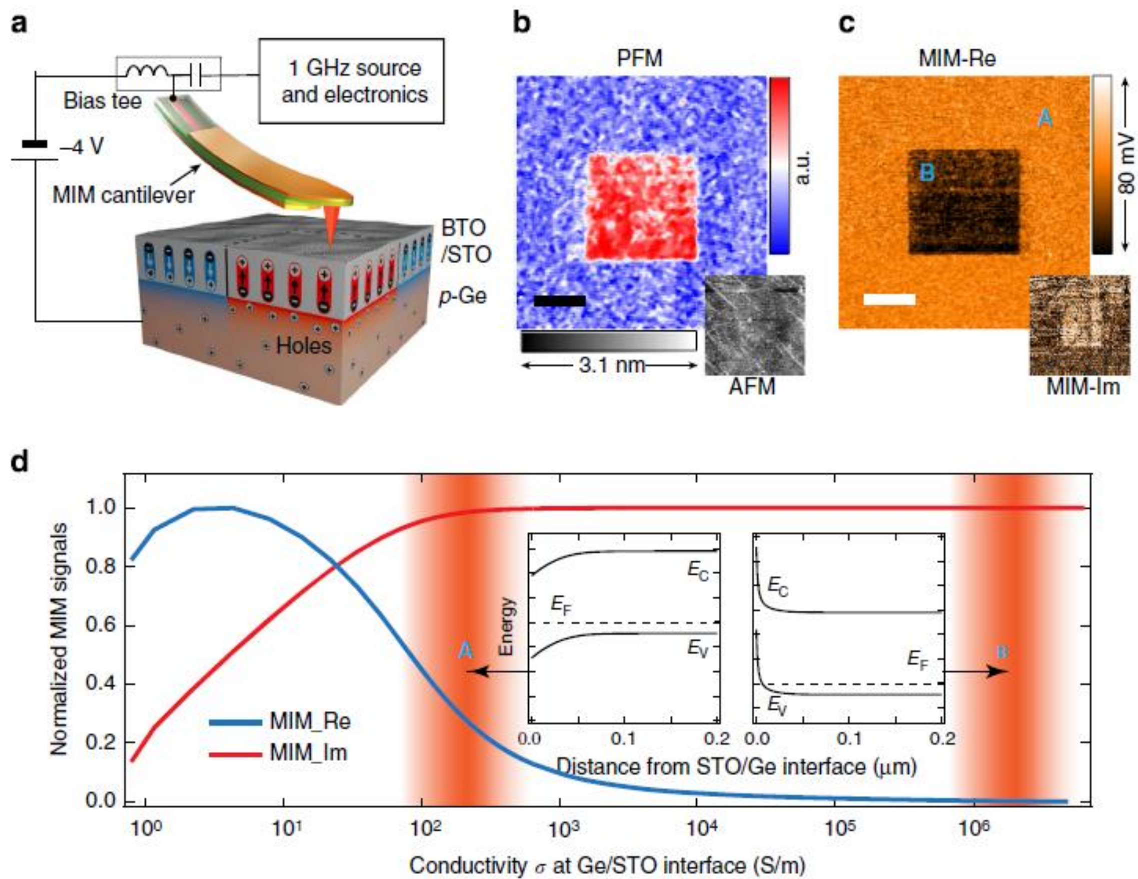

Figure 6.5: Ferroelectric switching and electrical detection, using microwave impedance microscopy (MIM): (a) Schematic diagram illustrating the measurement setup and configuration of samples. A negative-biased conductive scanning probe makes downward to upward switching in ferroelectric polarization of BTO layer, which modulates hole density at the BTO/p-Ge interface. PFM (b), AFM (bottom right corner in b), MIM real part (c) and MIM imaginary part (bottom right corner in c) images acquired after writing a 20 × 20 µm^2 square by applying -4 V DC bias on the tip (Scale bars: 10 µm). (d) Simulated MIM-Re (blue line) and MIM-Im (red line) signals as a function of conductivity at the BTO/Ge interface. Left and right insets, respectively, show band diagrams of Ge in regions A and B in panel (c).

utilize microwave impedance microscopy (MIM) to measure the conductivity of the underlying Ge [32-35]. MIM is a novel imaging tool used to spatially resolve the local permittivity and conductivity of materials [36-38], and was employed to demonstrate the ferroelectric field effect in the BTO/STO-Ge heterostructures. Here the 1 GHz excitation signal is delivered to a specially designed cantilever probe [39] and the evanescent wave from the tip apex, with a diameter of 20-100 nm, interacts with the sample underneath. The modulation of the carrier density at the ferroelectric-Ge interface results in appreciable impedance change of the tip, which is readily detected by the MIM electronics. As shown schematically in Figure 6.5(a), a DC voltage of -4 V is also applied to the conductive MIM tip through a bias-tee to locally switch the BTO polarization. After a $20 \times 20\ \mu m^2$ square was written, the DC bias was removed and a larger region concentric with the previous scan was then imaged by the same tip using PFM and MIM, both of which show clear contrast between the written and unwritten areas. The PFM contrast (Figure 6.5(b)) again confirms that BTO polarization is reversed by a sufficiently large negative tip bias, with no corresponding topographic features. In Figure 6.5(c), the poled area shows substantially lower MIM-Re and slightly higher MIM-Im signals than the intact region. Since neither the conductivity ($\sigma_{BTO} = 0$) nor the first-order dielectric constant (ε_{BTO}) of the BTO is affected by the polarization reversal, the MIM contrast must come solely from the underlying Ge layer accompanied by the poling process. We also confirmed that the PFM and MIM contrast is not observed for a smaller negative tip bias ($|V_{tip}| < 4$ V) or a positive bias up to +4 V, indicative of a ferroelectric switching process (Supplementary Fig. 3).

Finite-element modeling [37] was performed to analyze the effect of carrier modulation in Ge on the MIM signals. Since the near-field interaction is highly dependent on the exact tip-sample contact condition, the simulation only serves as a qualitative guide to the experimental data. As shown in Figure 6.5(d), the MIM-Im signal, which is proportional to the tip-to-ground capacitance, rises monotonically with σ at the BTO/STO-Ge interface. On the other hand, the MIM-Re signal, which represents electrical loss within the probing volume, peaks at an intermediate σ_{Ge} (Supplementary Fig. 4). The higher MIM-Im and lower MIM-Re signals in the patterned square hence indicate a larger interfacial σ_{Ge} than that of the unwritten area. As elaborated below, the MIM data clearly corroborate the conclusion of DFT calculations and STEM images that the polarization of the as-grown BTO layer is pointing towards the underlying Ge substrate. This as-grown ferroelectric polarization partially depletes holes in the p-type Ge (left inset of Figure 6.5(d), giving rise to a lower interface conductivity than the bulk. After the BTO polarization is reversed by a sufficiently large negative tip bias, the energy bands drastically bend upwards (right inset of Figure 6.5(d)) and holes accumulate near the BTO/STO-Ge interface. As a result, σ_{Ge} is much enhanced at the heterojunction, leading to the observed MIM contrast. To the best our knowledge, this is the first demonstration of carrier density modulation in semiconductors due to ferroelectric switching.

6.3 Conclusion

In conclusion, the ferroelectric field effect is clearly demonstrated for highly crystalline *c*-axis-oriented $BaTiO_3$, epitaxially grown on Ge(100) substrates using molecular beam epitaxy via a thin (20 Å) $SrTiO_3$ buffer layer. The ferroelectric properties of the BTO layer and its effects on the underlying Ge are confirmed using piezoelectric force microscopy and microwave impedance microscopy. Results of electron microscopy and piezoelectric force microscopy in regard to the microscopic nature of the effect can be well understood within the atomistic picture provided by first principles theory. Our results open the possibility of realizing a ferroelectric FET, leading to new non-volatile memories and low-power devices.

6.4 Methods

6.4.1 Film Deposition

For film growth, *p*-type Ga-doped Ge(100) wafers from MTI Crystal Inc. (ρ = 0.05 Ωcm) that were diced into 10×10 mm^2 pieces are used as substrates. The samples are grown using a DCA M600 oxide MBE system with a base pressure of 3×10^{-10} Torr and equipped with reflection-high-energy electron diffraction (RHEED). Elemental Sr, Ba, and Ti are evaporated using effusion cells. Growth rates are calibrated using a quartz crystal monitor to correspond to a deposition rate of one monolayer per minute where a monolayer refers to the number of atoms per unit area in unreconstructed, ideal Ge(100) surface. Growth rates are fine-tuned using a combination of the appearance of reconstruction spots in RHEED.

Sample cleaning is performed by alternately dipping the sample in HCl and H_20_2 to remove surface contamination, prior to exposing the sample to oxygen plasma for 30 min at 300 W *in situ* [28]. After annealing the sample to remove the newly formed oxide layer from the Ge surface, a ½ monolayer of strontium is deposited at a temperature of 500°C. This critical Sr template prevents germanium from oxidizing during growth of the STO buffer. Five unit cells of STO are deposited onto this template, by shuttering Sr and Ti effusion cells at a molecular oxygen pressure of 5.0×10^{-7} Torr at 200°C. In order to crystallize STO, the temperature is then increased to 550°C (ramp rate: 30°C min^{-1}) and 600°C (ramp rate: 20°C min^{-1}). After crystallization, the oxygen pressure is raised to 5.0×10^{-6} Torr in order to co-deposit BTO on the STO/Ge template at a temperature of 650°C. BTO crystallizes immediately as deposited. After growing the desired BTO thickness, the sample is then cooled to room temperature (ramp rate: 10°C min^{-1}).

6.4.2 Electron Microscopy

The probe-corrected electron microscopy was performed using a JEOL ARM-200F (camera length: 6 cm; probe convergence angle: 20 mrad; annular-dark-field collection angle: 90~170 mrad) operated at 200 keV. Samples suitable for cross-section observation were prepared by standard mechanical polishing and dimpling, followed by argon-ion milling at ~2.5 keV to minimize surface amorphization.

6.4.3 Density functional theory

All calculations are done using density functional theory in the local density approximation using plane augmented-wave pseudopotentials as included in the VASP code [40-45]. We employ the Perdew-Zunger form of exchange-correlation potential [46]. We use the valence configuration $3p^6 4s^2 3d^2$ for titanium, $5s^2 5p^6 6s^2$ for barium, $2s^2 2p^4$ for oxygen, and $3d^{10} 4s^2 4p^2$ for germanium, $4s^2 4p^6 5s^2$ for strontium, and $2s^2 2p^1$ for boron, and a 600 eV kinetic energy cutoff. For the Brillouin zone integration, we use a Monkhorst-Pack [47] 6×3×1 mesh for the BTO/STO/Ge heterostructure. For the BTO/STO heterostructure, the lateral unit cell is 3.98 Å, which is 1/√2 times the calculated lattice constant of Ge (5.63 Å).

6.4.4 Band-Excitation Piezo Force Microscopy and Spectroscopy

Band-Excitation PFM and voltage spectroscopy are performed on a commercially available Asylum AFM platform (Cypher instrument) using PXI-based National Instruments data acquisition cards and in-house built software at CNMS, ORNL. Data analysis is performed on Matlab v2013b. The BE-PFM image is captured with a frequency bandwidth of 110 kHz centered at 385 kHz, with an applied AC voltage of 2.25 V to the tip at a scan rate of 1 Hz. The BEPS measurements are all carried out in the off-field state with a reading voltage of V_{AC} = 1.5 V.

6.4.5 Microwave Impedance Microscopy

The MIM in this work is based on a standard AFM platform (ParkAFM XE-70). The customized shielded cantilevers are commercially available from PrimeNano Inc. The excitation 1 GHz microwave signal is set at -20 dBm or 10 μW. The reflected signal carries the information of tip-sample admittance, which is detected by the electronics to form the imaginary (MIM-Im) and real (MIM-Re) parts of the MIM images. Details of the MIM electronics can be found in Ref. [37]. The finite-element analysis is performed using commercial software COMSOL4.3.

6.5 References

[1] J. Hoffman, X. Pan, J. W. Reiner, F. J. Walker, J. P. Han, C. H. Ahn, T. P. Ma., Adv. Mater. **22,** 2957-2961 (2010).

[2] R. A. McKee, F. J. Walker, M. F. Chisholm, Phys. Rev. Lett. **81,** 3014-3017 (1998).

[3] A. Lin, X. Hong, V. Wood, A. A. Verevkin, C. H. Ahn, R. A. McKee, F. J. Walker, E. D. Specht, Appl. Phys. Lett. **78**, 2034-2036 (2001).

[4] Niu, F. & Wessels, B. W. J. Vac. Sci. Technol. B **25**, 1053–1057 (2007).

[5] V. Vaithyanathan, J. Lettieri, W. Tian, A. Sharan, A. Vasudevarao, Y. L. Li, A. Kochhar, H. Ma, J. Levy, P. Zschack, J. C. Woicik, L. Q. Chen, V. Gopalan, D. G. Schlom, J. Appl. Phys. **100,** 024108-024109 (2006).

[6] G. Niu, S. Yin, G. Saint-Girons, B. Gautier, P. Lecoeur, V. Pillard, G. Hollinger, B. Vilquin, Microelectron. Eng. **88**, 1232–1235 (2011).

[7] C. Dubourdieu, J. Bruley, T. M. Arruda, A. Posadas, J. Jordan-Sweet, M. M. Frank, E. Cartier, D. J. Frank,S. V.Kalinin, A. A. Demkov, V. Narayanan, Nat. Nanotechnol. **8,** 748-754 (2013).

[8] I. P. Batra, P. Wurfel, B. D. Silverman, Phys. Rev. B **8**, 3257-3265 (1973).

[9] D. Ito, N. Fujimura, T. Yoshimura, T. Ito, J. Appl. Phys. **93**, 5563–5567 (2003).

[10] Z. Yu, J. Ramdani, J. A. Curless, C. D. Overgaard, J. M. Finder, R. Droopad, K. W. Eisenbeiser, J. A. Hallmark, W. J. Ooms, V. S. Kaushik. J. Vac. Sci. Technol. B **18**, 2139-2145 (2000).

[11] R. A. McKee, F. J. Walker, J. R. Conner, E. D. Specht, D. E. Zelmon, Appl. Phys. Lett. **59**, 782-784 (1991).

[12] M.-B. Lee, M. Kawasaki, M. Yoshimoto, H. Koinuma, Appl. Phys. Lett. **66**, 1331-1333 (1995).

[13] M. P. Warusawithana, C. Cen, C. R. Sleasman, J. C. Woicik, Y. Li, L. F. Kourkoutis, J. A. Klug, H. Li, P. Ryan, L.-P. Wang, M. Bedzyk, D. A. Muller, L.-Q. Chen, J. Levy, D. G. Schlom, Science **324**, 367-370 (2009).

[14] R. Pillarisetty, Nature **479**, 324-328 (2011).

[15] G. Scappucci, O. Warschkow, G. Capellini, W. M. Klesse, D. R. McKenzie, M. Y. Simmons, Phys. Rev. Lett. **109**, 076101 (2012).

[16] S. Paleari, S. Baldovino, A. Molle, M. Fanciulli, Phys. Rev. Lett. **110**, 206101 (2013).

[17] K. C. Saraswat, C. O. Chui, T. Krishnamohan, A. Nayfeh, P. McIntyre, Microelec. Eng. **80**, 15-21 (2005).

[18] R. A. McKee, F. J. Walker, M. F. Chisholm, Science **293,** 468-471 (2001).

[19] C. Merckling, G. Saint-Girons, C. Botella, G. Hollinger, Marc Heyns, J. Dekoster, M. Caymax, Appl. Phys. Lett. **98**, 092901 (2011).

[20] J. H. Ngai, D. P. Kumah, C. H. Ahn, F. J. Walker, Appl. Phys. Lett. **104**, 062905 (2014).

[21] K. D. Fredrickson, P. Ponath, A. B. Posadas, M. R. McCartney, T. Aoki, D. J. Smith, A. A. Demkov, Appl. Phys. Lett. **104**, 242908 (2013).

[22] M. D. McDaniel, T. Q. Ngo, A. Posadas, C. Hu, S. Lu, D. J. Smith, E. T. Yu, A. A. Demkov, J. G. Ekerdt, Adv. Mater. Interfaces **1**, 1400081 (2014).

[23] W. Huang, Z. P. Wu, J. H. Hao, Appl. Phys. Lett. **94,** 032905 (2009).

[24] R. Contreras-Guerrero, J. P. Veazey, J. Levy, R. Droopad, Appl. Phys. Lett. **102**, 012907 (2013).

[25] J. B. Neaton, K. M. Rabe, Appl. Phys. Lett. **82**, 1586-1588 (2003).

[26] U. Diebold, Surf. Sci. Rep. **48,** 53-229 (2003).

[27] K. D. Fredrickson, A. B. Posadas, A. A. Demkov, C. Dubourdieu, J. Bruley, J. Appl. Phys. 113, 184102 (2013).

[28] P. Ponath, A. B. Posadas, R. C. Hatch, A. A. Demkov, J. Vac. Sc. Technol. B **31**, 031201 (2013).

[29] S. Jesse, S. V. Kalinin, R. Proksch, A. P. Baddorf, B. J. Rodriguez, Nanotechnology **18**, 435503 (2007).

[30] S. Jesse, A. Kumar, S. V. Kalinin, A. Gannepali, R. Proksch, R. Microscopy Today **18**, 34-40 (2010).

[31] S. Jesse, A. P. Baddorf, S. V. Kalinin, Appl. Phys. Lett. **88**, 062908 (2006).

[32] A. Tselev, N. V. Lavrik, A. Kolmakov, S. V. Kalinin, Advanced Functional Materials **23,** 2635 (2013).

[33] S. M. Anlage, V. V. Talanov, A. R. Schwartz, *Scanning Probe Microscopy: Electrical and Electromechanical Phenomena at the Nanoscale*, pp. 207–245 (Springer, New York, 2006).

[34] S. M. Anlage, D. E. Steinhauer, B. J. Feenstra, C. P. Vlahacos, F. C. Wellstood, *Microwave Superconductivity*, pp. 239–269 (Kluwer Academic Publishers, Amsterdam, 2001).

[35] X. D. Xiang, C. Gao, Mater. Charact. **48**, 117-125 (2002).

[36] B. T. Rosner. D. W. van derWeide, Rev. Sci. Instrum. **73**, 2505-2525 (2002).

[37] K. Lai, W. Kundhikanjana, M. Kelly, Z. X. Shen, Rev. Sci. Instrum. **79**, 063703 (2008).

[38] K. Lai, W. Kundhikanjana, M. Kelly, Z. X. Shen, Appl. Nanosci. **1**, 13-18 (2011).

[39] Y. Yang, K. Lai, Q. Tang, W. Kundhikanjana, M. A. Kelly, K. Zhang, Z.-X. Shen, X. Li. J. Micromech. Microeng. **22**, 115040 (2012).

[40] G. Kresse, J. Hafner, Phys. Rev. B, **47**, 558-561 (1993).

[41] G. Kresse, J. Hafner, Phys. Rev. B, **49**, 14251-14271 (1994).

[42] G. Kresse, J. Furthmüller, Comput. Mat. Sci. **6**, 15-50 (1996).

[43] G. Kresse, J. Furthmüller, J. Phys. Rev. B **54**, 11169-11186 (1996).

[44] P. E. Blöchl, Phys. Rev. B, **50**, 17953-17979 (1994).

[45] G. Kresse, D. Joubert, Phys. Rev. B **59**, 1758-1775 (1999).

[46] J. P. Perdew A. Zunger, Phys. Rev. B **23**, 5048-5079 (1981).

[47] H. J. Monkhorst, J. D. Pack, Phys. Rev. B **13**, 5188-5192 (1976).

Chapter 7. Monolithic integration of nanoscale $BaTiO_3$ MOSCAPs on Ge wafers

Titanates exhibit electronic properties highly desirable for field effect transistors such as very high permittivity and ferroelectricity. However, the difficulty of chemically etching titanates hinders their commercial use in device manufacturing. Here, we report the selective area *in finestra* growth of highly crystalline $BaTiO_3$ within photolithographically defined openings of a sacrificial SiO_2 layer on a Ge (001) wafer by molecular beam epitaxy. After the $BaTiO_3$ deposition, the sacrificial SiO_2 can be etched away, revealing isolated nanoscale gate stacks circumventing the need to etch the titanate thin film. Reflection high-energy electron diffraction in conjunction with scanning electron microscopy is carried out to confirm the crystallinity of the samples. X-ray diffraction is performed to determine the out-of-plane lattice constant and crystal quality of the BTO film. Electrical measurements are performed on electrically isolated Pt/$BaTiO_3$/$SrTiO_3$/Ge capacitor devices.

This work is done in collaboration with *Patrick Ponath, Agham Posadas, Michael Schmidt, Anne-Marie Kelleher, Mary White, Dan O'Connell, Paul Hurley, Ray Duffy, Alexander A. Demkov* and is unpublished so far.

7.1 Introduction

Titanates are an important class of materials that possess many interesting functional properties, i.e. ferroelectricity (BTO, PZT) [1,2], large dielectric constant ($CaTiO_3$, BTO, STO, BSTO) [3-8], and high Pockels coefficient (BTO) [9-13]. A wide variety of

applications exist for them, such as non-volatile memory [14,15], microwave device applications (BSTO) [16-18], and waveguides [10, 19-22]. Due to their very high dielectric constants and added functional behavior such as ferroelectricity and piezoelectricity [23-25], titanates could replace SiO_2 and even high-κ dielectrics like HfO_2 in the future as gate dielectrics in MOSFET devices [26-28]. However, practically all microelectronic device manufacturing is based on the ability to pattern such materials using some form of etching. The main problem in fabricating titanate-based devices on a sub-micron level is the lack of an easy way to etch and pattern this class of materials. Selective wet chemical etching of titanates is not available and even non-selective reactive ion etching is not suitable because it is extremely slow and degrades not only the quality of the titanate layer, but more importantly, the quality of the surrounding device areas as well. This "invulnerability" of titanates hinders their commercial use in device manufacturing. If one could find a way to pattern and integrate them into existing semiconductor processes, they could lead to great improvements in existing electronic devices such as microprocessors or new kinds of integrated architecture combining optical or sensor functionality and logic/memory on a single chip.

These problems can be circumvented by growing titanates as a gate-last process into openings of pre-deposited sacrificial layers of SiO_2 that then can be easily and selectively etched away. By depositing the titanate last on a pre-patterned sacrificial layer, and then by etching away this sacrificial SiO_2 layer, the need to selectively etch the titanate layer to fabricate devices is no longer necessary. Here, we report the growth of out of-plane polarized $BaTiO_3$ (BTO) on germanium by molecular beam epitaxy (MBE) within

microscopically patterned openings (*in finestra*) of a sacrificial SiO_2 layer on a Ge(001) substrate. A thin template layer of $SrTiO_3$ (STO) is grown on the Ge substrate to impose compressive strain on BTO which leads to an out of-plane polarization of BTO [29,30], followed by Pt metal deposition as a top electrode. Isolated Pt/BTO/STO/Ge capacitor structures are then formed by removing the SiO_2 pattern using buffered oxide etch (BOE). In order to evaluate the electrical performance of the stack, C-V and I-V measurements are performed. The technique described here is a method by which titanium oxides and titanates can be readily patterned into desired shapes and sizes down to the nanoscale by using a combination of existing processing techniques without the need to etch the titanate itself. This will allow titanates to be used in nanoscale devices, such as a super high-k gate dielectric material in capacitors and MOSFET devices.

7.2 Experimental details

Ge (001) wafers (p-type, 0.059 - 0.088 Ωcm) are first degreased with acetone and isopropyl alcohol and then wet chemical cleaned in an automated Spray acid tool. For a typically lift off experiment, a patterned bilevel photoresist profile is generally used, however, due to the higher growth temperature of MBE grown films, this is not an option for this work. In this case the lift off profile is achieved by the deposition of a two layer system (i) a PECVD silicon dioxide layer (200 nm or 500 nm) followed by (ii) a polycrystalline layer of silicon (100 nm). Openings in these layers are patterned using standard optical photoresist and UV lithography. The patterned openings are transferred through the polysilicon layer using a plasma etch process and the lift off profile is

realized by using a buffered oxide etchant (5:1) at room temperature to etch the underlying oxide layer to both expose the germanium in the openings and also to etch laterally under the defined polysilicon edge to create an overhang which is the desired profile for lift off. A schematic image of the final SiO_2 pattern on the germanium wafer is shown in Figure 1.

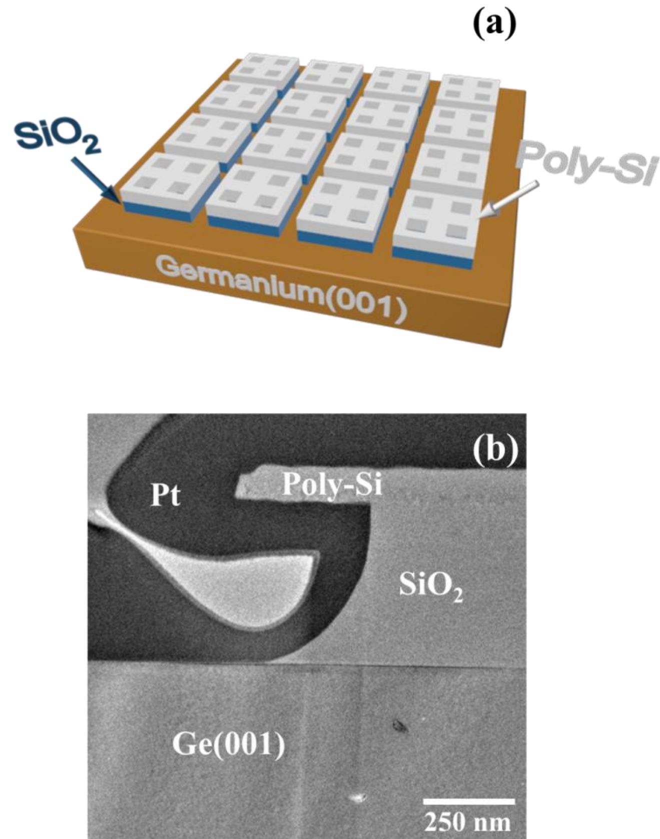

Figure 7.1: (a) Schematic of the lithographically defined polycrystalline Si overhang (white, 100 nm) and SiO_2 pattern (blue, 500 nm) on the p-type Ge wafer (brown). (b) Cross-sectional TEM image of the poly-Si/SiO_2/Ge structure. After the thin film and top gate deposition, the sacrificial SiO_2 can be lifted off by chemical etching, revealing nanoscale gate capacitor devices of 80×80 μm^2.

Prior to BTO growth, the patterned Ge wafer is diced into 10×10 mm^2 pieces. For the BTO thin film deposition, a customized DCA Instruments M600 MBE chamber with a base pressure of 3.0×10^{-10} torr is used. Ba, Sr, and Ti are evaporated using Knudsen effusion cells while an electron beam evaporation source is used for Pt. A quartz crystal monitor is used to calibrate the metal

deposition rate. Reflection high-energy electron diffraction (RHEED) from Staib Instruments with an electron energy of 21 keV and a grazing angle of 3° is used to monitor the crystal growth and surface quality. All samples are analyzed by x-ray photoelectron spectroscopy (XPS) using a VG Scienta custom analysis chamber with an R3000 electron energy analyzer and monochromated Al Kα radiation to fine tune the exact stoichiometry of the BTO and STO films. The MBE chamber is connected to the XPS through a vacuum buffer line to allow *in situ* sample transfer without breaking the vacuum. X-ray diffraction measurements are performed using a Rigaku Ultima IV diffractometer with a Cu Kα radiation source. The microstructure of the fabricated samples is analyzed by top–down scanning electron microscopy (SEM), which was performed on an FEI 650 FEG SEM. Cross-sectional Transmission Electron Microscopy (XTEM) was carried out using the JEOL 2100 HRTEM operated at 200 kV. Cross-section samples were obtained by using FEI's Dual Beam Helios Nanolab system. For electrical characterization the KEITHLEY 37100 and KEITHLEY 2602 are used.

Before loading the samples into the UHV system, the Ge substrates are degreased in acetone, isopropanol and de-ionized water for 10 min each using a sonicator. The samples are then transferred into the MBE where they are exposed to oxygen plasma for 30 min at 100°C, completely removing carbon contamination from the Ge surface. The plasma exposure also forms a thin oxide layer on the Ge surface, which has to be removed through a final vacuum anneal for 1 h at 750°C to obtain an atomically clean, 2 × 1 reconstructed Ge surface. The sharp and intense half ordered spots of the cleaned Ge surface can be clearly seen in Figure 2(a). The details of the Ge cleaning procedure used

can be found elsewhere [31]. It should be noted that unlike the Ge cleaning procedure described in Ref. [31], it is found in this case that a wet-etching step prior to the oxygen plasma cleaning is not critical in obtaining the same Ge surface quality [32].

After the final annealing step at 750°C, ½ monolayer of Ba is deposited at 200°C to form a Zintl template [33-37]. This template prevents Ge from forming germanium oxides during the growth of the STO buffer layer. 2 nm of STO are then grown by co-deposition of Sr and Ti on this Zintl template at 200°C using 5×10^{-7} torr molecular oxygen. This thin STO layer is needed to impose compressive strain on BTO to achieve an out of-plane polarization [29]. Increasing the substrate temperature to 750°C with a ramp rate of 30°C/min crystallizes the STO film, as can be seen in Figure 2(b). The narrow streaks are typical for epitaxial and smooth crystalline STO films [29]. The molecular oxygen pressure is then increased to 5×10^{-6} torr and 16 nm of BTO is deposited on the STO/Ge template at

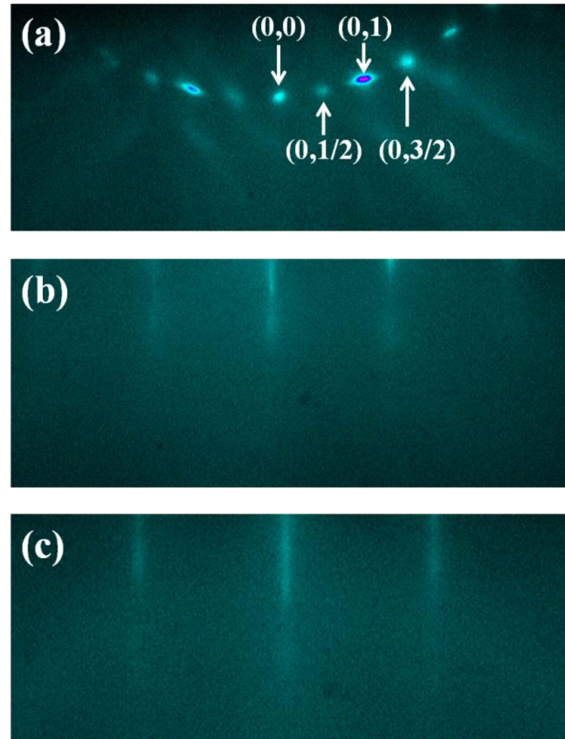

Figure 7.2: (a) 2 × 1 reconstructed Ge surface after oxygen plasma exposure followed by a thermal anneal at 750°C. (b) 2 nm thick STO on Ge(001) viewed along the [110] direction. (c) 16 nm of crystalline BTO grown on top of the STO/Ge viewed along the [110] direction.

750°C, by shuttering the Ba and Ti effusions cells. At this temperature BTO crystallizes as deposited, as observed by RHEED (see Figure 2(c)). When the desired film thickness is reached, the sample is cooled down to 200°C with a ramp rate of 30°C/min in an oxygen environment of 5×10^{-6} torr. Immediately after growth, the sample is transferred in vacuum into the XPS to verify the correct stoichiometry of the grown films. The samples are then transferred back into the MBE chamber where at least 10 nm of Pt is deposited at a substrate temperature of 100°C with a growth rate of around 1 Å/min using electron beam evaporation. After a sufficiently thick layer of Pt is deposited *in situ*, the sample is taken out of the vacuum system and additional Pt is sputtered on top *ex situ.* 100 nm of Pt is added by evaporation to make a top contact thick enough so it can be probed by the needles during electrical characterization without punching though to the substrate.

7.3 Materials Characterization

7.3.1 Reflection high-energy electron diffraction (RHEED)

A major MBE-growth-problem that arises when a substrate is almost completely covered with a sacrificial layer with only a few small openings to allow crystalline growth, is the very weak RHEED signal. The ratio between the amorphous SiO_2 layer covering most of the Ge substrate and the small areas of crystalline film is too small to obtain even qualitative RHEED information about the crystal quality. Due to the grazing angle of incidence of about 3° in RHEED, the aspect ratio of the SiO_2 openings (wall height and width) must also be considered, if one uses the RHEED signal coming from the

crystalline films within the openings. To work around this issue, the sacrificial SiO_2 is lithographically patterned in such a way that it forms islands of SiO_2 on the Ge surface with 4 openings inside them (see Figure 1). This results in the presence of relatively large areas of exposed Ge. By having a large area of the Ge substrate not covered by SiO_2, BTO not only crystallizes in the small openings inside the SiO_2 window, but also on the exposed areas between the SiO_2 islands. With this setup, a high coverage of crystalline BTO on Ge is obtained leading to a strong RHEED signal allowing one to control and monitor the crystal quality of the deposited BTO film.

7.3.2 X-Ray diffraction (XRD)

To determine the out of-plane lattice constant and overall crystal quality, X-ray diffraction measurements are performed. A symmetric 2θ-θ scan of a 16 nm thick BTO film on the STO/Ge template is shown in Figure 3 plotted on a log scale. Only peaks from single orientations of BTO, STO and the Ge substrate are observed. Typical high resolution scans around the BTO (002) peak indicate an out of-plane lattice constant between 4.03 and 4.05 Å, corresponding to the longer *c*-axis being out of plane and the shorter *a*-axis to be in-plane. Due to the direction of the long axis being out of plane, this implies that the BTO ferroelectric polarization points normal to the Ge surface [29]. Rocking curve scans around the BTO (002) Bragg peak reveal FWHM values lying in the range of 0.5–1.0° (see Figure 3 inset).

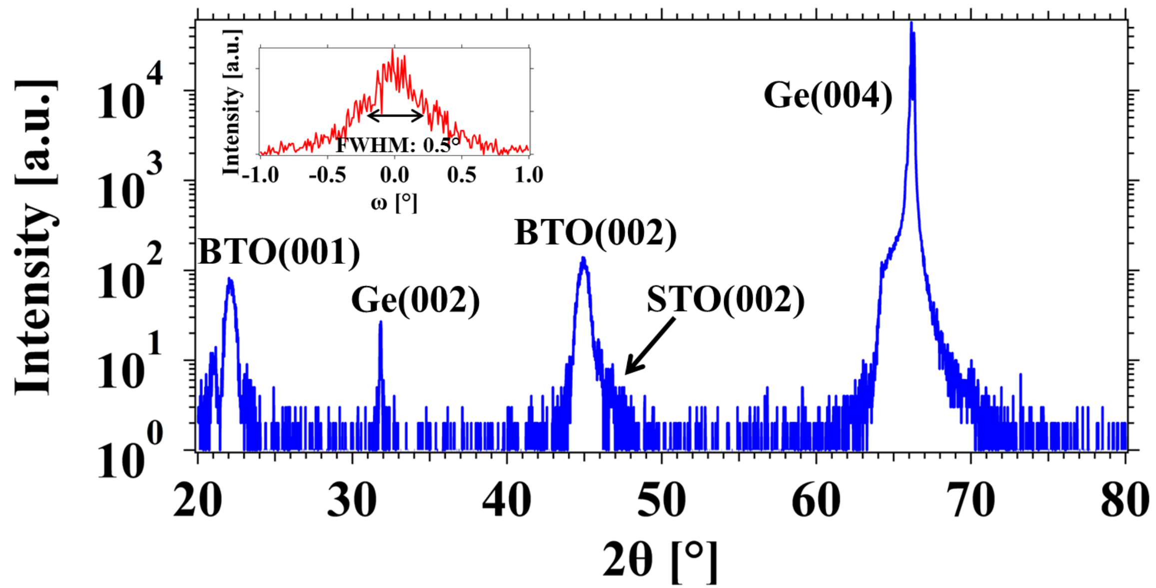

Figure 7.3: 2θ-θ scan of a 16 nm thick BTO film grown epitaxially on 2 nm STO on Ge(001). Only peaks from Ge, STO and BTO are observed. The *c* lattice parameter of BTO is between 4.03 and 4.05 Å and is directed out of plane. The inset shows the rocking curve around the BTO (002) peak for the same film with a FWHM value of 0.5°.

7.3.3 TEM and SEM

Figure 4 (a) shows a cross sectional transmission electron microscope (TEM) image of the deposited BTO film on the sacrificial poly-Si/SiO_2 structure on Ge. The polycrystalline Si overhang layer, preventing thin film deposition on the SiO_2 layer, can be removed using BOE. The crystal quality of the BTO and STO layer grown in an opening, as well as on the larger exposed germanium areas, is confirmed using cross-sectional TEM (Figure 4(b)). The absence of an amorphous GeO_2 layer between the STO and Ge substrate is confirmed and expected due to the use of a Zintl template. Both STO and BTO layers are highly crystalline with sharp interfaces between the different layers.

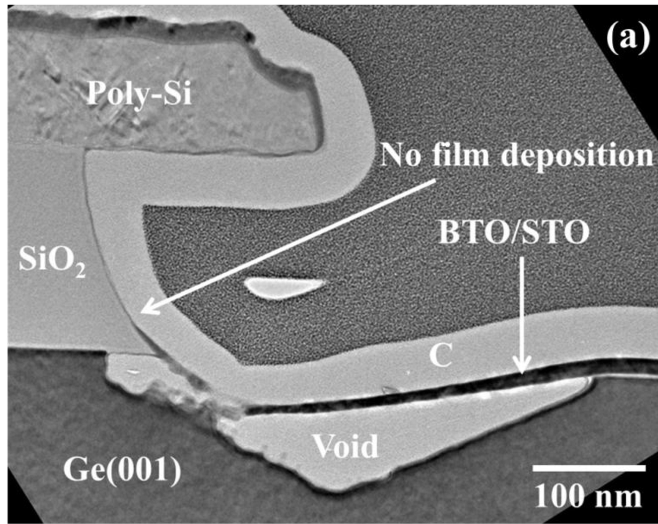

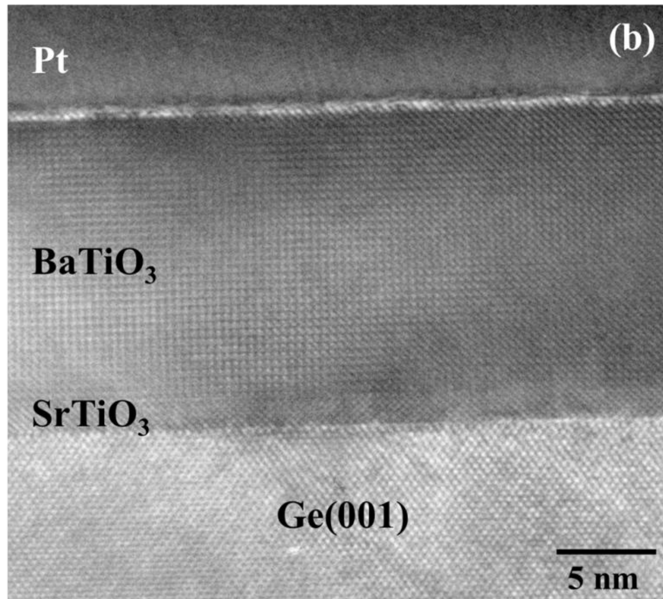

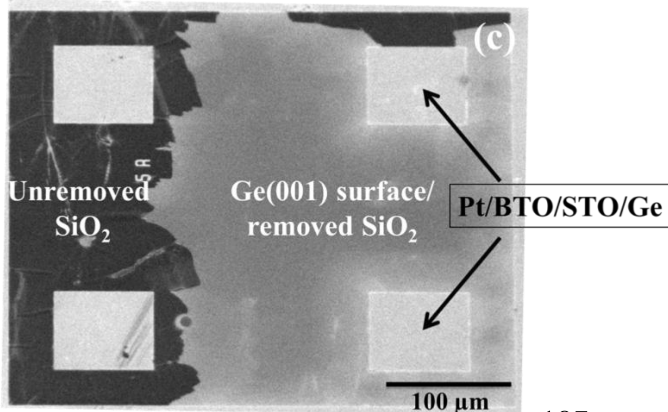

Figure 7.4: (a) Representative XTEM image of the structure shown schematically in Figure 1. The polycrystalline-Si overhang prevents film deposition on the sacrificial SiO_2 layer, allowing its removal with BOE. (b) XTEM confirming the crystal quality of the BTO and STO layer grown on the exposed Ge areas. Both STO and BTO layers are highly crystalline with sharp interfaces between the different layers. Both oxide layers show highly uniform growth in conjunction with a very low surface roughness, (c) top-view SEM image showing the test structure after the BOE etch, revealing patterned Pt/BTO/STO/Ge capacitor devices.

Both oxide layers show highly uniform growth in conjunction with a very low surface roughness. To form electrically isolated Pt/BTO/STO/Ge MOSCAP structures, the sacrificial SiO_2 layer is removed using BOE which also leads to the removal of the polycrystalline-Si layer on top of SiO_2. As can be seen in Figure 4(c), isolated square patterned Pt/BTO/STO/Ge MOSCAPs are revealed in areas where the SiO_2 layer is removed. Current vs. voltage measurements reveal a relative high leakage current through the BTO/STO/Ge gate precluding meaningful capacitance measurements. It is well-known that thin (<100 nm) MBE-grown BTO films are leaky as-grown because of incomplete oxygenation [38]. Furthermore, the conduction band offset between BTO/STO and Ge is nearly zero further adding to the leakage [39]. Further studies are ongoing to substantially reduce this leakage including growth in oxygen plasma, wet oxygen post-deposition annealing, Al doping, and N doping.

The SEM and TEM image confirm that the method of using a sacrificial oxide with openings can indeed be used to grow crystalline titanate films in small openings, and that the capacitor stacks can be revealed by means of a subsequent lift-off process.

7.4 Conclusions

In summary, we report the growth of highly crystalline *c*-axis oriented BTO in the photolithographically patterned openings of sacrificial SiO_2 (*in finestra*) on a germanium (001) wafer by molecular beam epitaxy. RHEED, XRD, SEM and TEM are performed to confirm the high crystal quality of the BTO film within the openings. Buffered oxide etch is then used to electrically isolate a given device from the rest of the film to perform

electrical measurements. Current vs voltage measurements reveal a relative high leakage current through the BTO/STO/Ge gate precluding meaningful capacitance measurements. This selective area deposition in conjunction with a general lift off process can be used to create nanoscale titanate capacitor structures, circumventing the problem of having to etch titanate materials. Such a process can ultimately be refined for the fabrication of titanate-based three-terminal devices.

Acknowledgements

The work is supported by the Air Force Office of Scientific Research under grants FA9550-14-1-0090 and FA9550-12-10494. We thank Kurt Fredrickson for useful discussions.

7.6 REFERENCES

[1] S. Mathews, R. Ramesh, T. Venkatesan, J. Benedetto, Science **11**, 238 (1997).

[2] A. von Hippel, Rev. Mod. Phys. **22**, 221 (1950).

[3] D. Fuchs, C. W. Schneider, R. Schneider, H. Rietschel, J. Appl. Phys. **85**, 7362 (1999).

[4] H. Tabata, H. Tanaka, T. Kawai, J. Appl. Phys. **65**, 1970 (1994).

[5] B. H. Hoerman, G. M. Ford, L. D. Kaufmann, B. W. Wessels, Appl. Phys. Lett. **73**, 2248 (1998).

[6] A. Kersch, D. Fischer, J. Appl. Phys. **106**, 014105 (2009).

[7] A. Linz, Jr., K. Herrington, Crystal, J. Chem. Phys. **28**, 824, (1958).

[8] A. Outzourhit, J. U. Trefny, T. Kito, B. Yarar, A. Naziripour, A. M. Hermann, Thin Solid Films, **259** , 218 (1995).

[9] D. Khatib, P. Jullien, B. Jannot, Ferroelectrics **145**, 181 (1993).

[10] S. Abel, T. Stoferle, C. Marchiori, C. Rossel, M. D. Rossell, R. Erni, D. Caimi, M. Sousa, A. Chelnokov, B. J. Offrein, J. Fompeyrine, Nat. Commun. **4**, 1671 (2013).

[11] K. Uchiyama, A. Kasamatsu, Y. Otani, T. Shiosaki, Jpn. J. Appl. Phys. **46**, 244 (2007).

[12] K. J. Kormondy, S. Abel, F. Fallegger, Y. Popoff, P. Ponath, A. B. Posadas, M. Sousa, D. Caimi, H. Siegwart, E. Uccelli, L. Czornomaz, C. Marchiori, J. Fompeyrine, A. A. Demkov, Microelectronic Eng. **147**, 215 (2015).

[13] K. J. Kormondy, Y. Popoff, M. Sousa, F. Eltes, D. Caimi, M. D. Rossell, M. Fiebig, P. Hoffmann, C. Marchiori, M. Reinke, M. Trassin, A. A. Demkov, J. Fompeyrine, S. Abel, Nanotechnology **28**, 075706 (2017).

[14] B. H. Park, B. S. Kang, S. D. Bu, T. W. Noh, J. Lee, W. Jo, Nature **401**, 682 (1999).

[15] R. Ramesh, S. Aggarwal, O. Auciello, Mater. Sci. Eng.: R: Report **32**, 191 (2001).

[16] W. Chang, J. S. Horwitz, A. C. Carter, J. M. Pond, Steven W. Kirchoefer, C. M. Gilmore, D. B. Chrisey, Appl. Phys. Lett. **74**, 1033 (1999).

[17] E. J. Cucauskas, S. W. Kirchoefer, W. J. DeSisto, J. M. Pond, Appl. Phys. Lett. **74**, 4034 (1999).

[18] J. Xu, W. Menesklou, E. Ivers-Tiffée, J. Eur. Ceram. Soc. **24**, 1735 (2004).

[19] B. W. Wessel, J. Cryst. Growth **195**, 706 (1998).

[20] Z. Liu, P.-T. Lin, B. W. Wessels, Appl. Phys. Lett. **90**, 201104 (2007).

[21] B. W. Wessels, Annu. Rev. Mater. Res. **37**, 659 (2007).

[22] C. Xiong, W. H. P. Pernice, J. H. Ngai, J. W. Reiner, D. Kumah, F. J. Walker, C. H. Ahn, H. X. Tang, Nano Lett. **14**, 1419 (2014).

[23] R. Guo, L. E. Cross, S-E. Park, B. Noheda, D. E. Cox, G. Shirane, Phys Rev. Lett. **84**, 5423 (2000).

[24] I. Kanno, S. Fujii, T. Kamada, R. Takayama, Appl. Phys. Lett. **70**, 1378-1380 (1997).

[25] B. Jaffe, W. R. Cook Jr., H. Jaffe, *Piezoelectric Ceramics*, (Academic press London and New York, 1971).

[26] Z. Yu, J. Ramdani, J. A. Curless, C. D. Overgaard, J. M. Finder, R. Droopad, K. W. Eisenbeiser, J. A. Hallmark, W. J. Ooms, V. S. Kaushik, J. Vac. Sci. Technol. B **18**, 2139 (2000).

[27] K. Eisenbeiser, J. M. Finder, Z. Yu, J. Ramdani, J. A. Curless, J. A. Hallmark, R. Droopad, W. J. Ooms, L. Salem, S. Bradshaw, C. D. Overgaard, Appl. Phys. Lett. **76**, 1324 (2000).

[28] H. Huff, David Gilmer, *High Dielectric Constant Materials: VLSI MOSFET Applications*, (Springer-Verlag, Berlin and Heidelberg, 2005).

[29] P. Ponath, K. Fredrickson, A. B. Posadas, Y. Ren, X. Wu, R. K. Vasudevan, M. B. Okatan, S. Jesse, T. Aoki, M. R. McCartney, D. J. Smith, S. V. Kalinin, K. Lai, A. A. Demkov, Nat. Commun. **6**, 6067 (2015).

[30] C. Dubourdieu, J. Bruley, T. M. Arruda, A. Posadas, J. Jordan-Sweet, M. M. Frank, E. Cartier, D. J. Frank, S. V. Kalinin, A. A. Demkov, V. Narayanan, Nat. Nanotechnol. **8**, 748 (2013).

[31] P. Ponath, A. B. Posadas, R. C. Hatch, A. A. Demkov, J. Vac. Sc. Technol. B **31**, 031201 (2013).

[32] P. Ponath, A. B. Posadas, A. A. Demkov, Appl. Phys. Rev. **4**, 021308 (2017).

[33] A. A. Demkov, H. Seo, X. Zhang, J. Ramdani, Appl. Phys. Lett. **100**, 071602 (2012).

[34] M. Choi, A. B. Posadas, H. Seo, R. C. Hatch, A. A. Demkov, Appl. Phys. Lett. **102**, 031604 (2013).

[35] H. Seo, M. Choi, A. B. Posadas, R. C. Hatch, A. A. Demkov, J. Vac. Sci. Technol. B **31**, 04D107 (2013).

[36] K. D. Fredrickson, H. Seo, A. A. Demkov, J. Appl. Phys. **120**, 065301 (2016).

[37] S. Hu, E. Lin, A. Hamze, A. B. Posadas, H. W. Wu, D. J. Smith, A. A. Demkov, J. G. Ekerdt, J. Chem. Phys. **146**, 052817 (2017).

[38] G. Niu, B. Gautier, S. Yin, G. Saint-Girons, P. Lecoeur, V. Pillard, G. Hollinger, B. Vilquin, Thin Solid Films **259**, 218 (1995).

[39] L. Kornblum, M. D. Morales-Acosta, E. N. Jin, C. H. Ahn, F. J. Walker, Adv. Mater. Interfaces **2**, 1500193 (2015).

Chapter 8. Contradictory nature of Co-doping in ferroelectric $BaTiO_3$

The growth of Co-substituted $BaTiO_3$ (BTO) films on Ge(001) substrates by molecular beam epitaxy is demonstrated. Energy-dispersive x-ray spectroscopy and transmission electron microscopy images confirm the uniform Co distribution. However, no evidence of magnetic ordering is observed in samples grown for Co concentrations between 2% and 40%. Piezoresponse force microscopy measurements show that a 5% Co-substituted BTO sample exhibits ferroelectric behavior. First-principles calculations indicate that while Co atoms couple ferromagnetically in the absence of oxygen vacancies, the occurrence of oxygen vacancies leads to locally antiferromagnetically coupled complexes with relatively strong spin coupling. The presence of a significant amount of oxygen vacancies is suggested by x-ray photoelectron spectroscopy measurements.

This work was published in Patrick Ponath, Andrew O'Hara, Hai-Xia Cao, Agham B. Posadas, Rama Vasudevan, M. Baris Okatan, S. Jesse, Morgann Berg, Zongyao Li, Desai Zhang, Andrew J. Kellock, Alex de Lozanne, Jianshi Zhou, Sergei Kalinin, David J. Smith, and Alexander A. Demkov, Phys. Rev. B ***94****, 205121 (2016).*

8.1 Introduction

Multiferroics are materials which simultaneously exhibit at least two of the four primary ferroic orders. However, the current focus of materials research for device development is mainly in the coexistence of ferroelectricity and ferromagnetism [1]. If both of these ferroic orders couple strongly then the electric polarization can be controlled by applying an external magnetic field or vice versa. This coupling could pave the way for new technologies and devices, since multiferroic materials could potentially lead to novel spin-based [2-4] or nonvolatile data-storage devices [5,6], where information is written electrically and read magnetically. Magnetism and ferroelectricity rarely coexist in single-phase compounds [7,8], and most multiferroics possess low magnetic ordering temperatures [5] even if the ferroelectric transition temperatures are above room temperature [9-11]. If ferroelectricity and ferromagnetism are both present in one material, their coupling, which is necessary for device applications, is not guaranteed [12,13]. Most ferroelectric materials are transition-metal oxides in which the transition-metal atoms possess an empty *d* shell, whereas partially filled *d* shells with unpaired spins are required for ferromagnetism [7].

Two well-known multiferroic materials, crystallizing in a distorted perovskite crystal structure (ABO_3), are $BiMnO_3$ and $BiFeO_3$ [13-16]. In both materials, ferroelectricity is caused by the active 6*s* lone pair of Bi, while in other ferroelectrics such as $BaTiO_3$ (BTO) the shift of the B atom with respect to the oxygen sublattice causes electric polarization. Due to the fact that ferromagnetism in both $BiMnO_3$ and $BiFeO_3$ is caused by the B-site atom, while ferroelectricity is realized by the displacement of the Bi ion,

coupling between the two ferroic orders is weak [13]. Another promising multiferroic material is magnetically doped compositions of the well-studied ferroelectric $BaTiO_3$. *Ab initio* calculations predict that Cr-, Mn-, and Fe-doped BTO are the most promising candidates for ferromagnetism in the transition-metal-doped $BaTi_{1-x}TM_xO_3$ system (TM = Sc, V, Cr, Mn, Fe, Co, Ni, Cu) [17-19]. In the early theoretical work of Nakayama *et al.* [17], only cubic BTO was considered with no additional correlation effects on top of the local spin density approximation, and the formation of oxygen vacancies and their influence on the formation of ferromagnetism was not considered. Several groups have tried to synthesize multiferroic BTO by replacing Ti with Fe [20-27] and Co [28-31]. Maier *et al.* were the first to show ferroelectricity and ferrimagnetism [20] in Fe-doped BTO. More recently, Rajamani *et al.* [21] and Xu *et al.* [24] showed ferromagnetism at room temperature in Fe-doped BTO samples. For Co-doped BTO, ferromagnetism at room temperature was shown by Lee *et al.* [29] and Lin *et al.* [30], but the existence of ferroelectricity in their samples was not addressed.

Integrating functional oxides with semiconductors offers an avenue for creating hybrid structures where one combines or even couples rich physical effects in TM oxides with electrically superior semiconductor materials [32]. In particular, integrating a magnet on a semiconductor has exciting applications in spintronics [33-37]. Room temperature ferromagnetism can be stabilized in Co-doped STO [37] and, using first principles calculations, can be traced to a subtle interaction between the dopant and oxygen vacancies that provide a self-compensation mechanism [38] Though it is possible to induce ferroelectricity in STO by epitaxial strain [39], one can hope that magnetic order

can be coupled to the electric one in Co-doped BTO. Integration of BTO on Si using MBE presents certain challenges, and particularly an SiO_2 interlayer forms separating the active oxide from the semiconductor [40]. One can avoid the interlayer formation by using a low temperature chemical route of deposition [41, 42] or by switching to Ge, where oxidation is less of a problem [43]. The approach presents a different challenge, as oxygen vacancies have been shown detrimental to ferroelectricity [44-46], but is definitely worth pursuing.

In this work, we demonstrate the epitaxial integration of Co-substituted BTO grown by molecular beam epitaxy (MBE) on Ge (001) substrates. Ferroelectricity is exhibited by a 5% Co-substituted BTO film, but no sign of magnetic ordering is observed, independent of Co concentration up to 40%. A limited set of first-principles calculations is performed to explore the possible role of oxygen vacancies in the magnetic ordering in $BaTi_{1-x}Co_xO_3$ (BTCO). The results suggest that the presence of oxygen vacancies in BTCO can quench ferromagnetism by creating locally antiferromagnetically coupled pairs of Co atoms that exhibit no net magnetic moment.

8.2 Experimental Details

In this study, Ga-doped germanium (001) wafers (0.019 Ω-cm) that are diced into 10 × 10 mm^2 squares and 5 × 5 mm^2 square single-crystalline $SrTiO_3$ (001) are used as substrates. The $SrTiO_3$ substrates are degreased with acetone, isopropyl alcohol (IPA), and deionized water (18.2 MΩ-cm) in a sonicator for 10 minutes, followed by a vacuum anneal at 750°C for 15 min prior to deposition. The Ge substrates are cleaned using a

combination of regular degreasing in acetone, IPA, and deionized water in a sonicator for 10 min each, followed by *in situ* exposure to oxygen plasma for 30 min and a subsequent anneal, leading to an atomically flat, 2×1 reconstructed and contamination-free surface. The details of the Ge cleaning process are given elsewhere [47]. Annealing and growth of the samples are performed in a customized DCA Instruments M600 MBE chamber. Effusion cells are utilized for Sr, Ti, and Ba deposition while electron beam evaporation is used for Co. A quartz crystal microbalance is used to calibrate the fluxes.

Prior to film growth on Ge, a ½ monolayer of barium metal is deposited on the clean Ge (001) surface at 200°C. This Zintl template prevents Ge from oxidizing during subsequent growth in an oxygen atmosphere. Five unit cells of amorphous strontium titanate (STO) are deposited at 200°C on the Zintl template, in an environment of 5×10^{-7} torr of molecular oxygen. The STO layer is crystallized by annealing the sample to 750°C with a ramp rate of 30°C/min. On top of the crystallized STO buffer layer, two unit cells of undoped BTO are first deposited prior to depositing $BaTi_{1-x}Co_xO_3$ (BTCO), where x denotes the Co concentration. To study the effect of Co concentration, samples are grown with Co concentrations in the range of x = 2 - 40%. Both undoped and Co-doped BTO films are deposited at 5×10^{-6} torr of molecular oxygen at 750°C with a growth rate of 1 unit cell per 2 minutes, and are crystalline as deposited. Samples with thicknesses ranging from 10 to 16 nm are grown and then cooled down to 200°C with a ramp rate of 30°C/min in an oxygen environment of 5×10^{-6} torr. During growth, reflection-high-energy electron diffraction (RHEED) with 21 keV electrons at a grazing angle of 3° is used to monitor the quality and crystallinity of the samples. Immediately after deposition,

the samples are transferred *in situ* to an x-ray photoelectron spectroscopy (XPS) system allowing XPS measurements without breaking vacuum. The XPS analysis chamber is equipped with a VG Scienta R3000 electron analyzer and a monochromatic Al Kα radiation (hν = 1486.6 eV) source with the x rays incident at 54.7° from normal. The analyzer is calibrated using a clean silver foil such that the Ag $3d_{5/2}$ binding energy is 368.28 eV. To determine the lattice constants of our samples, x-ray diffraction measurements of the BTCO films are carried out, using a Phillips XPERT θ-θ diffractometer with a Cu Kα radiation source. For determining the Co concentration, Rutherford backscattering spectroscopy (RBS) measurements are performed on selected samples with He^+ ions at 2.3 MeV using an NEC 3UH Pelletron. Cross-sectional transmission electron microscopy (TEM) is carried out on a sample with 25% Co using a JEOL 4000EX operated at 400 kV and a JEOL 2010F operated at 200 kV. For the energy-dispersive x-ray spectroscopy (EDXS) line profile, the JEOL 2010F is used with an energy dispersion of 10 eV per channel and 1 nm probe size. Scan time for each point lies between 20 and 30 seconds. Electron energy-loss spectroscopy (EELS) measurements are performed on a Nion UltraSTEM 100 operated at 60 keV. Band-excitation piezoresponse force microscopy (BE-PFM) and voltage spectroscopy are performed on a commercially available Asylum AFM platform (Cypher instrument) using PXI-based National Instruments data acquisition cards and in-house software at CNMS, ORNL. The BE piezoresponse spectroscopy (BEPS) measurements are all carried out in the off-field state and at room temperature. Magnetization vs magnetic field measurements are performed on a Quantum Design magnetic property measurement

system apparatus. Measurements are made at 5 K in a magnetic field ranging from ±5 kOe. Field-cooled and zero-field-cooled magnetization vs temperature scans are also carried out from 300 K to 5 K in 2 K increments under an applied field of 200 Oe. A commercial Veeco MultiMode V atomic force microscope (AFM) with a commercially available magnetic force microscopy (MFM) tip in lift mode is used to simultaneously image local topographic and magnetic contrast of the BTCO surface.

8.3 Computational details

First-principles calculations are performed using the Vienna *ab initio* simulation package (VASP) [48]. Projector-augmented wave pseudopotentials [49, 50] utilizing the local density approximation of Perdew and Zunger [51] are used to describe each atomic species. The chosen valence configurations are $4s^2 4p^6 5s^2$ for Ba, $3s^2 3p^6 4s^1 3d^1$ for Ti, $3d^8 4s^1$ for Co, and $2s^2 2p^4$ for O. In order to account for the electronic correlation effects of the 3*d* states for the Co atom, calculations are performed using the L(S)DA+U approach of Dudarev *et al.* [52] utilizing a U_{eff} of 4.0 eV, consistent with previous calculations and the spin state of Co^{4+} in $SrCoO_3$ [37, 38, 53]. The calculations employ a plane-wave cutoff energy of 600 eV and the Brillouin zone is sampled using a Γ-centered Monkhorst-Pack grid [54] of 12 × 12 × 12 for the primitive cell. Relaxations are performed with a threshold of 10^{-2} eV/Å and integration of the Brillouin zone for self-consistent total energy calculations is performed using the tetrahedron method with Blöchl corrections [55]. Incorporation of both Co and oxygen vacancies is performed using a variety of supercell configurations in which at least one primitive cell of BTO is

always included to separate the repeated image of the defect. In these cases, appropriately scaled k-point grids are used and all atomic coordinates are allowed to relax (with the lattice constants fixed to the theoretical values for nominal BTO).

8.4 RESULTS AND DISCUSSION

8.4.1 RHEED

Growing undoped BTO directly on Ge results in in-plane polarized BTO due to the lack of sufficient compressive strain to overcome thermal expansion mismatch between the film and substrate [56]. A thin layer of 2-nm-thick STO grown between the Ge substrate and BTO imposes compressive strain on the BTO film leading to out-of-plane polarization of the BTO film [43]. Growing two unit cells of undoped BTO on top of STO before growing BTCO improves crystallization of the BTCO layer. The crystalline quality of the BTCO samples appears to be highly sensitive to the actual metal flux ratios, as small variations from ideal stoichiometry lead to poor crystalline quality or even polycrystalline films. RHEED patterns of BTCO films grown on an STO(001) substrate with different Co concentrations are shown in Fig. 8.1. At Co concentrations between 15% and 25%, sharp and very streaky patterns are visible, indicative of a highly ordered surface. Increasing the Co concentration in the BTCO films up to 30 - 40% leads to broader streaks, indicating a rougher surface and more crystalline disorder. For most samples, no additional diffraction spots are visible in the RHEED patterns during and after growth, confirming the absence of Co clusters or secondary phases. Additional spots are detected only in rare cases, which usually result from nonstoichiometric BTCO due to

either excess Ti or Co. Only films that show good crystallinity are considered for subsequent characterization.

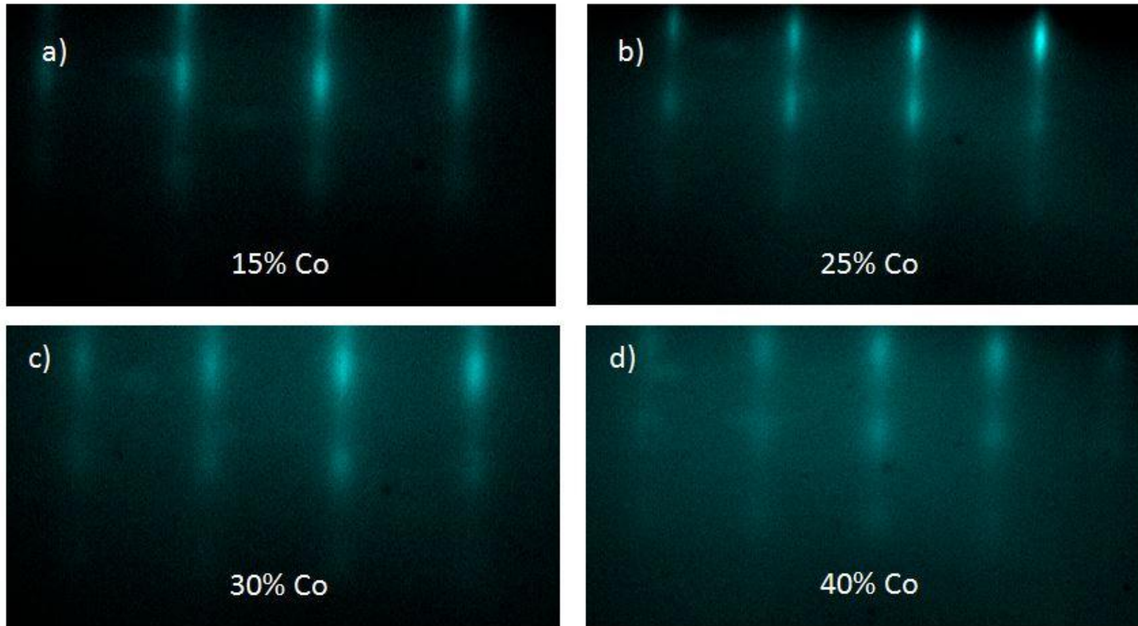

Figure 8.1: RHEED patterns of (a) 15%, (b) 25%, (c) 30%, and (d) 40% Co-substituted BTO films on STO(001) taken along the [100] direction. The BTCO thickness in all samples is 16 nm.

8.4.2 X-Ray Photoemission Spectroscopy

To quantify the Co concentration of the BTCO films, *in situ* XPS measurements are carried out immediately after growth. Due to the overlap of the Co $2p_{3/2}$ peak at 780 eV with the much stronger Ba $3d_{5/2}$ peak at the same binding energy, XPS analysis of BTCO films cannot easily be used for stoichiometry determination [57]. Since Co is only present in relatively small concentrations, other Co signals including Co Auger peaks are usually buried in the background and are too weak to be used for reliable analysis. For this

reason, two different techniques are used to estimate the Co concentrations. First, Rutherford backscattering spectroscopy (RBS) is performed on two different samples with nominal Co concentrations of 5 and 10% to confirm the accuracy of the assumed Co concentrations based on measured flux ratios. For the BTCO film with nominally 5% Co, a concentration of 7.3 ± 3.7% is measured. The nominally 10% Co-substituted sample exhibits 6.9 ± 3.9% Co. Both measurements indicate rough agreement with the nominal Co concentrations. The reason for the large error bars in RBS can be explained by the low Co concentrations and in addition, the small layer thicknesses also contribute to the uncertainty. The second technique is an indirect method using XPS to measure the Co concentrations. Right after growth of a BTCO sample, a $SrTi_{1-x}Co_xO_3$ (STCO) film is grown on another Ge substrate, with the same growth conditions, Co concentration and film thickness as the previous BTCO film. For these STCO films, XPS measurements can be used for determining the Co concentration since the Sr core levels do not overlap with the Co 2*p* peaks. The evaluation of the XPS spectra reveals that these STCO samples show good agreement with the nominal Co concentration. However, due to the high signal-to-noise ratio and weak intensity of the Co 2*p* spectra, peak fitting is not unambiguous. Based on the STCO XPS data, an absolute error of ±2.0% for the Co concentration in the grown BTCO samples is assumed.

XPS can also be used to determine the relative change in the oxygen content between BTCO and undoped BTO films. To do this, we measure Ba 4*d* and O 1*s* peaks in the BTCO films and in undoped BTO films for comparison. Doped and equivalent undoped samples are grown under the same growth conditions and have the same thickness. The

area ratio of the O 1*s* and Ba 4*d* peaks in both samples can then be used to determine the change in oxygen content in the BTCO films and subsequently extract an estimate of their oxygen vacancy concentrations. In a previous study of MBE-grown $SrTi_{1-x}Co_xO_3$ on Si by Posadas *et al.* [37], it was shown that the oxygen vacancy concentration correlates roughly with the amount of Co substitution in the STCO samples, indicating that Co doping promotes the formation of oxygen vacancies. Similar results are found for the grown BTCO films. For samples grown with Co concentrations between 5% and 15%, the amount of oxygen vacancies correlates roughly with the amount of Co, which is in good agreement with the previous result [37]. However, a somewhat different behavior is observed for higher Co concentrations in BTO. Only 20.8% oxygen vacancies are found for a nominally 30% Co-substituted BTCO film, while the amount of oxygen vacancies is determined to be as low as 26.4% for a nominally 40% Co-substituted sample. The role and importance of these oxygen vacancies on the magnetic ordering of BTCO is explained in detail in section 8.5.

8.4.3 X-ray diffraction

To further characterize the BTCO films, x-ray diffraction (XRD) is used to determine in-plane and out-of-plane lattice constants and overall crystalline quality. Figure 8.2 shows a symmetric 2θ-θ scan of a 10-nm-thick BTCO film with a Co concentration of 5% grown on an STO/Ge template. The high-resolution scan around the BTCO (002) peak gives an out-of-plane lattice constant of 4.06 Å. Rocking curve scans around the BTCO (002)

peak for films grown on Ge typically show a full- width at half maximum (FWHM) of 0.8 - 1.4° whereas BTCO films grown on an STO single-crystal substrate show a FWHM of 0.08 - 0.20°. Only peaks from Ge, STO, and a single orientation of the BTCO film are observed. The expanded out-of-plane lattice constant indicates an out-of-plane orientation of the polarization of the BTCO films. Out-of-plane lattice constant measurements for BTCO samples with Co concentrations ranging from 2% to 40% all show lattice constants in the range of 4.03 - 4.06 Å with no obvious trend with respect to Co concentration. No secondary phases are detectable (e.g., CoO at 2θ ~ 42°), indicative of uniform Co distribution.

It was shown by several groups [58-61] that an antiferromagnetic hexagonal phase of Co-doped BTO powder samples can be stabilized at room temperature. To rule out a potential hexagonal phase of BTCO, measurements around the expected position of the $(317)_{hex}$ reciprocal lattice point of a 25% Co-doped BTO sample are carried out. The reciprocal lattice point for this plane is only present for the hexagonal BTCO crystal structure and clearly differentiates it from the perovskite structure. The absence of this reciprocal lattice point leads us believe that our BTCO films are in the perovskite structure and not in the hexagonal phase, even for high Co concentrations. Additionally, grazing incidence $2\theta_{\chi}$-ϕ in-plane diffraction measurements confirm a square (and not rectangular) in-plane symmetry, which underlines our observation that our BTCO films grow with the perovskite crystal structure and with no other phases present.

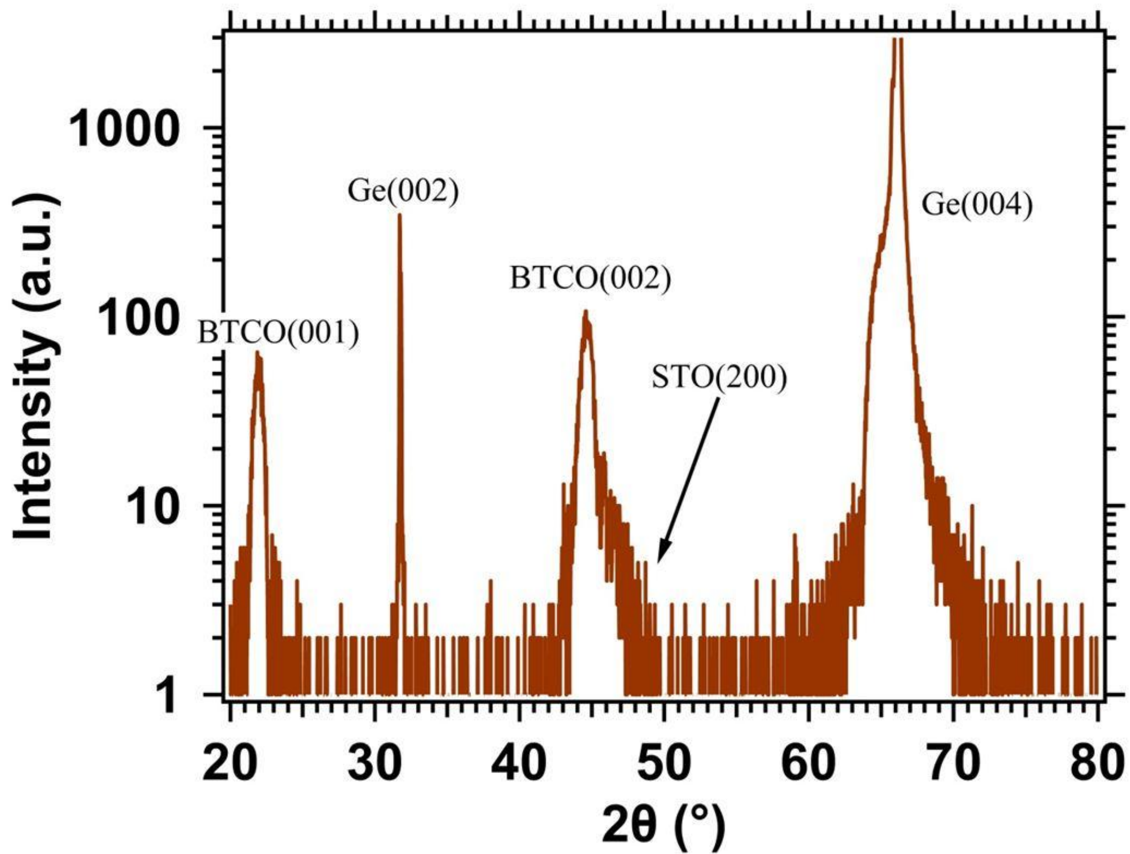

Figure 8.2: Typical x-ray diffraction 2θ-θ scan of 5% Co-substituted BTO film on STO/Ge. The film thickness is 10 nm. Only peaks from the substrate Ge as well as from STO and BTCO are observed.

8.4.4 Electron Microscopy

To confirm the crystal quality and uniform distribution of Co atoms in the BTCO films, cross-sectional high-angle annular- dark field (HAADF) TEM measurements are carried out. Figure 8.3(a) shows a HAADF image of a 12-nm-thick 25% Co-substituted BTCO film on 2-nm-thick STO on Ge. High crystallinity of the BTCO layer and the STO buffer,

as well as sharp interfaces between the layers without visible interdiffusion, is confirmed. No signs of Co clustering or CoO precipitates can be observed in the BTCO layer even for low-magnification imaging. To further investigate the distribution of Co within the sample, EDXS measurements are performed parallel to the Ge surface in the BTCO film. As can be seen in Figure 8.3(b), the Co atoms are uniformly distributed within the sample with only statistically insignificant fluctuations. Layer-resolved EELS measurements, which are performed on the same sample, reveal that the oxidation state of the Ti atoms changes within the film [Figs 8.3(c), 8.3(d)]. Ti atoms close to the Ge interface exhibit an oxidation state of +4 as can be seen by the splitting of the Ti L- edge. However, the split gradually weakens closer to the surface, indicating the presence of Ti atoms with an oxidation state of +3. This Ti reduction is an artifact attributed to argon-ion milling during the TEM sample preparation process, because only regions close to the surface are affected by it and XPS measurements, which were carried out immediately after growth, indicate no Ti^{3+} signal of the grown $BaTi_{1-x}Co_xO_{3-\delta}$ films independent of the Co concentration.

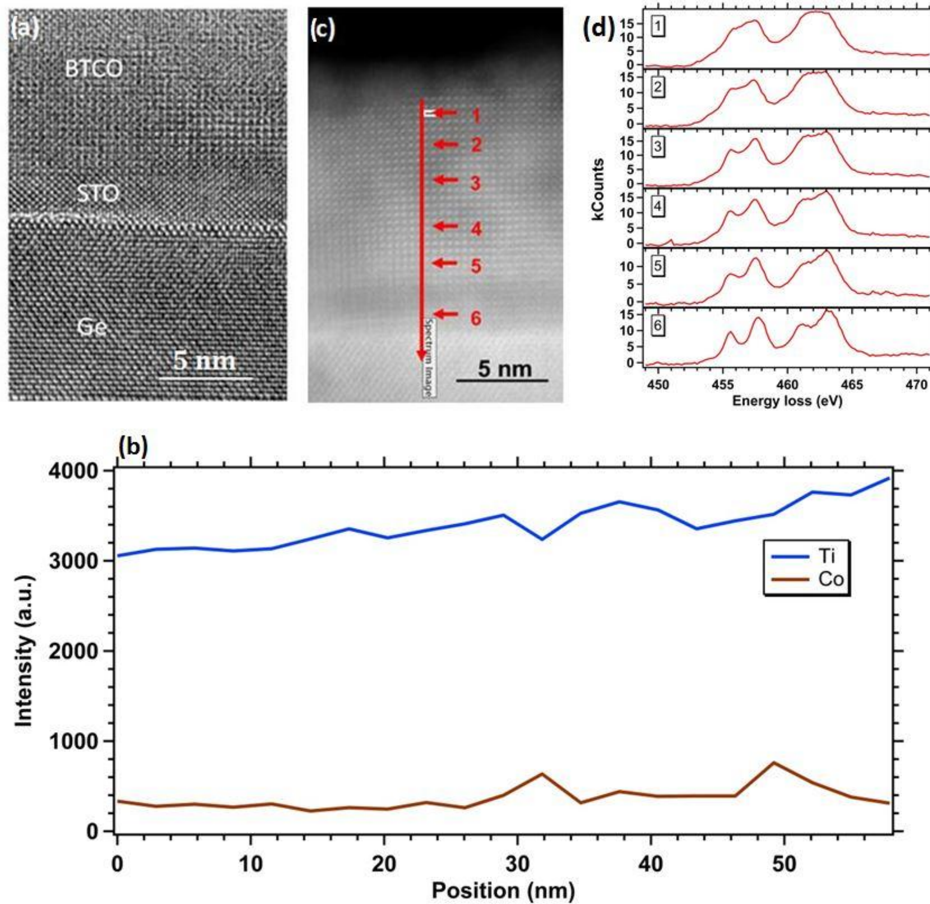

Figure 8.3: (a) High-resolution cross-section TEM image for a 25% Co-substituted BTO film on 5 unit cells $SrTiO_3$ on Ge. High crystallinity and a sharp interface between the STO buffer and BTCO film are confirmed. (b) EDXS line profile through the BTCO layer: a homogenous distribution of the Co atoms parallel to the interface is clearly shown, excluding the formation of Co clusters. (c) and (d) EELS measurements performed at 6 different positions in the sample. Ti atoms close to the Ge interface exhibit an oxidation state of +4 as can be seen by the splitting of the Ti L- edges. The gradual disappearance of the split closer to the surface indicates the presence of some Ti atoms with an oxidation state of +3, which is attributed to a sample preparation artifact due to argon-ion milling in thinner regions.

8.4.5 Piezo Force Microscopy measurement

The ferroelectric properties of the BTCO samples are evaluated using band-excitation piezoresponse force microscopy (BE-PFM). A BTCO sample with a Co concentration of 5% is used to demonstrate ferroelectricity. A typical result of a box-in-box switching experiment is shown in Figure 8.4(a). An area of $5 \times 5\ \mu m^2$ is initially poled with a tip held at -5 V while a smaller square of $2.5 \times 2.5\ \mu m^2$ within the bigger square is poled with a tip held at +5 V. Clear switching is observed and the vertical BE-PFM amplitude and phase [Figs 8.4(b), 8.4(c)] show clear and sharp boundaries indicating ferroelectric domains.

In conjunction with the BE-PFM tests, BEPS measurements are carried out on the same sample. 100 hysteresis loops across a 10×10 grid are measured and the average amplitude and phase response of the acquired loops are shown in Figs. 8.4(d) and (e). The amplitude curve exhibits a butterfly-like hysteresis which is characteristic for ferroelectric materials. The phase loop, however, appears to have a change somewhat less than 180°. However, there is significant variability in the switching behavior on the sample surface, and some points do not appear to switch well. This may be indicative of electrochemical phenomena in addition to the ferroelectric processes, high leakage current (which is spatially variable, e.g., due to defects), or both.

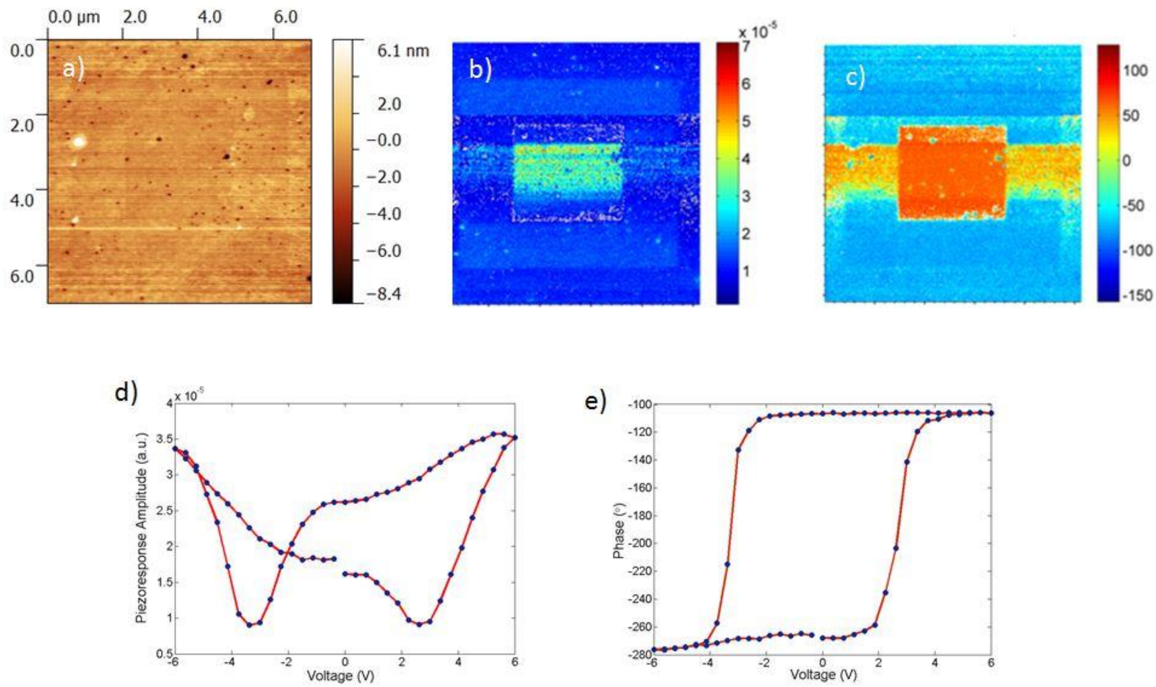

Figure 8.4: (a) AFM topography, (b) vertical BE-PFM amplitude, and associated (c) vertical BE-PFM phase after a box-in-box poling experiment. A box of size 5 × 5 μm^2 is poled with the tip held at -5 V, and a smaller box of size 2 × 2 μm^2 within the larger square is poled with the tip held at +5 V. On the same sample, 100 hysteresis loops are acquired with BE spectroscopy across a 10 × 10 spatial grid, with the average of the 100 loops shown in (d) amplitude and (e) phase plots.

8.4.6 Magnetic Measurements

To determine whether the BTCO films are magnetic, superconducting quantum interference device (SQUID) and MFM measurements are performed. For SQUID measurements, BTCO films are grown on single-crystal STO substrates to facilitate crystallization of the BTCO layer. For magnetization vs field and magnetization vs temperature measurements, the background signal of the STO substrate is subtracted by

measuring the specific substrate separately, immediately before growth of the BTCO layer.

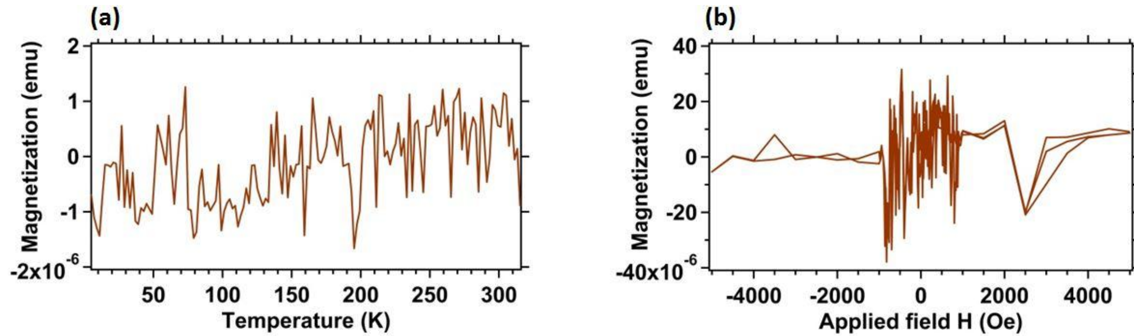

Figure 8.5: (a) Magnetization vs. field measurement at 5 K for a nominally 25% Co-substituted BTCO film on an STO single crystal (001) substrate. No hysteresis curve could be obtained, confirming the absence of ferromagnetism. (b) Magnetization vs. temperature scan shows no temperature dependency for the measured film.

The magnetization vs. field and magnetization vs. temperature behavior of several BTCO samples with different Co concentrations (5, 10, 20, 25%) are measured. However, after subtracting the background signal of the STO substrate, the magnetization vs field measurements show no sign of ferromagnetism. A hysteresis curve, typical for ferromagnetism, is not observed for any samples, independent of the Co concentration (see Fig. 8.5 for a 25% Co-substituted 16-nm-thick BTCO film), with only very weak paramagnetism in some samples. When performing magnetization vs temperature measurements, a rather unusual behavior is obtained, as the magnetization showed a slight decrease with temperature throughout the cooling process from 300 to 5 K, without any jumps or other anomalies.

For room temperature MFM measurements, two 16-nm-thick BTCO samples on an STO/Ge template with 15 and 30% Co concentration, respectively, are scanned to detect any signals of magnetic moments on the surfaces of the BTCO films. For both samples, low surface roughness is confirmed. For the 30% Co-substituted BTCO sample, a surface roughness between 0.65 and 1.3 nm is measured, depending on the scanned area, while a rms of only 0.25 nm is detected for the 15% Co-substituted sample. In both cases, the lack of magnetic contrast in the frequency shift images is very clear, indicating that the samples are either nonmagnetic or the magnetic signal is not detectable within the limits of the MFM. The apparent absence of magnetism is in agreement with the SQUID measurements, which also did not reveal any sign of ferromagnetism.

8.5 Theoretical Modeling

Theoretical modeling was performed in order to shed light on the experimental lack of detectable magnetism or even paramagnetic response despite the presence of cobalt in the film. Depending upon the oxygen vacancy ratio, cobalt can be in the Co^{4+} state (no vacancies), Co^{3+} state (a $\frac{1}{2}$ of an oxygen vacancy per cobalt), or Co^{2+} state (one oxygen vacancy per cobalt). In the following section, we explore each spin state in an effort to provide a possible explanation for the lack of observed magnetic signature when oxygen vacancies are included in either ratio.

For undoped BTO, lattice constants of a = 3.945 Å and c = 3.989 Å (c/a ratio of 1.011) are obtained, consistent with experimental values of a = 3.990 Å, $\frac{c}{a}$ = 1.011 [62]. In order

to model Co-doped BTO, we first consider a single Co atom replacing a titanium atom in a $2 \times 2 \times 2$ supercell. In a tetragonal crystal such as BTO, there is an elongation of the octahedral complex which can lead to further breaking of the *d*-state degeneracy from the usual t_{2g} and e_g states into e_g, b_{2g}, a_{1g}, and b_{1g} states. Therefore, for a Co^{4+} ion with five electrons, there are three possible spin states: low spin ($\mu = 1\ \mu_B$), intermediate spin ($\mu = 3\ \mu_B$), and high spin ($\mu = 5\ \mu_B$). It is also possible that hybridization can suppress any magnetic moment, as has been reported for Co-doped cubic BTO [17, 63]. Our calculations show that the low-spin state is the ground state for Co-doped BTO in the absence of oxygen vacancies (favored by 6 meV relative to the intermediate-spin state, 162 meV relative to the non-spin-polarized state, and 180 meV relative to the high-spin state). For the low-spin state, the total cell moment is 1.00 μ_B with 0.96 μ_B locally on the Co atom and the system is insulating, with the occupied Co states hybridized at the bottom of the O-2*p* band and a reduced gap (compared to undoped BTO) due to the presence of the unoccupied Co states just below the bulk Ti 3*d* derived conduction band.

We next consider the inclusion of two neighboring Co atoms oriented either parallel (apical) or perpendicular (basal) to the tetragonal axis using $2 \times 2 \times 3$ and $3 \times 2 \times 2$ supercells, respectively. In the nearest-neighbor configuration, the Co atoms prefer the intermediate-spin state. For the apical pair, ferromagnetic coupling is preferred and while the total cell magnetic moment is 6.00 μ_B, individually the Co atoms have slightly differing moments of $\mu_{Co} = 2.24\ \mu_B$ and $\mu_{Co} = 2.61\ \mu_B$. It should be noted that this is not a "mixed spin" state as the (higher in energy) ferromagnetic high-spin state can be stabilized with $\mu_{total} = 10.00\ \mu_B$ and the high-spin local moment is calculated to be $\mu_{Co} =$

3.17 μ_B. Furthermore, the antiparallel arrangement is actually a two-site antiferrimagnetic state with a total moment of $|\mu_{total}| = 0.60\ \mu_B$ and is 16 meV higher in energy.
Similarly, the basal pair favors an intermediate spin state with $\mu_{total} = 6.02\ \mu_B$ and again has slightly differing moments of $\mu_{Co} = 2.20\ \mu_B$ and $\mu_{Co} = 2.76\ \mu_B$. As in the apical case,

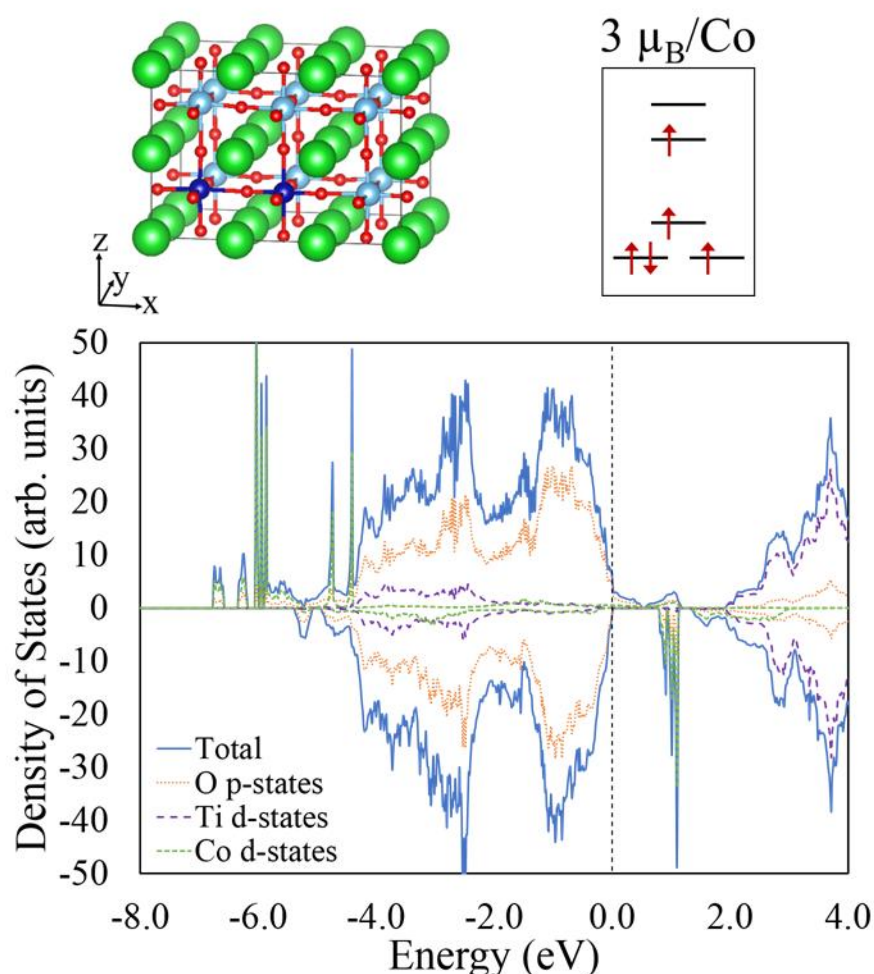

Figure 8.6: Atomistic arrangement, local site spin configuration, and projected density of states for a pair of cobalt atoms with no vacancies in a 3 × 2 × 2 supercell showing that this configuration, found to be lowest in energy, is both metallic and has a net magnetic moment.

the differing moments lead to an antiparallel arrangement that is higher in energy (ΔE = 44 meV) and a nonzero total moment ($|\mu_{total}|$ = 1.04 μ_B). Overall, the basal ferromagnetic arrangement is lowest in energy; its density of states is shown in Fig. 8.6. As for the single Co case, the occupied Co states are partially hybridized with the lower portion of the oxygen 2*p* states. More states are present in this region than before due to the increased spin moment, and hybridization pushes the top of the majority spin channel oxygen bands above the Fermi energy making the system metallic. In fact, all four of the above described states are metallic in nature (i.e., nonzero density of states at the Fermi energy) as opposed to the single Co atom case. Furthermore, in comparison to the dilute limit (i.e., isolated cobalt substitution), clustering of cobalt is energetically preferred.

The experimental data show vacancy concentrations ranging from approximately one oxygen vacancy for every two Co atoms (Co^{3+}) to one oxygen vacancy for every Co atom (Co^{2+}). Furthermore, the above results imply that in the absence of oxygen vacancies, there should be a detectable magnetic signal and that the material would be metallic for clustered Co. Therefore, calculations are performed for the two primary ratios of oxygen vacancies to Co atoms in order to provide a better comparison.

In order to simulate Co^{3+}, we require a simulation cell containing two Co atoms and a single oxygen vacancy. A defect arrangement for transition-metal impurity atoms resulting in the 3+ state is for two impurity atoms to occupy neighboring sites with an oxygen vacancy situated in between. Such a defect structure has been confirmed using experimental and theoretical techniques, for example for Fe^{3+} in $SrTiO_3$ [64]. It is also similar to the observance of linearly oriented clustered defects in Co:$SrTiO_3$ [37] and

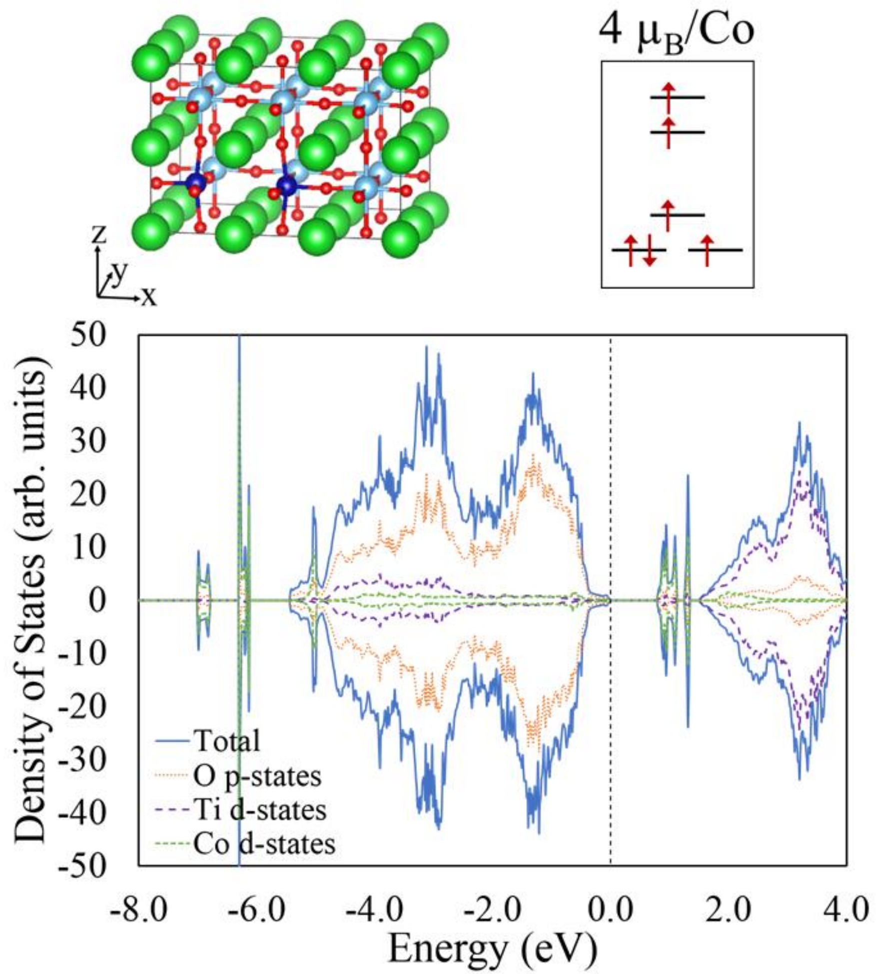

Figure 8.7: Atomistic arrangement, local site spin configuration, and projected density of states for a Co^{3+} configuration consisting of two cobalt atoms and a vacancy in a 3 × 2 × 2 supercell. The lowest energy spin configuration results in two antiparallel high-spin atoms (no net moment) and an insulator.

consistent with clustering of Co. Therefore, this defect is considered as the most plausible for the one vacancy per two Co dopant atoms, and we construct such a defect aligned as both an apical defect (a 2 × 2 × 3 supercell) and a basal defect (a 3 × 2 × 2 supercell). The latter is shown in Fig. 8.7.

A Co atom in the Co^{3+} state has six electrons which implies that for the tetragonally distorted octahedral crystal field, the Co can have low-spin ($\mu = 0\ \mu_B$), intermediate-spin ($\mu = 2\ \mu_B$), or high-spin ($\mu = 4\ \mu_B$) configurations. For both geometric orientations, the lowest energy spin configuration is an antiferromagnetic high-spin configuration (locally $|\mu_{Co}| = 2.96\ \mu_B$) with the basal plane defect having the lowest energy of the considered geometrical configurations. The difference in energy for the antiferromagnetic and ferromagnetic arrangements is 23 meV and 29 meV for basal and apical defects, respectively. As shown in Fig. 8.7, the density of states shows the occupied Co *d*-states either below the oxygen 2*p* states in energy or hybridized at the bottom of the oxygen 2*p* bands. The unoccupied Co *d*-states sit just below the nominal conduction band implying that the material is an insulator with a reduced gap compared to undoped BTO. The ferroelectric distortion (as indicated by the relative distortion of Ti and O atoms along the *c* axis) is maintained for this configuration with a small reduction for the Ti atoms (and oxygen in between) that sit immediately over the Co atoms. In comparison, the low-spin Co^{3+} state, which would also have explained the lack of magnetic moment, is found to be significantly higher in energy (590 meV) than the low-energy antiparallel high-spin state.

For a one-to-one ratio, we expect a Co^{2+} oxidation state which has seven electrons and can thus be in either a low-spin ($\mu = 1\ \mu_B$) or high-spin ($\mu = 3\ \mu_B$) state. Furthermore, due

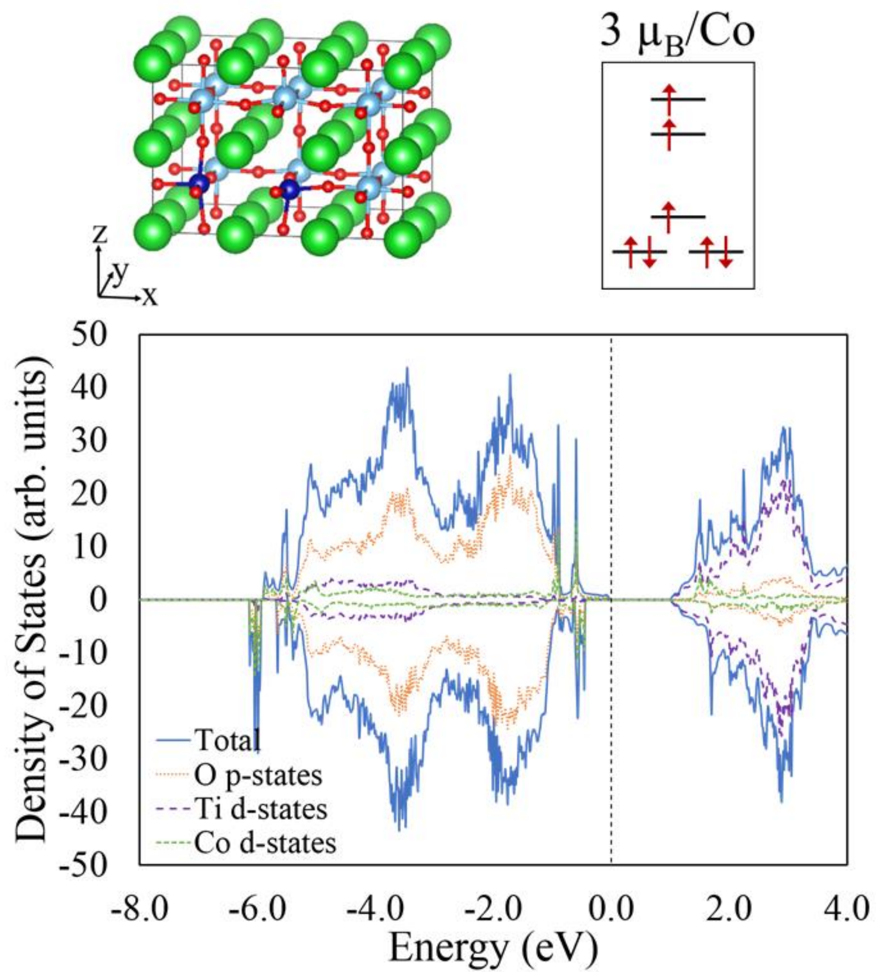

Figure 8.8: Atomistic arrangement, local site spin configuration, and projected density of states for a Co^{2+} configuration [two cobalt atoms and two oxygen vacancies in a 3 × 2 × 2 supercell which results in an insulating state with an antiparallel spin alignment (no net moment)].

to the tetragonal symmetry of the cell, the oxygen vacancy (similar to the case of two Co atoms) can be created at an oxygen site parallel to the tetragonal axis (apical) or perpendicular (basal). For the calculation of this ratio, a 2 × 2 × 2 supercell is used for the apical vacancy neighboring the Co atom. Energetically, the vacancy prefers to form at a site neighboring the Co dopant atom. In all cases, the high-spin state is favorable with the apical complex lowest in energy. Locally, the Co atom has a magnetic moment of 2.60 μ_B, while the total cell moment is 3.00 μ_B. Such a defect is insulating with the majority spin Co states hybridized at the bottom oxygen 2*p* band and the minority spin Co states hybridized at the top of the oxygen 2*p* band. The unoccupied Co states overlap with the Ti states in the conduction band.

Given that two Co atoms with a single oxygen vacancy in between display antiferromagnetic coupling, we next consider a neighboring pair of Co-vacancy complexes. Essentially, the considered structure can be described as adding an additional oxygen vacancy to the two Co/one oxygen vacancy configuration described earlier, with this additional vacancy either along the same axis as the previous defect or perpendicular to it. Therefore, as in the case of the 2 Co/1 V_O case, we use 2 × 2 × 3 and 3 × 2 × 2 supercells. Of the five symmetrically distinct configurations possible for such a defect, the arrangement with a basal Co pair and oxygen vacancy and an additional perpendicular, apical vacancy has the lowest energy (see Fig. 8.8 for the structure). Such a defect stabilizes as an antiferromagnetically coupled high-spin state with the ferromagnetic arrangement being 8 meV higher in energy. The AFM configuration has a calculated μ_{total} = 0.00 μ_B and local moments of μ_{Co} = 2.61 μ_B and μ_{Co} = -2.52 μ_B (the

slight discrepancy is due to excess magnetization on neighboring oxygen). Similar to a single Co-V_O complex, placing two such complexes at neighboring sites leads to an insulating material. Here the spin majority and spin minority channels mirror each other approximately. The reason the states do not line up exactly is that the specific energy levels of the orbitals are shifted slightly due to distortions caused by the local geometry of the two Co atoms being slightly different. The two Co/two oxygen vacancy complex, unlike a single pair, supports the experimental result of a simultaneous nonmagnetic and insulating film with Co.

In order to understand why no magnetism (including a noticeable paramagnetic signal) is detected at the field strengths considered in the magnetic measurements, we use an effective Heisenberg Hamiltonian which includes the Heisenberg term (H_H) and Zeeman term (H_Z):

$$H = H_H + H_Z = -2\sum_{i<j} J_{ij}\hat{S}_i \cdot \hat{S}_j - g\mu_B H_0 \sum_i S_{iz}, \qquad (1)$$

where $\hat{S}_i$ is the electronic spin of the given site, J_{ij} the coupling strength between spins, g is the electron spin g-factor, μ_B is the Bohr magneton, and H_0 the applied magnetic field. Since density functional theory is a 0 K theory and the measurements are taken at low temperature, we can safely ignore temperature effects. By expanding the Hamiltonian given in Eq. (1) for both the case of two locally ferromagnetic spins and the case of two locally antiferromagnetic spins, the field strength at which the parallel alignment is favored over antiparallel alignment can be determined as

$$H_0 \geq -\frac{\Delta E}{2g\mu_B S}, \quad (2)$$

where $\Delta E = E_{AFM} - E_{FM}$ and can be related to the spin coupling strength J. Of the reported configurations, the smallest ΔE occurs for the described lowest-energy two-vacancy/two-Co (Co^{2+}). For this configuration, ΔE = 8 meV and S = $\frac{3}{2}$ which implies that a magnetic field strength of H_0 = 23 T would be needed to overcome the coupling, significantly above that used for the SQUID measurements. In the case of the locally antiferromagnetic, high-spin Co^{3+}, the field strength would be even higher due to the previously mentioned increased ΔE. Furthermore, since the thermal energy at 300 K is 25.8 meV, such a configuration for Co^{3+} would not be detected in the magnetization vs temperature sweeps.

8.6 Discussion

For ferroelectric materials, it is known that the introduction of sufficient oxygen vacancies results in the disappearance of the polarization and the lowering of the Curie temperature [45]. For that reason the amount and distribution of oxygen vacancies in our $BaTi_{0.95}Co_{0.05}O_3$ film is essential to understand the existence of ferroelectricity. Our XRD and RHEED measurements, as well as cross-sectional TEM images, show the absence of phase segregations or clustering of Co atoms in our BTCO films independent of the Co concentration. As a matter of fact, EDXS measurements indicate a uniform distribution of Co atoms in our films. This is in accordance with the PFM measurements which reveal that there is no substantial phase segregation within the resolution limit of the instrument.

Additionally, the detection of a magnetic signal would be likely if Co clusters had formed. Theoretical calculations of Fe-doped $SrTiO_3$ [64] and Co-doped $BaTiO_3$ [65] show that the TM-V_O-TM complex is the preferred structure. Based on these findings, we assume that the oxygen vacancies prefer to form next to Co atoms and are not randomly distributed throughout the film. However, due to the small amount of induced oxygen vacancies in a 5% Co-doped BTCO film, the polarization of $BaTiO_3$ is only expected to be attenuated and not completely suppressed with respect to undoped $BaTiO_3$.

Our experimental and theoretical results also indicate that the Co-V_O complex plays a crucial role in the formation of magnetic ordering in Co-substituted metal oxide films, which has been already shown for Co:STO (STCO) by Florez *et al.* [66] and Posadas *et al.* [37] as well as for Co:TiO_2 by Roberts *et al.* [67]. In agreement with these studies, we show that the partial substitution of Co atoms facilitates the formation of oxygen vacancies in their close proximity, leading to Co-V_O pairs. From DFT calculations, in the case where there are no oxygen vacancies, which imparts Co with a valence state of 4+, the results for STCO and BTCO are very similar. Co stabilizes in the low spin state and interacts ferromagnetically with adjacent Co atoms but the interaction is very short range. However, Posadas *et al.* showed that if oxygen vacancies are present in STCO with a concentration equal to the Co concentration, then Co stabilizes in the 2+ valence state. They showed theoretically that the Co(II)/V_O complex is responsible for the ferromagnetic and insulating behavior of their films. Interestingly, the ferromagnetic behavior due to the 2 Co/2 V_O complex, which is present in STCO, is not observed for BTCO films. Even though we also observe a correlation between the Co concentration

and the amount of oxygen vacancies formed in BTCO similar to the case of STCO, the presence of oxygen vacancies in BTCO leads to an antiferromagnetic ordering instead. This lack of a magnetic moment is confirmed by both SQUID and MFM measurements. The numerical estimate of the magnetic field strength needed to overcome the antiferromagnetic ordering confirms our observations of the absence of any magnetic signal in BTCO films.

The finding of a lack of magnetism in BTCO films is contrary to reports by Lin *et al.* [30] and Lee *et al.* [29], which both observed ferromagnetism in Co-substituted BTO films. Lin *et al.* used pulsed laser deposition (PLD) to deposit $BaTi_{0.95}Co_{0.05}O_3$ thin films of various thicknesses on Nb:STO substrates and found that the Co atoms are in a 3+ valence state. Lee *et al.* used ion implantation to create 3 and 5% Co-substituted BTO layers which showed ferromagnetic behavior. Similar to our study, both groups report the absence of Co clusters using XRD and TEM. However, both PLD growth and ion implantation, being far from equilibrium processes, are prone to forming nanoscale clusters that could be small enough to be measured by a SQUID magnetometer but without being detectable in XRD. In both studies the presence of oxygen vacancies was not investigated, despite the assumption by Lin *et al.* to be the origin of ferromagnetism in their films. In the case of $Co:TiO_2$ [67] that was grown by rf-magnetron sputter deposition at 4×10^{-3} torr, it was shown that a vacuum anneal promotes the formation of oxygen vacancies. Since PLD and ion implantation operate under similar pressures between 10^{-1} and 10^{-5} torr, it is possible that at these higher pressures, the formation of oxygen vacancies in BTCO is suppressed. The lack of vacancies in these ferromagnetic

BTCO films would be consistent with our theoretical results, which predict ferromagnetism in fully oxidized BTCO films.

8.7 Conclusion

In summary, we have investigated ferroic order in Co-substituted BTO films grown on Ge(001) and STO(001) substrates by MBE. XPS measurements show that the formation of oxygen vacancies depends on the Co concentration in the sample. The existence of ferroelectricity of a 5% Co-substituted BTCO film is confirmed using PFM. However, SQUID and MFM measurements show no sign of magnetism, including paramagnetism, for any Co concentration. First-principles calculations demonstrate that while BTCO would exhibit a net moment in the absence of oxygen vacancies, the observed lack of detectable moments in the presence of oxygen vacancies may be due to Co and oxygen vacancies forming defect complexes that are locally antiferromagnetic. The field required to overcome this antiferromagnetism is on the order of 20 T. Furthermore, calculations of these low-energy defects show them to be insulating and ferroelectric in agreement with experiment.

8.8 References

[1] W. Eerenstein, N. D. Mathur, J. F. Scott, Nature **442**, 759-765 (2006).

[2] H. Béa, M. Gajek, M. Bibes, A. Barthélémy, J. Phys.: Condens. Matter **20**, 434221 (2008).

[3] M. Bibes, A. Barthélémy, Nature Mater.**7**, 425 426 (2008).

[4] M. Bibes, J. E. Villlegas, A. Barthélémy, Adv. Phys. **60**, 5 84 (2011).

[5] M. Gajek, M. Bibes, S. Fusil, K. Bouzehouane, J. Fontcuberta, A. Barthélémy, A. Fert, Nature Mater. **6**, 296 302 (2007).

[6] Z. Yan, Y. Guo, G. Zhang, J.M. Liu, Adv. Mater. **23**, 1351 (2011).

[7] N. A. Hill, J. Phys. Chem. B **104**, 6694–6709 (2000).

[8] H. Schmid, Ferroelectrics **162,** 317–338 (1994).

[9] S. W. Cheong, M. Mostovoy, Nature Mater. **6**, 13 (2007).

[10] R. Ramesh, N. A. Spaldin, Nature Mater. **6**, 21 (2007).

[11] W. Prellier, M. P. Singh, P. Murugavel, J. Phys.: Condens. Matter **17**, 803-832 (2005).

[12] T. Katsufuji, S. Mori, M. Masaki, Y. Moritomo, N. Yamamoto, H. Takagi, Phys. Rev. B **64**, 104419 (2001).

[13] T. Kimura, S. Kawamoto, I. Yamada, M. Azuma, M. Takano, Y. Tokura, Phys. Rev. B **67**, 180401 (2003).

[14] J. Wang, J. B. Neaton, H. Zheng, V. Nagarajan, S. B. Ogale, B. Liu, D. Viehland, V. Vaithyanathan, D. G. Schlom, U. V. Waghmare, N. A. Spaldin, K. M. Rabe, M. Wuttig, R. Ramesh, Science **299**, 1719-1722 (2003).

[15] A. Moreira dos Santos, S. Parashar, A. R. Raju, Y. S. Zhao, A. K. Cheetham, C. N. R. Rao, Solid State Commun. **122**, 49-52 (2002).

[16] X. H. Zhu, H. Béa, M. Bibes, S. Fusil, K. Bouzehouane, E. Jacquet, A. Barthélémy, D. Lebeugle, M. Viret, D. Colson, Appl. Phys. Lett. **93**, 082902 (2008).

[17] H. Nakayama, H. Katayama-Yoshida, Jpn. J. Appl. Phys. **40**, 1355-1358 (2001).

[18] H. K. Chandra, K. Gupta, A. K. Nandy, P. Mahadevan, Phys. Rev. B **87**, 214110 (2013).

[19] V. Sharma, G. Pilania, G. A. Rossetti Jr., K. Slenes, R. Ramprasad, Phys. Rev. B **87**, 134109 (2013).

[20] R. Maier, J. L. Cohn, Appl. Phys. Lett. **78**, 2536-2538 (2001).

[21] A. Rajamani, G. F. Dionne, D. Bono, C. A. Ross, J. Appl. Phys. **98**, 063907 (2005).

[22] S. Ray, P. Mahadevan, S. Mandal, S. R. Krishnakumar, C. S. Kuroda, T. Sasaki, T. Taniyama, M. Itoh, Phys. Rev. B **77**, 104416 (2008).

[23] F. Lin, D. Jiang, X. Ma, W. Shi, J. Magn. Magn. Mater. **320**, 691-694 (2008).

[24] B. Xu, K. B. Yin, J. Lin, Y. D. Xia, X. G. Wan, J. Yin, X. J. Bai, J. Du, Z. G. Liu, Phys. Rev. B **79**, 134109 (2009).

[25] Z. Chao, C. L. Wang, J. C. Li, K. Yang, Chin. Phys. **16**, 1422 (2007).

[26] E. V. Ramana, S. M. Yang, R. Jung, M. H. Jung, B. W. Lee, C. U. Jung, J. Appl. Phys. **113**, 187219 (2013).

[27] A. Zorko, M. Pregelj, M. Gomilsek, Z. Jaglicic, D. Pajic, M. Telling, I. Arcon, I. Mukulska, M. Valant, Sci. Rep. **5**, 7703 (2015).

[28] S. Ray, Y. V. Kolen'ko, K. A. Kovnir, O. I. Lebedev, S. Turner, T. Chakraborty, R. Erni, T. Watanabe, G. van Tendeloo, M. Yoshimura, M. Itoh, Nanotechnology **23**, 025702 (2012).

[29] J. S. Lee, Z. G. Khim, Y. D. Park, D. P. Norton, N. A. Theodoropoulou, A. F. Hebard, J. D. Budai, L. A. Boatner, S. J. Pearton, R. G. Wilson, Solid State Electron. **47**, 2225-2230 (2003).

[30] Y.-H. Lin, S. Zhang, C. Deng, Y. Zhang, X. Wang, C.W. Nan, Appl. Phys. Lett. **92**, 112501 (2008).

[31] L. B. Luo, Y. G. Zhao, H. F. Tian, J. J. Yang, H. Y. Zhang, J. Q. Li, J. J. Ding, B. He, S. Q. Wei, C. Gao, Appl. Phys. Lett. **92**, 232507 (2008).

[32] A. A. Demkov, A. B. Posadas, *Integration of Functional Oxides with Semiconductors*, (Springer, New York, 2014).

[33] A. Posadas, M. Berg, H. Seo, D. J. Smith, H. Celio, A. P. Kirk, D. Zhernokletov, R. M. Wallace, A. de Lozanne, A. A. Demkov, Appl. Phys. Lett. **98**, 055104 (2011).

[34] A. B. Posadas, M. Berg, H. Seo, D. J. Smith, A. P. Kirk, D. Zhernokletov, R. M. Wallace, A. de Lozanne, A. A. Demkov, Microelectron. Eng. **88**, 1444 (2011).

[35] H. Seo, A. B. Posadas, A. A. Demkov, Phys. Rev. B **86**, 014430 (2012).

[36] C. Hu, K. W. Park, A. B. Posadas, J. L. Jordan-Sweet, Alexander A. Demkov, E. T. Yu, J. Appl. Phys. **114**, 183909 (2013).

[37] A. B. Posadas, C. Mitra, C. Lin, A. Dhamdhere, D. J. Smith, M. Tsoi, A. A. Demkov, Phys. Rev. B **87**, 144422 (2013).

[38] C. Mitra, C. Lin, A. B. Posadas, A. A. Demkov, Phys. Rev. B **90**, 125130 (2014).

[39] J. H. Haeni, P. Irvin, W. Chang, R. Uecker, P. Reiche, Y. L. Li, S. Choudhury, W. Tian, M. E. Hawley, B. Craigo, A. K. Tagantsev, X. Q. Pan, S. K. Streiffer, L. Q. Chen, S. W. Kirchoefer, J. Levy, D. G. Schlom, Nature **430**, 758-761 (2004).

[40] C. Dubourdieu, J. Bruley, T. M. Arruda, A. B. Posadas, J. Jordan-Sweet, M. M. Frank, E. Cartier, D. J. Frank, S. V. Kalinin, A. A. Demkov, V. Narayanan, Nat. Nanotechnol. **8**, 748-754 (2013).

[41] T. Q. Ngo, A. B. Posadas, M. D. McDaniel, C. Hu, J. Bruley, E. T. Yu, A. A. Demkov, J. G. Ekerdt, Appl. Phys. Lett. **104**, 082910 (2014).

[42] M. D. McDaniel, T. Q. Ngo, A. B. Posadas, C. Hu, S. Lu, D. J. Smith, E. T. Yu, A. A. Demkov, J. G. Ekerdt, Adv. Mater. Interfaces **1**, 1400081 (2014).

[43] P. Ponath, K. Fredrickson, A. B. Posadas, Y. Ren, X. Wu, R. K. Vasudevan, M. B. Okatan, S. Jesse, T. Aoki, M. R. McCartney, D. J. Smith, S. V. Kalinin, K. Lai, A. A. Demkov, Nat. Commun. **6**, 6067 (2015).

[44] W. L. Warren, D. Dimos, R. M. Waser. MRS Bull. **21**, 40–45 (1996).

[45] K. H. Härdtl, R Wernicke, Solid State Commun. **10**, 153-157 (1972).

[46] M. V. Raymond, J. Chen, D. M. Smyth, Integr. Ferroelectr. **5**, 73–78 (1994).

[47] P. Ponath, A. Posadas, R. Hatch, A. A. Demkov, J. Vac. Sci. Technol. B **31**, 031201 (2013).

[48] G. Kresse, J. Furthmüller, Phys. Rev. B **54**, 11169 (1996).

[49] P. Blöchl, Phys. Rev. B **50**, 17953 (1994).

[50] G. Kresse, D. Joubert, Phys. Rev. B **59**, 1758 (1999).

[51] J. Perdew, A. Zunger, Phys. Rev. B **23**, 5048 (1981).

[52] S. Dudarev, G. Botton, Phys. Rev. B **57**, 1505 (1998).

[53] Y. Long, Y. Kaneko, S. Ishiwata, Y. Taguchi, Y. Tokura, J. Phys. Condens. Matter **23**, 245601 (2011).

[54] H. Monkhorst, J. Pack, Phys. Rev. B **13**, 5188 (1976).

[55] P. Blöchl, O. Jepsen, O. Andersen, Phys. Rev. B **49**, 16223 (1994).

[56] K. Fredrickson, P. Ponath, A. B. Posadas, M. McCartney, T. Aoki, D. J. Smith, A. A Demkov, Appl. Phys. Lett. **104**, 242908 (2014).

[57] J. F. Moulder, W. F. Stickle, P. E. Sobol, K. D. Bomben, *Handbook of X-Ray Photoelectron Spectroscopy* (Physical Electronics, Inc., Eden Prairie, 1995).

[58] L. Miranda, K. Boulahya, M. Hernando, D. C. Sinclair, F. Jimenez-Villacorta, A. Varela, J. M. Gonzalez-Calbet, M. Parras, Chem. Mater. **23**, 1050-1060 (2011).

[59] J. G. Dickson, L. Katz, R. Ward, J. Am. Chem. Soc. **83**, 3026-3029 (1961).

[60] G. M. Keith, M. J. Rampling, K. Sarma, N. Mc Alford, D. C. Sinclair, J. Eur. Ceram. Soc. **24**, 1721-1724 (2004).

[61] J. Wang, H. Zhang, D. Xue, Z. Li, J. Phys. D: Appl. Phys. **42**, 235103 (2009).

[62] C. Li, D. Cui, Y. Zhou, H. Lu, Z. Chen, Appl. Surf. Sci. **136**, 173 (1998).

[63] C. Mitra, AIP Adv. **2**, 032148 (2012).

[64] E. Blokhin, E. Kotomin, A. Kuzmin, J. Purans, R. Evarestov, J. Maier, Appl. Phys. Lett. **102**, 112913 (2013).

[65] D. Cao, B. Liu, H. Yu, W. Hu, M. Cai, Eur. Phys. J. B **88**, 75 (2015).

[66] J. M. Florez, S. P. Ong, M. C. Onbasli, G. F. Dionne, P. Vargas, G. Ceder, C. A. Ross, Appl. Phys. Lett. **100**, 252904 (2012).

[67] K. G. Roberts, M. Varela, S. Rashkeev, S. T. Pantelides, S. J. Pennycook, K. M. Krishnan, Phys. Rev. B. **78**, 014409 (2008).

Chapter 9. Summary and outlook

9.1 SUMMARY

A cleaning method for the Ge(001) surface is developed, using a combination of *ex situ* wet-etching and *in situ* oxygen plasma exposure in combination with a thermal anneal. After degreasing the Ge surface, the wafer is wet-etched by dipping the sample four times alternately into HCl (15%) and H_2O_2 (7%) for 20 s and 30s, respectively, with a final H_2O_2 dip of 60s. This step removes most of the contamination while forming a thin passivation layer of germanium oxide. A subsequent *in situ* oxygen plasma exposure removes all remaining carbon contamination from the surface, but also forms a thick layer of germanium oxide which is removed by annealing the sample to above 650°C. XPS confirms the absence of any carbon or oxygen left on the Ge surface. AFM measurements indicate a surface roughness of only 3 Å and ARPES measurements reveal features from the Ge surface state, indicative of an extremely clean Ge(001) surface.

A review about the existing surface cleaning methods for the Ge(001) surface is presented. The review examines the effects of UV light, O_2 plasma, H_2 plasma, ion sputtering including Ge regrowth, and wet-etching on the Ge(001) surface. The cleaning methods are compared with respect to their carbon and oxygen removal efficiency as well as their influence on the surface roughness.

We demonstrated the modulation of charge carriers in a Ge substrate by switching the polarization of a 16 nm thick epitaxial layer of BTO which was grown on top of Ge. XRD measurements confirm that a thin layer of STO acting as a buffer layer between Ge and BTO imposes compressive strain, leading to single orientation c-axis oriented BTO.

PFM measurements confirm that the BTO films are ferroelectric, while TEM images demonstrate high quality crystalline film with sharp interfaces between the different epitaxial layers. Switching the polarization in an area of $5 \times 5\ \mu m^2$ of the BTO films and scanning the same area with MIM reveals that the conductivity of the Ge substrate underneath can be significantly changed, demonstrating the modulation of charge carriers by switching the polarization of BTO.

To pattern the BTO/STO heterostructure grown on Ge, a lift-off process involving patterned sacrificial poly-Si/SiO_2 islands on the Ge wafer is proposed. Thin films of BTO on STO are grown in openings of the island structures. TEM images confirm that the high crystallinity of the films is retained with abrupt interfaces between the layers. Etching the wafers in BOE for a couple of hours removes the poly-Si/SiO_2 pattern and reveals patterned BTO/STO/Ge heterostructures.

The attempt to create a multiferroic material consisting of Co-doped BTO is described. Epitaxial crystalline films of $BaTi_{1-x}Co_xO_3$ with varying Co concentrations on an STO/Ge template or STO substrate were grown. PFM measurements demonstrate ferroelectricity for a 5% Co substituted BTCO film. XPS measurements clearly show a correlation between Co concentration and the formation of oxygen vacancies. MFM and SQUID measurements demonstrate that none of the samples, independent of their Co concentration, showed any ferromagnetic response. Theoretical calculations are carried out and reveal a strong influence of oxygen vacancies on the magnetic order for this system. Without oxygen vacancies, ferromagnetism is predicted, while strong

antiferromagnetism is expected for oxygen vacancies located next to Co atoms, which explains the lack of ferromagnetic response in the experimental results.

9.2 Outlook and future work

The overarching goal of this thesis was to develop a Ge-based ferroelectric field-effect transistor. A reliable and reproducible cleaning method for the Ge(001) surface has been developed and $BaTiO_3$ has been successfully integrated on Ge with the *c*-axis normal to the semiconductor surface, which is one of the requirements for a FeFET. Modulation of charge carriers in the Ge substrate was demonstrated, laying the foundation for the realization of a FeFET on Ge. A method to create patterned BTO films was demonstrated as well. This procedure can be used as a back end of the line process to fabricate FeFETs on Ge using a pre-processed Ge wafer that already contains the transistor structures required.

Special attention has to be paid to the metal gate choice. The band offsets between BTO and several metals, specifically TiN and Pt, have been investigated using XPS. It turns out that the Fermi level of TiN lies above the conduction band of BTO, making TiN not suitable as a gate electrode on BTO due to the lack of a Schottky barrier. The Fermi level of Pt, on the other hand, aligns close but below the conduction band of BTO. Ideally the Fermi level should be aligned midgap. A more promising metal could be W (because it has a comparable work function as Pt) or Cr.

Additionally, some more research has to be done on reducing the leakage current of the BTO/STO/Ge heterostructures. Post growth *in situ* oxygen plasma anneal, *ex situ* oxygen

furnace anneal, or a rapid thermal anneal in O_2 did not seem to have any significant influence on the relatively high leakage currents in our films. The insertion of a thin layer of BaO between BTO and STO layer helped reduce the leakage current by 2-3 orders of magnitude. BaO has a similar lattice constant as STO but exhibits a much larger band gap, which is why it might be interesting to further explore the incorporation of BaO into the BTO/STO/Ge heterostructure.

Appendix

First author publications

(1) **<u>Ponath, P.</u>**, Posadas, A. B., Demkov, A. A. *Ge(001) surface cleaning methods for device integration.* Appl. Phys. Rev. **4**, 021308 (2017)

(2) **<u>Ponath, P.</u>**, O'Hara, A., Cao, H.-X., Posadas, A. B., Vasudevan, R., Berg, M., Li, Z., Zhang, D., Kellock, A. J. de Lozanne, A., Zhou, J., Kalinin, A., Smith, D. J. & Demkov, A. A. *Contradictory nature of Co doping in ferroelectric* $BaTiO_3$. Phys. Rev. B. **94**, 205121 (2016)

(3) **<u>Ponath, P.</u>**, Fredrickson, K. D., Posadas, A. B., Ren, Y., Wu, X., Vasudevan, R. K., Okatan, M. B., Jesse, S., Aoki, T., McCartney, M. R., Smith, D. J., Kalinin, S. V., Lai, K. & Demkov, A. A. *Carrier Density Modulation in Ge Heterostructure by Ferroelectric Switching*. Nat. Commun. **6**, 6067 (2015)

(4) **<u>Ponath, P.</u>**, Posadas, A. B., Hatch, R. C. & Demkov, A. A. *Preparation of a clean Ge(001) surface using oxygen plasma cleaning*. J. Vac. Sci. Technol. B. **31**, 031201 (2013)

Co-Author publications

(1) Wu, H., Lu, S., Aoki, T. **Ponath, P**., Ekerdt, J. G., Demkov, A. A., McCartney, M. R., Smith, D. J. *Integration of ferroelectric $BaTiO_3$ with Ge: The role of a $SrTiO_3$ buffer layer investigated using aberration-corrected STEM*. Appl. Phys. Lett. 110, 252901 (2017)

(2) Posadas, A., Kormondy, K. J., Guo, W., **Ponath, P.**, Kremer, J. G., Hadamek, T. & Demkov, A. A. *Scavenging of oxygen from $SrTiO_3$ during oxide thin film deposition and the formation of interfacial 2DEGs*. J. Appl. Phys. **121**, 105302 (2017)

(3) Smith, D. J., Wu, H., Lu, S., Aoki, T., **Ponath, P.**, Fredrickson, K., McDaniel, M. D., Lin, E., Posadas, A. B., Demkov, A. A., Ekerdt, J. & McCartney, M. R. *Recent studies of oxide-semiconductor heterostructures using aberration-corrected scanning transmission electron microscopy*. J. Mater. Res. **0**, 1-9 (2016)

(4) Kormondy, K. J., Abel, S., Fallegger, F., Popoff, Y., **Ponath, P.**, Posadas, A. B., Sousa, M., Caimi, D., Siegwart, H., Uccelli, E., Czornomaz, L., Marchiori, C., Fompeyrine, J. & Demkov, A. A., *Analysis of the Pockels effect in ferroelectric barium titanate thin films on Si(001)* Microelectron. Eng. **147**, 215-218 (2015).

(5) Demkov, A. A., **Ponath, P.**, Fredrickson, K., Posadas, A. B., McDaniel, M. D., Ngo, T. Q. & Ekerdt, J. G., *Integrated films of transition metal oxides for information technology* Microelectron. Eng. **147**, 285-289 (2015)

(6) Seo, H., Hatch, R. C., **Ponath, P.**, Choi, M., Posadas, A. B. & Demkov, A. A. *Critical difference in the surface electronic structure of Ge(001) and Si(001): Ab-Initio theory and angle-resolved photoemission spectroscopy*. Phys. Rev. B **89**, 115318 (2014)

(7) Fredrickson, K. D., **Ponath, P.**, Posadas, A. B., McCartney, M. R., Aoki, T., Smith, D. J. & Demkov, A. A. *Atomic and electronic structure of the ferroelectric $BaTiO_3$/Ge(001) interface*. Appl. Phys. Lett. **104**, 242908 (2014)

(8) Demkov, A. A., Posadas, A. B., Seo, H., Choi, M., Kormondy, K., **Ponath, P.**, Hatch, R. C., McDaniel, M. D., Ngo, T. Q. & Eckert, J. G. *Monolithic Integration of Oxides on Semiconductors*. ECS Trans. **54**, 255-269 (2013)

Technical Presentations

- "Advances towards the ferroelectric field-effect transistor on Ge(001)" (oral), International Conference on IC Design and Technology (ICICDT), Austin, Texas, USA, *May 2017*
- "Selective area growth of $BaTiO_3$ for ferroelectric field-effect transistor application" (oral), American Physical Society (APS) March meeting, New Orleans, Louisiana, USA, *March 2017*
- "Formation of nanoscale $BaTiO_3$ MOSCAPs on Ge without wet-etching" (oral), 19th International Conference on Molecular Beam Epitaxy (IC-MBE 2016), Montpellier, Hérault department, France, *September 2016*

- “Formation of nanoscale $BaTiO_3$ MOSCAPs for ferroelectric field-effect transistor application” (oral), 5th International Conference for Smart and Multifunctional Materials, Structures & Systems (CIMTEC), Perugia, Umbria, Italy, *June 2016*
- “The nature of Co doped $BaTiO_3$” (poster), Material Research Society (MRS) meeting 2016, Phoenix, Arizona, USA, *March 2016*
- “Nanoscale $BaTiO_3$ MOSCAP formation for ferroelectric field-effect transistor application” (oral) American Physical Society (APS) March meeting, Baltimore, Maryland, USA, *March 2016*
- “Formation of nanoscale $BaTiO_3$-MOSCAPs without wet-etching” (poster), Semiconductor Interface Specialists Conference (SISC), Arlington, Virginia, USA, *December 2015*
- “Advances towards the Ferroelectric Field-Effect Transistor - Epitaxial $BaTiO_3$ on Ge(001)” (oral), Material Research Society (MRS), Boston, Massachusetts, USA, *December 2015*
- “The road towards the ferroelectric-FET – Carrier density modulation by ferroelectric switching in $BaTiO_3$/Ge” (oral), American Physical Society (APS) March meeting, San Antonio, Texas, USA, *March 2015*
- “Carrier Density Modulation in Ge Heterostructure by Ferroelectric Switching” (poster), Physics & Chemistry of Surfaces & Interfaces (PCSI), Snowbird, Utah, USA, *January 2015*

- "Carrier Density Modulation in Ge Heterostructure by Ferroelectric Switching" (oral), Semiconductor Interface Specialists Conference (SISC), San Diego, California, USA, *December 2014*
- "Epitaxial $BaTiO_3$ on Ge(001)" (poster), International Conference on the Physics of Semiconductors (ICPS), Austin, Texas, USA, *August 2014*
- "Epitaxial growth of $BaTiO_3$ on germanium" (oral) American Physical Society (APS) March meeting, Denver, Colorado, USA, *March 2014*
- "Epitaxial growth of $BaTiO_3$ on germanium" (oral) Material Research Society (MRS) meeting, San Francisco, California, USA, *April 2013*
- "Epitaxial growth of $BaTiO_3$ on germanium" (oral) American Physical Society (APS) March meeting, Baltimore, Maryland, USA, *March 2013*

Bibliography

A. Basit, H. K. Kim, J. Blachere, Appl. Phys. Lett. **73**, 3941-3943 (1998).

A. Bolon, C. O. Kunz, Polym. Eng. Sci. **12**, 109-111 (1972).

A. Demkov, H. Seo, X. Zhang, J. Ramdani, Appl. Phys. Lett. **100**, 071602 (2012).

A. Hill, J. Phys. Chem. B **104**, 6694–6709 (2000).

A. Kittl, K. Opsomer, M. Popovici, N. Menou, B. Kaczer, X. P. Wang, C. Adelmann, M. A. Pawlak, K. Tomida, A. Rothschild, B. Govoreanu, R. Degraeve, M. Schaekers, M. Zahid, A. Delabie, J. Meersschaut, W. Polspoel, S. Clima, G. Pourtois, W. Knaepen, C. Detavernier, V. V. Afanas'ev, T. Blomberg, D. Pierreux, J. Swerts, P. Fischer, J. W. Maes, D. Manger, W. Vandervorst, T. Conard, A. Franquet, P. Favia, H. Bender, B. Brijs, S. Van Elshocht, M. Jurczak, J. Van Houdt, D. J. Wouters, Microelectron. Engin. **86**, 1789-1795 (2009).

A. Kubby, J. E. Griffith, R. S. Becker, J. S. Vickers, Phys. Rev. B **36**, 6079 (1987).

A. Kubby, J. J. Boland, Surf. Sci. Rep. **26**, 61-204 (1996).

A. Lucas, C. S. Dower, D. F. McMorrow, G. C. L. Wong, F. J. Lamelas, P. H. Fuoss, Phys. Rev. B **47**, 10375 (1993).

A. McKee, F. J. Walker, J. FL Conner, E. D. Specht, D. E. Zelmon, Appl. Phys. Lett. **59**, 782 (1991).

A. McKee, F. J. Walker, M. F. Chisholm, Phys. Rev. Lett. **81,** 3014-3017 (1998).

A. McKee, F. J. Walker, M. F. Chisholm, Science **293**, 468-471 (2001).

A. Peña, J. L. G. Fierro, Chem. Rev. **101**, 1981-2007 (2001).

A. Reinhardt, W. Kern, *Handbook of Silicon Wafer Cleaning Technology* (William Andrew, Norwich, 1993) Chapter 9.

A. Rost, H. Lin, T. A. Rabson, Appl. Phys. Lett. **59**, 3654 (1991).

A. Stolk, D. J. Eaglesham, H.-J. Gossmann, J. M. Poate, Appl. Phys. Lett. **66**, 1370 (1994).

Abel, T. Stoferle, C. Marchiori, C. Rossel, M. D. Rossell, R. Erni, D. Caim, M. Sousa, A. Chelnokov, B. J. Offrein, J. Fompeyrine, Nat. Commun. **4**, 1671 (2013).

Aizawa, B.-E. Park, Y. Kawashima, K. Takahashi, H. Ishiwara, Appl. Phys. Lett. **85**, 3199-3201 (2004).

Akane, J. Tanaka, H. Okumura. S. Matsumoto, Appl. Surf. Sci. **108**, 303-305 (1997).

Als-Nielsen, D. McMorrow, *Elements of Modern X-ray Physics* (John Wiley & Sons, Ltd, West Sussex, England, 2001).

B. Klein, in *Photorefractive materials and their applications I*, 195-236 (2005) (Springer, Berlin Heidelberg).

B. Luo, Y. G. Zhao, H. F. Tian, J. J. Yang, H. Y. Zhang, J. Q. Li, J. J. Ding, B. He, S. Q. Wei, C. Gao, Appl. Phys. Lett. **92**, 232507 (2008).

B. Neaton, K. M. Rabe, Appl. Phys. Lett. **82**, 1586-1588 (2003).

B. Posadas, C. Mitra, C. Lin, A. Dhamdhere, D. J. Smith, M. Tsoi, A. A. Demkov, Phys. Rev. B **87**(14), 144422 (2013).

B. Posadas, M. Berg, H. Seo, D. J. Smith, A. P. Kirk, D. Zhernokletov, R. M. Wallace, A. de Lozanne, A. A. Demkov, Microelectron. Eng. **88**, 1444 (2011).

Bardeen, W. H. Brattain, Phys. Rev. **74**, 230-231 (1948).

Béa, M. Gajek, M. Bibes, A. Barthélémy, J. Phys.: Condens. Matter **20**, 434221 (2008).

Behrisch, K Wittmaack, *Sputtering by Particle Bombardment III* (Springer Verlag, Berlin 1991).

Belkind, S. Gershman, *Vacuum Coating and Technology November* 2008, 46-57.

Bibes, A. Barthélémy, Nature Mater.**7**, 425 426 (2008).

Bibes, J. E. Villlegas, A. Barthélémy, Adv. Phys. **60**, 5 84 (2011).

Binnig, C. F. Quate, C. Gerber, Phys. Rev. Lett. **56**, 930-934 (1986).

Blöchl, O. Jepsen, O. Andersen, Phys. Rev. B **49**, 16223 (1994).

Blöchl, Phys. Rev. B **50**, 17953 (1994).

Blokhin, E. Kotomin, A. Kuzmin, J. Purans, R. Evarestov, J. Maier, Appl. Phys. Lett. **102**, 112913 (2013).

Blumenstein, S. Meyer, A. Ruff, B. Schmid, J. Schäfer, R. Claessen, J. Chem. Phys. **135**, 064201 (2011).

Bodlaki, H. Yamamoto, D. H. Waldeck, E. Borguet, Surf. Sci. **543**, 63-74 (2003).

Bosi, G. Attolini, Prog. Cryst. Growth Ch. **56**, 146-174 (2010).

Braun W, *Applied RHEED: Reflection High-Energy Electron Diffraction During Crystal Growth* (Springer-Verlag, Berlin, 1999).

C. Fernandez, W. S. Yang, H. D. Shih, F. Jona, D. W. Jepsen, P. M. Marcus, J. Phys. C. Solid State Phys. **14**, L55-60 (1981).

C. Payne, N. Roberts, R. J. Needs, M. Needels, J. D. Joannopoulos, Surf. Sci. **211/212**, 1-20 (1989).

C. Riviere, Contemp. Phys. **14**, 513-539 (1973).

C. Saraswat, C. O. Chui, T. Krishnamohan, A. Nayfeh, P. McIntyre, Microelec. Eng. **80**, 15-21 (2005).

Cao, B. Liu, H. Yu, W. Hu, M. Cai, Eur. Phys. J. B **88**, 75 (2015).

Chandra, P. B. Littlewood, "A Landau primer for ferroelectrics. In *Physics of ferroelectrics,"* (pp. 69-116) (Springer, Berlin Heidelberg, 2007).

Chang, J. S. Horwitz, A. C. Carter, J. M. Pond, Steven W. Kirchoefer, C. M. Gilmore, D. B. Chrisey, Appl. Phys. Lett. **74**, 1033 (1999).

Chao, C. L. Wang, J. C. Li, K. Yang, Chin. Phys. **16**, 1422 (2007).

Chau, S. Datta, M. Doczy, B. Doyle, J. Kavalieros, M. Metz, IEEE Electr. Device L. **25**(6), 408-410 (2004).

Cho, R. J. Nemanich, Phys. Rev. B **46**, 12421-12426 (1992).

Choi, A. B. Posadas, H. Seo, R. C. Hatch, A. A. Demkov, Appl. Phys. Lett. **102**, 031604 (2013).

Choi, J. M. Buriak, Langmuir **16**, 7737-7741 (2000).

Claeys, E. Simoen, *Germanium-based technology* (Elsevier, Oxford, 2007).

Coffinier, G. Piret, M. R. Das, R. Boukherroub, C. R. Chim. **16**, 65–72 (2013).

Contreras-Guerrero, J. P. Veazey, J. Levy, R. Droopad, Appl. Phys. Lett. **102**, 012907 (2013).

Cross, Nature **432**, 24-25 (2004).

D. Apalkov, B. Dieny, P. IEEE **104**, 1796-1830 (2016).

D. Cressler, IEEE T. Microw. Theory **46**, 572-589 (1998).

D. Damjanovic, P. Muralt, N. Setter, IEEE Sens. J. **1**, 191-206 (2001).

D. Fredrickson, A. B. Posadas, A. A. Demkov, C. Dubourdieu, J. Bruley, J. Appl. Phys. 113, 184102 (2013).

D. Fredrickson, H. Seo, A. A. Demkov, J. Appl. Phys. **120**, 065301 (2016).

D. Fredrickson, P. Ponath, A. B. Posadas, M. R. McCartney, T. Aoki, D. J. Smith, A. A. Demkov, Appl. Phys. Lett. **104**, 242908 (2013).

D. Kevan, N. G. Stoffel, Phys. Rev. Lett. **53**, 702-705 (1984).

D. Kevan, Phys. Rev. B **32**, 2344 (1985).

D. Kevan, R. H. Gaylord, Phys. Rev. B **33**, 5809-5818 (1986).

D. McDaniel, T. Q. Ngo, A. B. Posadas, C. Hu, S. Lu, D. J. Smith, E. T. Yu, A. A. Demkov, J. G. Ekerdt, Adv. Mater. Interfaces **1**, 1400081 (2014).

D. Megaw, Proc. Phys. Soc. **58**, 133 (1946).

D. Plummer, M. D. Deal, P. B. Griffin, *Silicon VLSI Technology*, (Prentice Hall, Upper Saddle River, 2013).

D. Schmeisser, R. D. Schnell, A. Bogen, F. J. Himpsel, D. Rieger, G. Landgren, J. F. Morar, Surf. Sci. **172**, 455-465 (1986).

D. Schnell, F. J. Himpsel, A. Bogen, D. Rieger, W. Steinmann, Phys. Rev. B. **32**, 8052-8056 (1985).

D. Sen, C. K. Jørgensen, *Electronegativity* (Springer, Berlin, 1987) p.9.

D. Xiang, C. Gao, Mater. Charact. **48**, 117-125 (2002).

D. Ye, G. D. Wilk, J. Kwo, B. Yang, H.-J. L. Gossmann, M. Frei, S. N. G. Chu, J. P. Mannaerts, M. Sergent, M. Hong, K. K. Ng, J. Bude, IEEE Electron. Device Letters **24**, 209-211 (2003).

Dallaporta, M. Liehr, J. E. Lewis, Phys. Rev. B. **41**, 5075 (1990).

Debye, Phisik. Zeits. **13**, 97-100 (1912).

Deegan, G. Hughes, Appl. Surf. Sci. **123/124**, 66-70 (1998).

Demkov, A. B. Posadas, *Integration of Functional Oxides with Semiconductors*, (Springer, New York, 2014).

Diebold, Surf. Sci. Rep. **48,** 53-229 (2003).

Dimoulas, E. Gusev, P. C. McIntyre, M. Heyns, *Advanced Gate Stacks for High-Mobility Semiconductors* (Springer, New York 2007).

Dubourdieu, J. Bruley, T. M. Arruda, A. B. Posadas, J. Jordan-Sweet, M. M. Frank, E. Cartier, D. J. Frank, S. V. Kalinin, A. A. Demkov, V. Narayanan, Nat. Nanotechnol. **8**, 748-754 (2013).

Dudarev, G. Botton, Phys. Rev. B **57**, 1505 (1998).

E. Blöchl, Phys. Rev. B, **50**, 17953-17979 (1994).

E. Farnsworth, R. E. Schlier, T. H. George, R. M. Burger, J. Appl. Phys. **29**, 1150 (1958).

E. Haller, W. L. Hansen, P. Luke, R. McMurray, B. Jarrett, IEEE T. Nucl. Sci. **29**, 745-750 (1982).

E. Jones, J. P. Pelz, Y. H. Xie, P. J. Silverman, E. A. Fitzgerald, Surf. Sci. Lett. **341**, 1005-1010 (1995).

E. Rase, R. Roy, J. Am. Ceram. Soc. **38**, 102 (1955).

E. Van Nostrand, S. J. Chey, M.-A. Hasan, D. G. Cahill, J. E. Greene, Phys. Rev. Lett. **74**, 1127 (1995).

E. Vella, F. Messina, M. Cannas, R. Boscaino, Phys. Rev. B **83**, 174201 (2011).

Ederer, N. A. Spaldin, Phys. Rev. Lett. **95**, 257601 (2005).

Eerenstein, N. D. Mathur, J. F. Scott, Nature **442**, 759-765 (2006)

Einstein, Ann. Phys. **322** (6), 132-148 (1905).

Eisenbeiser, J. M. Finder, Z. Yu, J. Ramdani, J. A. Curless, J. A. Hallmark, R. Droopad, W. J. Ooms, L. Salem, S. Bradshaw, C. D. Overgaard, Appl. Phys. Lett. **76**, 1324 (2000).

El-Kareh, *Fundamentals of Semiconductor Processing Technologies, (*Springer US, New York, 1995).

F. Devonshire, Philos. Mag. **40**(309), 1040-1063 (1949).

F. Ehman, J. W. Faust Jr., W. B. White, J. Electrochem. Soc. **118** (9) 1443-1447 (1971).

F. Moulder, W. F. Stickle, P. E. Sobol, K. D. Bomben, *Handbook of x-ray photoelectron spectroscopy* (Physical electronics Inc., Eden Prairie, 1995).

Fredrickson, P. Ponath, A. B. Posadas, M. McCartney, T. Aoki, D. J. Smith, A. A Demkov, Appl. Phys. Lett. **104**, 242908 (2014).

Fuchs, C. W. Schneider, R. Schneider, H. Rietschel, J. Appl. Phys. **85**, 7362 (1999).

Fukuda, T. Ogino, Phys. Rev. B **56**, 13190 (1997).

G. Dickson, L. Katz, R. Ward, J. Am. Chem. Soc. **83**, 3026-3029 (1961).

G. Günther, Z. Naturforschg. A. **13** (12), 1081-1089 (1958).

G. Roberts, M. Varela, S. Rashkeev, S. T. Pantelides, S. J. Pennycook, K. M. Krishnan, Phys. Rev. B. **78**, 014409 (2008).

G. Schrott, J. A. Misewich, V. Nagarajan, R. Ramesh, Appl. Phys. Lett. **82**, 4770 (2003).

G. Shard, Surf. Interface Anal. **46**, 175-185 (2014).

G. Streetman, S. Banerjee, *Solid State electronic Devices,* p. 524 (Hall, New Jersey, 2000).

Gajek, M. Bibes, S. Fusil, K. Bouzehouane, J. Fontcuberta, A. Barthélémy, A. Fert, Nature Mater. **6**, 296 302 (2007).

Gan, L. Li, T. Nguyen, H. Qi, R. F. Hicks, M. Yang, Surf. Sci. **395**, 69-74 (1998).

Gene H. Haertling, J. Am. Ceram. Soc. **82** (4), 797–818 (1999).

Guo, L. E. Cross, S-E. Park, B. Noheda, D. E. Cox, G. Shirane, Phys Rev. Lett. **84**, 5423 (2000).

Gupta, V. L. Colvin, S. M. George, Phys. Rev. B **37**, 8234-8243 (1988).

Gurlu, H. J. W. Zandvliet, B. Poelsema, Phys. Rev. Lett. **93**, 066101 (2004).

Gutowski, J. E. Jaffe, Mater. Res. Soc. Symp. Proc. 716, B 3.2.1 - B 3.2.5 (2002).

H. Ahn, R. H. Hammond, T. H. Geballe, M. R. Beasley, J. M. Triscone, M. Decroux, O. Fisher, A. Antognazza, K. Char, Appl. Phys. Lett. **70**, 206 (1997).

H. C. Parker, "*The Technology and Physics of Molecular Beam Epitaxy,"* (Plenum Press, New York and London, 1985).

H. Chan, E. I. Altman, Y. Liang, J. Vac. Sci. Technol. **19**, 976-981 (2001).

H. Choi, Y. Mao, J. P. Chang, Mater. Sci. Eng. R. **72**(6), 97-136 (2011).

H. Comfort, G. L. Patton, J. D. Cressler, W. Lee, E. F. Crabbe, B. S.Meyerson, J. Y.-C. Sun, J. M. C. Stork, P.-F. Lu, J. N. Burghartz, J. Warnock, K. Kenkins, K.-Y. Toh, M. D'Agostino, G. Scilla, Tech. Dig. Int. Electron. Device Meeting, 21–24 (1990).

H. Engelhard, *Handbook of Deposition Technologies for Films and Coatings* (Elsevier, Boston, 2010).

H. Gries, Surf. Interface Anal. **24**, 38 (1996).

H. Haeni, P. Irvin, W. Chang, R. Uecker, P. Reiche, Y. L. Li, S. Choudhury, W. Tian, M. E. Hawley, B. Craigo, A. K. Tagantsev, X. Q. Pan, S. K. Streiffer, L. Q. Chen, S. W. Kirchoefer, J. Levy, D. G. Schlom, Nature **430**, 758-761 (2004).

H. Hoerman, G. M. Ford, L. D. Kaufmann, B. W. Wessels, Appl. Phys. Lett. **73**, 2248 (1998).

H. Huang, M. Y. Yang, Albert Chin, W. J. Chen, C. X. Zhu, B. J. Cho, M.-E Li, and D. L. Kwon, 2003 VLSI Tech. Dig. 119-120 (2003).

H. Lu, M. J. Graham, X. H. Feng, B. X. Yang, Appl. Phys. Let. **60**, 2773 (1992).

H. Ngai, D. P. Kumah, C. H. Ahn, F. J. Walker, Appl. Phys. Lett. **104**, 062905 (2014).

H. Park, B. S. Kang, S. D. Bu, T. W. Noh, J. Lee, W. Jo, Nature **401**, 682 (1999).

H. Schmid, Ferroelectrics **162,** 317–338 (1994).

H. Seo, A. B. Posadas, A. A. Demkov, Phys. Rev. B **86**, 014430 (2012).

H. Seo, K. B. Chung, J. P. Long, G. Lucovsky, J. Electrochem. Soc. **156** (11), 813-817 (2009).

H. Seo, M. Choi, A. B. Posadas, R. C. Hatch, A. A. Demkov, J. Vac. Sci. Technol. B **31**, 04D107 (2013).

H. Seo, R. C. Hatch, P. Ponath, M. Choi, A. B. Posadas, A. A. Demkov, Phys. Rev. B **89**, 115318 (2014).

H. Shang, H. Okom-Schmidt, K. K. Chan, M. Copel, J. A. Ott, P. M. Kozlowski, S. E. Steen, S. A. Cordes, H.-S. P. Wong, E. C. Jones, W. E. Haensch, Int. El. Devices Meet. 441-444 (2002).

H. Shang, H. Okorn-Schimdt, J. Ott, P. Kozlowski, S. Steen, E. C. Jones, H.-S. P.Wong, and W. Hanesch, IEEE Electr. Device L. **24** (4), (2003).

H. Shang, M. M. Frank, E. P. Gusev, J. O. Chu, S. W. Bedell, K. W. Guarini, M. Ieong, IBM J. Res. & Dev. **50**, 377-386 (2006).

H. T. Hall, J. Phys. Chem. **59**, 1144-1146 (1955).

H. Tabata, H. Tanaka, T. Kawai, J. Appl. Phys. **65**, 1970 (1994).

H. Takasu, J. Electroceram. **4:2/3**, 327 (2000).

H. Ubara, T. Imura, A. Hiraki, Solid State Commun. 50, 673-675 (1984).

H. Wu, N. Conrad, W. Luo, and P. D. Ye, 2014 Int. El. Devices. Meet. 227-230 (2014).

H. Zhang, Y. Guimond, Y. Bellec, J. Non-Cryst. Solids **326**, 519–523 (2003).

H. Zhu, H. Béa, M. Bibes, S. Fusil, K. Bouzehouane, E. Jacquet, A. Barthélémy, D. Lebeugle, M. Viret, D. Colson, Appl. Phys. Lett. **93**, 082902 (2008).

H.-Y. Yu, S.-l. Cheng, J.-H. Park, A. K. Okyay, M. C. Onba, B. Ercan, Y. Nishi, K. C. Saraswat, Appl. Phys. Lett. **97**, 063503 (2010).

Harari, J. Appl. Phys. **49**, 2478-2489 (1978).

Hattori, Crit. Rev. Solid State **20**, 339-382 (1995).

Hattori, *Ultraclean Surface Processing of Silicon Wafers* (Springer, Berlin, 1998).

Hoffman, X. Pan, J. W. Reiner, F. J. Walker, J. P. Han, C. H. Ahn, T. P. Ma, Adv. Mater **22**, 2957-2961 (2010).

Horio, Y. Hashimoto, A. Ichimiya, Appl. Surf. Sci. **100/101**, 292-296 (1996).

http://cccbdb.nist.gov/bondlengthmodel2.asp?method=12&basis=5 for the bond length of Ge-Cl and Ge-F.

http://usa.jpk.com/index.2.us.html

http://www.casaxps.com/

http://www.wiredchemist.com/chemistry/data/bond_energies_lengths.html for the bond energy of Ge-Cl.

Hu, E. Lin, A. Hamze, A. B. Posadas, H. W. Wu, D. J. Smith, A. A. Demkov, J. G. Ekerdt, J. Chem. Phys. **146**, 052817 (2017).

Hu, K. W. Park, A. B. Posadas, J. L. Jordan-Sweet, Alexander A. Demkov, E. T. Yu, J. Appl. Phys. **114**, 183909 (2013).

Huang, Z. P. Wu, J. H. Hao, Appl. Phys. Lett. **94,** 032905 (2009).

Huff, David Gilmer, *High Dielectric Constant Materials: VLSI MOSFET Applications*, (Springer-Verlag, Berlin and Heidelberg, 2005).

I. Davydov, *Germanium* (Gordon and Breach, New York, 1966) p.150 & p.160.

I. Scace, G. A. Slack, J. Chem. Phys. **30**, 1551 (1959).

Ichimiya, P. I. Cohen, *Reflection High Energy Electron Diffraction* (Cambridge University Press 2004).

Imada, A. Fujimori, Y. Tokura, Rev. Mod. Phys. **70**, 1039 (1998).

International Union for Vacuum Science Technique and Application http://iuvsta.org/iuvsta2/index.php?id=643

Ishizaka, Y. Shiraki, J. Electrochem. Soc. **133**, 666-671 (1986).

Ito, N. Fujimura, T. Yoshimura, T. Ito, J. Appl. Phys. **93**, 5563–5567 (2003).

Iwai, Microelectron. Eng. **86**, 1520-1528 (2009).

J. Bottomley, M. Iwami, Y. Uehara, S. Ushioda, J. Vac. Sci. Technol. A **17**, 698 (1999).

J. Chadi, Phys. Rev. Lett. **43**, 43 (1979).

J. Cucauskas, S. W. Kirchoefer, W. J. DeSisto, J. M. Pond, Appl. Phys. Lett. **74**, 4034 (1999).

J. Johnson, Appl. Phys. Lett. **7**, 221 (1965).

J. Kim, S. Liu, S. Tan, J. McVittie, K. Saraswat, Y. Nishi, ECS Trans. **3**, 1191-1196 (2006).

J. Kuhr, W. Ranke, Surf. Sci. **201**, 408-418 (1988).

J. M. Florez, S. P. Ong, M. C. Onbasli, G. F. Dionne, P. Vargas, G. Ceder, C. A. Ross, Appl. Phys. Lett. **100**, 252904 (2012).

J. M. Hartmann, A. Abbadie, J. P. Barnes, J. M. Fédéli, T. Billon, L. Vivien, J. Cryst. Growth **312**, 532–541 (2010).

J. Millis, Boris I. Shraiman, R. Mueller, Phys. Rev. Lett. **77**, 175 (1996).

J. Monkhorst, J. D. Pack, Phys. Rev. B **13**, 5188-5192 (1976).

J. Oh, J. C. Campbell, S. G. Thomas, S. Bharatan, R. Thoma, C. Jasper, R. E. Jones, T. E. Zirkle, IEEE J. Quantum Elect. **38**, 1238-1241 (2002).

J. P. Perdew A. Zunger, Phys. Rev. B **23**, 5048-5079 (1981).

J. R. Arthur Jr., J. Appl. Phys. **39** (8), 4032-4034 (1968).

J. R. Vig, J. Vac. Sci. Technol. A **3**, 1027 (1985).

J. Robertson, R. M. Wallace, Mater. Sci. Eng. R. **88**, 1-41 (2015).

J. S. Hovis, R. J. Hamers, C. M. Greenlief, Surf. Sci. **440**, 815-819 (1999).

J. S. Lee, Z. G. Khim, Y. D. Park, D. P. Norton, N. A. Theodoropoulou, A. F. Hebard, J. D. Budai, L. A. Boatner, S. J. Pearton, R. G. Wilson, Solid State Electron. **47**, 2225-2230 (2003).

J. S. Meena, S. M. Sze, U. Chand, T.-Y. Tseng, Nanoscale Res. Lett. **9**, 526 (2014).

J. Sandroff, R. N. Nottenburg. J.-C. Bischoff, R. Bhat, Appl. Phys. Lett. **51**, 33 (1987).

J. Senzaki, K. Kurihara, N. Nomura, O. Mitsunaga, Y. Iwasaki, T. Ueno, Jpn. J. Appl. Phys. 37, 5150-5153 (1997).

J. Stone, J. Appl. Phys. **62**, 4371 (1987).

J. Valasek, Phys. Rev. **17**, 475–81 (1921).

J. W. Zandvliet, A. van Silfhout, M. J. Sparnaay, Phys. Rev. B **39**, R5576 (1989).

J. W. Zandvliet, B. S. Swartzentruber, W. Wulfhekel, B. J. Hattink, B. Poelsema, Phys. Rev. B **57**, R6803-R6806 (1998).

J. W. Zandvliet, Phys. Rep. **388**, 1-40 (2003).

J. W. Zandvliet, W. Wulfhekel, B. L. M. Hendriksen, B. J. Hattink, B. Poelsema, Phys. Rev. B **57**, 1356 (1998).

J. Wang, H. Zhang, D. Xue, Z. Li, J. Phys. D: Appl. Phys. **42**, 235103 (2009).

J. Wang, J. B. Neaton, H. Zheng, V. Nagarajan, S. B. Ogale, B. Liu, D. Viehland, V. Vaithyanathan, D. G. Schlom, U. V. Waghmare, N. A. Spaldin, K. M. Rabe, M. Wuttig, R. Ramesh, Science **299**, 1719-1722 (2003).

J. Wang, T. A. Arias, J. D. Joannopoulos, Phys. Rev. B **47**, 10497-10508 (1993).

J. Xu, W. Menesklou, E. Ivers-Tiffée, J. Eur. Ceram. Soc. **24**, 1735 (2004).

J. Y. Maeng, J. Y. Lee, Y. E. Cho, S. Kima, S. K. Jo, Appl. Phys. Lett. **81**, 3555-3557 (2002).

J. Yu, Z. Hong, W. Zhou, G. Cao, J. Xie, X. Li, S. Li, Z. Li, Appl. Phys. Lett. **70**, 490 (1996)

J. Zhang, G. Xue, A. Agarwal, R. Tsu, M. A. Hasan, J. E. Greene, A. Rockett, J. Vac. Sci. Technol. A **11**, 2553 (1993).

J.-H. Chen, N. A. Bojarczuk, Jr., H. Shang, M. Copel, J. B. Hannon, J. Karasinski, E. Preisler, S. K. Banerjee, IEEE T. Electron. Dev. **51**, 1441-1447, (2004).

Jablonski, Surf. Interface Anal. **20**, 317 (1993).

Jaffe, W. R. Cook Jr., H. Jaffe, *Piezoelectric Ceramics*, (Academic press London and New York, 1971).

John F. Watts, John Wolstenholme, *An Introduction to Surface Analysis by XPS and AES* (John Wiley & Sonst Ltd, West Sussex, England, 2003).

Johnsson, P. Lemmens, *Handbook of magnetism and advanced magnetic materials*, (John Wiley & Sons, Hoboken NJ, 2005).

K Suzuki, K. Kijima, Jpn. J. Appl. Phys. **44**, 2081-2082 (2005).

K. Chandra, K. Gupta, A. K. Nandy, P. Mahadevan, Phys. Rev. B **87**, 214110 (2013).

K. H. Härdtl, R Wernicke, Solid State Commun. **10**, 153-157 (1972).

K. H. Wedepohl, Geochim. Chosmochim. Acta **59**, 1217-1232 (1995).

K. I. Sakayori, Y. Matsui, H. Abe, E. Nakamura, M. Kenmoku, T. Hara, D. Ishikawa, A. Kokubu, K.-I. Hirota, T. Ikeda, Jpn. J. Appl. Phys. **34**(9S), 5443 (1995).

K. Ismail, J. O. Chu, B. S. Meyerson, Appl. Phys. Lett. **64**, 3124-3126 (1994).

K. J. Choi, M. Biegalski, Y. L. Li, A. Sharan, J. Schubert, R. Uecker, P. Reiche, Y. B. Chen, X. Q. Pan, V. Gopalan, L.-Q. Chen, D. G. Schlom, C. B. Eom, Science **306**, 1005 (2004).

K. J. Kormondy, S. Abel, F. Fallegger, Y. Popoff, P. Ponath, A. B. Posadas, M. Sousa, D. Caimi, H. Siegwart, E. Uccelli, L. Czornomaz, C. Marchiori, J. Fompeyrine, A. A. Demkov, Microelectronic Eng. **147**, 215 (2015).

K. J. Kormondy, Y. Popoff, M. Sousa, F. Eltes, D. Caimi, M. D. Rossell, M. Fiebig, P. Hoffmann, C. Marchiori, M. Reinke, M. Trassin, A. A. Demkov, J. Fompeyrine, S. Abel, Nanotechnology **28**, 075706 (2017).

K. Kiantaj, T. Kaufman-Osborn, A. C. Kummel, Silicon-Germanium Technology and Device Meeting (ISTDM), 2012 International, 1-2 (2012).

K. Kita, Appl. Phys. Lett. **254**, 6100-6105 (2008).

K. Lai, W. Kundhikanjana, M. Kelly, Z. X. Shen, Appl. Nanosci. **1**, 13-18 (2011).

K. Lai, W. Kundhikanjana, M. Kelly, Z. X. Shen, Rev. Sci. Instrum. **79**, 063703 (2008).

K. M. Horn, E. Chason, J. Y. Tsao, J. A. Floro, S. T. Picraux, Surf. Sci. **320**, 174-184 (1994).

K. M. Rabe, M. Dawber, C. Lichtensteiger, C. H. Ahn, J.-M. Triscone, (Springer, Berlin, Heidelberg, 2007).

K. Mistry, C. Allen, C. Auth, B. Beattie, D. Bergstrom, M. Bost, M. Brazier, M. Buehler, A. Cappellani, R. Chau, C.-H. Choi, G. Ding, K. Fischer, T. Ghani, R. Grover, W. Han, D. Hanken, M. Hattendorf, J. He, J. Hicks, R. Heussner, D. Ingerly, P. Jain, R. James, L. Jong, S. Joshi, C. Kenyon, K. Kuhn, K. Lee, H.

Liu, J. Maiz, B. McIntyre, P. Moon, J. Neirynck, S. Pae, C. Parker, D. Parsons, C. Prasad, L. Pipes, M. Prince, P. Ranade, T. Reynolds, J. Sandford, L. Shifren, J. Sebastian, J. Seiple, D. Simon, S. Sivakumar, P. Smith, C. Thomas, T. Troeger, P. Vandervoorn, S. Williams, K. Zawadzki, 2007 Int. El. Devices Meet. 247-250 (2007).

K. O. Hill, B. Malo, F. Bilodaeu, D. C. Johnson, J. Albert, Appl. Phys. Lett. **62**, 1035 (1993).

K. Oda, E. Ohue, M. Tanabe, H. Shimamoto, K. Washio, Thin Solid Films **369**, 358-361 (2000).

K. Prabhakaran, F. Maeda, Y. Watanabe, T. Ogino, Appl. Phys. Let. **76**, 2244 (2000).

K. Prabhakaran, T. Ogino, Surf. Sci. **325,** 263-271 (1995).

K. Prabhakarana, T. Ogino, R. Hull, J. C. Bean, L. J. Peticolas, Surf. Sci. **316**, 1031-1033 (1994).

K. Saraswat, C. O. Chui, T. Krishnamohan, D. Kim, A. Nayfeh, A. Pethe, Mater. Sci. Eng. B **135,** 242-249 (2006).

K. Sugibuchi, Y. Kurogi, N. Endo, J. Appl. Phys. **46**, 2877 (1975).

K. Uchiyama, A. Kasamatsu, Y. Otani, T. Shiosaki, Jpn. J. Appl. Phys. **46**, 244 (2007).

K. Washio, E. Ohue, H. Shimamoto, K. Oda, R. Hayami, Y. Kiyota, M. Tanabe, M. Kondo, T. Hashimoto, T. Harada, IEEE T. Electron. Dev. **49**, 271- 278 (2002).

Kamata, Mater Today **11**, 30-38 (2008).

Kanno, S. Fujii, T. Kamada, R. Takayama, Appl. Phys. Lett. **70**, 1378-1380 (1997).

Katsufuji, S. Mori, M. Masaki, Y. Moritomo, N. Yamamoto, H. Takagi, Phys. Rev. B **64**, 104419 (2001).

Kern, D. A. Puotinen, RCA Rev. **31**, 187-206 (1970).

Kern, *Handbook of semiconductor wafer cleaning technology* (Noyes Publications, Park Ridge, 1993) Chapter 6.

Kern, J. Electrochem. Soc. **137**, 1887-1892 (1990).

Kersch, D. Fischer, J. Appl. Phys. **106**, 014105 (2009).

Khatib, P. Jullien, B. Jannot, Ferroelectrics **145**, 181 (1993).

Kiessig, Ann. Phys. **402** (6), 715-769 (1931).

Kim, J. McVittie, K. Saraswat, Y. Nishi, Solid State Phenom. **134**, 33-36 (2008).

Kim, K. Saraswat, Y. Nishi, 2005 ECS Meeting, Abstract #779 (2005).

Kornblum, M. D. Morales-Acosta, E. N. Jin, C. H. Ahn, F. J. Walker, Adv. Mater. Interfaces **2**, 1500193 (2015).

Kresse, D. Joubert, Phys. Rev. B **59**, 1758 (1999).

Kresse, J. Furthmüller, Comput. Mat. Sci. **6**, 15-50 (1996).

Kresse, J. Furthmüller, J. Phys. Rev. B **54**, 11169-11186 (1996).

Kresse, J. Hafner, Phys. Rev. B, **47**, 558-561 (1993).

Kresse, J. Hafner, Phys. Rev. B, **49**, 14251-14271 (1994).

L. E. Cross, Mater. Chem. Phys. **43**, 108-115 (1996).

L. Jolly, *Modern Inorganic Chemistry* (McGraw-Hill Inc., New York, 1984), p.207.

L. Li, L. Q. Chen, Appl. Phys. Lett. **88**, 072905 (2006).

L. P. Rotondaro, T. Q. Hurd, A. Kaniava, J. Vanhellemont, E. Simoen, M. M. Heyns, C. Claeys, G. Brown, J. Electrochem. Soc. **143**, 3014-3019 (1996).

L. Warren, D. Dimos, R. M. Waser. MRS Bull. **21**, 40–45 (1996).

Landau, Zh. Eksp. Teor. Fiz. **7**, 19-32 (1937).

Landemark, C. J. Karlsson, L. S. O. Johansson, R. I. G. Uhrberg, Phys. Rev. B **49**, 16523-16533 (1994).

Levinshtein, S. Rumyantsev, M. Shur, *Handbook series on Semiconductor parameters*, (World scientific, Singapore, 2000).

Li, D. Cui, Y. Zhou, H. Lu, Z. Chen, Appl. Surf. Sci. **136**, 173 (1998).

Liehr, J. E. Lewis, G. W. Rubloff, J. Vac. Sci. Technol. A **5**, 1559 (1987).

Lin, D. Jiang, X. Ma, W. Shi, J. Magn. Magn. Mater. **320**, 691-694 (2008).

Lin, X. Hong, V. Wood, A. A. Verevkin, C. H. Ahn, R. A. McKee, F. J. Walker, E. D. Specht, Appl. Phys. Lett. **78**, 2034-2036 (2001).

Linz, Jr., K. Herrington, Crystal, J. Chem. Phys. **28**, 824, (1958).

Liu, P.-T. Lin, B. W. Wessels, Appl. Phys. Lett. **90**, 201104 (2007).

Long, Y. Kaneko, S. Ishiwata, Y. Taguchi, Y. Tokura, J. Phys. Condens. Matter **23**, 245601 (2011).

Lu, W. Bai, A. Ramirez, C. Mouli, A. Ritenour, M. L. Lee, and D. Antoniadis, D. L. Kwong, Appl. Phys. Lett. **87** (5), 1922 (2005).

M. Goldschmidt, Naturwissenschaften **14**, 295-297 (1926).

M. Keith, M. J. Rampling, K. Sarma, N. Mc Alford, D. C. Sinclair, J. Eur. Ceram. Soc. **24**, 1721-1724 (2004).

M. Klesse, G. Scappucci, G. Capellini, M. Y. Simmons, Nanotechnology **22**, 145604 (2011).

M. Needels, M. C. Payne, J. D. Joannopoulos, Phys. Rev. B **38**, 5543-5546 (1988).

M. Needels, M. C. Payne, J. D. Joannopoulos, Phys. Rev. B. **58**, 1765-1768 (1987).

M. Ombaba, S. B. Inayat, M. S. Islam, *Encyclopedia of Nanotechnology* (Springer, Netherlands, 2016).

M. P. Seah, W. A. Dench, Surf. Interface Anal. **1**, 2-11 (1979).

M. P. Warusawithana, C. Cen, C. R. Sleasman, J. C. Woicik, Y. Li, L. F. Kourkoutis, J. A. Klug, H. Li, P. Ryan, L.-P. Wang, M. Bedzyk, D. A. Muller, L.-Q. Chen, J. Levy, D. G. Schlom, Science **324**, 367-370 (2009).

M. Rodahl, F. Höök, A. Krozer, P. Brzezinski, B. Kasemo, Rev. Sci. Instrum. **66**(7), 3924-3930 (1995).

M. T. Bohr, R. S. Chau, T. Ghani, K. Mistry, IEEE Spectrum **44** (29), (2007).

M. V. Raymond, J. Chen, D. M. Smyth, Integr. Ferroelectr. **5**, 73–78 (1994).

M. W. J. Prins, K.-O. Grosse-Holz, G. Müller, J. F. M. Cillessen, J. B. Giesbers, R. P. Weening, R. M. Wolf, Appl. Phys. Lett. **68**, 3650-3652 (1996).

M. Walker, M. S. Tedder, J. D. Palmer, J. J. Mudd, C. F. McConville, Appl. Surf. Sci. **379**, 1-7 (2016).

M. Yasaka, X-ray thin-film measurement techniques, The Rigaku Journal **26**(2), (2010).

M.-B. Lee, M. Kawasaki, M. Yoshimoto, H. Koinuma, Appl. Phys. Let. **66**, 1331 (1995).

Maeno, H. Hashimoto, K. Yoshida, S. Nishizaki, Nature **372**, 532 (1994).

Maier, J. L. Cohn, Appl. Phys. Lett. **78**, 2536-2538 (2001).

Maroun, F. Ozanam, J.-N. Chazalviel, J. Phys. Chem. B **103**, 5280-5288 (1999).

Mavrou, P. Tsipas, A. Sotiropoulos, S. Galata, Y. Panayiotatos, A. Dimoulas, C. Marchiori, J. Fompeyrine, Appl. Phys. Lett. **93**, 212904 (2008).

Mavrou, S. F. Galata, A. Sotiropoulos, P. Tsipas, Y. Panayiotatos, A. Dimoulas, E. K. Evangelou, J. W. Seo, C. Dieker, Microelectron. Eng. **84**, 2324-2327 (2007).

Mazet, S. M. Yang, S. V. Kalinin, S. Schamm-Chardon, C. Dubourdieu, Sci. Technol. Adv. Mater. **16**, 036005 (2015).

Ménoret, J. M .Kiat, B. Dkhil, M. Dunlop, H. Dammak, O. Hernandez, Phys. Rev. B **65**, 224104 (2002).

Merckling, G. Saint-Girons, C. Botella, G. Hollinger, Marc Heyns, J. Dekoster, M. Caymax, Appl. Phys. Lett. **98**, 092901 (2011).

Meyer, N. M. Amer, Appl. Phys. Lett. **53**, 1045 (1988).

Micoulaut, L. Cormier, G. S. Henderson, J. Phys.: Condens. Matter **18**, R753 (2006).

Miranda, K. Boulahya, M. Hernando, D. C. Sinclair, F. Jimenez-Villacorta, A. Varela, J. M. Gonzalez-Calbet, M. Parras, Chem. Mater. **23**, 1050-1060 (2011).

Mitra, AIP Adv. **2**, 032148 (2012).

Mitra, C. Lin, A. B. Posadas, A. A. Demkov, Phys. Rev. B **90**, 125130 (2014).

Molle, M. N. K. Bhuiyan, G. Tallarida, M. Fanciulli, Mat. Sci. Semicon. Proc. **9**, 673-678 (2006).

Monkhorst, J. Pack, Phys. Rev. B **13**, 5188 (1976).

Moreira dos Santos, S. Parashar, A. R. Raju, Y. S. Zhao, A. K. Cheetham, C. N. R. Rao, Solid State Commun. **122**, 49-52 (2002).

Moriyama, N. Hirashita, K. Usuda, S. Nakaharai, N. Sugiyama, E. Toyoda, S.-I. Takagi, Appl. Surf. Sci. **256**, 823–829 (2009).

Nakayama, H. Katayama-Yoshida, Jpn. J. Appl. Phys. **40**, 1355-1358 (2001).

Nayfeh, C. O. Chui, K. C. Saraswat, T. Yonehara, Appl. Phys Lett. **85**, 2815 (2004).

Niu, B. Gautier, S. Yin, G. Saint-Girons, P. Lecoeur, V. Pillard, G. Hollinger, B. Vilquin, Thin Solid Films **259**, 218 (1995).

Niu, F. & Wessels, B. W. J. Vac. Sci. Technol. B **25**, 1053–1057 (2007).

Niu, S. Yin, G. Saint-Girons, B. Gautier, P. Lecoeur, V. Pillard, G. Hollinger, B. Vilquin, Microelectron. Eng. **88**, 1232–1235 (2011).

O. Chui, F. Ito, K. C. Saraswat, IEEE Electr. Device L. **25** (9), (2004).

O. Chui, H. Kim, D. Chi, B. B. Triplett, P. C. McIntyre, and K. C. Saraswat, Int. El. Devices Meet. 437-440 (2002).

O. Chui, H. Kim, D. Chi, P. C. McIntyre, K. C. Saraswat, IEEE T. Electron. Dev. **53**(7), 1509-1516 (2006).

O. Chui, H. Kim, P. C. McIntyre, K. C. Saraswat, IEEE Electr. Device L. **25**, 274-276 (2004).

O. Chui, H. Kim, P. C. McIntyre, K. C. Saraswat, IEEE Electr. Device L. **25**, 5, (2004).

O. Chui, S. Ramanathan, B. B. Triplett, P. C. McIntyre, K. C. Saraswat, IEEE Elect. Dev. Letters, **23**, 473-475 (2002).

Okumura, T. Akane, S. Matsumoto, Appl. Surf. Sci. **125**, 125-128 (1998).

Onsia, T. Conard, S. De Gendt, M. Heyns, I. Hoflijk, P. Mertens, M. Meuris, G. Raskin, S. Sioncke, I. Teerlinck, A. Theuwis, J. Van Steenbergen, C. Vinckier, Solid State Phenom. **103-104**, 19-22 (2005).

Outzourhit, J. U. Trefny, T. Kito, B. Yarar, A. Naziripour, A. M. Hermann, Thin Solid Films, **259** , 218 (1995).

P. A. M. Bakkers, J. A. van Dam, S. De Franceschi, L. P. Kouwenhoven, M. Kaiser, M. Verheijen, H.Wondergem, P. van der Sluis, Nat. Mater. 3, 769-773 (2004).

P. Bai, N. Lu, J. Liu, A. Ramirez, D. L. Kwong, D. Wristers, A. Ritenour, L. Lee, D. Antoniadis, 2003 VLSI Tech. Dig. 121-122 (2003).

P. Batra, P. Wurfel, B. D. Silverman, Phys. Rev. B **8**, 3257-3265 (1973).

P. Brunco, B. De Jaeger, G. Eneman, J. Mitard, G. Hellings, A. Satta, V. Terzieva, L. Souriau, F. E. Leys, G. Pourtois, M. Houssa, G. Winderickx, E. Vrancken, S. Sioncke, K. Opsomer, G. Nicholas, M. Caymax, A. Stesmans, J. Van

Steenbergen, P. W. Mertens, M. Meuris, M. M. Heynsa, J. Electrochem. Soc. **155** (7), H552-H561 (2008).

P. Gusev, C. Cabral Jr., M. Copel, C. D'Emic, M. Gribelyuk, Microelectron. Eng. **69**, 145–151 (2003).

P. Gusev, H. Shang, M. Copel, M. Gribelyuk, C. D'Emic, P. Kozlowski, and T. Zabel, Appl. Phys. Lett. **85**, 2334 (2004).

P. Pavan, R. Bez, P. Olivo, E. Zanoni, P. IEEE **85**, 1248-1271 (1997).

Pillarisettty, Nature **479**, 324-328 (2011).

Pizzi, K. L. Mittal, *Handbook of Adhesive Technology* (Marcel Dekker Inc., New York, 2003).

Poelman, P. Clauws, B. Depuydt, Solar Energy Materials and Solar Cells 76, 167-173 (2003).

Ponath, A. B. Posadas, A. A. Demkov, Appl. Phys. Rev. **4**, 021308 (2017).

Ponath, A. B. Posadas, R. C. Hatch, A. A. Demkov, J. Vac. Sc. Technol. B **31**, 031201 (2013).

Ponath, K. Fredrickson, A. B. Posadas, Y. Ren, X. Wu, R. K. Vasudevan, M. Baris Okatan, S. Jesse, T. Aoki, M. R. McCartney, D. J. Smith, S. V. Kalinin, K. Lai, A. A. Demkov, Nat. Commun. **6**, 6067 (2015).

Posadas, M. Berg, H. Seo, D. J. Smith, H. Celio, A. P. Kirk, D. Zhernokletov, R. M. Wallace, A. de Lozanne, A. A. Demkov, Appl. Phys. Lett. **98**, 055104 (2011).

Prellier, M. P. Singh, P. Murugavel, J. Phys.: Condens. Matter **17**, 803-832 (2005).

R. Camp, J. Electrochem. Soc. **102**, 586-593 (1955).

R. Grove, Philos. Mag **5**, 203 (1853).

R. J. Cava, J. Am. Ceram. Soc. **83**, 5-28 (2000).

R. Lide, *Handbook of Chemistry and Physics* (CRC Press, Boca Raton, 1994), p. 8/45.

R. M. Cornell, U. Schwertmann, *The iron oxides: structure, properties, reactions, occurrences and uses* (Wiley-VCH, Weinheim, 2003).

R. Sutherland, E. H. Sargent, Nat. Photon. **10**, 295-302 (2016).

R. W. Olesinski, G. J. Abbaschian, J. Phase Equilib. **5**, 484-486 (1984).

R. Xie, M. Yu, M. Y. Lai, L. Chan, C. Zhu, Appl. Phys. Lett. **92**, 163505 (2008)

R. Zhang, P. C. Huang, N. Taoka, M. Takenaka, S. Takagi, IEEE VLSI symp. 161-162 (2012).

Rajamani, G. F. Dionne, D. Bono, C. A. Ross, J. Appl. Phys. **98**, 063907 (2005).

Ramesh, N. A. Spaldin, Nature Mater. **6**, 21 (2007).

Ramesh, S. Aggarwal, O. Auciello, Mater. Sci. Eng.: R: Report **32**, 191 (2001).

Rogalski, *Infrared detectors* (CRC Press, Boca Raton, 2011).

Rong, Y. Ge, Y. Huo, M. Fiorentino, M. R. T. Tan, T. I. Kamins, T. J. Ochalski, G. Huyet, J. S. Harris Jr., IEEE J. Sel. Top. Quant. **16**, 85-92 (2010).

S. Bhalla, R. Guo, R. Roy, Mat. Res. Innovat. **4**, 3-26 (2000).

S. Jesse, A. Kumar, S. V. Kalinin, A. Gannepali, R. Proksch, R. Microscopy Today **18**, 34-40 (2010).

S. Jesse, A. P. Baddorf, S. V. Kalinin, Appl. Phys. Lett. **88**, 062908 (2006).

S. Jesse, S. V. Kalinin, R. Proksch, A. P. Baddorf, B. J. Rodriguez, Nanotechnology **18**, 435503 (2007).

S. Kagawa, T. Mikawa, T. Kaneda, Jpn. J. Appl. Phys. **21** (11), 1616-1618 (1982).

S. M. Anlage, D. E. Steinhauer, B. J. Feenstra, C. P. Vlahacos, F. C. Wellstood, *Microwave Superconductivity*, pp. 239–269 (Kluwer Academic Publishers, Amsterdam, 2001).

S. M. Anlage, V. V. Talanov, A. R. Schwartz, *Scanning Probe Microscopy: Electrical and Electromechanical Phenomena at the Nanoscale*, pp. 207–245 (Springer, New York, 2006).

S. Mathews, R. Ramesh, T. Venkatesan, J. Benedetto, Science **11**, 238 (1997).

S. Mathews, R. Ramesh, T. Venkatesan, J. Benedetto, Science **276**, 238-240 (1997).

S. Matsubara, S. Miura, Y. Miyasaka, N. Shohata, J. Appl. Phys. **66**, 5826 (1989).

S. Paleari, S. Baldovino, A. Molle, M. Fanciulli, Phys. Rev. Lett. **110**, 206101 (2013).

S. R. Amy, Y. J Chabal, F. Amy, A. Kah, C. Krugg, P. Kirsch, Mater. Res. Soc. Symp. Proc. **917**, (2006).

S. Ray, P. Mahadevan, S. Mandal, S. R. Krishnakumar, C. S. Kuroda, T. Sasaki, T. Taniyama, M. Itoh, Phys. Rev. B **77**, 104416 (2008).

S. Ray, Y. V. Kolen'ko, K. A. Kovnir, O. I. Lebedev, S. Turner, T. Chakraborty, R. Erni, T. Watanabe, G. van Tendeloo, M. Yoshimura, M. Itoh, Nanotechnology **23**, 025702 (2012).

S. Rivillon, Y. J. Chabal, F. Amy, A. Kahn, Appl. Phys. Lett. **87**, 253101 (2005).

S. Roberts, Phys. Rev. **71**, 890 (1947).

S. Salahuddin, S. Datta, Nano Lett. **8**, 405-410 (2008).

S. Sioncke, D. P. Brunco, M. Meuris, O. Uwamahoro, J. Van Steenbergen, E. Vrancken, M. M. Heyns, ECS Trans. **16** (10), 451-460 (2008).

S. Sun, Y. Sun, Z. Liu, D.-I. Lee, S. Peterson, P. Pianetta, Appl. Phys. Lett. **88**, 021903 (2006).

S. Tanuma, C. J. Powell, D. R. Penn, Surf. Interface Anal. **21**, 165 (1994).

S. Van Elshocht, B. Brijs, M. Caymax, T. Conard, T. Chiarella, S. De Gendt, B. De Jaeger, S. Kubicek, M. Meuris, B. Onsia, O. Richard, I. Teerlinck, J. Van Steenbergen, C. Zhao, and M. Heyns, Appl. Phys. Lett. **85**, 3824 (2004).

S. Verhaverbeke, M. Meuris, P. W. Mertens, M. M. Heyns, A. Philipossian, D. Graf, A. Schnegg, 1991 Int. El. Devices. Meet. 71-74 (1991).

S. W. Cheong, M. Mostovoy, Nature Mater. **6**, 13 (2007).

S. Yang, X. D. Wang, K. Cho, J. Kishimoto, S. Fukatsu, T. Hashizume, T. Sakurai, Phys. Rev. B **50**, 2406 (1994).

S. Yu, C. H. Huang, A. Chin, C. Zhu, M. F. Li, B. J. Cho, and D.-L. Kwong, IEEE Electr. Device L. **25** (3), (2004).

Sauerbrey, Z. Phys. **155** (6)**,** 206-222 (1959).

Scappucci, O. Warschkow, G. Capellini, W. M. Klesse, D. R. McKenzie, M. Y. Simmons, Phys. Rev. Lett. **109**, 076101 (2012).

Schulze, M. Henzler, Surf. Sci. **73**, 553-559 (1978).

Sharma, G. Pilania, G. A. Rossetti Jr., K. Slenes, R. Ramprasad, Phys. Rev. B **87**, 134109 (2013).

Simoen, J. Mitard, G. Hellings, G. Eneman, B. De Jaeger, L. Witters, B. Vincent, R. Loo, A. Delabie, S. Sioncke, M. Caymax, C. Claeys, Materials Science in Semiconductors Processing **15**, 588-600 (2012).

Suryanarayana, M. Grant Norton, *X-Ray diffraction - A practical approach*, (Springer US, New York, 1998).

T. Endoh, H. Koike, S. Ikeda, T. Hanyu, H. Ohno, IEEE J. Em. Sel.Top. C. **6**, 109-119 (2016).

T. Kaufman-Osborn, K. Kiantaj, C.-P. Chang, A. C. Kummel, Surf. Sci. **630**, 254-259 (2014).

T. Kimura, S. Kawamoto, I. Yamada, M. Azuma, M. Takano, Y. Tokura, Phys. Rev. B **67**, 180401 (2003).

T. Krishnamohan, Z. Krivokapic, K. Uchida, Y. Nishi, K. C. Saraswat, IEEE Trans. Elect. Dev. **53**, 990-999 (2006).

T. Maruyama, H. Akagi, J. Electrochem. Soc. **143**, 4087-4089 (1996).

T. Nishimura, S. Kabuyanagi, W. Zhang, C. H. Lee, T. Yajima, K. Nagashio, A. Toriumi, Appl. Phys. Express **7**, 051301 (2014).

T. P. Ma, J.-P. Han, IEEE Electron Device Lett. **23**, 386 (2002).

T. P. Schneider, D. A. Aldrich, J. Cho, R. J. Nemanich, Mat. Res. Soc. Symp. Proc. **220**, 21 (1991).

T. Q. Ngo, A. B. Posadas, M. D. McDaniel, C. Hu, J. Bruley, E. T. Yu, A. A. Demkov, J. G. Ekerdt, Appl. Phys. Lett. **104**, 082910 (2014).

T. Rosner. D. W. van derWeide, Rev. Sci. Instrum. **73**, 2505-2525 (2002).

T. S. Böscke, J. Müller, D. Bräuhaus, U. Schröder, U. Böttger, Appl. Phys. Lett. **99**, 102903 (2011).

T. Tybell, C. H. Ahn, J.-M. Triscone, Appl. Phys. Lett. **75**, 856-858 (1999).

T. Zhao, S. B. Ogale, S. R. Shinde, R. Ramesh, R. Droopad, J. Yu, K. Eisenbeiser, J. Misewich, Appl. Phys. Lett. 84, 750-752 (2004).

Tabet, M. Faiz, N. M. Hamdan, Z. Hussain, Surf. Sci. **523**, 68–72 (2003).

Takahisa, Surf. Sci. 255, 229-236 (1991).

Tao, A. Yelon, E. Sacher, Z. H. Lu, M. J. Graham, Appl. Phys. Lett. **60**, 2669 (1992).

Taylor, N. J. Doyle, Scr. Metal. **1**, 161-162 (1967).

Toriumi, T. Tabata, C. H. Lee, T. Nishimura, K. Kita, K. Nagashio, Microelectron. Eng. **86**, 1571-1576 (2009).

Tselev, N. V. Lavrik, A. Kolmakov, S. V. Kalinin, Advanced Functional Materials **23,** 2635 (2013).

V. Hamza, G. D. Kubiak, R. H. Stulen, Surf. Sci. **237**, 35-52 (1990).

V. Ramana, S. M. Yang, R. Jung, M. H. Jung, B. W. Lee, C. U. Jung, J. Appl. Phys. **113**, 187219 (2013).

V. Stuart, *Vacuum technology, thin films, and sputtering: an introduction* (Academic Press, New York, 1983).

Vaithyanathan, J. Lettieri, W. Tian, A. Sharan, A. Vasudevarao, Y. L. Li, A. Kochhar, H. Ma, J. Levy, P. Zschack, J. C. Woicik, L. Q. Chen, V. Gopalan, D. G. Schlom, J. Appl. Phys. **100,** 024108-024109 (2006).

von Hippel, Rev. Mod. Phys. **22**, 221 (1950).

W. Anderson, M. C. Hanf, P. R. Norton, Z. H. Lu, M. J. Graham, Appl. Phys. Lett. **66**, 1123 (1995).

W. Ashcroft, N. D. Mermin, *Solid State physics* (Harcourt, Orlando, 1976) p.76.

W. Laubengayer, D. S. Morton, J. Am. Chem. Soc. **54**, 2303-2320 (1932).

W. Trucks, K. Raghavachari, G. S. Higashi, Y. J. Chabal, Phys. Rev. Lett. **65**, 504-507 (1990).

W. Wessel, J. Cryst. Growth **195**, 706 (1998).

W. Wessels, Annu. Rev. Mater. Res. **37**, 659 (2007).

Watanabe, Appl. Phys. Lett. **66**, 1770 (1995).

Wu, Q. Zhang, C. Zhu, IEEE Elect. Dev. Letters, **25**, 631-633 (2004)

Wurfel, I. P. Batra, Phys. Rev. B **8**, 5126 (1973).

www.ajaint.com

www.mantisdeposition.com

www.piezo-parts.co.jp

www.scientaomicron.com

Xiong, W. H. P. Pernice, J. H. Ngai, J. W. Reiner, D. Kumah, F. J. Walker, C. H. Ahn, H. X. Tang, Nano Lett. **14**, 1419 (2014).

Xu, K. B. Yin, J. Lin, Y. D. Xia, X. G. Wan, J. Yin, X. J. Bai, J. Du, Z. G. Liu, Phys. Rev. B **79**, 134109 (2009).

Y. Cho, F. K. Reinhart, Appl. Phys. Lett. **21** (8), 355-356 (1972).

Y. Cho, J. R. Arthur, Prog. Solid State Chem. **10**, 157-191 (1975).

Y. L. Shen, Surf. Sci. **47**, 685-691 (1975).

Y. Yoshimoto, Y. Nakamura, H. Kawai, M. Tsukada, M. Nakayama, Phys. Rev. B **61**, 1965-1970 (2000).

Y.-H. Kuo, Y. K. Lee, Y. Ge, S. Ren, J. E. Roth, T. I. Kamins, D. A. B. Miller, J. S. Harris, Nature **437**, 1334-1336 (2005).

Y.-H. Lin, S. Zhang, C. Deng, Y. Zhang, X. Wang, C.W. Nan, Appl. Phys. Lett. **92**, 112501 (2008).

Y.-S. Lin, R. Puthenkovilakam, and J. P. Chang, Appl. Phys. Lett. **81**(11), 2041-2043 (2002).

Yang, K. Lai, Q. Tang, W. Kundhikanjana, M. A. Kelly, K. Zhang, Z.-X. Shen, X. Li. J. Micromech. Microeng. **22**, 115040 (2012).

Z. Qin, D. Shi, W. Ji, S. Pan, H.-J. Gao, Nanotechnology **17**, 2396-2398 (2006).

Z. Yan, Y. Guo, G. Zhang, J.M. Liu, Adv. Mater. **23**, 1351 (2011).

Z. Yu, J. Ramdani, J. A. Curless, C. D. Overgaard, J. M. Finder, R. Droopad, K. W. Eisenbeiser, J. A. Hallmark, W. J. Ooms, V. S. Kaushik. J. Vac. Sci. Technol. B **18**, 2139-2145 (2000).

Z.-A. Ren, G.-C. Che, X.-L. Dong, J. Yang, W. Lu, W. Yi, X.-L. Shen, Z.-C. Li, L.-L. Sun, F. Zhou, Europhys. Lett. **83**, 17002 (2008).

Zachariasen, Z. Kristallogr. **67**, 226 (1928).

Zorko, M. Pregelj, M. Gomilsek, Z. Jaglicic, D. Pajic, M. Telling, I. Arcon, I. Mukulska, M. Valant, Sci. Rep. **5**, 7703 (2015).